Studies using $B^{\pm} \to Dh^{\pm}$ decays in the LHCb Run I data

Donal Hill
St. Cross College, University of Oxford

Thesis submitted in fulfilment of the requirements for the degree of Doctor of Philosophy
at the University of Oxford
Hilary Term, 2015

Abstract

Using data equivalent to an integrated luminosity of 3fb^{-1} collected by the LHCb experiment during Run I (2011-2012), studies of beauty mesons decaying to a final state containing open charm are performed, concluding with a number of new results.
Direct $\mathcal{CP}$-violation is explored in $B^{\pm} \to Dh^{\pm}$ decays through several measurements of $\mathcal{CP}$ violating observables, where the charmed meson D is reconstructed in both 2-track and 4-track final states. A measurement of the $B^{\pm}$production asymmetry at LHCb is reported using $B^{\pm} \to D\pi^{\pm}$decays, and a complementary measurement of the $\mathcal{CP}$ asymmetry in $B^{\pm} \to J/\psi K^{\pm}$ decays made. A search for the rare $B_c^- \to \bar{D}^{(*)}\pi^-$ and $B_c^- \to \bar{D}^{(*)}K^-$ decays concludes this work.

Acknowledgements

Firstly, I would like to thank the Science and Technology Facilities Council (STFC) for funding my studentship at Oxford and enabling me to work on location at CERN for two years during my PhD. I am also grateful to St. Cross College, the Institute of Physics (IOP) and the Oxford particle physics sub-departments for funding my attendance at the Kruger 2014 conference.

This thesis owes a great deal to the hard work and dedication of many LHCb collaborators. I am particularly indebted to my supervisor Malcolm John for his passionate support over the past number of years. It has been a privilege to learn under his expert guidance, and I am extremely proud of the work we have completed together.

The wider Oxford LHCb family, including those that have since moved onto pastures new, have been crucial in the development of the work presented within this thesis. I offer my thanks to Guy Wilkinson, Neville Harnew, Sneha Malde, Mat Charles, Andrew Powell, Chris Thomas, Denis Derkach, Dan Johnson, Andrea Contu, Philip Hunt, Sophie Redford, Hamish Gordon, Rhorry Gauld, Ed Greening, Nick Torr and Ed Smith for their insight and assistance.

A special thanks to Nazim Hussain and Scott Stevenson for their support during our time as LHCb students together, and to the rest of the Oxford particle physics academic staff and student body. My sincere thanks also to the Oxford secretaries Sue Geddes, Kim Proudfoot and Francesca Oliver, for their tireless effort in guaranteeing the smooth operation of the sub-department. It has been a pleasure to be part of such a vibrant and successful community.

Many thanks to Mika Vesterinen and Marian Stahl for their expert assistance in the $B^{\pm}$ production asymmetry measurement, and to Paolo Gandini for his efforts in developing the 1 fb^{-1} iteration of the ADS/GLW analysis. I am grateful to all members of the B decays to Open Charm, Semileptonic B decays and B hadrons and Quarkonia

working groups for their invaluable input on my work, and would like to thank the RICH sub-detector community for their support and guidance throughout my PhD.

Finally, my love and thanks to Mum, Dad and Claire for all of their support and care. Without them, none of this would have been possible.

Preface

This thesis describes three analyses performed using $B^\pm \to Dh^\pm$ decays in the LHCb Run I data, where D refers to the neutral charmed meson produced in the B decay and $h \in \{\pi, K\}$ refers to the companion pion or kaon produced along with the D. The thesis is organised as follows:

- **Chapter 1:** An overview of B physics at the LHC is given, outlining the production of heavy mesons in proton-proton collisions and their study at LHCb. A discussion of $\mathcal{CP}$-violation within the Standard Model is also provided.
- **Chapter 2:** The LHCb detector is described, with specific focus on the use of each sub-detector for physics analysis.
- **Chapter 3:** The ADS/GLW technique using $B^\pm \to Dh^\pm$ decays is introduced. The selection strategy and background suppression are discussed.
- **Chapter 4:** Building on Chapter 3, the invariant mass fit used to measure $\mathcal{CP}$ observables in $B^\pm \to Dh^\pm$ decays is detailed. Results for each of the $\mathcal{CP}$ observables are presented.
- **Chapter 5:** The $B^\pm$ production asymmetry at LHCb is measured using $B^\pm \to D\pi^\pm$ decays, adopting the selection strategy from Chapter 3 and the fit technique from Chapter 4. This result is immediately used in a measurement of the $\mathcal{CP}$ asymmetry in $B^\pm \to J/\psi K^\pm$ decays.
- **Chapter 6:** A search for $B_c^- \to \bar{D}^{(*)} h^-$ decays is performed, using the $B^- \to D^0\pi^-$ decay as a normalisation channel. This analysis recycles much of what has been developed in earlier Chapters, providing an interesting extension to the work.
- **Chapter 7:** A conclusion is drawn.

In addition to the work presented within this thesis, an analysis carried out during my first year was published in PRD. Within this work, a first observation of the $B^0 \to D^{*-}K^+\pi^-\pi^+$

decay was made, along with an improved measurement of the $B^0 \to D^{*-}\pi^+\pi^-\pi^+$ branching fraction. The publication is reproduced in a dedicated appendix for reference.

All of the work contained within this thesis is my own, with the exception of the detection asymmetries described in Section 5.3, which were measured by Rainer Borchardt and Mika Vesterinen, and the background PDFs detailed in Section 3.4.1, which were conceived by Paolo Gandini. All of the analyses presented are currently within internal review, with the aim of producing publications in Spring 2015.

Contents

"You can know the name of a bird in all the languages of the world,
but when you're finished, you'll know absolutely nothing whatever about the bird...
So let's look at the bird and see what it's doing – that's what counts."

— Richard P. Feynman

Chapter 1.

Hadronic B physics at the Large Hadron Collider

In this Chapter, an introduction to the field of heavy flavour physics at hadron colliders is given. In Section 1.1, the LHC accelerator is introduced. The production of various B meson species at LHCb is detailed in Section 1.2, with specific focus on the production asymmetry of $B^{\pm}$ mesons (measured in Chapter 5) and the creation of B_c mesons (studied in Chapter 6). The concept of $\mathcal{CP}$-violation in $B^{\pm}$ decays is outlined in Section 1.3, paving the way for the measurement of $\mathcal{CP}$ violating observables in Chapter 4.

1.1. The Large Hadron Collider

Residing under the Franco-Swiss border near the city of Geneva, the Large Hadron Collider (LHC) at CERN represents the state of the art in particle accelerator technology. With the ability to collide beams of protons at a maximum centre of mass energy of $\sqrt{s} = 14$ TeV and a design luminosity of 10^{34} cm^{-2}s^{-1}, the LHC is the most powerful particle collider ever built [1]. The 27 km circumference synchrotron is situated in the same tunnel used to house the LEP e^+e^- collider, which was decommissioned in 2000 after over a decade of successful operation.

The LHC, as illustrated in Figure 1.1, consists of eight octants and two separate rings, one for each proton beam. Unlike its predecessor LEP, which consisted of only one ring, the LHC employs a two-ring design due to the identical charge of the colliding proton beams. The like charges and opposite directions of motion of the beams demand the use of oppositely oriented magnetic fields within each ring. High field strengths of up to 8 T

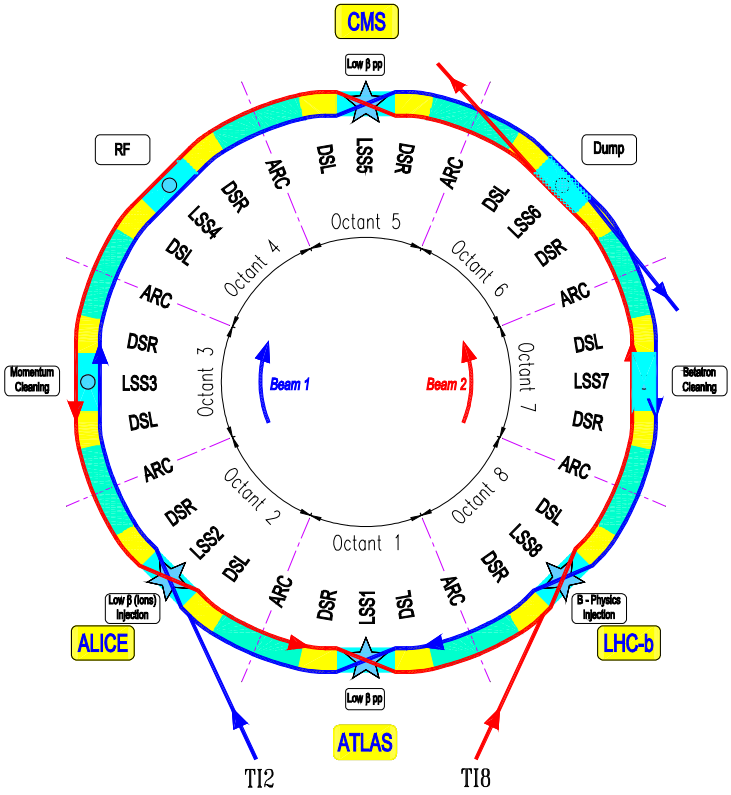

Figure 1.1.: Layout of the LHC accelerator [6], with each of the eight octants and four interaction points shown. LHCb is located in Octant 8.

are provided by several superconducting dipole magnets, which are cooled to 1.9 keV using superfluid helium and positioned at several points around the ring circumference. A cross-section of an LHC dipole is shown in Figure 1.2, where the oppositely oriented magnetic fields in each ring are clearly visible.

Protons are injected from the Super Proton Synchrotron (SPS) at an energy of 450 GeV, and accelerated to their collision energy of 3.5 (4) TeV, corresponding to a total centre of mass energy of $\sqrt{s} = 7$ (8) TeV in 2011 (2012). The proton beams are kept separate in the machine, and cross only at four interaction points (IP). At each of these points, one of the main LHC experiments is situated: ATLAS [2] at IP1, ALICE [3] at IP2, CMS [4] at IP5 and LHCb [5] at IP8. The general purpose ATLAS and CMS detectors are designed to run at the peak machine luminosity of 10^{34} cm^{-2}s^{-1}, whereas LHCb is designed to run at a reduced instantaneous luminosity of 10^{32} cm^{-2}s^{-}1. This luminosity is delivered in high intensity bunches containing 10^{11} protons, where the bunches are separated by 50 ns intervals. The design bunch spacing of the LHC is 25 ns, corresponding to a maximum bunch crossing frequency of 40 MHz.

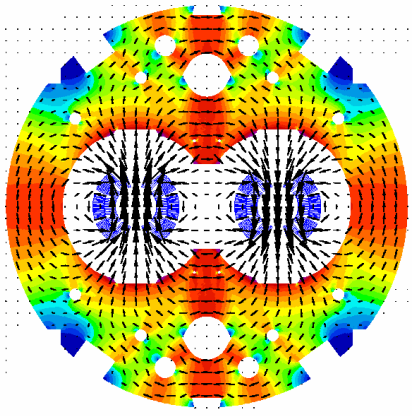

Figure 1.2.: Cross-section magnetic field map of an LHC dipole, indicating the oppositely oriented fields for each ring [6]. The colour scale represents the magnitude of the magnetic flux at each point, where red (blue) regions indicate ares of high (low) magnetic flux.

1.2. Heavy flavour production at LHCb

LHCb is focused on the study of heavy flavour hadrons, with the goal of performing precision measurements of $\mathcal{CP}$-violation and rare decay phenomena. As a hadron collider experiment, LHCb is uniquely placed to take advantage of the high production cross-section of $b\bar{b}$ pairs in LHC proton-proton collisions [7], allowing it to collect the worlds largest sample of $\sim 10^{12}$ exclusively reconstructed charm and beauty decays during Run I. LHCb also benefits from a larger boost than the e^+e^- B factories [8, 9], and is capable of studying all species of b hadrons.

1.2.1. Production asymmetries

The production rates of each type of b and $\bar{b}$ hadron in pp collisions are not expected to be identical. This phenomenon, collectively referred to as the production asymmetry, arises from the fact that coalescence between a perturbatively produced b or $\bar{b}$ quark and a u or d valence quark from the beam remnant can occur, resulting in a slight excess in the production of B^+ and B^0 mesons ($\bar{b}u$ and $\bar{b}d$, respectively) relative to B^- and $\bar{B}^0$ mesons. As the production asymmetry is driven by non-perturbative effects, precise predictions are not available. However, the B^0 meson production asymmetry, defined as:

$$A_{B_d} = \frac{\sigma(pp \to B^0 + X) - \sigma(pp \to \bar{B}^0 + X)}{\sigma(pp \to B^0 + X) + \sigma(pp \to \bar{B}^0 + X)} \tag{1.1}$$

has been studied [10], where σ denotes the production cross-section. It is predicted to be small at low rapidity and transverse momentum, with an increase to several percent at high transverse momentum and rapidity. In the latter case, the b and $\bar{b}$ quarks reside closer to the beam remnant, which is composed predominantly of up-type quarks, resulting in an excess of B^0 mesons. This trend is illustrated in Figure 1.3 (b), where the production asymmetry is seen to initially rise at high rapidity.

At very high values of rapidity (beyond the LHCb acceptance), the colour connection to di-quark combinations in the undissociated proton drags the b (rather than the $\bar{b}$) to even higher rapidity, via non-hadronised *buu* and *bud* combinations. This results in an excess of b quarks over $\bar{b}$ quarks at highest rapidity, and a resulting excess of $\bar{B}^0$ mesons. The sign of A_{B_d} is caused to change, explaining the feature at highest rapidity in Figure 1.3. This behaviour is expected to apply equally to $B^\pm$ mesons.

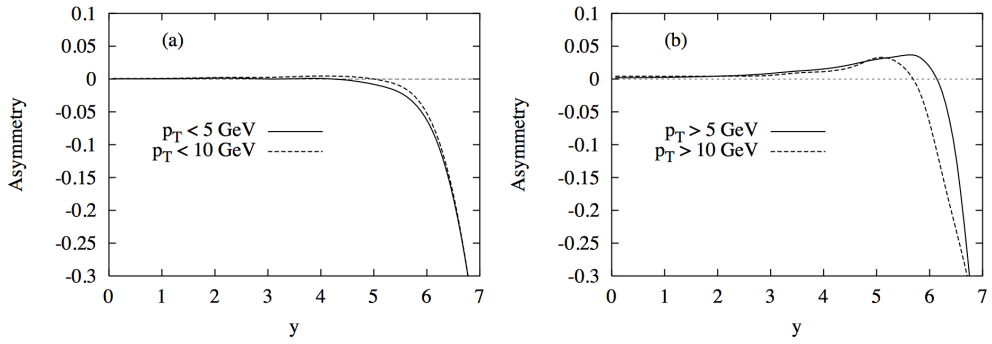

Figure 1.3.: Predictions for the B^0 production asymmetry as a function of rapidity (y), at both low (a) and high (b) transverse momentum [10]. The asymmetry is defined in Equation 1.1, where the anti-quark containing B^0 meson cross section is subtracted from the quark containing $\bar{B}^0$ cross section. Note that this is opposite to the definition of A_{B_u} used in this thesis, as shown in Equation 1.2.

The production asymmetry of $B^\pm$ mesons is defined as:

$$A_{B_u} = \frac{\sigma(pp \to B^- + X) - \sigma(pp \to B^+ + X)}{\sigma(pp \to B^- + X) + \sigma(pp \to B^+ + X)} \tag{1.2}$$

where it is important to note that the asymmetry is defined in the opposite sense to A_{B_d} in Equation 1.1. The production asymmetry effect can contribute considerable uncertainty in searches for small $\mathcal{CP}$-violation effects, for example in the measurement of the semileptonic asymmetry $a^d_{\rm sl}$, where a background from $B^\pm$ decays can fake anomalous $\mathcal{CP}$-violation in B^0 mixing due to the production asymmetry [11]. Measuring A_{B_u} with improved precision is thus well motivated, and forms the focus of Chapter 5.

Previous measurements of A_{B_u} at LHCb have employed the $B^\pm \to J/\psi K^\pm$ final state, where external input on the $\mathcal{CP}$ asymmetry in this decay is required. Previously, using $A_{CP}^{J/\psi K} = (0.3 \pm 0.6)\%$ [12], LHCb have measured $A_{B_u} = (-0.6 \pm 0.6)\%$ [13], where the limiting factor is the precision with which $A_{CP}^{J/\psi K}$ is known. LHCb has also performed measurements of the B^0 meson production asymmetry [14] and the analogous production asymmetries in $D^\pm$ and $D_s^\pm$ mesons [15], measuring values in the 1% region or less.

1.2.2. B_c production

In addition to the study of $B^\pm$ and B^0 mesons, a unique advantage of LHCb is its ability to produce and study the heavier B hadrons, namely B_s^0, $B_c^\pm$ and Λ_b^0. The study of B_s^0 mesons is of particular interest in the domain of time-dependent $\mathcal{CP}$-violation, where LHCb has performed precise measurements of the $\mathcal{CP}$ violating phase ϕ_s during Run I [16], something the previous generation of experiments could not achieve due to either a lack of energy, statistics or mass resolution.

The study of B_c mesons has also developed into an active area of research, driven by the high event yields obtained in Run I data [17–19]. Mesons of this type are difficult to produce by virtue of the fact that they contain a companion charm quark, such that production cross-sections are suppressed by a factor f_c/f_u with respect to $B^\pm$ production, where f_c and f_u are the fragmentation fractions for c and u quarks, respectively. The higher than expected B_c yields in Run I imply a larger value of the fragmentation fraction f_c than was previously expected, opening up the possibility of measuring various B_c decays modes in the Run I data. A search for fully hadronic $B_c^- \to \bar{D}^{(*)} h^-$ decays is presented in Chapter 6.

1.3. $\mathcal{CP}$-violation in B decays

A central area of research focus at LHCb is the measurement of $\mathcal{CP}$-violation in B decays, both through the study of direct $\mathcal{CP}$-violation and the interference between mixing and decay processes. The study of $\mathcal{CP}$-violation is of great importance, as it remains the only observed means by which matter and antimatter can exhibit differences in their behaviour. In addition, characterising the degree of $\mathcal{CP}$-violation in the Standard Model provides a strong benchmark against which any matter-antimatter asymmetry effects arising from New Physics can be judged.

The measurement of direct $\mathcal{CP}$-violation in $B^{\pm} \to Dh^{\pm}$ decays have particularly strong relevance to tests of Standard Model $\mathcal{CP}$-violation, and forms the focus of Chapter 4. What follows is a discussion of the phenomenon of $\mathcal{CP}$-violation as it appears within the Standard Model, including an introduction to $\mathcal{CP}$-violation in mixing processes, decay processes and in the interference between mixing and decay processes.

1.3.1. $\mathcal{C}, \mathcal{P}$ and $\mathcal{T}$ symmetries

The concept of symmetry lies at the heart of many scientific disciplines, and elementary particle physics is no exception. Symmetries are deeply connected to conservation laws in a relationship embodied by Noether's theorem: any symmetry of a physical system that is differentiable has a corresponding conservation law [20]. For instance, the laws of physics are symmetric with respect to translations in time - they work in the same way today as they did yesterday. Noether's theorem relates this time invariance to the conservation of energy.

Systems exhibiting translational invariance conserve momentum, and any system symmetrical under rotations about a point will conserve angular momentum. Similarly, the invariance of electrodynamics under gauge transformations results in the conservation of electric charge. Such gauge symmetries are central to the current understanding of fundamental physics, and form the foundations of the Standard Model of particle physics.

Given the evident invariance of physical law under continuous symmetries, one might expect the same behaviour from discrete symmetries. Of specific relevance to this thesis are the discrete symmetries of charge conjugation (C), parity (P) and time-reversal (T), with their respective operators $\mathcal{C}, \mathcal{P}$ and $\mathcal{T}$ defined as:

- $\mathcal{C}$: Converts a particle into its antiparticle, leaving all other properties unchanged. For particles associated with a field ϕ, $\mathcal{C}$ transforms this into the related field $\phi^{\dagger}$ with opposite U(1) charges: electric charge, baryon number, lepton number and flavour quantum numbers.
- $\mathcal{P}$: Inversion of the spatial coordinates such that $(t, \vec{x}) \to (t, -\vec{x})$
- $\mathcal{T}$: Inversion of the time coordinate such that $(t, \vec{x}) \to (-t, \vec{x})$

Experiments have demonstrated however that these symmetries can individually be broken. For instance, the weak interaction violates $\mathcal{C}$ and $\mathcal{P}$ separately, a fact first revealed by Wu in her famous experiment with Co^{60} nuclei [21].

The weak decay of the charged pion $\pi^+ \to \mu^+\nu_\mu$ provides the clearest evidence for this breaking of discrete symmetries. The anti-muon is never produced right-handed, in a display of maximal parity violation. The same process also demonstrates $\mathcal{C}$ violation; the charge-conjugated decay $\pi^- \to \mu^-\bar{\nu}_\mu$ would involve the production of a left-handed muon, whereas the muon is always produced right-handed [22]. If the $\mathcal{C}$ and $\mathcal{P}$ operations are combined, however, the left-handed anti-muon transforms to a right-handed muon, matching experimental observations and restoring a sense of order. For this reason, in addition to strong theoretical arguments suggesting that the combined transformation $\mathcal{CPT}$ must be an exact symmetry of nature [23], $\mathcal{CP}$ invariance was assumed to hold true.

This belief persisted until 1964, when a small but highly significant violation of the combined symmetry of $\mathcal{CP}$ was observed in the neutral kaon system [24], earning its discoverers Kronin and Fitch the Nobel Prize in 1980. This effect, now known as $\mathcal{CP}$-violation, has since been studied extensively in the B sector, with observations made throughout the 2000's by the B-factories [8, 9] and Tevatron [25, 26] experiments.

The phenomenon of $\mathcal{CP}$-violation manifests itself in three distinct ways:

1. $\mathcal{CP}$-violation in neutral meson mixing, or *indirect* $\mathcal{CP}$-violation. This occurs when the two neutral mass eigenstates are not simultaneously $\mathcal{CP}$-eigenstates.

2. $\mathcal{CP}$-violation in decay, or *direct* $\mathcal{CP}$-violation. This occurs in both charged and neutral meson decays, when the amplitude for a decay and its $\mathcal{CP}$ conjugate process are not equal in magnitude.

3. $\mathcal{CP}$-violation in the interference between decays with and without mixing. This occurs when a common final state is accessible to both a neutral meson and its corresponding anti-meson.

In Chapter 4, an exhaustive study of direct $\mathcal{CP}$-violation in $B^\pm \to Dh^\pm$ decays is presented.

1.3.2. $\mathcal{CP}$-violation in the Standard Model

A mechanism for $\mathcal{CP}$-violation naturally arises in three-generation quark mixing, first introduced by Kobayashi and Maskawa in 1973 [27] as a generalisation of the mixing mechanism originally derived by Cabibbo in 1963 [28]. Quark mixing is governed by a single three-dimensional matrix, within which one complex phase resides. This phase

is the source of all $\mathcal{CP}$-violating effects in the SM, and can only be introduced in the presence of three fermion generations. As such, the prediction of a third quark generation preceded its eventual discovery in 1977, when the beauty quark was first observed [29].[1]

Quark mixing, the Higgs and the CKM matrix

In the Standard Model, the masses and mixing of the quarks have a common origin. They arise from Yukawa interactions with the Higgs [12], which are described by the following Lagrangian for three quark generations in the weak-eigenstate basis:

$$\mathcal{L}_Y = -Y^d_{ij}\,\overline{Q^I_{Li}}\,\phi\,d^I_{Rj} - Y^u_{ij}\,\overline{Q^I_{Li}}\,\epsilon\,\phi^*\,u^I_{Rj} + \text{h.c.} \tag{1.3}$$

where ϕ is the Higgs field, i, j are quark generation labels, Q^I_L are the left-handed $\mathrm{SU}(2)_L$ quark doublets, ϵ is the 2×2 antisymmetric Levi-Civita tensor, and d^I_R and u^I_R are the right-handed down- and up-type quark singlets, respectively. In this basis, $Y^{u,d}$ are 3×3 complex matrices which determine the coupling strength of each quark type to the Higgs. Mass terms for the quarks can appear in Equation 1.3 when the Higgs field acquires a vacuum expectation value, $<\phi>=(0, v/\sqrt{2})$. Such mass terms are described by the Lagrangian:

$$\mathcal{L}_m = -M^d_{ij}\,\overline{d^I_{Li}}\,d^I_{Rj} - M^u_{ij}\overline{u^I_{Li}}\,u^I_{Rj} + \text{h.c} \tag{1.4}$$

where the 3×3 mass matrices $M^{u,d}$, which govern the mixing of quarks due to their non-diagonal nature, are given by:

$$M^u = \frac{vY^u}{\sqrt{2}} \qquad M^d = \frac{vY^d}{\sqrt{2}} \tag{1.5}$$

These matrices can be diagonalised by moving from the weak-eigenstate basis to the mass eigenstate basis via the unitary transformations:

$$U^u_L\,M^u\,U^{u\dagger}_R = \mathrm{diag}(m_u, m_c, m_t) \tag{1.6}$$

$$U^d_L\,M^d\,U^{d\dagger}_R = \mathrm{diag}(m_d, m_s, m_b) \tag{1.7}$$

where m represent the quark mass eigenstates, and U represent the unitary transformation matrices. When rotations are performed on the left-handed quarks in a corresponding

[1] Even the charm quark didn't make an appearance until 1974 [30], highlighting just how prescient this prediction was.

manner:

$$d'_{Li} = U^d_{Lij} d_{Lj} \qquad u'_{Li} = U^u_{Lij} u_{Lj} \tag{1.8}$$

the weak currents, normally written as:

$$J^\mu_{W^+} = \frac{1}{\sqrt{2}}(\bar{\nu}_L \gamma^\mu e_L + \bar{u}_L \gamma^\mu d_L) \qquad J^\mu_{W^-} = \frac{1}{\sqrt{2}}(\bar{e}_L \gamma^\mu \nu_L + \bar{d}_L \gamma^\mu u_L) \tag{1.9}$$

contain quark interaction terms that transform as follows:

$$\bar{u}_L \gamma^\mu d_L \to \bar{u}_L \gamma^\mu (U^{u\dagger}_L U^d_L) d_L \qquad \bar{d}_L \gamma^\mu u_L \to \bar{d}_L \gamma^\mu (U^{d\dagger}_L U^u_L) u_L \tag{1.10}$$

The fact that, in general, $U^d_L \neq U^u_L$, has an important effect in charged current interactions and leads to the definition of the CKM quark mixing matrix:

$$V_{CKM} = U^{u\dagger}_L U^d_L = \begin{pmatrix} V_{ud} & V_{us} & V_{ub} \\ V_{cd} & V_{cs} & V_{cb} \\ V_{td} & V_{ts} & V_{tb} \end{pmatrix}. \tag{1.11}$$

This matrix is non-diagonal, and responsible for all of the mixing between different generations of up- and down-type quarks in charged current interactions. Importantly, neutral current interactions are left unaltered due to the unitary nature of U^d_L and U^u_L, since $\bar{d}_i d_i \to \bar{d}_i U_d U^\dagger_d d_i \equiv \bar{d}_i d_i$. No tree level flavour changing neutral currents are permitted within the SM; such processes, for example $b \to s$ transitions, occur only at loop level and are thus suppressed.

V_{CKM} is a 3×3 complex unitary matrix, and can be parameterised by $3^2 = 9$ real numbers. After arbitrary phases of the quark fields are reabsorbed, three rotation angles and a single complex phase remain, the latter of which is responsible for all $\mathcal{CP}$-violation effects in the SM. Although the SM describes the nature of V_{CKM}, it does not predict the value of each matrix element; these must be determined experimentally. The precise experimental determination of each element of V_{CKM} provides strong constraints on the validity of the SM, which explicitly requires the matrix to be unitary. Without precise knowledge of SM $\mathcal{CP}$-violation effects, any potential $\mathcal{CP}$-violation arising from New Physics cannot be correctly interpreted.

Parameterising the CKM matrix

Several options exist for parameterising V_{CKM}. In the Chau-Keung parameterisation [31], the three rotation angles are defined as θ_{12}, θ_{13}, θ_{23} and the complex phase as δ_{13}, giving:

$$V_{CKM} = \begin{pmatrix} c_{12}c_{13} & s_{12}c_{13} & s_{13}e^{-i\delta_{13}} \\ -s_{12}c_{23} - c_{12}s_{23}e^{i\delta_{13}} & c_{12}c_{23} - s_{12}s_{23}s_{13}e^{i\delta_{13}} & s_{23}c_{13} \\ s_{12}c_{23} - c_{12}s_{23}e^{i\delta_{13}} & -c_{12}c_{23} - s_{12}s_{23}s_{13}e^{i\delta_{13}} & c_{23}s_{13} \end{pmatrix} \tag{1.12}$$

where $c_{ij} = \cos(\theta_{ij})$ and $s_{ij} = \sin(\theta_{ij})$ for the generation labels $i, j =$ (1,2), (1,3) or (2,3). The angle θ_{12} is also known as the Cabibbo angle, θ_C.

A hierarchical pattern in the CKM elements exists ($s_{13} \ll s_{23} \ll s_{12} \ll 1$), where each of the diagonal elements are close to one and the off-diagonal elements move closer to zero the further away from they diagonal they reside. Expressing the order of magnitude of each CKM matrix element in terms of sines of the Cabibbo angle, $\lambda \equiv \sin(\theta_{12}) \approx 0.23$, one obtains:

$$\begin{pmatrix} 1 & \lambda & \lambda^3 \\ \lambda & 1 & \lambda^2 \\ \lambda^3 & \lambda^2 & 1 \end{pmatrix}. \tag{1.13}$$

The Wolfenstein parameterisation [32] exploits this pattern by expanding each CKM element in increasing powers of λ. Up to $\mathcal{O}(\lambda^3)$, the CKM matrix can then be written as:

$$V_{CKM} = \begin{pmatrix} 1 - \frac{1}{2}\lambda^2 & \lambda & A\lambda^3(\rho - i\eta) \\ -\lambda & 1 - \frac{1}{2}\lambda^2 & A\lambda^2 \\ A\lambda^3(1 - \rho - i\eta) & -A\lambda^2 & 1 \end{pmatrix}. \tag{1.14}$$

where A, ρ and η are all real parameters of order unity. This representation is unitary to all orders in λ, and has the advantageous feature that the total amount of $\mathcal{CP}$-violation in the SM is closely related to the phase-independent quantity $(\rho - i\eta)$. It is interesting to note that larger $\mathcal{CP}$-violation is expected in the B system rather than the kaon system, due to the presence of the CKM element V_{ub} in certain B decays. The complex phase responsible for $\mathcal{CP}$-violation is found only in V_{ub} and V_{td} at $\mathcal{O}(\lambda^3)$. This feature also explains why large $\mathcal{CP}$-violation in the interference between mixing and decay has been

observed in the B^0 system [33] but not in the B_s^0 system [16] - in the latter instance, the mixing diagrams involve V_{ts}, whereas in B^0 mixing the element V_{td} features. To have any complex contribution to V_{ts}, one must go to $\mathcal{O}(\lambda^5)$ in the Wolfenstein expansion.

Unitarity Triangles

The unitarity of the CKM matrix, $(V_{CKM}V_{CKM}^\dagger)_{ij} = (V_{CKM}^\dagger V_{CKM})_{ij} = \delta_{ij}$ leads to a set of nine independent equations, three of which are equal to unity and the remaining six are equal to zero. Each of the vanishing combinations listed below can be represented geometrically as a triangle in the complex plane:

$$V_{ud}^* V_{us} + V_{cd}^* V_{cs} + V_{td}^* V_{ts} = 0 \tag{1.15}$$
$$V_{us}^* V_{ub} + V_{cs}^* V_{cb} + V_{ts}^* V_{tb} = 0 \tag{1.16}$$
$$V_{ud}^* V_{td} + V_{us}^* V_{ts} + V_{ub}^* V_{tb} = 0 \tag{1.17}$$
$$V_{cd}^* V_{ud} + V_{cs}^* V_{us} + V_{cb}^* V_{ub} = 0 \tag{1.18}$$
$$V_{cd}^* V_{td} + V_{cs}^* V_{ts} + V_{cb}^* V_{tb} = 0 \tag{1.19}$$
$$V_{ub}^* V_{ud} + V_{cb}^* V_{cd} + V_{tb}^* V_{td} = 0 \tag{1.20}$$

In the absence of any $\mathcal{CP}$-violation, each of these triangles degenerates to a line along the real axis. The area of each triangle is thus a direct measure of the amount of $\mathcal{CP}$-violation in the SM. All six triangles have the same area $|J|/2$, where J is the Jarlskog invariant [34]:

$$J = \mathrm{Im}(V_{ij} V_{kl} V_{il}^* V_{kj}^*) \qquad (i \neq j, k \neq l) \tag{1.21}$$

for $i, j, k, l \in \{1, 2, 3\}$.

Beyond their visual appeal, unitarity triangles also have the useful property of being parameterisation-independent: no matter how you choose to parametrise the CKM matrix, the angles and lengths of each side remain the same for every triangle. The only thing that changes is the orientation of the triangles within the complex plane. As such, unitarity triangles are a central component of $\mathcal{CP}$-violation parametrisation within the SM.

The angles α, β and γ

Each of the triangles listed in Section 1.3.2 are flat and close to degenerate, with the exception of the one defined in Equation 1.20. This triangle is known as *the* Unitarity Triangle (UT), and is commonly used to represent the $\mathcal{CP}$-violating content of the CKM matrix. Rotating the UT, such that $V_{cb}^* V_{cd}$ is real and of unit magnitude, yields a triangle with vertices at (0,0) and (1,0) in the $(\bar{\rho}, \bar{\eta})$ plane, as illustrated in Figure 1.4. The third coordinate lies at:

$$\bar{\rho} = \rho(1 - \lambda^2/2) \qquad \bar{\eta} = \eta(1 - \lambda^2/2) \tag{1.22}$$

The three angles of the UT are defined as:

$$\alpha \equiv \arg\left[-\frac{V_{td}V_{tb}^*}{V_{ud}V_{ub}^*}\right] \qquad \beta \equiv \arg\left[-\frac{V_{cd}V_{cb}^*}{V_{td}V_{tb}^*}\right] \qquad \gamma \equiv \arg\left[-\frac{V_{ud}V_{ub}^*}{V_{cd}V_{cb}^*}\right] \tag{1.23}$$

Precisely determining the sides and angles of the CKM matrix provides a critical test of the CKM mechanisms validity. By performing several independent measurements of CKM matrix elements, comparisons can be made in the $(\bar{\rho}, \bar{\eta})$ plane in order to over-constrain the UT triangle; in this way, potential deviations from unitarity caused by New Physics can effectively be probed.

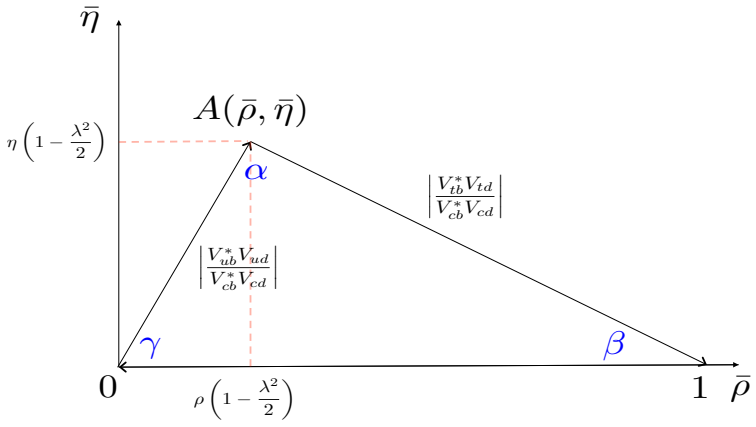

Figure 1.4.: The Unitarity Triangle in the complex plane, with sides normalised to $V_{cb}^* V_{cd}$. The horizontal axis represents the real axis, while the vertical axis represents the imaginary axis. The angles of the UT are α, β and γ, as defined in Equation 1.23.

Parameter	Value $\pm 1\sigma$ (CKMfitter)	Value $\pm 1\sigma$ (UTfit)
A	$0.813\ ^{+0.015}_{-0.027}$	0.821 ± 0.012
λ	$0.22551\ ^{+0.00068}_{-0.00035}$	0.22534 ± 0.00065
ρ	$0.149\ ^{+0.016}_{-0.008}$	0.136 ± 0.024
η	$0.342\ ^{+0.013}_{-0.011}$	0.361 ± 0.014
$J(10^{-5})$	$2.97\ ^{+0.18}_{-0.20}$	3.11 ± 0.09

Table 1.1.: CKMfitter and UTfit best fit values for the Wolfenstein parameters and Jarlskog invariant [35, 36]. The uncertainties quoted represent the total uncertainty on each parameter after global combination fits are performed.

Parameter	Value $\pm 1\sigma$ (CKMfitter)	Value $\pm 1\sigma$ (UTfit)
α	$(85.4\ ^{+4.0}_{-3.9})^\circ$	$(88.6 \pm 3.3)^\circ$
β	$(21.50\ ^{+0.75}_{-0.74})^\circ$	$(22.03 \pm 0.86)^\circ$
γ	$(70.0\ ^{+7.7}_{-9.0})^\circ$	$(68.3 \pm 7.5)^\circ$

Table 1.2.: CKMfitter and UTfit best fit values for the CKM angles α, β and γ using only direct measurements [35, 36].

Current UT constrains

The unitarity of V_{CKM} is tested with each measurement of its parameters. The CKMfitter [35] and UTfit [36] groups perform global fits to the UT, including measurements of both tree and loop level processes in order to constrain the UT parameters. The current best fit values for the Wolfenstein parameters and Jarlskog invariant are listed in Table 1.1, and in Table 1.2 the best fit values for each of the UT angles found using only direct measurements are shown. The current CKMfitter constraints in the $(\bar{\rho}, \bar{\eta})$ plane are shown in Figure 1.5, with the equivalent constraints determined by UTfit shown in Figure 1.6.

All direct measurements are currently in good agreement with the CKM mechanism. The angles α and β are precisely determined, but γ still has a large uncertainty. Measuring γ with improved precision is a central physics objective of LHCb, and indeed motivates the $\mathcal{CP}$ asymmetry work presented in this thesis. It is the only UT angle that has no top quark coupling in its definition (see Equation 1.23), with the important consequence that it can be measured using tree level B decays. The parameter γ is thus the only angle that can be measured in both tree and loop level processes.

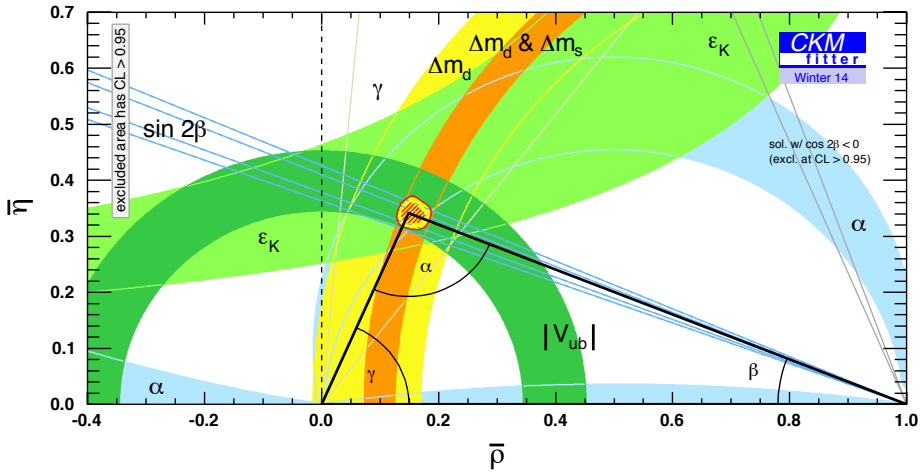

Figure 1.5.: CKMfitter constraints in the $(\bar{\rho}, \bar{\eta})$ plane [35]. The various coloured regions indicate areas of allowed parameter space for the angles and sides of the UT, where each colour corresponds to a different class of $\mathcal{CP}$-violation measurement. A global fit is performed using all of these measurements as input, in order to determine central values and uncertainties for α, β and γ.

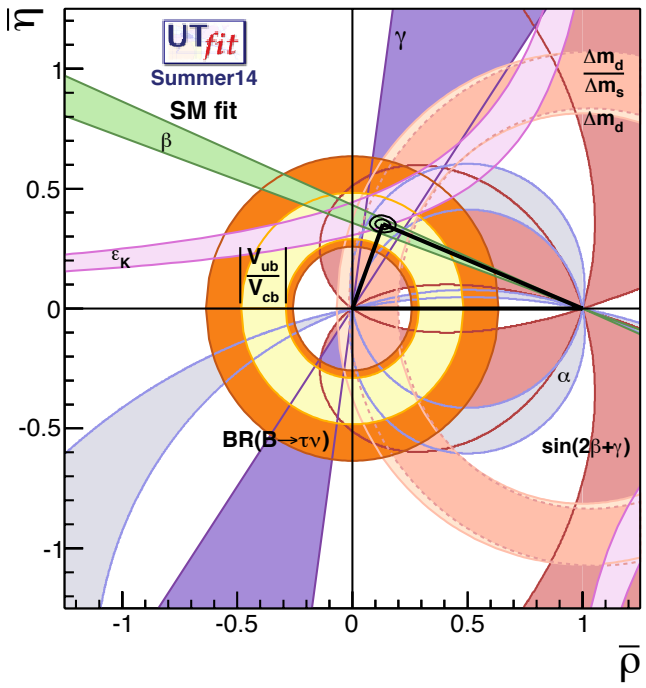

Figure 1.6.: UTfit constraints in the $(\bar{\rho}, \bar{\eta})$ plane [36].

As New Physics effects are expected to appear only at loop level, the precise determination of γ in tree level decays provides a Standard Model benchmark against which any New Physics contributions can be compared. In Chapter 3, the formalism for measuring γ at tree level using $B^{\pm} \to DK^{\pm}$ decays will be developed, forming the theoretical foundation for the $\mathcal{CP}$ asymmetry measurements presented in Chapter 4. These measurements will provide important constraints in future measurements of γ using LHCb data.

Chapter 2.

The LHCb experiment

LHCb is a single-arm spectrometer with a forward angular coverage from approximately 15 mrad to 300 (250) mrad in the horizontal bending (vertical non-bending) plane [5]. This corresponds to a pseudorapidity coverage of $1.9 < \eta < 4.9$, where $\eta = -\ln\tan(\theta/2)$ and θ is the angle between the particle momentum and the beam pipe. The detector occupies a space of 20 m along the longitudinal direction (z-axis), 12 m in the horizontal direction (x-axis) and 10 m in the vertical direction (y-axis), as shown in Figure 2.2. This choice of detector geometry is driven by the fact that at high energies, the production of b- and $\bar{b}$-hadrons is highly correlated due to the lab frame boost, such that they are predominantly produced in the same forward or backward cone. This effect is illustrated in Figure 2.1, where the angular acceptance of LHCb is highlighted in red. At LHC energies, the proton parton density function is dominated by the gluon component, such that $b\bar{b}$ pair production at LHCb proceeds predominantly through gluon-gluon fusion processes.

LHCb is composed of several sub-detectors, which can be grouped into the following categories:

- **Tracking system:** VErtex LOcator (VELO, Section 2.2), dipole magnet (Section 2.3), Tracker Turicensis (TT, Section 2.4), Inner Tracker (IT, Section 2.4.1), Outer Tracker (OT, Section 2.4.2)
- **Ring Imaging CHerenkov detectors:** RICH1, RICH2 (Section 2.5)
- **Calorimeters:** Scintillating Pad Detector (SPD, Section 2.6.1), Pre-Shower detector (PS, Section 2.6.1), Electromagnetic CALorimeter (ECAL, Section 2.6.2), Hadronic CALorimeter (HCAL, Section 2.6.3)

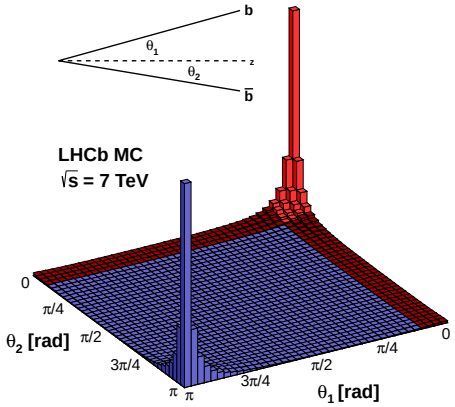

Figure 2.1.: Angular correlation of the b quarks produced in proton-proton collisions at the LHC [37]. The angles Θ_b and $\Theta_{\bar{b}}$ are formed with respect to the beam axis. The region highlighted in red corresponds to the LHCb acceptance. Events are simulated with the PYTHIA event generator [38].

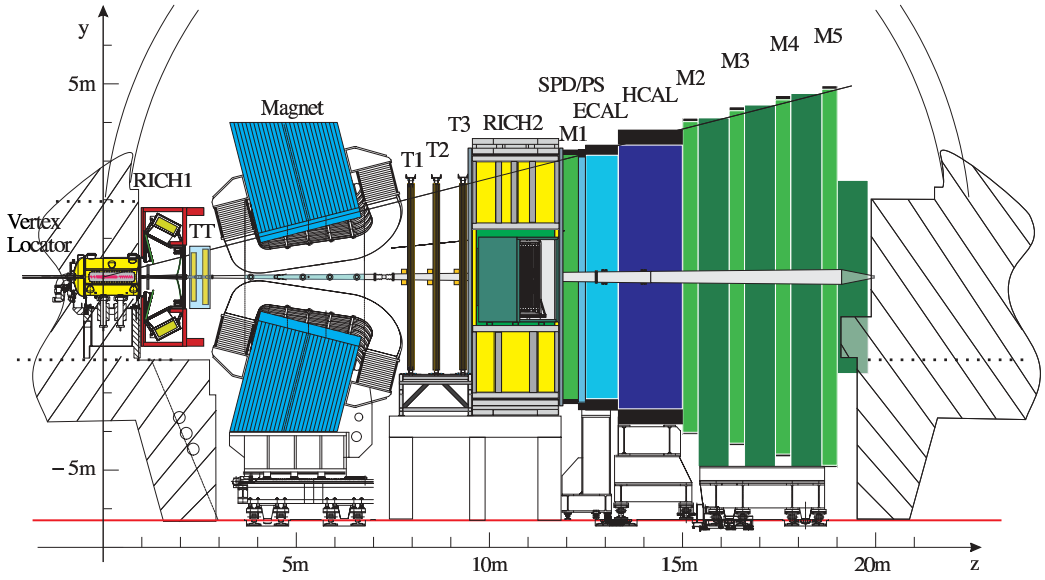

Figure 2.2.: Cross-section view of LHCb, cut in the non-bending y–z plane [39]. RICH1 and RICH2 refer to the two Ring Imaging CHerenkov detectors within LHCb. TT, T1, T2 and T3 refer to the tracking stations. SPD and PS refer to the Scintillating Pad Detector and Pre Shower detector, respectively. ECAL and HCAL refer to the electromagnetic an hadronic calorimeters, while M1−M5 refer to the various muon stations.

- **Muon stations:** M1 – M5 (Section 2.7)
- **Trigger:** Level 0 hardware trigger (L0, Section 2.8.1), High Level software Trigger 1 (HLT1, Section 2.8.2), High Level software Trigger 2 (HLT2, Section 2.8.3)

Each sub-detector will be detailed briefly in the following sections. Full details are available in the LHCb performance paper [39], from which all of the detector parameters quoted within this Chapter are taken.

In order for precision physics measurements to be made in the high-background LHC environment, stringent performance requirements are imposed on LHCb. Central to these are the following:

- **Vertex and impact parameter resolution:** Secondary vertices from b- and c- hadron decays must be well resolved from primary proton-proton interaction vertices, which requires excellent vertex resolution. In addition, displaced secondary tracks must be well resolved from prompt background tracks originating from the primary vertex. In LHCb, vertexing is performed by the VErtex LOcator (VELO) sub-detector, which surrounds the pp collision region at the closest possible distance, allowing the vertices from b- and c-hadron decays to be detected.
- **Time resolution:** Proper time resolution is critical for many analyses, for example in b- and c- hadron lifetime measurements and time dependent $\mathcal{CP}$-violation studies. In the latter, the fast oscillations of the B_s^0 system require a time resolution much smaller than the oscillation period in order to be resolved.
- **Momentum and mass resolution:** In physics analyses involving purely hadronic final states, the combinatorial background rate is considerable. To distinguish heavy flavour hadrons from random combinations of background tracks, good momentum and mass resolution are required.
- **Particle identification:** Distinguishing between various particle types is crucial in correctly identifying signal events. Of specific importance is the discrimination between different hadronic species, particularly pions and kaons. Hadron identification is performed by the RICH sub-detectors, which provide high kaon identification efficiencies with low corresponding pion misidentification rates. This feature of LHCb is exploited throughout this thesis to distinguish $B^\pm \to DK^\pm$ and $B^\pm \to D\pi^\pm$ decays, which differ only in the species of the particle produced along with the D meson in the B decay (referred to throughout as the bachelor particle).

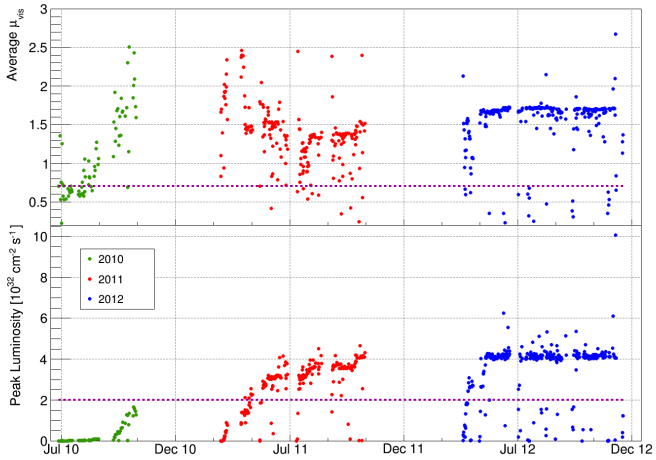

Figure 2.3.: Average number of visible interactions per bunch crossing (top) and instantaneous luminosity (bottom) at the LHCb interaction point in the period 2010-2012 [39]. The dotted lines show the design values for both parameters, indicating that LHCb operated well beyond design specifications in both 2011 and 2012.

- **Trigger:** A visible inelastic collision takes place at a rate of 10 MHz in LHCb, much too high for every event to be stored on disk. It is thus important to select only the subset of data that exhibits interesting features, in order to reduce the bandwidth to a manageable rate. The LHCb trigger performs this task in three stages (one hardware and two software), reducing the rate to around 3 kHz. The trigger system must be both efficient and versatile, selecting as many B final states as possible while adapting in real time to changing LHC running conditions.

2.1. Conditions during Run I

At the end of 2009, LHCb recorded its first pp collisions at the LHC injection energy of $\sqrt{s} = 0.9$ TeV. Throughout 2010, operating conditions changed quickly due to the ramp-up of the LHC luminosity. An important quantity to consider along with the luminosity is the pile-up μ_{vis}, defined as the average number of visible interactions per beam crossing. The variation in LHCb operating conditions during Run I can be seen in Figure 2.3, where luminosities began at $\sim 10^{28}$ cm^{-2}s^{-1} with almost no pile-up, reaching luminosities of 10^{32} cm^{-2}s^{-1} with $\mu_{\text{vis}} \approx 2.5$.

The LHC beam energy was 3.5 TeV during 2010 and 2011, where the number of circulating bunches was increased gradually to a maximum of around 1300 in 2011. During

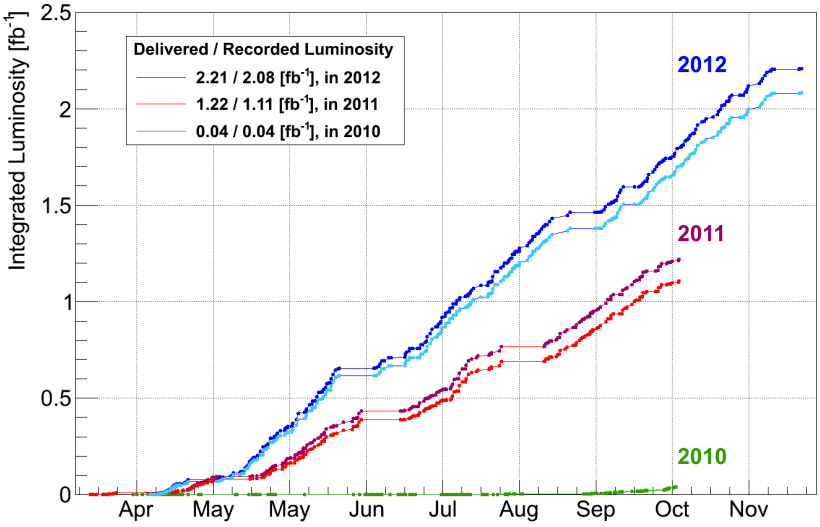

Figure 2.4.: Integrated luminosity in LHCb during the three years of LHC Run I [39]. The figure shows the curves for the delivered (dark coloured lines) and recorded (light coloured lines) integrated luminosities.

this time, LHCb took a majority of data at a luminosity of 3.5×10^{32} cm^{-2}s^{-1}, almost twice the design luminosity. In 2011, a luminosity levelling procedure was introduced to maintain a constant luminosity within $\sim 5\%$ over the course of a fill, by adjusting the transverse beam overlap. This minimised luminosity decay, allowing the same trigger configuration during a fill and reducing systematic uncertainties in detector occupancy.

In 2012, the beam energy was increased to 4 TeV, and LHCb took data at a luminosity of 4×10^{32} cm^{-2}s^{-1}. The LHC delivered stable beams for around 30% of the operational year, and a novel approach was adopted at LHCb to make use of the processing power which would otherwise be idle during the remaining 70%. Around 20% of L0 accepted events were stored to temporary disk during stable beams, allowing them to be processed at a later stage between fills by the HLT software triggers. This allowed LHCb to increase the total data sample available for physics analysis at no additional cost.

The integrated luminosity recorded by LHCb was 38 pb^{-1} in 2010, 1.11 fb^{-1} in 2011 and 2.08 fb^{-1} in 2012, where the evolution in integrated luminosity for each year is shown in Figure 2.4. The average operational efficiency, defined as the ratio of recorded to delivered luminosity, was 93% during Run I, reaching 95% on average in 2012.

The LHCb magnet deflects positive and negative particles in opposite directions in the $x - z$ plane, which can lead to charge detection asymmetries arising from differences

in performance of the left and right sides of the detector. To minimise this effect, the LHCb dipole magnetic field was changed regularly (around twice per month) during running, such that any left-right asymmetry cancels in the combined dataset. This is an important consideration for the $\mathcal{CP}$ charge asymmetry analysis presented within this thesis, which has been performed on polarity averaged datasets only.

2.2. VErtex LOcator (VELO)

The VELO [40] performs precise measurements of track coordinates close to the interaction region. This enables the accurate reconstruction of primary and secondary vertices, where the latter is of particular importance in b- and c-hadron decays. In order to measure lifetimes and impact parameters with respective resolutions of ~ 40 fs and ~ 20 μm, the VELO reconstructs vertices with a resolution of ~ 10 μm. To achieve this level of precision, the VELO is located as close as possible to the interaction region.

The VELO is illustrated in Figure 2.5. It consists of 21 silicon modules located around the interaction region, positioned perpendicular to the beam direction. Independent measurements of the cylindrical coordinates r and ϕ are made by each module using dedicated R- and ϕ-sensors, with the z coordinate given by the fixed position of the module. The silicon in the R-sensor is implanted within concentric semi-circles, whereas in the ϕ-sensor the silicon is arranged in radial strips running outward from the inner to outer module radius. The use of this cylindrical geometry enables much faster reconstruction of tracks and vertices in the trigger relative to a cartesian geometry.

Each VELO station is formed from two semi-circular modules, with a sensitive region starting 8.2 mm radially outward from the beam axis when the detector is in the closed position (bottom left of Figure 2.5). The aperture increases during the LHC injection phase to the open position (bottom right of Figure 2.5), and is only brought to the fully closed position once stable beams are declared. Both halves of the VELO are mounted on a dedicated automated positioning system, located inside a vacuum vessel. The 21 modules are positioned between $z = -18$ cm and $z = 88$ cm, with the nominal beam interaction point defined at $z = 0$ cm with an uncertainty of around 5 cm. The VELO thus provides comprehensive coverage of the interaction region.

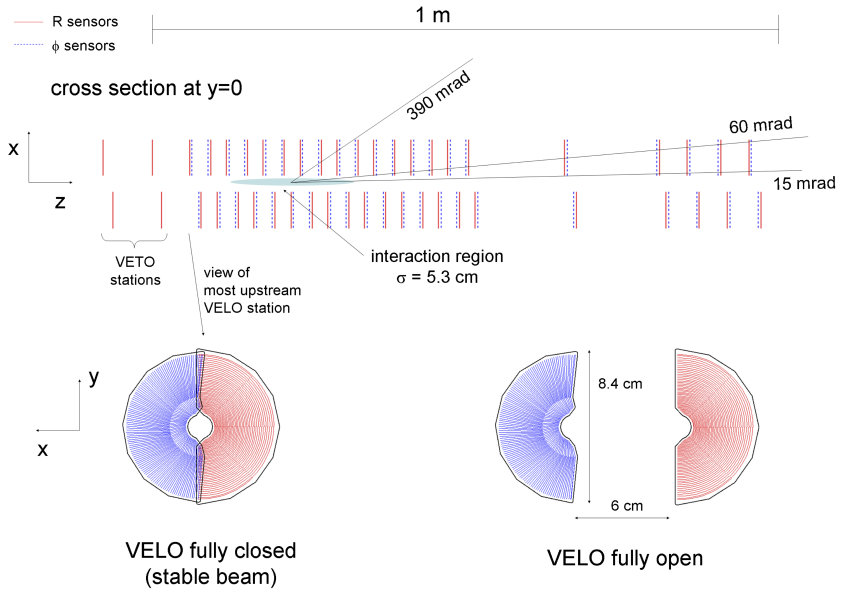

Figure 2.5.: VELO sensor layout in the $x - z$ plane (top) [41]. VELO module geometry in the closed and open configurations (bottom).

2.3. Dipole magnet

LHCb is by design a spectrometer, and as such performs precision momentum measurements with a resolution of $\delta p/p \approx 0.5\%$ over a wide momentum range up to 200 GeV/c. To achieve this, a 1600 tonne non-superconducting dipole magnet providing an integrated field of 3.6 Tm is employed, as shown in Figure 2.6. The magnet deflects charged particles only in the horizontal plane, and is situated downstream of the VELO and the first RICH detector, RICH1.

An important design feature of the magnet is the minimisation of the residual magnetic field within both the VELO and RICH1, in the former case to validate the fitting of straight tracks for input to the HLT and in the latter case to minimise the magnetic deflection of photoelectron paths produced within the RICH1 Hybrid Photon Detectors (HPDs). Corrections are applied to account for any residual distortion of photoelectrons using a dedicated Magnetic Distortion Correction System (MDCS) in RICH1, which provides an important improvement to the Cherenkov photon position resolution, ultimately improving the particle identification ability of the RICH (see Section 2.5).

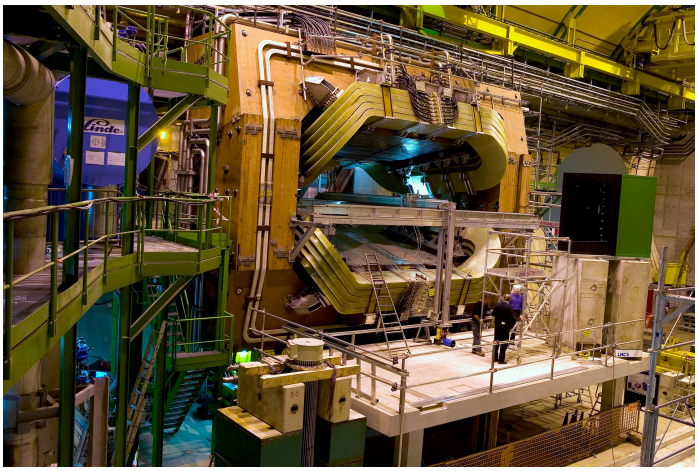

Figure 2.6.: A picture (2002) of the 1600 tonne LHCb dipole magnet, with two coils mounted within an iron yoke. Three humans provide scale.

2.4. Tracking stations

In addition to the VELO, the LHCb tracking system consists of five tracking stations. Two of these constitute the Tracker Turicensis (TT) and are placed before the magnet; the additional three trackers (T1, T2 and T3) make up the Inner Tracker (IT) and Outer Tracker (OT). The tracking stations together cover the entire geometrical acceptance of LHCb.

Tracker Turicensis (TT)

The Tracker Turicensis (TT)[1], is a silicon microstrip detector consisting of four detection layers. The first and fourth layers have vertically oriented readout strips (x-layers), whereas the second and third layers have readout strips oriented at stereo angles of $+5°$ and $-5°$, respectively (u- and v-layers). This geometry allows the transverse component of the particle trajectory to be resolved. The first and last layers of the TT are illustrated in Figure 2.7.

Each silicon strip has a pitch of ~ 200 μm, providing a spatial resolution of 50 μm. The TT enables long-lived K_s^0 particles, which decay outside the VELO, to be reconstructed. It also enables the reconstruction of low momentum tracks that are swept out of the detector acceptance by the magnet before reaching T1 $-$ T3 (see Section 2.9).

[1] Turicensis is Latin for Zurich, the institution who built this sub-detector.

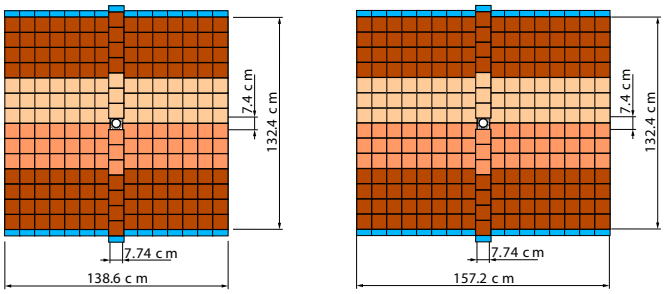

Figure 2.7.: Layout of the first (left) and last (right) TT layers, with the beam pipe visible in the middle [42]. The two areas left and right of the beam pipe are covered by nine eleven-sensor long ladders each. Five-sensor long ladders fill the areas directly above and below the beam pipe. Vertically, each ladder is subdivided into several readout sectors, as indicated by different shadings.

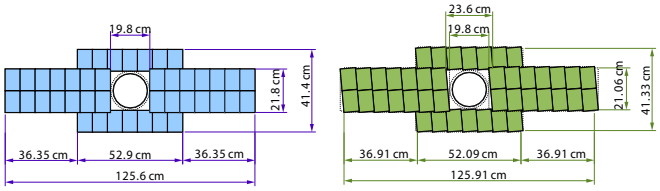

Figure 2.8.: Layout of the x-layer (left) and u-layer (right) of the IT, with the cross-shaped configuration [42]. The beam pipe is visible in the middle.

2.4.1. Inner Tracker (IT)

The Inner Tracker (IT) composes the central region of the T1 − T3 tracking stations, where particle fluxes are largest. In each of the three tracking layers, the IT consists of four detector planes. Each plane (or box) employs the same silicon microstrip technology as used in the TT, and despite its limited effective area coverage of 1.3% of the total detector acceptance, the IT accepts around 20% of all charged tracks produced close to the interaction point. The cross-shaped geometry of the IT is illustrated in Figure 2.8; this geometry is motivated by the orientation of the LHCb bending plane. The bending plane of LHCb is horizontal in this image, and intersects the page at 90 degrees.

2.4.2. Outer Tracker (OT)

The Outer Tracker (OT) [43], illustrated in Figure 2.9, covers the large region outside the acceptance of the inner tracker, in each of the tracking stations T1 − T3. Each OT

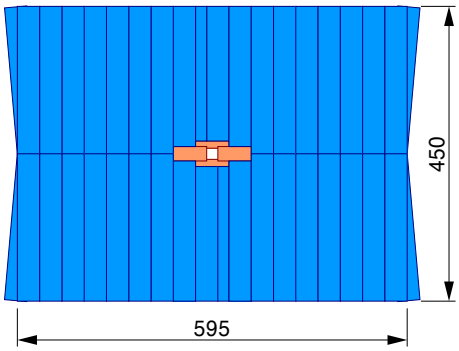

Figure 2.9.: Layout of an OT station [44]. In the centre, the four boxes of the IT are highlighted.

module is composed of four layers of vertically oriented drift tubes, arranged in the same $x-u-v-x$ geometry as the TT. Within each layer, 64 drift tubes provide measurements with a drift time of less than 50 ns. This drift time ensures that the tracking algorithms meet the required performance, and is achieved through the use of a 4.9 mm drift tube diameter and a mixture of Argon (70%) and CO_2 (30%) drift gas.

2.5. Ring Imaging CHerenkov detectors (RICH)

Of central importance in precision flavour physics is the concept of particle identification. In LHCb, identification of various charged particle species (p, e, μ, K, π) is achieved using Ring Imaging CHerenkov (RICH) detectors [45]. The RICH system is divided into two parts: RICH1, located between the VELO and the TT, and RICH2, located between T3 and the calorimeters (see Figure 2.2). This combined system provides excellent separation of kaons and pions across a wide momentum range of $2-100$ GeV/c, which is of vital importance for the analyses presented within this thesis and many others.

Cherenkov radiation is emitted by a charged particle when it passes through a medium at a speed greater than the speed of light in that medium. The velocity of charged particles traversing the RICH detectors is found by measuring the emission angle of Cherenkov photons with respect to the particle trajectory. This angle, θ_{CK}, depends on the particle velocity $\beta = v/c$ as follows:

$$cos(\theta_{CK}) = \frac{1}{n\beta} \tag{2.1}$$

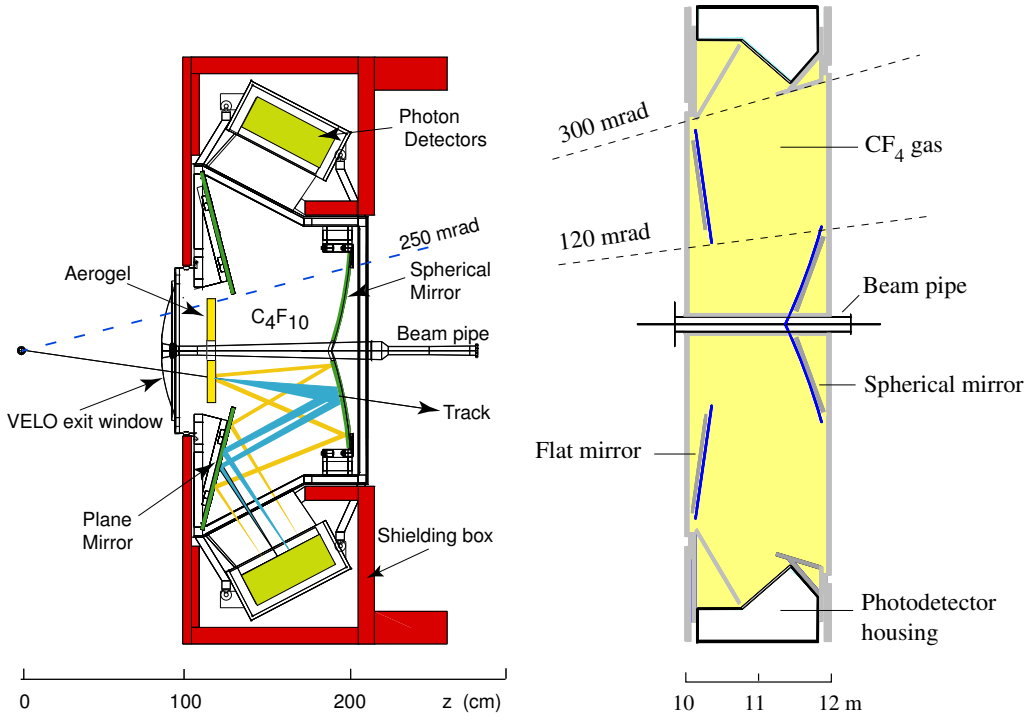

Figure 2.10.: The LHCb RICH detectors [46]. On the left, a vertical cross-section of RICH1 is shown, and on the right, a horizontal cross-section of RICH2 is illustrated.

where n is the refractive index of the RICH radiator medium. A measurement of β, coupled with the knowledge of the particles momentum from the tracking, allows the mass of the particle and thus its identity to be determined. The Cherenkov effect occurs only above a certain momentum threshold, which depends upon n and the particle type. In addition, for a given n, most of the particle identification (PID) sensitivity is lost at high momentum due to saturation in the Cherenkov angle at velocities approaching c:

$$\cos(\theta_{CK}^{\max}) \approx \frac{1}{n} \quad \text{for} \quad \beta \to 1 \tag{2.2}$$

To ensure coverage across a majority of the momentum spectra for tracks produced in collisions, three different radiators, each with different optical properties, are used in the RICH.

In RICH1 (illustrated on the left of Figure 2.10), where particle discrimination at low momentum ($1 - 60$ GeV/c) is the objective, aerogel ($n = 1.03$)[2] and C_4F_{10} ($n = 1.0014$)

[2] The aerogel has been removed since Run I, and will not be used going into Run II; it was determined that it brought minimal performance benefits, at the cost of Cherenkov photon yield.

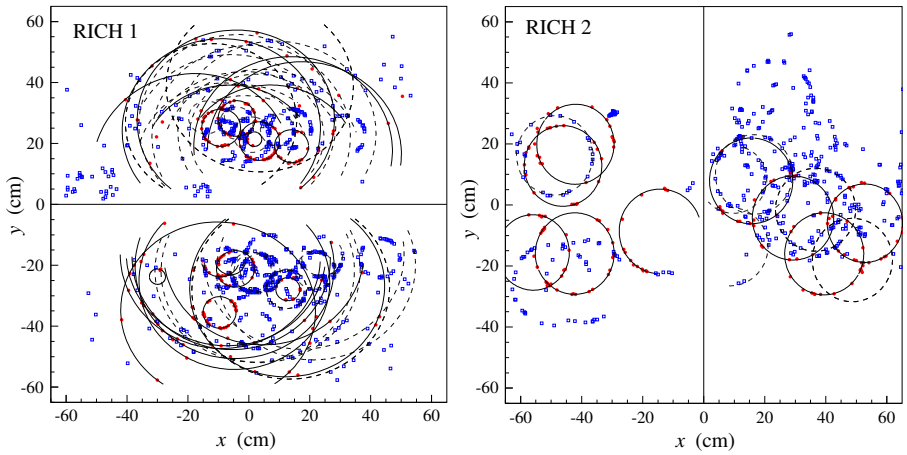

Figure 2.11.: A typical event in the detection planes of RICH1 (left) and RICH2 (right) [39]. Solid lines indicate the reconstructed rings for tracks which extend from the VELO to the final tracking station T3, corresponding to the photon hits marked in red. The rings for all other tracks are drawn with dotted lines, with there corresponding photon hits marked in blue.

are used. RICH1 covers the full angular acceptance of LHCb. In RICH2 (shown on the right of Figure 2.10), high momentum ($15 - 100$ GeV/c) particle discrimination is achieved using C_4F_{10} gas with $n = 1.0005$. RICH2 covers a limited angular acceptance of ± 15 mrad to ± 200 mrad in the horizontal plane, and ± 100 mrad in the vertical plane.

In both RICH detectors, Cherenkov light is deflected outside of the geometrical detector acceptance by a system of spherical and flat mirrors. The mirrors focus the Cherenkov light onto arrays of Hybrid Photon Detectors (HPDs); there are 196 (288) HPDs in RICH1 (RICH2). Within each HPD, phototubes detect the Cherenkov light through the production of photoelectrons, which are subsequently focused onto a silicon chip via an electrostatic field. The incident photon positions on the HPD window are measured from the final photoelectron positions, and this information is used to reconstruct the Cherenkov cones originating from each charged track. The cones are observed as rings of hits on the HPD planes, as illustrated in Figure 2.11.

2.6. Calorimeters

In LHCb, the calorimeters are used in the Level 0 trigger (see Section 2.8.1) to select events containing particles with a high transverse energy, one strong signature of a B meson decay. The transverse energy is defined as the energy component transverse to

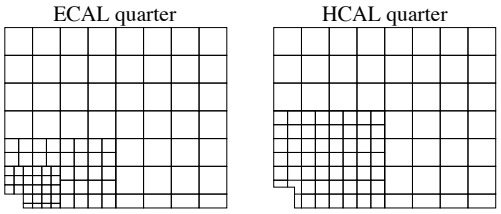

Figure 2.12.: Lateral segmentation of an ECAL (left) and HCAL (right) quarter [47]. Each square shown represents 16 (4) pads in the ECAL (HCAL). The SPD and PS detectors have the same segmentation as the ECAL.

the beam axis, and is calculated from the magnitude and position of an energy deposit in the calorimeter with respect to the z axis. Aside from their use in the trigger, the calorimeters also allow the identification of electrons and the reconstruction of photons and neutral pions ($\pi^0 \to \gamma\gamma$).

The calorimeter layout follows a traditional arrangement, with the electromagnetic calorimeter (ECAL) placed in front of the hadronic calorimeter (HCAL). Two additional detectors are also employed, namely the Scintillating Pad Detector (SPD) and Pre-Shower detector (PS). The calorimeters are positioned between the first (M1) and second (M2) muon stations, each employing the same technology of segmented scintillators coupled with wavelength shifting fibres and photo-multiplier tubes.

2.6.1. SPD and PS

The SPD and PS provide useful information on the initial electromagnetic shower development, helping to improve the particle identification of the ECAL. Charged particles are first identified by the SPD before they shower, through the ionisation they produce. The SPD is thus used to distinguish electrons from photons. Between the SPD and PS, a 12 mm thick lead wall initiates an electromagnetic shower. The role of the PS is to detect this shower, helping to discriminate between electrons and hadrons.

Both detection planes of the SPD and PS consist of 15 mm thick scintillator pads, with a total thickness in z of 180 mm. The SPD and PS are laterally segmented into three sections with different granularity, as shown in Figure 2.12. This segmentation is shared by the ECAL. The smallest pad size is reserved for those pads nearest the beam pipe, where the particle flux is highest.

2.6.2. ECAL

The remaining shower from electrons and photons is detected in the "shashlik" style modules of the ECAL, which consists of alternating 4 mm thick scintillating tiles and 2 mm thick lead sheets. One full ECAL module contains 66 such layers, oriented perpendicular to the z axis. The density per module of the wavelength shifting fibres is highest in the inner and middle sections at 144, whereas the outer sections have a fibre density per module of 64. The energy is measured with a resolution given by:

$$\frac{\sigma(E)}{E} = \frac{8.5 - 9.5\%}{\sqrt{E}} \oplus 0.8\% \oplus 0.003/E \tag{2.3}$$

with E measured in GeV and $\oplus$ means addition in quadrature of the first stochastic term, the second constant term and the third noise term [48]. The module responses in the ECAL are found to be uniform within 8%, and measured parameters are consistent with design expectations [47].

2.6.3. HCAL

Although hadrons can develop into showers within the ECAL, they are primarily absorbed within the HCAL. The HCAL is constructed from 4 mm thick scintillator tiles, alternated with 16 mm iron plates and oriented perpendicular to the z axis. With total dimensions of 8.4 m in height, 6.8 m in width and 1.65 m in length, the detector thickness is only 5.6 radiation lengths due to space constraints in the experimental cavern. As a result, hadronic showers are not fully absorbed in the HCAL, leading to a modest energy resolution given by:

$$\frac{\sigma(E)}{E} = \frac{(69 \pm 5)\%}{\sqrt{E}} \oplus (9 \pm 2)\% \tag{2.4}$$

where E is expressed in GeV. The resolution is in agreement with design expectations [47].

2.7. Muon stations

Since muons are the only particles that penetrate the full calorimeter system (with the obvious exception of neutrinos), a dedicated system is required in order to detect them. For this purpose, the muon system [49] is located at the end of the detector to provide

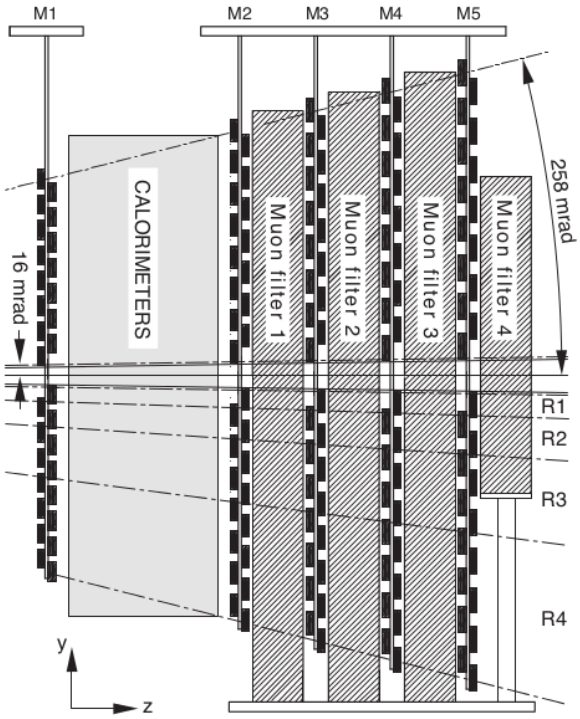

Figure 2.13.: Layout of the muon chambers (black chequered areas) and iron absorbers (solid grey areas) [50]. M1 is placed before the calorimeter system to improve the p_T measurement for use in the Level 0 muon trigger.

efficient muon identification and triggering. It is composed of five stations with 130 chambers in total, where each station is rectangular.

The first station, M1, is located before the calorimeters in order to decrease the total error on the momentum measurement due to scattering of particles in the calorimeter material. The remaining four stations (M2 − M5) are located downstream of the HCAL, alternated with 80 cm thick iron plates put in place to prevent punch-through of hadrons from the HCAL and select only penetrating muons. Only muons with a momentum in excess of 6 GeV/c can pass through to the final station, M5. An additional iron shield protects M5 against particles emerging from the opposite LHC beam. The muon system is illustrated in Figure 2.13.

The total angular acceptance of the muon system is $20 - 306$ mrad in the bending plane, and $16 - 258$ mrad in the non-bending plane. Multi-Wire Proportional Chambers (MWPCs) are used in all muon stations, with the exception of M1 where triple-GEM (Gas Electron Multiplier) detectors have been employed by virtue of their higher radiation hardness.

2.8. The LHCb trigger

LHCb employs a three-stage trigger [51], in order to reduce the detector output rate to the bandwidth limit for storage of $3-4$ kHz. The trigger must select a wide variety of B decays efficiently in a high background environment. In Run I, LHCb operated in a higher pile-up and higher luminosity environment than it was designed for (see Figure 2.3). As such, the trigger working conditions had to be adjusted to account for a higher online processing time. The total trigger output in 2011 was about 3 kHz, exceeding the design specification by 50%. In 2012, the trigger output rate was increased further to 4.5 kHz.

The trigger system is divided into two levels: the Level 0 (L0) trigger and the High Level Trigger (HLT). The L0 is a hardware trigger that operates in sync with the LHC clock, while the HLT is fully implemented in software and processes the L0 output on the Event Filter Farm (EFF), a system of over 20,000 parallel-processing CPU cores. The HLT is further sub-divided into two stages: the first stage, HLT1, performs a partial event reconstruction to reduce the rate by a factor of roughly 20. These events are then passed to HLT2, where a full online event reconstruction is performed in order to select events for storage.

2.8.1. L0 hardware trigger

The L0 trigger reduces the event rate to around 1 MHz, the maximum rate at which LHCb can be read out. The trigger is implemented in the front-end electronics of the detector, and provides a decision with a latency of 4 μs, corresponding to the buffer time of the read-out chips. The trigger runs synchronously with the LHC clock.

The hardware trigger utilises both the calorimeter and muon systems independently, searching for the highest E_T hadron, electron and photon clusters in the calorimeters and the highest p_T muon or muon pairs in the muon stations. In general, high transverse energy and momentum particles are clean experimental signatures of heavy B hadron decays, since such decays produce daughters of higher p_T relative to the large background of soft QCD processes. The calorimeter and muon decisions are read in parallel, and a final decision provided by the L0 Decision Unit (L0 DU) from the logical *or* of their outputs.

The L0 calorimeter trigger forms 2×2 calorimeter cell clusters, selecting those with the highest E_T deposits. Depending on the corresponding energy deposits in the SPD/PS

and HCAL, the clusters are tagged as an electron (`L0Electron`), photon (`L0Photon`) or hadron (`L0Hadron`). The number of SPD hits is also used to reject events with very high multiplicity (where the number of tracks exceeds 1000), which would take too long to process in the HLT.

The L0 muon trigger searches for high p_T muon tracks (`L0Muon` or `L0DiMuon`), using a procedure whereby hits in the muon stations compatible with a straight line pointing towards the interaction point are found. For this decision, the highest p_T muon segments are used.

2.8.2. HLT1 software trigger

HLT1 reconstructs particles in the VELO, giving a first measure of the position of any primary vertices (PVs) in the event. The aim of this first software trigger stage is to reduce the rate to around 50 kHz, allowing the subsequent HLT2 stage to perform a complete reconstruction of every selected event. This trigger stage has a total decision time of around 15 ms, where a number of trigger decision lines run in parallel on the EFF.

A single track trigger `Hlt1Track` searches for a displaced track of high momentum in the event. Such tracks are characteristic of long-lived b- and c-hadron decays, where a secondary vertex well displaced from the primary vertex is present. Tracks reconstructed within the VELO, which are of sufficient quality and have a large impact parameter (IP) with respect to the PV, are used as input for the trigger decision. No L0 decision is imposed at this point.

A muon trigger also runs in HLT1, for events that have been triggered by either the `L0Muon` or `L0DiMuon` lines. Depending on the momentum of the particles and the invariant mass of any composite dimuon objects, a single muon or dimuon HLT1 line is run. For this trigger, tracks in the VELO are extrapolated and matched with the muon segments used in the L0 decision. Electron and photon triggers are also executed in HLT1, which make use of information from the electromagnetic calorimeter.

2.8.3. HLT2 software trigger

The second software trigger stage, HLT2, performs a complete candidate reconstruction, using selection criteria that mirror those used in offline analysis selections as much as

possible. HLT2 trigger lines access the full event information, searching for secondary vertices and composite particles, while applying some Global Event Cuts (GECs) to remove events with very high track multiplicities that would take too long to process.

The HLT2 muon trigger is similar to the one executed in HLT1, with more refined track selection criteria applied. Generic $B \to X$ decays are searched for with the n-body topological trigger lines, which make use of general features of b-hadron decays to perform a candidate selection. In particular, the `Topo2Body`, `Topo3Body` and `Topo4Body` triggers search for $B \to DX$ candidates, where the D meson decays to 2,3 or 4 tracks, respectively. The lines execute a fast multivariate selection using the Boosted Decision Tree (BDT) [52, 53] classifier, providing high levels of background rejection and signal efficiency. The logical *or* of these trigger lines is employed along with the `HLT1Track` trigger in this thesis. Events passing HLT2 are stored permanently, ready to be used in offline analysis.

2.8.4. Trigger Configuration Keys (TCKs)

Data-taking conditions varied over the course of Run I, resulting in changes to the trigger configuration over time. To document precisely what trigger configurations were used at any given time, Trigger Configuration Keys (TCKs) were employed. These keys record the specific sequence of algorithms and trigger lines that run in the L0, HLT1 and HLT2 at any time, including the parameters of their configuration and any thresholds. A single 32-bit number encodes each TCK, where the first 16 bits are reserved for the L0 and the second 16 for the HLT.

2.9. Track reconstruction

The concept of track reconstruction underpins much of the previous discussion relating to each of the sub-detectors and the trigger. The LHCb track reconstruction [54] uses information from the VELO, TT, IT and OT to fit charged particle trajectories. Tracks in LHCb can be divided into several categories, depending upon the specific properties of their trajectories; each class of track is illustrated in Figure 2.14, and they are summarised here:

- **Long tracks** pass through the full tracking system from the VELO to the T3 tracking station. These tracks have the best momentum resolution of all tracks in LHCb, and are the only ones considered in the reconstruction of B candidates in this thesis.
- **Upstream tracks** pass through the VELO and TT, but are swept out of the detector by the dipole magnet due to their lower momentum. On their way to the TT, upstream tracks pass through RICH1 and may leave a Cherenkov cone. As such, these tracks are useful for calibrating the RICH detector, but typically have poor momentum resolution.
- **Downstream tracks** traverse only the TT and T stations. Tracks of this type typically originate from the decay of long-lived mesons such as the K^0_S, which decay outside the VELO acceptance.
- **VELO tracks** leave the detector acceptance after the VELO, and are used mainly for PV reconstruction.
- **T tracks** leave hits only in the T stations, and prove useful for understanding the contribution from downstream secondary particles in the RICH2 global pattern recognition.

Seed tracks in the VELO and TT are used for the full track reconstruction, as these sub-detectors experience the lowest magnetic fields and thus have hit patterns that are most consistent with straight lines. After seed tracks are found, hits from the different sub-detectors are matched and their trajectories refitted with a Kalman filter fit, where multiple scattering and $\mathrm{d}E/\mathrm{d}x$ energy loss are accounted for. During this process, poor quality tracks (those with large χ^2_{track} values) and duplicate tracks are removed.

The overall performance of the track reconstruction is quantified using two factors, namely the reconstruction efficiency and the ghost rate. The reconstruction efficiency is defined as the fraction of reconstructible tracks that are subsequently reconstructed. To be deemed reconstructible, a track must have a sufficient number of hits and fall within the acceptance of each sub-detector. The average long track reconstruction efficiency in Run I was 96% in the momentum range $5 < p < 200$ GeV/c and in the pseudorapidity range $2 < \eta < 5$, which covers the phase space of LHCb.

A track is classified as a ghost if it is not associated to any charged particle in the event. Ghost tracks are formed from uncorrelated real and noise hits, and are typically of low momentum. The ghost rate is defined as the average fraction of ghost tracks in

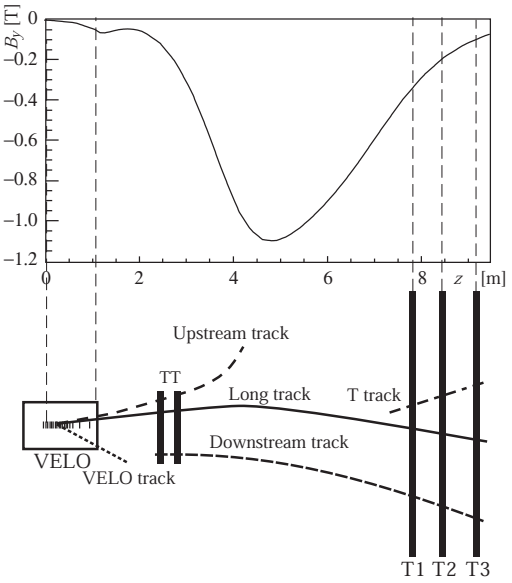

Figure 2.14.: The various types of charged track in LHCb [41]. Tracks are classified according to the detectors used in their reconstruction. The different track types are: Long, Upstream, Downstream, VELO and T. The main B-field component, B_y, is plotted as a function of z position for reference on the same scale.

an event. Tools have been developed to minimise the effect of ghosts in offline analyses, employing a multivariate method to distinguish ghost tracks and normal tracks using various kinematic and track properties. As such, ghosts do not contribute a background to any of the analyses presented within this thesis.

2.10. Particle identification (PID)

Charged tracks in LHCb are identified using a combination of information from the RICH detectors, the calorimeters and the muon stations. For each track, a log-likelihood difference between a given particle hypothesis x ($x \in K, p, \mu, e$) and the pion hypothesis is constructed, where the pion hypothesis is chosen as an arbitrary reference. The global PID likelihood function is defined as:

$$\Delta LL_{x/\pi} = \ln L(x) - \ln L(\pi) \tag{2.5}$$

where $L(x)$ is the likelihood of a given track being a particle, x. This global likelihood is defined for each particle type, and is formed by multiplying the different likelihoods from

each sub-detector:

$$L(K) = L^{\mathrm{RICH}}(K) \times L^{\mathrm{CALO}}(\text{non-}e) \times L^{\mathrm{MUON}}(\text{non-}\mu) \tag{2.6}$$

$$L(\pi) = L^{\mathrm{RICH}}(\pi) \times L^{\mathrm{CALO}}(\text{non-}e) \times L^{\mathrm{MUON}}(\text{non-}\mu) \tag{2.7}$$

$$L(\mu) = L^{\mathrm{RICH}}(\mu) \times L^{\mathrm{CALO}}(\text{non-}e) \times L^{\mathrm{MUON}}(\mu) \tag{2.8}$$

$$L(e) = L^{\mathrm{RICH}}(e) \times L^{\mathrm{CALO}}(e) \times L^{\mathrm{MUON}}(\text{non-}\mu) \tag{2.9}$$

Absolute likelihoods L are, however, not a good measure - the likelihood scale changes between each event, due to differences in kinematics and underlying event multiplicity. As a result, ΔLL values with respect to a reference likelihood are constructed. The $\Delta LL_{x/x'}$ between any x and x' particle hypotheses can be derived from $\Delta LL_{x/\pi}$ as follows:

$$\Delta LL_{x/x'} = \Delta LL_{x/\pi} - \Delta LL_{x'/\pi} = \ln L(x) - \ln L(x') \tag{2.10}$$

2.10.1. Hadron identification

Hadrons are identified primarily using the RICH detectors. The circular rings observed on the detector planes, as shown in Figure 2.11, are compared with the expected pattern under a given particle hypothesis, h. A likelihood $L^{\mathrm{RICH}}(h)$ is then constructed from this comparison. The RICH PID performance is validated using a high statistics calibration sample of $D^{*\pm} \to [K^{\mp}\pi^{\pm}]_D \pi^{\pm}$ decays, where particle types can be unambiguously determined from the charges of each daughter (see Section 3.3.3).

The RICH detectors provide excellent K/π separation over a wide momentum range, as illustrated in Figure 2.15 where the RICH kaon identification efficiency (red) and pion misidentification rate (black) as a function of track momentum are shown [55]. Two different $\Delta LL_{K/\pi}$ requirements have been imposed on the sample, resulting in the open and filled marker distributions. In the filled (open) case, a tighter (looser) kaon identification requirement has been applied. Looser cuts result in higher kaon efficiencies, but also higher pion misidentification rates.

At high values of track momentum the Cherenkov cones saturate, resulting in poorer PID discrimination. At low momentum, the particles do not radiate sufficiently as they pass through the radiator gases, resulting in low photon yield and poor ring reconstruction. This decrease in performance is illustrated by the drop in kaon efficiency at low momentum, and the corresponding bump in pion misidentification rate in the same region. The PID performance of the RICH is also known to depend on particle rapidity,

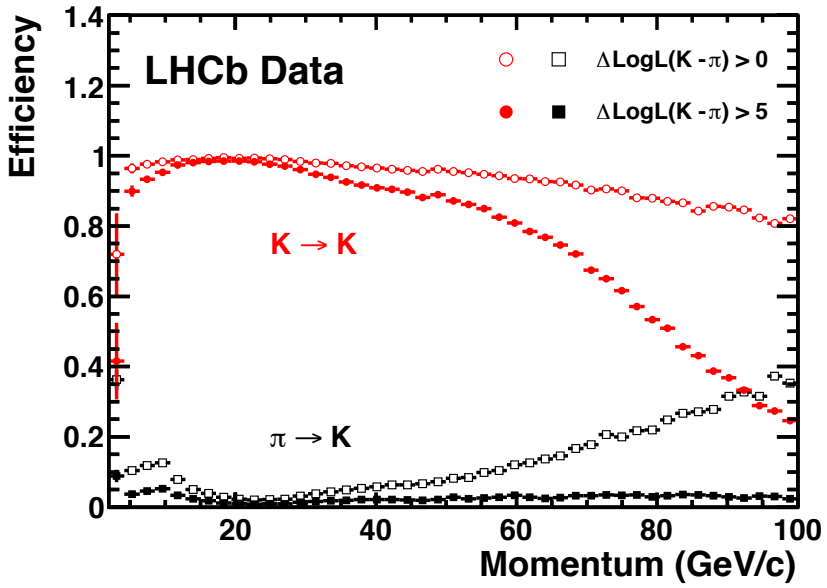

Figure 2.15.: RICH kaon identification efficiency (red) and pion misidentification rate (black) as a function of track momentum [55].

as well as the track multiplicity of an event [55]. The K/π separation ability of the RICH is exploited throughout this thesis in order to differentiate between $B^{\pm} \to DK^{\pm}$ and $B^{\pm} \to D\pi^{\pm}$ decays.

2.10.2. Muon identification

Muon identification using the muon stations can be performed only for muons above a threshold momentum of 3 GeV/c, the minimum required to reach M2. Tracks are flagged as muons if they are associated with a minimum number of hits in the muon stations, where the required number of hits in each station depends upon the track momentum. Hits are deemed to be consistent with a track if they are found within a Field Of Interest (FOI), where the size of the FOI depends upon the track momentum and the region of the detector traversed. Likelihoods are computed for both the muon and non-muon cases, and can be combined with the RICH muon hypothesis to provide a global $\Delta LL_{\mu/\pi}$ variable.

2.10.3. Identification of electrons and neutrals

The calorimeter can be used to construct likelihoods L^{CALO} for electrons and photons, by assessing the difference in E_T cluster shapes for each particle. Neutral pion decays to two photons can also be reconstructed, by merging pairs of photon clusters to produce an invariant mass. Candidate π^0 hadrons are then selected based on the invariant mass of the combination. Although electrons and neutrals are not considered in the analyses presented in this thesis, successful measurements of $\mathcal{CP}$-violating observables have recently been made at LHCb using $B^\pm \to DK^\pm$ decays where the D decays to a final state involving a π^0 [56].

Chapter 3.

ADS/GLW analysis of $B^{\pm} \to DK^{\pm}$ and $B^{\pm} \to D\pi^{\pm}$ decays

In this Chapter, the Atwood-Dunietz-Soni/Gronau-London-Wyler (ADS/GLW) analysis of $B^{\pm} \to [hh]_D h^{\pm}$ and $B^{\pm} \to [hhhh]_D h^{\pm}$ decays is introduced, where the D meson is reconstructed in the final states $K^{\pm}\pi^{\mp}$, $\pi^{\pm}K^{\mp}$, $K^{\pm}K^{\mp}$, $\pi^{\pm}\pi^{\mp}$, $K^{\pm}\pi^{\mp}\pi^{\pm}\pi^{\mp}$, $\pi^{\pm}K^{\mp}\pi^{\pm}\pi^{\mp}$ and $\pi^{\pm}\pi^{\mp}\pi^{\pm}\pi^{\mp}$. The theoretical formalism for the measurement is developed in Section 3.1, and a discussion of previous measurements outlined in Section 3.2. The selection strategy is described in Section 3.3. All backgrounds considered in the analysis are described in Section 3.4. The invariant mass fit used to measure event yields and asymmetries is the subject of Chapter 4.

3.1. Determining γ at tree level with $B^{\pm} \to DK^{\pm}$ decays

In essence, γ as defined in Equation 1.23 is the relative phase of the CKM elements V_{ub}/V_{cb}. It can be measured by exploiting the interference between $b \to c(\bar{u}s)$ and $b \to u(\bar{c}s)$ transitions in $B^{\pm} \to DK^{\pm}$ decays, a method first proposed by Gronau, London and Wyler [57, 58]. As shown in Figure 3.1, $B^{\pm} \to DK^{\pm}$ decays can proceed through two different amplitudes, namely $B^{-} \to D^0 K^{-}$ and $B^{-} \to \bar{D}^0 K^{-}$ (charge conjugation is implied throughout). These amplitudes interfere when both the D^0 and $\bar{D}^0$ flavour eigenstates decay to the same final state, f.

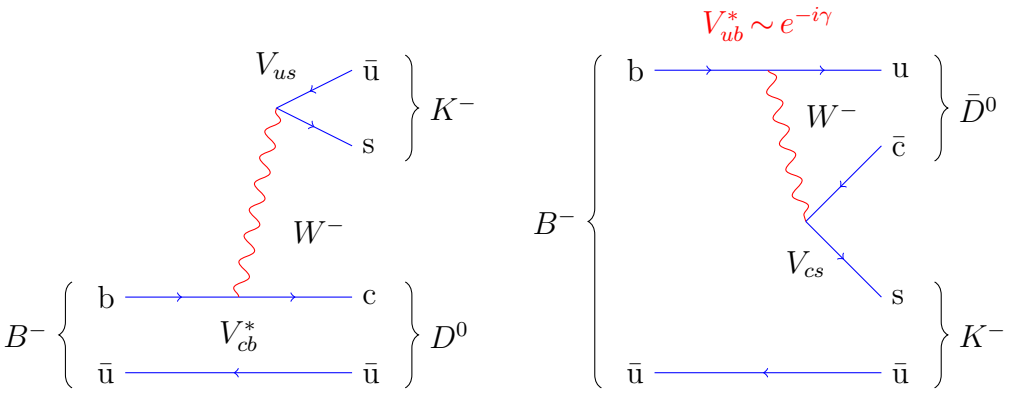

Figure 3.1.: Feynman diagrams for the decays $B^- \to D^0 K^-$ and $B^- \to \bar{D}^0 K^-$. There is a relative phase $\delta_B - \gamma$ and a magnitude ratio r_B between the two interfering amplitudes. The diagram on the left is referred to as *colour favoured*, whereas the right diagram is referred to as *colour suppressed*.

Since $V_{ub} \sim e^{-i\gamma}$, the four amplitudes involved in the decay can be written as:

$$A(B^- \to D^0 K^-) \propto 1 \tag{3.1}$$
$$A(B^- \to \bar{D}^0 K^-) \propto r_B e^{i(\delta_B - \gamma)} \tag{3.2}$$
$$A(B^+ \to \bar{D}^0 K^+) \propto 1 \tag{3.3}$$
$$A(B^+ \to D^0 K^+) \propto r_B e^{i(\delta_B + \gamma)} \tag{3.4}$$

where each of the amplitudes have been normalised to the corresponding favoured ($b \to c(\bar{u}s)$) amplitudes. Three real parameters enter into the amplitude expressions:

- The modulus of the colour suppressed/favoured amplitudes, $r_B = |A_{\text{sup}}/A_{\text{fav}}|$. The suppressed amplitude describes the $B^- \to \bar{D}^0 K^-$ decay, while the favoured amplitude describes the $B^- \to D^0 K^-$ decay.
- The $\mathcal{CP}$-invariant strong phase deference, δ_B. In quantum field theory, all amplitudes have associated arbitrary phases. The parameter δ_B describes the difference in arbitrary strong phase between the two interfering diagrams.
- The $\mathcal{CP}$-violating weak phase difference, γ.

The amplitudes for the complete decay chain including the D decay[1] can be written as:

$$A(B^- \to [f]_D K^-) \propto A_f + r_B e^{i(\delta_B - \gamma)} \bar{A}_f \tag{3.5}$$

$$A(B^+ \to \left[\bar{f}\right]_D K^+) \propto r_B e^{i(\delta_B + \gamma)} A_f + \bar{A}_f \tag{3.6}$$

where A_f and $\bar{A}_f$ represent the amplitudes for D^0 and $\bar{D}^0$ decays to the final state f, respectively. The interference between the two amplitudes gives rise to detectable $\mathcal{CP}$-violation, but the small value of r_B arising from the colour suppression in Figure 3.1 limits the size of any interference effects. The current world average values for r_B and δ_B in $B^\pm \to DK^\pm$ decays are [12, 35]:

$$r_B[B \to DK] \equiv r_B^K = 0.0972^{+0.0063}_{-0.0064} \tag{3.7}$$

$$\delta_B[B \to DK] \equiv \delta_B^K = (121.1^{+8.2}_{-9.2})^\circ \tag{3.8}$$

It is worth noting that $B^\pm \to D\pi^\pm$ decays can also be used to gain γ sensitivity. The limitation here is that r_B^π is an order of magnitude smaller than its $B^\pm \to DK^\pm$ counterpart ($r_B^\pi \approx 0.01$) [35], limiting the size of any interference effects that can potentially be observed. The real power of this method, however, lies in the large number of available D final states; in this thesis, use is made of both $D \to h^+h^-$ and $D \to h^+h^-h^+h^-$ decays, taking full advantage of the statistical muscle of LHCb in providing high statistics $B^\pm \to Dh^\pm$ samples.

3.1.1. The GLW method

The GLW method [57,58] considers final states of the D which are an exact $\mathcal{CP}$ eigenstate, $f = f_{CP}$. In this case, $A_f = \bar{A}_f$, such that Equations 3.5 and 3.6 reduce to:

$$A(B^- \to [f_{CP}]_D K^-) \propto 1 + r_B e^{i(\delta_B - \gamma)} \tag{3.9}$$

$$A(B^+ \to [f_{CP}]_D K^+) \propto r_B e^{i(\delta_B + \gamma)} + 1 \tag{3.10}$$

leading to the following partial width expressions:

$$\Gamma(B^- \to [f_{CP}]_D K^-) \propto \left|A(B^- \to [f_{CP}]_D K^-)\right|^2 \propto 1 + r_B^2 + 2r_B \cos(\delta_B - \gamma) \tag{3.11}$$

$$\Gamma(B^+ \to [f_{CP}]_D K^+) \propto \left|A(B^+ \to [f_{CP}]_D K^+)\right|^2 \propto 1 + r_B^2 + 2r_B \cos(\delta_B + \gamma) \tag{3.12}$$

[1] D refers now to either D^0 or $\bar{D}^0$.

where the size of r_B^2 relative to the leading unity term limits the degree of measurable interference. The GLW modes considered in this thesis are: $D \to K^+K^-$, $D \to \pi^+\pi^-$ and $D \to \pi^+\pi^-\pi^+\pi^-$. The use of the latter multi-body D decay introduces a further term $\kappa^{\pi\pi\pi\pi} = 2F_+ - 1$, where F_+ is the effective CP^+ fraction of the multi-body final state. This term accounts for the internal resonant structure in the multi-body D decay, which can reduce the overall level of sensitivity to γ. It appears in the partial width expressions:

$$\Gamma(B^- \to [\pi\pi\pi\pi]_D K^-) \propto \left|A(B^- \to [\pi\pi\pi\pi]_D K^-)\right|^2 \propto 1 + r_B^2 + 2\kappa^{\pi\pi\pi\pi} r_B \cos(\delta_B - \gamma) \tag{3.13}$$

$$\Gamma(B^+ \to [\pi\pi\pi\pi]_D K^+) \propto \left|A(B^+ \to [\pi\pi\pi\pi]_D K^+)\right|^2 \propto 1 + r_B^2 + 2\kappa^{\pi\pi\pi\pi} r_B \cos(\delta_B + \gamma) \tag{3.14}$$

This factor is currently being measured by the CLEOc collaboration [59], and will be used as external input in the measurement of γ.

3.1.2. The ADS method

Rather than using D decays to a $\mathcal{CP}$ eigenstate, the ADS method proposes the use of non-$\mathcal{CP}$ eigenstates such as $D \to K^\pm\pi^\mp$ and $D \to K^\pm\pi^\mp\pi^\pm\pi^\mp$ [60, 61]. In this case, two amplitudes for the D decay exist, as illustrated in Figure 3.2. The D decay can proceed via a diagram containing two diagonal elements of V_{CKM}, the so-called Cabibbo favoured (CF) case $\bar{D}^0 \to K^+\pi^-$, or via a diagram containing two off-diagonal V_{CKM} elements, known as the doubly Cabibbo suppressed (DCS) case $\bar{D}^0 \to K^-\pi^+$.

In a similar fashion to the $B^\pm \to DK^\pm$ amplitudes defined in Section 3.1, the two D decay amplitudes can be expressed as:

$$A(\bar{D}^0 \to K^+\pi^-) \propto 1 \tag{3.15}$$

$$A(D^0 \to K^+\pi^-) \propto r_D e^{-i\delta_D} \tag{3.16}$$

where two additional parameters enter, namely the strong phase difference between the two D decays, δ_D, and the modulus of the suppressed/favoured amplitude ratio for the decays, r_D. Both parameters depend upon the specific D final state, and in the case of multi-body D decays can vary across the decay phase space. The ADS modes considered in this thesis are $D \to K^\pm\pi^\mp$ and $D \to K^\pm\pi^\mp\pi^\pm\pi^\mp$.

Overall, two decay paths are possible:

- A colour favoured B decay followed by a doubly Cabibbo suppressed D decay.
- A colour suppressed B decay followed by a Cabibbo favoured D decay.

where both paths are illustrated in Figure 3.3. The overall amplitudes for both decay paths are comparable in size, owing to the similar magnitude of r_B and r_D. This leads to larger interference effects than in the GLW case, resulting in potentially larger experimental asymmetries. The presence of such large asymmetries makes the ADS method a highly sensitive probe of γ.

The ADS amplitudes are similar in structure to those presented in Equations 3.9 and 3.10 for the GLW case, with the addition of r_D and δ_D:

$$A(B^- \to [K^+\pi^-(\pi^+\pi^-)]_D K^-) \propto r_D^{K\pi(\pi\pi)} e^{i\delta_D^{K\pi(\pi\pi)}} + r_B e^{i(\delta_B - \gamma)} \tag{3.17}$$

$$A(B^+ \to [K^-\pi^+(\pi^-\pi^+)]_D K^+) \propto r_D^{K\pi(\pi\pi)} e^{i\delta_D^{K\pi(\pi\pi)}} + r_B e^{i(\delta_B + \gamma)} \tag{3.18}$$

$$A(B^- \to [K^-\pi^+(\pi^-\pi^+)]_D K^-) \propto 1 + r_B r_D^{K\pi(\pi\pi)} e^{i(\delta_B - \gamma)} e^{i\delta_D^{K\pi(\pi\pi)}} \tag{3.19}$$

$$A(B^+ \to [K^+\pi^-(\pi^+\pi^-)]_D K^-) \propto 1 + r_B r_D^{K\pi(\pi\pi)} e^{i(\delta_B + \gamma)} e^{i\delta_D^{K\pi(\pi\pi)}} \tag{3.20}$$

where $r_D^{K\pi}, \delta_D^{K\pi}$ and $r_D^{K\pi\pi\pi}, \delta_D^{K\pi\pi\pi}$ refer to the amplitude ratio and strong phase difference for $D \to K^{\pm}\pi^{\mp}$ and $D \to K^{\pm}\pi^{\mp}\pi^{\pm}\pi^{\mp}$ decays, respectively. It is important to note that the signature of suppressed mode decays is that the kaons produced in the B and D decays are of *opposite charge*.

The partial widths for the suppressed decay can be written as:

$$\Gamma(B^- \to [K^+\pi^-(\pi^+\pi^-)]_D K^-) \propto \left(r_D^{K\pi(\pi\pi)}\right)^2 + r_B^2 + 2\kappa^{K\pi(\pi\pi)} r_D^{K\pi(\pi\pi)} r_B \cos(\delta_B + \delta_D - \gamma) \tag{3.21}$$

$$\Gamma(B^+ \to [K^-\pi^+(\pi^-\pi^+)]_D K^+) \propto \left(r_D^{K\pi(\pi\pi)}\right)^2 + r_B^2 + 2\kappa^{K\pi(\pi\pi)} r_D^{K\pi(\pi\pi)} r_B \cos(\delta_B + \delta_D + \gamma) \tag{3.22}$$

and similarly for the favoured decay:

$$\Gamma(B^- \to [K^-\pi^+(\pi^-\pi^+)]_D K^-) \propto 1 + \left(r_D^{K\pi(\pi\pi)}\right)^2 r_B^2 + 2\kappa^{K\pi(\pi\pi)} r_D^{K\pi(\pi\pi)} r_B \cos(\delta_B - \delta_D - \gamma) \tag{3.23}$$

$$\Gamma(B^+ \to [K^+\pi^-(\pi^+\pi^-)]_D K^+) \propto 1 + \left(r_D^{K\pi(\pi\pi)}\right)^2 r_B^2 + 2\kappa^{K\pi(\pi\pi)} r_D^{K\pi(\pi\pi)} r_B \cos(\delta_B - \delta_D + \gamma) \tag{3.24}$$

Parameter	Value $\pm 1\sigma$
$r_D^{K\pi}$	$(6.16 \pm 0.15)\%$
$\delta_D^{K\pi}$	$(202.4\ ^{+9.7}_{-11.0})^\circ$
$r_D^{K\pi\pi\pi}$	$(5.69 \pm 0.28)\%$
$\delta_D^{K\pi\pi\pi}$	$(114 \pm 25)^\circ$
$\kappa^{K\pi\pi\pi}$	0.33 ± 0.25

Table 3.1.: External inputs from charm physics used in the ADS analysis of $B^\pm \to Dh^\pm$ with $D \to K^\pm\pi^\mp\,(\pi^\pm\pi^\mp)$ [12, 35].

where $\kappa^{K\pi(\pi\pi)}$ is the coherence factor. A small value of $\kappa^{K\pi(\pi\pi)}$ indicates a lack of coherence between the intermediate states involved in the D decay, a situation expected when there are many resonances contributing; a value close to one occurs when the resonances are largely in phase, such that one state dominates. By definition, $\kappa^{K\pi} = 1$ for the two-body $D \to K^\pm\pi^\mp$ decay. Independent measurements of $r_D^{K\pi}$, $\delta_D^{K\pi}$, $r_D^{K\pi\pi\pi}$, $\delta_D^{K\pi\pi\pi}$ and $\kappa^{K\pi\pi\pi}$ are employed in this thesis, using the values listed in Table 3.1.

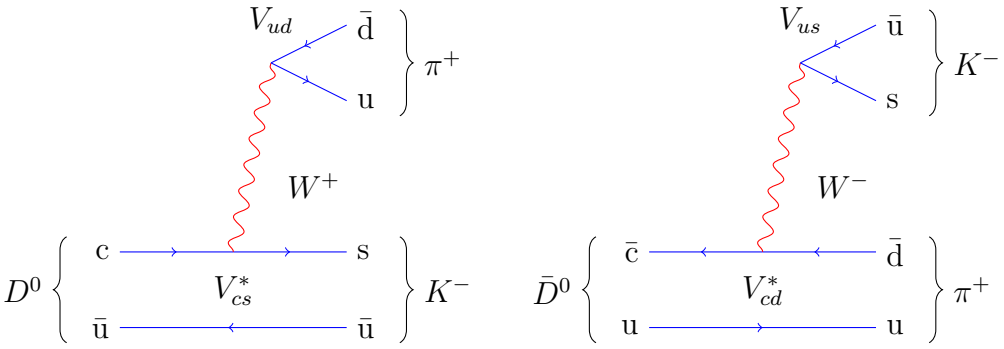

Figure 3.2.: Feynman diagrams for the decays $D^0 \to K^-\pi^+$ and $\bar{D}^0 \to K^-\pi^+$. There is a relive phase $\delta_D^{K\pi}$ and magnitude ratio $r_D^{K\pi}$ between the corresponding amplitudes of each diagram. The diagram on the left is referred to as Cabibbo favoured (CF), with an amplitude proportional to two diagonal CKM matrix elements. The diagram on the right is referred to as doubly Cabibbo suppressed (DCS), since its amplitude is proportional to two off-diagonal CKM elements.

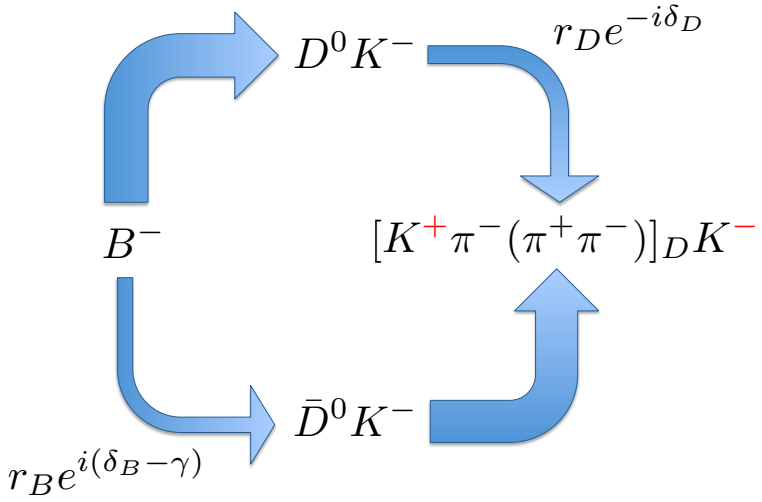

Figure 3.3.: Schematic diagram of the interfering ADS amplitudes for suppressed $B^{\pm} \to DK^{\pm}$ decays. The hallmark of suppressed decays is the opposite charge of the kaons produced in the B and D decays, as indicated in red. A colour favoured $B^- \to DK^-$ decay (charge conjugation implied) is followed by a doubly Cabibbo suppressed D decay in one instance; in the second instance, a colour suppressed B decay is followed by a Cabibbo favoured D decay. The interference between these decay paths is large, owing to the similar magnitude of r_B and r_D, and gives experimental sensitivity to γ.

3.1.3. From partial widths to physical observables

The partial width expressions introduced in Sections 3.1.1 and 3.1.2 can be manipulated to construct measurable observables that relate to the parameters of interest r_B, δ_B and γ. In this thesis, ratios of partial widths are measured at all times in order to largely cancel systematic uncertainties. With this approach, the analysis reduces to a simple counting experiment.

The ratio of favoured $B^\pm \to DK^\pm$ decays relative to favoured $B^\pm \to D\pi^\pm$ decays is measured for the $D \to K^\pm\pi^\mp$ and $D \to K^\pm\pi^\mp\pi^\pm\pi^\mp$ modes:

$$R_{K/\pi}^{K\pi(\pi\pi)} = \frac{\Gamma(B^- \to [K^-\pi^+(\pi^-\pi^+)]_D K^-) + \Gamma(B^+ \to [K^+\pi^-(\pi^+\pi^-)]_D K^+)}{\Gamma(B^- \to [K^-\pi^+(\pi^-\pi^+)]_D \pi^-) + \Gamma(B^+ \to [K^+\pi^-(\pi^+\pi^-)]_D \pi^+)} \tag{3.25}$$

where the superscript denotes the favoured D decay, and the subscript reflects the fact that this is a ratio of $B^\pm \to DK^\pm / B^\pm \to D\pi^\pm$ decays. For the GLW modes $D \to K^+K^-, \pi^+\pi^-, \pi^+\pi^-\pi^+\pi^-$, the following double ratios are measured:

$$R_{CP}^{KK} = \frac{R_{K/\pi}^{KK}}{R_{K/\pi}^{K\pi}} \tag{3.26}$$

$$R_{CP}^{\pi\pi} = \frac{R_{K/\pi}^{\pi\pi}}{R_{K/\pi}^{K\pi}} \tag{3.27}$$

$$R_{CP}^{\pi\pi\pi\pi} = \frac{R_{K/\pi}^{\pi\pi\pi\pi}}{R_{K/\pi}^{K\pi\pi\pi}} \tag{3.28}$$

where the subscript CP denotes that the GLW modes are CP eigenstates in the 2-body case and CP eigenstate-like in the 4-body case. Charge asymmetries are also measured in each of the above cases, and are defined as:

$$A_K^{K\pi(\pi\pi)} = \frac{\Gamma(B^- \to [K^-\pi^+(\pi^-\pi^+)]_D K^-) - \Gamma(B^+ \to [K^+\pi^-(\pi^+\pi^-)]_D K^+)}{\Gamma(B^- \to [K^-\pi^+(\pi^-\pi^+)]_D K^-) + \Gamma(B^+ \to [K^+\pi^-(\pi^+\pi^-)]_D K^+)} \tag{3.29}$$

$$A_\pi^{KK} = \frac{\Gamma(B^- \to [K^+K^-]_D \pi^-) - \Gamma(B^+ \to [K^+K^-]_D \pi^+)}{\Gamma(B^- \to [K^+K^-]_D \pi^-) + \Gamma(B^+ \to [K^+K^-]_D \pi^+)} \tag{3.30}$$

$$A_K^{KK} = \frac{\Gamma(B^- \to [K^+K^-]_D K^-) - \Gamma(B^+ \to [K^+K^-]_D K^+)}{\Gamma(B^- \to [K^+K^-]_D K^-) + \Gamma(B^+ \to [K^+K^-]_D K^+)} \tag{3.31}$$

$$A_\pi^{\pi\pi(\pi\pi)} = \frac{\Gamma(B^- \to [\pi^+\pi^-(\pi^+\pi^-)]_D \pi^-) - \Gamma(B^+ \to [\pi^+\pi^-(\pi^+\pi^-)]_D \pi^+)}{\Gamma(B^- \to [\pi^+\pi^-(\pi^+\pi^-)]_D \pi^-) + \Gamma(B^+ \to [\pi^+\pi^-(\pi^+\pi^-)]_D \pi^+)} \tag{3.32}$$

$$A_K^{\pi\pi(\pi\pi)} = \frac{\Gamma(B^- \to [\pi^+\pi^-(\pi^+\pi^-)]_D K^-) - \Gamma(B^+ \to [\pi^+\pi^-(\pi^+\pi^-)]_D K^+)}{\Gamma(B^- \to [\pi^+\pi^-(\pi^+\pi^-)]_D K^-) + \Gamma(B^+ \to [\pi^+\pi^-(\pi^+\pi^-)]_D K^+)} \tag{3.33}$$

$$\tag{3.34}$$

where $A_\pi^{K\pi}$ and $A_\pi^{K\pi\pi\pi}$ are both assumed to be zero, since favoured $B \to D\pi$ decays proceed via a single dominant tree amplitude such that no significant interference effects are present. This assumption allows the production asymmetry of $B^\pm$ mesons at LHCb to be measured using favoured $B^\pm \to D\pi^\pm$ decays:

$$A_{B_u} = \frac{\mathcal{N}(B^- \to [K^-\pi^+(\pi^-\pi^+)]_D\pi^-) - \mathcal{N}(B^+ \to [K^+\pi^-(\pi^+\pi^-)]_D\pi^+)}{\mathcal{N}(B^- \to [K^-\pi^+(\pi^-\pi^+)]_D\pi^-) + \mathcal{N}(B^+ \to [K^+\pi^-(\pi^+\pi^-)]_D\pi^+)} \tag{3.35}$$

as will be discussed in detail in Chapter 5.

For the suppressed $B^\pm \to DK^\pm$ and $B^\pm \to D\pi^\pm$ modes, the following observables are measured:

$$R_{\mathrm{ADS}(\pi)}^{K\pi(\pi\pi)} = \frac{\Gamma(B^- \to [K^+\pi^-(\pi^+\pi^-)]_D\pi^-) + \Gamma(B^+ \to [K^-\pi^+(\pi^-\pi^+)]_D\pi^+)}{\Gamma(B^- \to [K^-\pi^+(\pi^-\pi^+)]_D\pi^-) + \Gamma(B^+ \to [K^+\pi^-(\pi^+\pi^-)]_D\pi^+)} \tag{3.36}$$

$$R_{\mathrm{ADS}(K)}^{K\pi(\pi\pi)} = \frac{\Gamma(B^- \to [K^+\pi^-(\pi^+\pi^-)]_DK^-) + \Gamma(B^+ \to [K^-\pi^+(\pi^-\pi^+)]_DK^+)}{\Gamma(B^- \to [K^-\pi^+(\pi^-\pi^+)]_DK^-) + \Gamma(B^+ \to [K^+\pi^-(\pi^+\pi^-)]_DK^+)} \tag{3.37}$$

$$A_{\mathrm{ADS}(\pi)}^{K\pi(\pi\pi)} = \frac{\Gamma(B^- \to [K^+\pi^-(\pi^+\pi^-)]_D\pi^-) - \Gamma(B^+ \to [K^-\pi^+(\pi^-\pi^+)]_D\pi^+)}{\Gamma(B^- \to [K^+\pi^-(\pi^+\pi^-)]_D\pi^-) + \Gamma(B^+ \to [K^-\pi^+(\pi^-\pi^+)]_D\pi^+)} \tag{3.38}$$

$$A_{\mathrm{ADS}(K)}^{K\pi(\pi\pi)} = \frac{\Gamma(B^- \to [K^+\pi^-(\pi^+\pi^-)]_DK^-) - \Gamma(B^+ \to [K^-\pi^+(\pi^-\pi^+)]_DK^+)}{\Gamma(B^- \to [K^+\pi^-(\pi^+\pi^-)]_DK^-) + \Gamma(B^+ \to [K^-\pi^+(\pi^-\pi^+)]_DK^+)} \tag{3.39}$$

In total 22 observables are measured, with A_{B_u} being measured in two independent samples, $B^- \to [K^-\pi^+]_D\pi^-$ and $B^- \to [K^-\pi^+\pi^-\pi^+]_D\pi^-$. With the exception of A_{B_u}, each of the remaining 21 observables can be related to the r_B, δ_B and γ parameters using the expressions from Sections 3.1.1 and 3.1.2:

$$R_{K/\pi}^{K\pi(\pi\pi)} = R\frac{1 + \left(r_B^K r_D^{K\pi(\pi\pi)}\right)^2 + 2\kappa^{K\pi(\pi\pi)} r_B^K r_D^{K\pi(\pi\pi)} \cos\left(\delta_B^K - \delta_D^{K\pi(\pi\pi)}\right)\cos\gamma}{1 + \left(r_B^\pi r_D^{K\pi(\pi\pi)}\right)^2 + 2\kappa^{K\pi(\pi\pi)} r_B^\pi r_D^{K\pi(\pi\pi)} \cos\left(\delta_B^\pi - \delta_D^{K\pi(\pi\pi)}\right)\cos\gamma} \tag{3.40}$$

$$R_{CP}^{KK} = R_{CP}^{\pi\pi} = R_{CP}^{\pi\pi\pi\pi} = 1 + \left(r_B^K\right)^2 + 2r_B^K \cos\delta_B^K \cos\gamma \tag{3.41}$$

$$A_K^{K\pi(\pi\pi)} = \frac{2\kappa^{K\pi(\pi\pi)} r_B^K r_D^{K\pi(\pi\pi)} \sin\left(\delta_B^K - \delta_D^{K\pi(\pi\pi)}\right)\sin\gamma}{1 + \left(r_B^K r_D^{K\pi(\pi\pi)}\right)^2 + 2\kappa^{K\pi(\pi\pi)} r_B^K r_D^{K\pi(\pi\pi)} \cos\left(\delta_B^K - \delta_D^{K\pi(\pi\pi)}\right)\cos\gamma} \tag{3.42}$$

$$A_K^{KK} = A_K^{\pi\pi} = A_K^{\pi\pi\pi\pi} = \frac{2r_B^K \sin\delta_B^K \sin\gamma}{1 + \left(r_B^K\right)^2 + 2r_B^K \cos\delta_B^K \cos\gamma} \tag{3.43}$$

$$A_\pi^{KK} = A_\pi^{\pi\pi} = A_\pi^{\pi\pi\pi\pi} = \frac{2r_B^\pi \sin\delta_B^\pi \sin\gamma}{1 + \left(r_B^\pi\right)^2 + 2r_B^\pi \cos\delta_B^\pi \cos\gamma} \tag{3.44}$$

$$R_{\mathrm{ADS}(K)} = \frac{\left(r_B^K\right)^2 + \left(r_D^{K\pi(\pi\pi)}\right)^2 + 2\kappa^{K\pi(\pi\pi)} r_B^K r_D^{K\pi(\pi\pi)} \cos\left(\delta_B^K + \delta_D^{K\pi(\pi\pi)}\right)\cos\gamma}{1 + \left(r_B^K r_D^{K\pi(\pi\pi)}\right)^2 + 2\kappa^{K\pi(\pi\pi)} r_B^K r_D^{K\pi(\pi\pi)} \cos\left(\delta_B^K - \delta_D^{K\pi(\pi\pi)}\right)\cos\gamma} \tag{3.45}$$

$$A_{\mathrm{ADS}(K)} = \frac{2\kappa^{K\pi(\pi\pi)} r_B^K r_D^{K\pi(\pi\pi)} \sin\left(\delta_B^K + \delta_D^{K\pi(\pi\pi)}\right)\sin\gamma}{\left(r_B^K\right)^2 + \left(r_D^{K\pi(\pi\pi)}\right)^2 + 2\kappa^{K\pi(\pi\pi)} r_B^K r_D^{K\pi(\pi\pi)} \cos\left(\delta_B^K + \delta_D^{K\pi(\pi\pi)}\right)\cos\gamma} \tag{3.46}$$

$$R_{\mathrm{ADS}(\pi)} = \frac{\left(r_B^\pi\right)^2 + \left(r_D^{K\pi(\pi\pi)}\right)^2 + 2\kappa^{K\pi(\pi\pi)} r_B^\pi r_D^{K\pi(\pi\pi)} \cos\left(\delta_B^\pi + \delta_D^{K\pi(\pi\pi)}\right)\cos\gamma}{1 + \left(r_B^\pi r_D^{K\pi(\pi\pi)}\right)^2 + 2\kappa^{K\pi(\pi\pi)} r_B^\pi r_D^{K\pi(\pi\pi)} \cos\left(\delta_B^\pi - \delta_D^{K\pi(\pi\pi)}\right)\cos\gamma} \tag{3.47}$$

$$A_{\mathrm{ADS}(\pi)} = \frac{2\kappa^{K\pi(\pi\pi)} r_B^\pi r_D^{K\pi(\pi\pi)} \sin\left(\delta_B^\pi + \delta_D^{K\pi(\pi\pi)}\right)\sin\gamma}{\left(r_B^\pi\right)^2 + \left(r_D^{K\pi(\pi\pi)}\right)^2 + 2\kappa^{K\pi(\pi\pi)} r_B^\pi r_D^{K\pi(\pi\pi)} \cos\left(\delta_B^\pi + \delta_D^{K\pi(\pi\pi)}\right)\cos\gamma} \tag{3.48}$$

where

$$R = \frac{\Gamma(B^- \to D^0 K^-)}{\Gamma(B^- \to D^0 \pi^-)} \tag{3.49}$$

$$r_B^K = \left|\frac{A(B^- \to \bar{D}^0 K^-)}{A(B^- \to D^0 K^-)}\right| \tag{3.50}$$

$$r_B^\pi = \left|\frac{A(B^- \to \bar{D}^0 \pi^-)}{A(B^- \to D^0 \pi^-)}\right| \tag{3.51}$$

$$r_D^{K\pi(\pi\pi)} = \left|\frac{A(\bar{D}^0 \to K^-\pi^+(\pi^-\pi^+))}{A(D^0 \to K^-\pi^+(\pi^-\pi^+))}\right| \tag{3.52}$$

$$\delta_B^K = \arg(B^- \to \bar{D}^0 K^-) - \arg(B^- \to D^0 K^-) \tag{3.53}$$

$$\delta_B^\pi = \arg(B^- \to \bar{D}^0 \pi^-) - \arg(B^- \to D^0 \pi^-) \tag{3.54}$$

$$\delta_D^{K\pi(\pi\pi)} = \arg(\bar{D}^0 \to K^-\pi^+(\pi^-\pi^+)) - \arg(D^0 \to K^-\pi^+(\pi^-\pi^+)) \tag{3.55}$$

By measuring each of the physics observables listed here, it will be possible to construct a 3-dimensional space of allowed values for the parameters r_B, δ_B and γ, ultimately helping to improve the precision of γ as measured in tree level B decays. All possible charge asymmetries and relative decay rates are measured for each of the modes considered, such that this list of observables is exhaustive.

3.2. Previous measurements

The CP observables described above, with the exception of $R_{CP}^{\pi\pi\pi\pi}$, $A_\pi^{\pi\pi\pi\pi}$ and $A_K^{\pi\pi\pi\pi}$, have previously been measured by LHCb in 1 fb^{-1} data [62,63]. The work in this thesis builds

upon the previous measurements, taking advantage of the higher statistics available and developing the description of various background components in the invariant mass fit.

No measurement of A_{B_u} was performed in the previous analyses - rather, the $\mathcal{CP}$ asymmetries $A_\pi^{K\pi}$ and $A_\pi^{K\pi\pi\pi}$, both assumed to be zero in this thesis, were measured. The $\mathcal{CP}$ observables $R_{h^+}^{\pi K(\pi\pi)}$ and $R_{h^-}^{\pi K(\pi\pi)}$ were also measured previously, which relate to the $R_{\mathrm{ADS}(h)}$ and $A_{\mathrm{ADS}(h)}$ observables:

$$R_{\mathrm{ADS}(h)}^{\pi K(\pi\pi)} = \frac{R_{h^-}^{\pi K(\pi\pi)} + R_{h^+}^{\pi K(\pi\pi)}}{2} \tag{3.56}$$

$$A_{\mathrm{ADS}(h)}^{\pi K(\pi\pi)} = \frac{R_{h^-}^{\pi K(\pi\pi)} - R_{h^+}^{\pi K(\pi\pi)}}{R_{h^-}^{\pi K(\pi\pi)} + R_{h^+}^{\pi K(\pi\pi)}} \tag{3.57}$$

The previous measurements are reproduced below for reference, both for the 2-body and 4-body analyses.

Previous 1 fb^{-1} $B^\pm \to [hh]_D h^\pm$ results

$R_{K/\pi}^{K\pi}$	=	0.0774	$\pm$ 0.0012 (stat.)	$\pm$ 0.0018 (syst.)
$R_{K/\pi}^{KK}$	=	0.0773	$\pm$ 0.0030 (stat.)	$\pm$ 0.0018 (syst.)
$R_{K/\pi}^{\pi\pi}$	=	0.0803	$\pm$ 0.0056 (stat.)	$\pm$ 0.0017 (syst.)
A_{B_u}	=	not measured		
$A_\pi^{K\pi}$	=	$-$ 0.0001	$\pm$ 0.0036 (stat.)	$\pm$ 0.0095 (syst.)
$A_K^{K\pi}$	=	0.0044	$\pm$ 0.0144 (stat.)	$\pm$ 0.0174 (syst.)
A_π^{KK}	=	$-$ 0.0199	$\pm$ 0.0091 (stat.)	$\pm$ 0.0116 (syst.)
A_K^{KK}	=	0.1480	$\pm$ 0.0369 (stat.)	$\pm$ 0.0097 (syst.)
$A_\pi^{\pi\pi}$	=	$-$ 0.0009	$\pm$ 0.0165 (stat.)	$\pm$ 0.0099 (syst.)
$A_K^{\pi\pi}$	=	0.1351	$\pm$ 0.0661 (stat.)	$\pm$ 0.0095 (syst.)
$R_{K^-}^{K\pi}$	=	0.0073	$\pm$ 0.0023 (stat.)	$\pm$ 0.0004 (syst.)
$R_{K^+}^{K\pi}$	=	0.0232	$\pm$ 0.0034 (stat.)	$\pm$ 0.0007 (syst.)
$R_{\pi^-}^{K\pi}$	=	0.00469	$\pm$ 0.00038 (stat.)	$\pm$ 0.00008 (syst.)
$R_{\pi^+}^{K\pi}$	=	0.00352	$\pm$ 0.00033 (stat.)	$\pm$ 0.00007 (syst.)

from which the following results can be derived:

$$
\begin{array}{lcrll}
R^{\pi K}_{\mathrm{ADS}(\pi)} & = & 0.00410 & \pm 0.00025(\mathrm{stat.}) & \pm 0.00005(\mathrm{syst.}) \\
R^{\pi K}_{\mathrm{ADS}(K)} & = & 0.0152 & \pm 0.0020(\mathrm{stat.}) & \pm 0.0004(\mathrm{syst.}) \\
A^{\pi K}_{\mathrm{ADS}(\pi)} & = & 0.143 & \pm 0.062(\mathrm{stat.}) & \pm 0.011(\mathrm{syst.}) \\
A^{\pi K}_{\mathrm{ADS}(K)} & = & -0.52 & \pm 0.15(\mathrm{stat.}) & \pm 0.02(\mathrm{syst.})
\end{array}
$$

Previous 1 fb^{-1} $B^\pm \to [hhhh]_D h^\pm$ results

$$
\begin{array}{lcrll}
R^{K\pi\pi\pi}_{K/\pi} & = & 0.0771 & \pm 0.0017\ (\mathrm{stat.}) & \pm 0.0026\ (\mathrm{syst.}) \\
A_{B_u} & = & \text{not measured} & & \\
A^{K\pi\pi\pi}_{\pi} & = & -0.006 & \pm 0.005\ (\mathrm{stat.}) & \pm 0.010\ (\mathrm{syst.}) \\
A^{K\pi\pi\pi}_{K} & = & -0.029 & \pm 0.020\ (\mathrm{stat.}) & \pm 0.018\ (\mathrm{syst.}) \\
R^{\pi K\pi\pi}_{\pi^-} & = & 0.00417^{+0.00054}_{-0.00050}\ (\mathrm{stat.}) & \pm 0.00011\ (\mathrm{syst.}) & \\
R^{\pi K\pi\pi}_{\pi^+} & = & 0.00321^{+0.00048}_{-0.00045}\ (\mathrm{stat.}) & \pm 0.00011\ (\mathrm{syst.}) & \\
R^{\pi K\pi\pi}_{K^-} & = & 0.0072^{+0.0036}_{-0.0032}\ (\mathrm{stat.}) & \pm 0.0008\ (\mathrm{syst.}) & \\
R^{\pi K\pi\pi}_{K^+} & = & 0.0175^{+0.0043}_{-0.0039}\ (\mathrm{stat.}) & \pm 0.0010\ (\mathrm{syst.}) &
\end{array}
$$

which gave:

$$
\begin{array}{lcrl}
R^{\pi K\pi\pi}_{\mathrm{ADS}(\pi)} & = & 0.0037(\mathrm{stat.}) & \pm 0.0004(\mathrm{syst.}) \\
R^{\pi K\pi\pi}_{\mathrm{ADS}(K)} & = & 0.0124(\mathrm{stat.}) & \pm 0.0027(\mathrm{syst.}) \\
A^{\pi K\pi\pi}_{\mathrm{ADS}(\pi)} & = & 0.13(\mathrm{stat.}) & \pm 0.10(\mathrm{syst.}) \\
A^{\pi K\pi\pi}_{\mathrm{ADS}(K)} & = & -0.42 & \pm(\mathrm{stat.})0.22(\mathrm{syst.})
\end{array}
$$

where the uncertainties quoted are the combination of the statistical and systematic contributions.

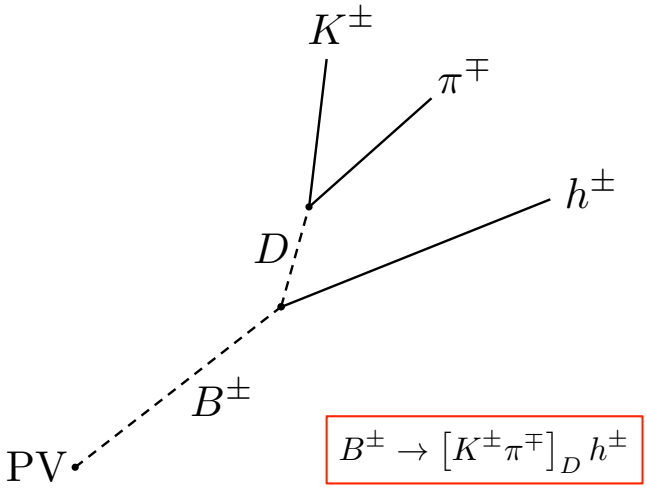

Figure 3.4.: Topology of a favoured $B^\pm \to [K^\pm\pi^\mp]_D\, h^\pm$ decay. Other $B \to [hh]_D h$ decays exhibit the same topology, with $B \to [hhhh]_D\, h$ decays differing by the addition of two charged tracks to the D decay vertex.

3.3. Candidate selection

The analysis reconstructs the decays $B^\pm \to Dh^\pm$ with $D \to h^+h^-(h^+h^-)$, where h represents either a pion or a kaon (excluding the cases $D \to 4K, 3K\pi, KK\pi\pi$, which are not considered). No distinction is made between the intermediate flavour eigenstates D^0 and $\bar{D}^0$, since only the final state $B \to [hh(hh)]_D\, h$ is accessible. All decays proceed via two interfering amplitudes, as detailed in Sections 3.1.1 and 3.1.2, although this interference is generally negligible in the most abundant modes. In Figure 3.4, the general decay topology is illustrated.

In total, 28 different invariant mass combinations are considered: 16 in the $B^\pm \to [hh]_D\, h^\pm$ case, and 12 in the $B^\pm \to [hhhh]_D\, h^\pm$ case. Of these, six involve $\mathcal{CP}$ eigenstate D decays, namely $D \to K^+K^-$ and $D \to \pi^+\pi^-(\pi^+\pi^-)$, with the remaining contributions corresponding to the favoured $D \to K^+\pi^-(\pi^+\pi^-)$ and suppressed $D \to \pi^+K^-(\pi^+\pi^-)$ decay modes. These D candidates are then combined with another charged track in the event to form B candidates; these tracks will be referred to as *bachelors* for the remainder of this thesis, while daughter tracks from the D decay are denoted as *daughter* tracks.

The following notation will be adopted throughout this Chapter:

- $B \to [K\pi(\pi\pi)]_D \pi$ and $B \to [K\pi(\pi\pi)]_D K$ refer to the favoured $B^\pm \to [K^\pm\pi^\mp(\pi^\pm\pi^\mp)]_D h^\pm$ decays, where $h \in \{\pi, K\}$.
- $B \to [\pi K(\pi\pi)]_D \pi$ and $B \to [\pi K(\pi\pi)]_D K$ refer to the suppressed $B^\pm \to [\pi^\pm K^\mp(\pi^\pm\pi^\mp)]_D h^\pm$ decays.
- $B \to [KK]_D \pi$ and $B \to [KK]_D K$ refer to the $B^\pm \to [K^\pm K^\mp]_D h^\pm$ decays.
- $B \to [\pi\pi(\pi\pi)]_D \pi$ and $B \to [\pi\pi(\pi\pi)]_D K$ refer to the $B^\pm \to [\pi^\pm\pi^\mp(\pi^\pm\pi^\mp)]_D h^\pm$ decays.

The key characteristic of suppressed decays is that the bachelor track from the B decay and the kaon track from the D decay are of *opposite* charge. This is in contrast to favoured decays, where the tracks have the same charge. The favoured mode is used to model the suppressed mode line shape in the analysis, benefiting from the large statistics of favoured decays at LHCb. The favoured mode also acts as a model for the $\mathcal{CP}$ eigenstate modes, but differences in invariant mass resolution due to the presence of fewer or greater numbers of kaons are allowed (see Section 4.1.1).

3.3.1. LHCb stripping and trigger

The B candidates considered in this analysis must first pass a set of offline pre-selection cuts prior to the application of any optimised analysis selection. This pre-selection is known as the *stripping*, and is applied in order to reduce the disk space and CPU time required for offline analysis. The candidates used in this thesis are taken from the `Beauty2Charm` stripping module, using the specific stripping lines `StrippingB2D0PiD2HH`, `StrippingB2D0KD2HH`, `StrippingB2D0PiD2HHHH` and `StrippingB2D0KD2HHHH`.

The `Beauty2Charm` module provides access to a wide variety of $B \to DX$ candidates, covering over 800 final states. It begins with candidates accepted by the single track HLT1 trigger `Hlt1Track` [64,65], and applies loose cuts on displaced B and D candidates in order to reject background events. The vertex quality of B and D candidates, χ^2_{vtx}, is required to be below 10, while the proper lifetime of B candidates is required to exceed 0.2 ps in order to select candidates that are well displaced from the PV. The invariant mass of D candidates is required to fall within ± 100 MeV/c^2 of the PDG D^0 mass, while B candidates must have an invariant mass in excess of 4750 MeV/$c^2$and below 7000 MeV/c^2.

A Global Event Cut (GEC) on the number of tracks in the event is applied prior to the formation of any combinations, in order to remove high multiplicity events that would take too long to process. The number of tracks in an event is required to be less than 500. All tracks used in the combination must be well reconstructed, with a track quality χ^2_{tr} below 4, ensuring that fake tracks are not considered. A loose multivariate selection based on a Boosted Decision Tree classifier (BDT) [52, 53] is applied to all B candidates in the stripping, using as input the momentum of the B candidate and its flight distance significance, as well as the sum total of all χ^2_{vtx} values in the decay chain (in this case $\chi^2_{\text{vtx}}(B) + \chi^2_{\text{vtx}}(D)$). The flight distance significance is defined as:

$$\frac{V_B - \text{PV}}{\sigma}$$

where V_B is the B decay vertex position, PV is the primary vertex position and $\sigma = \sqrt{\sigma^2_{V_B} + \sigma_{\text{PV}}}$ represents the overall flight distance uncertainty. The candidates selected by the stripping are stored on disk, ready for optimised offline selections to be performed.

The first cuts applied to stripping selected $B \to [hh]_D\, h$ and $B \to [hhhh]_D\, h$ candidates in this analysis are a set of trigger requirements. All events are required to have been triggered at L0 by either:

- the signal candidate, using the `L0HadronDecision_TOS` trigger (TOS stands for Triggered On Signal), or
- a non-signal candidate in the event, using the `L0Global_TIS` trigger (TIS stands for Triggered Independent of Signal).

TIS events are those where some activity in the event not corresponding to the signal $B^\pm$ caused the event to be triggered. In contrast, TOS events are those where one of the daughters of the signal $B^\pm$ candidate triggered the event. All candidates pass the `Hlt1Track` single track trigger by default, as these are the only candidates considered within the stripping pre-selection. Only those candidates accepted by the logical *or* of the 2-body (`Hlt2Topo2Body`), 3-body (`Hlt2Topo3Body`) and 4-body (`Hlt2Topo4Body`) HLT2 topological triggers are accepted in this analysis. At the HLT stage, only those events that are Triggered On Signal (TOS) are considered.

3.3.2. Analysis selection

Trigger and stripping selected candidates are subject to additional offline selection cuts prior to the analysis, in order to greatly reduce the combinatoric background level. This selection proceeds in two stages: the application of a pair of multivariate classifiers, and the application of rectangular cuts.

Multivariate selection using Boosted Decision Trees (BDTs)

The use of multivariate analysis techniques is well established within the flavour physics community. In this analysis, a pair of Boosted Decision Trees (BDT1 and BDT2)[2] are utilised to provide two output classifiers that can be used to reject combinatoric background events. This technique builds upon the methods previously employed in the 1 fb^{-1}ADS/GLW analysis of $B^{\pm} \to Dh^{\pm}$decays [62, 63], where samples of signal and background events are used along with a set of separating variables to determine an overall signal probability for each B candidate in data. Separate BDTs are trained for the $D \to hh$ and $D \to hhhh$ modes in the analysis, due to their different signal topologies. There are thus four BDTs in total: BDT1($2h$), BDT2($2h$), BDT1($4h$) and BDT2($4h$).

The first ingredient needed for the BDT training is a sample of combinatoric background events, where combinatoric refers to the combination of true signal tracks with tracks from the rest of the event that did not originate from the signal B. In this analysis, samples of combinatoric background events are taken from the subset of stripping and trigger selected data that falls well above the true $B^{\pm}$ mass at 5279 MeV/c^2. This is illustrated in Figure 3.5, where the range of candidates used as background events in the training of BDT1($2h$) and BDT2($2h$) are shown; the same ranges are used to select background candidates for the $D \to 4h$ BDTs, BDT1($4h$) and BDT2($4h$).

BDT1 is trained on those events that have a B candidate invariant mass above 5900 MeV/c^2 and a D candidate invariant mass falling further than 30 MeV/c^2 away from the nominal D^0 mass, indicated by the red boxes in Figure 3.5. These high B mass combinatoric candidates result from the combination of a fake D candidate with a bachelor track. Similarly, BDT2 is trained on those events with a B invariant mass in excess of 5900 MeV/c^2. Here, however, the D candidate invariant mass must fall within ± 25 MeV/c^2 of the nominal D mass. These combinatoric candidates result from the

[2] Both BDTs use the gradient boost method (BDTG) [52, 53], which is available within the TMVA framework [66].

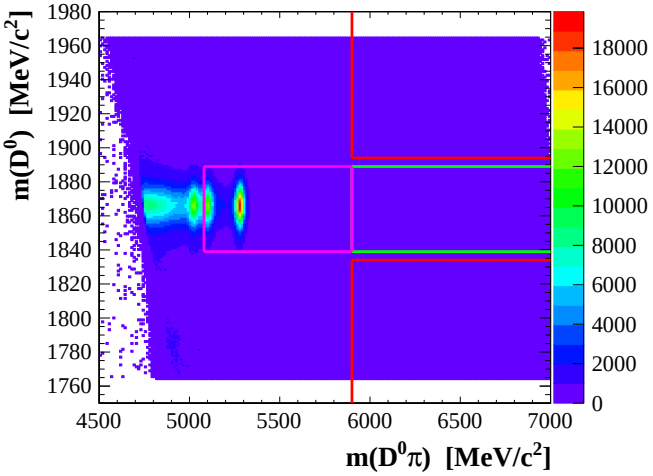

Figure 3.5.: Ranges used to select combinatoric background candidates in data, for use in the BDT training. The red regions correspond to those used by BDT1, whereas BDT2 used the region shown in green. The pink region indicates the candidates considered in the final mass fit (prior to any post-stripping offline selection cuts).

combination of a real D meson candidate with a random track from the rest of the event, and fall within the green box in Figure 3.5. The two BDTs focus on different categories of background, namely those containing a real D candidate (BDT2) and those containing no genuine D candidate (BDT1).

The second ingredient required for the BDT training is a sample of pure $B^{\pm} \to Dh^{\pm}$ signal candidates. In this analysis, signal candidates for use in the $2h$ ($4h$) BDTs are taken from generated Monte Carlo samples[3] of favoured $B^{\pm} \to [K^{\pm}\pi^{\mp}(\pi^{\pm}\pi^{\mp})]_D \pi^{\pm}$ decays, where only those candidates passing the trigger and stripping selections outlined in Section 3.3.1 are used. The use of Monte Carlo signal events is well motivated from studies that demonstrate that, for the list of separating variables used in the BDT training, data and simulation are in excellent agreement [67].

Just such a list of variables is the final component required for the BDT training. A variable is deemed to have good separation power between signal and background when the distribution of that variable is very different in signal and background: the more different the underlying distributions are, the easier it is to tell signal from background. An example of this is shown in Figure 3.6, where the transverse momentum of the bachelor particle in $B^{\pm} \to [K^{\pm}\pi^{\mp}]_D \pi^{\pm}$ is plotted in signal (blue) and background (red). The separating variables used by both BDT1 and BDT2 are listed in Table 3.2, ordered by

[3] More details of the simulated samples used are given in Section 3.3.4.

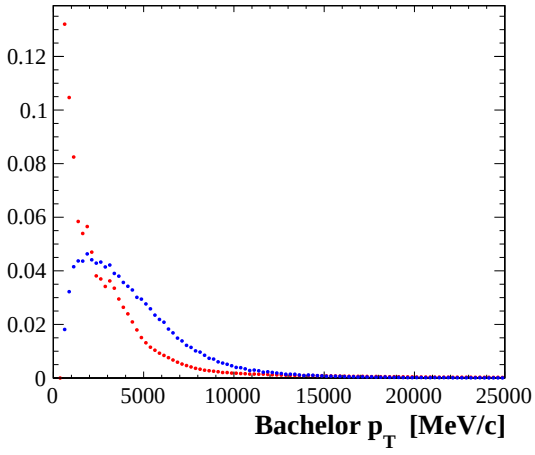

Figure 3.6.: Bachelor transverse momentum in the signal MC (blue) and data background (red) samples used to train BDT1($2h$). Both distributions have been scaled to unit integral. The BDT training exploits the difference between signal and background variable distributions to produce a single classifier variable, which can subsequently be used to reject large amounts of combinatoric background in data. The bachelor transverse momentum is found to be the most discriminating variable between signal and background.

their relative importance in BDT1($2h$). The same importance hierarchy is shown in BDT2($2h$), BDT1($4h$) and BDT2($4h$).

The performance of each BDT is summarised in Figures 3.7 and 3.8, for the $2h$ and $4h$ BDTs, respectively. The distribution of the output classifiers are shown for signal candidates (blue) and background candidates (red), where signal is shown to peak close to 1 and background close to -1. A high degree of separation power is exhibited by all four BDTs, highlighting their ability to reject large amounts of combinatoric background while retaining signal events with a high efficiency. This ability is further demonstrated by the signal efficiency vs. background rejection curves, also plotted in Figures 3.7 and 3.8. In the ideal case, a BDT will keep 100% of signal while rejecting 100% of background, corresponding to the apex in the top right of plots (a) and (b). All BDTs in this analysis closely approach the apex, indicating a high degree of performance in each case.

After the BDTs have been trained, their output classifiers are used to assign *response values* to the stripping and trigger selected candidates. Signal-like candidates are characterised by response values that fall closer to 1, whereas the candidates appearing most background-like are assigned values closer to -1. A high purity sample of signal

Variable	Description	BDTG Importance ($\times 10^{-2}$)
Bach_PT	Bachelor transverse momentum	8.07
log10(Bu_RHO_BPV)	$\Delta(\rho)$ (cylindrical co-ordinates) between the end vertex of the B and the best primary vertex	7.31
Bu_ptasy_1.50	p_{T} asymmetry of the B candidate using a cone radius of 1.50	7.22
Bach_P	Bachelor momentum	6.61
log10(1 - D0_DIRA_BPV)	DIRA is the cosine of the angle between the D momentum and the vector from the primary to the secondary vertex	5.76
log10(D0_RHO_BPV)	$\Delta(\rho)$ (cylindrical co-ordinates) between the end vertex of the D and the best primary vertex	5.46
log10(Bu_IP_OWNPV)	Impact parameter of the B with respect to the primary vertex	5.02
P_PT	D daughter pion transverse momentum	4.94
log(K_MIPCHI2_PV)	Minimal χ^2 for the impact parameter of the D daughter kaon, with respect to several vertices	4.67
log(P_MIPCHI2_PV)	Minimal χ^2 for the impact parameter of the D daughter pion, with respect to several vertices	4.59
Bu_MAXDOCA	Distance of closest approach between B daughters	4.56
log(Bu_FDCHI2_OWNPV)	Flight distance χ^2 of the B with respect to the primary vertex	4.29
D0_PT	D transverse momentum	4.06
D0_AMAXDOCA	Distance of closest approach of the D daughters	3.68
log(1 - Bu_DIRA_BPV)	DIRA is the cosine of the angle between the B momentum and the vector from the primary to the secondary vertex	3.68
log10(Bu_MIPCHI2_PV)	Minimal χ^2 for the impact parameter of the B, with respect to the primary vertex	3.38
log10(D0_IP_OWNPV)	Impact parameter of the D with respect to the primary vertex	2.77
log(D0_MIPCHI2_PV)	Minimal χ^2 for the impact parameter of the D, with respect to the primary vertex	2.59
log(D0_FDCHI2_OWNPV)	Flight distance χ^2 of the D with respect to the primary vertex	2.52
D0_VTXCHI2DOF	Vertex χ^2 per degree of freedom of the D	2.48
K_PT	D daughter kaon transverse momentum	1.69
Bu_VTXCHI2DOF	Vertex χ^2 per degree of freedom of the B	1.57
log10(Bu_FD_BPV)	Flight distance of the B with respect to the primary vertex	1.12
D0_LT_BPV	D lifetime (lab frame) with respect to the primary vertex	1.02
log10(D0_FD_OWNPV)	Flight distance of the D with respect to the primary vertex	0.75
P_P	D daughter pion momentum	0.19

Table 3.2.: Variables used in the training of both BDT1 and BDT2, ranked by importance. BDT2 also uses the output response variable of BDT1 as an input variable. The variable name Bach refers to the bachelor particle, Bu to the $B^{\pm}$, D0 to the D^0 and K (P) to the D^0 daughter kaon (pion).

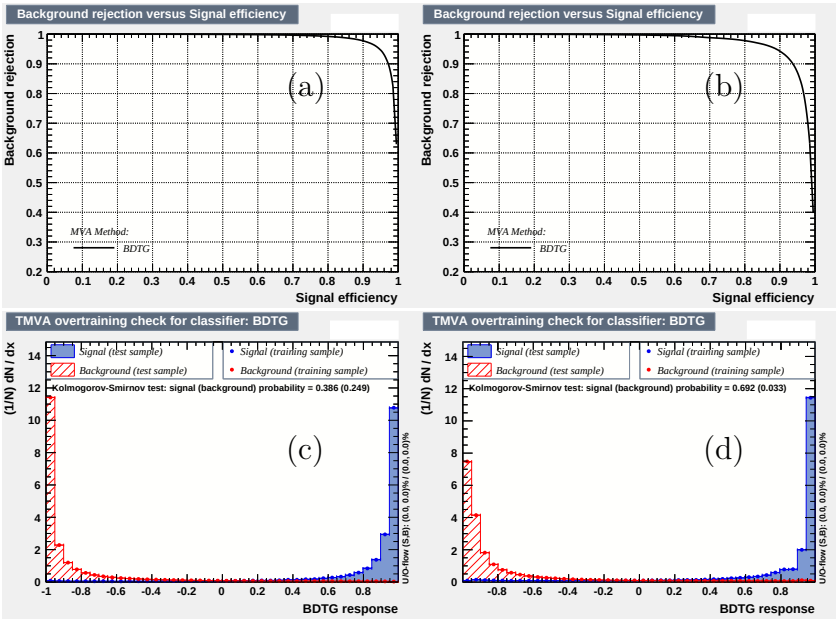

Figure 3.7.: BDT1($2h$) and BDT2($2h$) output classifier distributions and their corresponding signal efficiency vs. background rejection. In (a), the signal efficiency vs. background rejection curve for BDT1($2h$) is shown, with the output classifier response for signal (blue) and background (red) shown in (c). The corresponding plots for BDT2($2h$) are shown in (b) and (d), respectively.

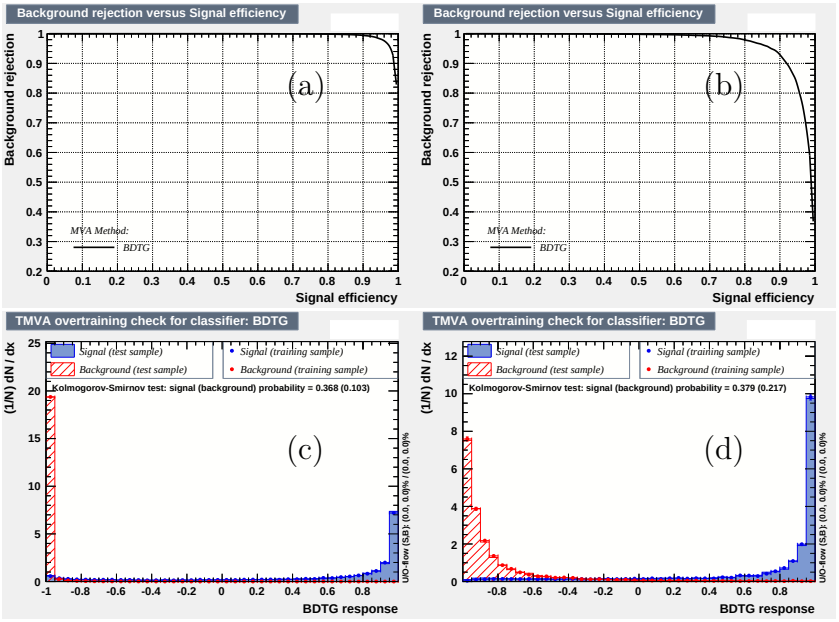

Figure 3.8.: BDT1($4h$) and BDT2($4h$) output classifier distributions and their corresponding signal efficiency vs. background rejection curves.

candidates[4] is selected by cutting on the response value, retaining only those candidates with the most positive values.

[4] The remaining candidate sample also contains physics backgrounds which are not differentiated from signal by the BDT; by design, the BDTs act to suppress only the combinatoric background level.

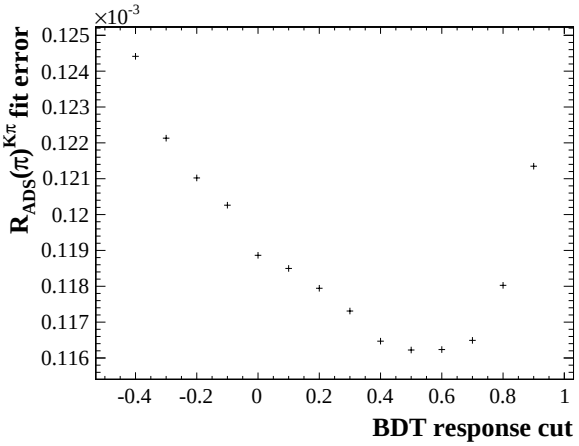

Figure 3.9.: Value of the fit error on the blinded fit parameter $R^{K\pi}_{\mathrm{ADS}(\pi)}$ as a function of BDT2($2h$) cut. The minimum visible at 0.5 guided the choice of BDT cut applied to the $D \to hh$ modes; a similar approach was adopted to determine the optimal BDT2($4h$) cuts for the $D \to hhhh$ modes.

The same BDTs are used for all $2h/4h$ modes in the analysis. For instance, $B \to [K\pi]_D h$, $B \to [KK]_D h$, $B \to [\pi\pi]_D h$ and $B \to [\pi K]_D h$ decays are all selected using the same BDT that was trained using $B \to [K\pi]_D \pi$ signal and background decays. This choice is motivated by the similarity of the separation variable distributions across each of the D final states. The specific response value cuts applied for each mode, however, can be different.

Loose cuts at BDT1 > -0.9 are applied for all modes in the analysis, to remove a majority of combinatoric background prior to the training of BDT2. The BDT2 cut values for each mode are optimised by studying the measured fit error of the sensitive $\mathcal{CP}$ observables in the full fit (see Section 4.1) as a function of applied BDT2 cut. An example of this is shown in Figure 3.9 for the case of $B \to [hh]_D h$. Here, the fit error on the blinded value of $R^{K\pi}_{\mathrm{ADS}(\pi)}$ (see Equation 3.47 for definition) is plotted as a function of applied BDT2 cut in the fit. The minimum at 0.5 motivates the cut applied in the analysis. The BDT2 cuts applied for each mode in the analysis are listed in Table 3.3; the efficiency of the BDT cuts, as well as the rectangular cuts described below, are evaluated in Section 3.3.4 using simulated events.

Further rectangular cuts and multiple candidate selection

In addition to the multivariate selection designed to reduce the combinatoric background rate, a series of rectangular cuts are also applied. They can be summarised as follows:

Mode	BDT2 cut value
$B \to [K\pi]_D h$	> 0.5
$B \to [KK]_D h$	> 0.5
$B \to [\pi\pi]_D h$	> 0.5
$B \to [\pi K]_D h$	> 0.5
$B \to [K\pi\pi\pi]_D h$	> 0
$B \to [\pi\pi\pi\pi]_D h$	> -0.9
$B \to [\pi K\pi\pi]_D h$	> 0

Table 3.3.: BDT2 cut values applied for each mode in the analysis. A loose cut of BDT1 > -0.9 is applied to all modes in the analysis, to reject the majority of combinatoric background prior to training the second stage BDTs. The same cuts are applied to $B^\pm \to DK^\pm$ and $B^\pm \to D\pi^\pm$ decays in all instances. Maximum sensitivity in the $B \to [\pi\pi\pi\pi]h$ modes is found at a looser cut value.

- The invariant mass of B candidates is required to fall in the range $5079 - 5899$ MeV/c^2, which includes all fully reconstructed $B^\pm \to Dh^\pm$ signal candidates. The invariant mass of D candidates is required to fall within ± 25 MeV/c^2 of the nominal D^0 mass. These cuts correspond to the pink region highlighted in Figure 3.5.

- The bachelor momentum is required to exceed 5 GeV/c, and must be below 100 GeV/c. The transverse momentum of the bachelor must be larger than 0.5 GeV/c, and must not exceed 10 GeV/c. These cuts ensure that all bachelor tracks fall within the kinematic range where the RICH detectors provide accurate K/π separation information [45].

- The flight distance significance of the D candidates in the z direction must exceed a value of 2. This variable is defined as:

$$\sigma^z_{\mathrm{FD}} = \frac{V_D^{\mathrm{Dec}} - V_D^{\mathrm{Orig}}}{\sqrt{\left(\sigma_D^{\mathrm{Dec}}\right)^2 + \left(\sigma_D^{\mathrm{Orig}}\right)^2}} \tag{3.58}$$

  where V_D^{Orig} and σ_D^{Orig} (V_D^{Dec} and σ_D^{Dec}) are the z positions and uncertainties of the D origin (decay) vertex. This requirement selects D candidates which have flown some distance from the B decay vertex, reducing the contribution from $B \to hhh(hh)$ decays where no charmed meson is involved (see Section 3.4.2).

In addition to these cuts, a further requirement is placed on the favoured $B \to [K\pi(\pi\pi)]_D h$ and suppressed $B \to [\pi K(\pi\pi)]_D h$ modes. It is possible to misidentify the D daughter kaon as a pion in the favoured mode, while simultaneously misidentifying a daughter pion of opposite charge as a kaon. Since the only difference between the favoured and suppressed mode final states is the sign of the kaon charge relative to the bachelor charge, this has the result of making the favoured decay appear like a suppressed decay. There is thus a large contribution from doubly misidentified favoured decays in the suppressed sample, due to the much higher rate of favoured decays relative to their suppressed counterparts.

To counter this, the D invariant mass is recalculated after the pion mass hypothesis is assigned to the D daughter kaon, while the kaon mass hypothesis is simultaneously assigned to one of the pions of opposite charge to the kaon. In cases where a favoured decay has been doubly misidentified to end up in the suppressed sample, this new D invariant mass, $m(D)^{\text{swap}}$, will peak around the nominal D mass. It is required that $m(D)^{\text{swap}}$ falls further than 15 MeV/c^2 away from the normal D invariant mass of a candidate, which greatly reduces the contribution from favoured decays in the suppressed modes. This requirement is detailed fully in Section 3.4.3.

It is possible for more than one signal candidate to be present in a single event. Only one candidate is chosen per event for this analysis, where the B candidate with the best vertex quality $\chi^2_{\text{vtx}}(B)$ is retained. In the $B \to [hh]_D h$ modes, around 0.1% of events contain multiple candidates, whereas the rate is around 1% for the $B \to [hhhh]_D h$ modes. The rate is higher in the 4-body case due to the higher track multiplicity of the final state, where a greater number of combinations is possible.

3.3.3. Particle identification requirements

In this analysis, the ability to distinguish between kaons and pions is crucial in order to separate $B^\pm \to DK^\pm$ and $B^\pm \to D\pi^\pm$ decays. To achieve this, particle identification (PID) requirements such as those outlined in Section 2.10 are placed on bachelor tracks. The difference in log likelihood between the kaon and pion mass hypothesis, $\Delta LL_{K/\pi}$, is required to exceed 12 for the bachelor in $B^\pm \to DK^\pm$ decays, whereas in $B^\pm \to D\pi^\pm$ the bachelor $\Delta LL_{K/\pi}$ value must be below 12. This requirement ensures a high purity sample of $B^\pm \to DK^\pm$ decays, with minimal pollution from misidentified $B^\pm \to D\pi^\pm$ decays. Any $B^\pm \to DK^\pm$ ($B^\pm \to D\pi^\pm$) candidates failing this particle identification requirement end up in the $B^\pm \to D\pi^\pm$ ($B^\pm \to DK^\pm$) sample. This en-

sures that all candidates are accounted for, but that no candidate appears in both the $B^\pm \to DK^\pm$ and $B^\pm \to D\pi^\pm$ samples simultaneously.

In Section 4.1 a simultaneous fit strategy is employed to determine signal yields, where the $B^\pm \to DK^\pm$ and $B^\pm \to D\pi^\pm$ samples are fit together. This allows the total number of $B^\pm \to DK^\pm$ and $B^\pm \to D\pi^\pm$ signal candidates to be determined, by summing the number of correctly identified and misidentified decays. This approach requires that the efficiency of the $\Delta LL_{K/\pi}$ cut applied to bachelors is known, such that the proportion of the total signal yield coming from correctly identified decays is fully determined. The efficiency of the $\Delta LL_{K/\pi} > 12$ requirement applied to bachelors in $B^\pm \to DK^\pm$ will be referred to as $\epsilon^K_{\rm PID}$, whereas the efficiency of the $\Delta LL_{K/\pi} < 12$ requirement applied to bachelors in $B^\pm \to D\pi^\pm$ will be referred to as $\epsilon^\pi_{\rm PID}$.

In this analysis, the efficiencies of the bachelor PID requirements are determined using a fully data-driven procedure, exploiting high statistics decay modes that can be reconstructed cleanly using only kinematic cuts. The aim of the method is to calibrate the performance of the RICH detectors in identifying kaons and pions, using a high statistics calibration sample of $D^{*+} \to [K^-\pi^+]_{D^0}\pi^+$ decays (charge conjugation implied). In this decay, both the kaon and pion D^0 daughter tracks are self-tagged by the relative charge of the pion from the D^{*+} decay. This means that the track types of all decay daughters can be unambiguously determined without the use of any RICH PID information[5], thus providing a high purity sample of kaon and pion tracks. The calibration samples come from the full 3fb^{-1} LHCb dataset collected in 2011 and 2012 i.e. the same data that is used in the analysis.

It is known that the PID performance of the RICH depends on several factors, including the momentum p and pseudorapidity η of tracks, as well as the total number of tracks $n_{\rm Tr}$ in the event [55]. To account for this, the $D^{*\pm}$ calibration samples are re-weighted such that their p, η and $n_{\rm Tr}$ spectra match those of $B \to [hh(hh)]_D\pi$ signal decays. Each sample is then binned into $18 \times 4 \times 4$ bins in p, η and $n_{\rm Tr}$, in order to take into account the different RICH response across these variables.

For each bin, the PID performance is determined from the calibration sample by determining the number of calibration tracks that pass the $\Delta LL_{K/\pi}$ requirement in that bin. The total, effective efficiencies of each $\Delta LL_{K/\pi}$ cut applied to the various modes in the analysis are then given by the weighted average of the $D^{*\pm}$ efficiencies in each bin.

[5] The doubly Cabibbo suppressed decay $D^{*+} \to [K^+\pi^-]_{D^0}\pi^+$ is vetoed in the D^* sample selection.

The results of this procedure are shown in Tables 3.4−3.8, where the kaon efficiencies $\epsilon^K_{\rm PID}$ and corresponding pion efficiencies $\epsilon^\pi_{\rm PID}$ are listed for each mode in the analysis. Efficiencies are determined for B^+ and B^- candidates separately, as well as for each magnet polarity. This accounts for any left-right variation in the detector response that could potentially alter the RICH PID performance. As magnet polarity is summed over in the analysis however, only the weighted average efficiencies over magnet polarity are considered. The values of $\epsilon^K_{\rm PID}$ quoted will be employed as fixed terms in the invariant mass fit (as described in section 4.1) with a corresponding systematic uncertainty that is determined in Section 4.2. The pion PID requirements are very loose and almost 100% efficient. As such, a single value of $\epsilon^\pi_{\rm PID}$ shared by all modes floats freely in the fit to data.

PID requirements are also applied to D daughters in the analysis, where kaons are required to have $\Delta LL_{K/\pi}$ above 2 and pions must have $\Delta LL_{K/\pi}$ below -2. This reduces any potential contributions from misidentified D decays across the various modes considered, and helps to reduce the background from favoured decays in the suppressed modes (see Section 3.4.2). The efficiencies of the D daughter requirements are not evaluated using the calibration method detailed here, as all measurements in the analysis are constructed as ratios where the D final state is common to the numerator and denominator.

Bachelor PID requirement	2011, B^+(%)	2011, B^-(%)	2012, B^+(%)	2012, B^-(%)
$\epsilon^K_{\rm PID}$, $\Delta LL_{K/\pi} > 12$	69.20 ± 0.25	69.09 ± 0.25	68.24 ± 0.16	68.02 ± 0.17
$\epsilon^\pi_{\rm PID}$, $\Delta LL_{K/\pi} < 12$	99.48 ± 0.01	99.49 ± 0.01	99.58 ± 0.01	99.56 ± 0.01

Table 3.4.: PID efficiencies for the bachelor in $B \to [K\pi]_D h$ and $B \to [\pi K]_D h$ decays, for both B^+ and B^- candidates in 2011 and 2012 data. The uncertainties quoted are systematic and arise predominantly from the use of finite samples of signal tracks in the calibration procedure, as detailed in Section 4.1.5.

Bachelor PID requirement	2011, B^+(%)	2011, B^-(%)	2012, B^+(%)	2012, B^-(%)
$\epsilon^K_{\rm PID}$, $\Delta LL_{K/\pi} > 12$	69.04 ± 0.66	69.59 ± 0.67	67.87 ± 0.45	67.70 ± 0.45
$\epsilon^\pi_{\rm PID}$, $\Delta LL_{K/\pi} < 12$	99.49 ± 0.02	99.48 ± 0.02	99.58 ± 0.01	99.56 ± 0.01

Table 3.5.: PID efficiencies for the bachelor in $B \to [KK]_D h$ decays, for both B^+ and B^- candidates in 2011 and 2012 data.

Bachelor PID requirement	2011, B^+(%)	2011, B^-(%)	2012, B^+(%)	2012, B^-(%)
$\epsilon^K_{\rm PID}$, $\Delta LL_{K/\pi} > 12$	69.31 ± 1.24	69.68 ± 1.26	67.45 ± 0.86	67.85 ± 0.83
$\epsilon^\pi_{\rm PID}$, $\Delta LL_{K/\pi} < 12$	99.48 ± 0.03	99.47 ± 0.03	99.57 ± 0.01	99.57 ± 0.01

Table 3.6.: PID efficiencies for the bachelor in $B \to [\pi\pi]_D h$ decays, for both B^+ and B^- candidates in 2011 and 2012 data.

Bachelor PID requirement	2011, B^+(%)	2011, B^-(%)	2012, B^+(%)	2012, B^-(%)
$\epsilon^K_{\rm PID}$, $\Delta LL_{K/\pi} > 12$	64.99 ± 0.25	64.64 ± 0.25	64.26 ± 0.16	64.01 ± 0.17
$\epsilon^\pi_{\rm PID}$, $\Delta LL_{K/\pi} < 12$	99.57 ± 0.01	99.57 ± 0.01	99.63 ± 0.01	99.63 ± 0.01

Table 3.7.: PID efficiencies for the bachelor in $B \to [K\pi\pi\pi]_D h$ and $B \to [\pi K\pi\pi]_D h$ decays, for both B^+ and B^- candidates in 2011 and 2012 data.

Bachelor PID requirement	2011, B^+(%)	2011, B^-(%)	2012, B^+(%)	2012, B^-(%)
$\epsilon^K_{\rm PID}$, $\Delta LL_{K/\pi} > 12$	66.28 ± 1.24	65.19 ± 1.26	65.40 ± 0.86	64.66 ± 0.83
$\epsilon^\pi_{\rm PID}$, $\Delta LL_{K/\pi} < 12$	99.54 ± 0.03	99.52 ± 0.03	99.60 ± 0.01	99.59 ± 0.01

Table 3.8.: PID efficiencies for the bachelor in $B \to [\pi\pi\pi\pi]_D h$ decays, for both B^+ and B^- candidates in 2011 and 2012 data.

3.3.4. Monte Carlo samples and selection efficiencies

Large samples of Monte Carlo (MC) simulated events are generated for all of the signal decays and several background modes. Approximately 1.5 million simulated events for each $B \to [hh]_D h$ and $B \to [hhhh]_D h$ decay mode are used to study signal line shapes (see Section 4.1.1) and selection efficiencies. Simulated events are produced within the LHCb computing framework [68], with pp collisions simulated using a tuned version of Pythia [38,69]. The average number of pp interactions per bunch crossing, ν, is required to be 2.5, in order to reasonably reproduce the running conditions in 2011 and 2012, as summarised in Figure 2.3. Collisions are generated at a centre of mass energy of $\sqrt{s} = 7$ TeV for 2011 simulation, and $\sqrt{s} = 8$ TeV for 2012 simulation. EvtGen [70] is then used to model the particle decay chains, and Geant4 [71] is used to describe the interaction of simulated particles with the detector. All generated signal tracks are required to lie in

Decay mode	$\epsilon_{\rm gen}(\%)$	$\epsilon_{\rm sel}(\%)$	$\epsilon_{\rm tot}(\%)$
$B \to [K\pi]_D\pi$	17.1 ± 0.2	3.39 ± 0.02	0.58 ± 0.01
$B \to [K\pi]_D K$	17.5 ± 0.2	3.36 ± 0.02	0.59 ± 0.01
$B \to [K\pi\pi\pi]_D\pi$	15.8 ± 0.2	1.06 ± 0.01	0.167 ± 0.003
$B \to [K\pi\pi\pi]_D K$	16.2 ± 0.2	1.05 ± 0.01	0.170 ± 0.003

Table 3.9.: Total selection efficiencies, $\epsilon_{\rm tot}$, for the favoured 2-body and 4-body modes. The efficiency of the LHCb detector acceptance cut applied in the MC generation phase, $\epsilon_{\rm gen}$, and the full efficiency of the reconstruction, trigger, stripping and offline selection, $\epsilon_{\rm sel}$, are also given. The final efficiencies $\epsilon_{\rm tot} = \epsilon_{\rm acc} \times \epsilon_{\rm sel}$ are employed in the fit within correction ratios $R_\epsilon^{K\pi(\pi\pi)} = \epsilon_{\rm tot}(B \to [K\pi(\pi\pi)]_D\pi)/\epsilon_{\rm tot}(B \to [K\pi(\pi\pi)]_D K)$.

the LHCb detector acceptance, which boosts the number of signal decays available for analysis after generation.

The total efficiency, $\epsilon_{\rm tot}$, for selecting a particular decay is given by the product of the detector acceptance efficiency, $\epsilon_{\rm acc}$, with the efficiency of the combined reconstruction, trigger, stripping and offline selection, $\epsilon_{\rm sel}$. The efficiencies for favoured $B \to [K\pi]_D h$ and $B \to [K\pi\pi\pi]_D h$ decays are listed in Table 3.9. These favoured efficiencies are used to describe the efficiencies of all other D modes in the analysis, as only ratios of efficiencies enter into calculations where the D final state is common to the numerator and denominator.

The efficiency can in principle be different for $B^\pm \to DK^\pm$ and $B^\pm \to D\pi^\pm$ decays, due to differences in kaon and pion reconstruction and selection. The ratios relating $B^\pm \to DK^\pm$ and $B^\pm \to D\pi^\pm$ yields in this analysis, namely $R_{K/\pi}^{K\pi(\pi\pi)}$, R_{CP}^{KK} and $R_{CP}^{\pi\pi\pi\pi}$, must be corrected to account for this difference. Corrections of the form:

$$R_\epsilon^{K\pi(\pi\pi)} = \frac{\epsilon_{\rm tot}(B \to [K\pi(\pi\pi)]_D\pi)}{\epsilon_{\rm tot}(B \to [K\pi(\pi\pi)]_D K)} \tag{3.59}$$

are applied in the fit to data as fixed terms where appropriate, to account for the difference in $B^\pm \to DK^\pm$ and $B^\pm \to D\pi^\pm$ selection efficiencies. Taking the values in Table 3.9, the corrections are found to be $R_\epsilon^{K\pi} = 0.983 \pm 0.024$ and $R_\epsilon^{K\pi\pi\pi} = 0.982 \pm 0.026$ for the 2-body and 4-body modes, respectively. Both corrections are consistent with unity, with systematic uncertainties arising from the use of finite MC samples in determining efficiencies (see Section 4.1.5).

3.4. Background studies

Various sources of background contribute to the fit described in Section 4.1. This Section describes each background contribution in turn, making use of simulation to determine invariant mass shapes, and data where appropriate to estimate expected background rates. Shape parameters and yields taken from these studies are fixed in the fit to data, with associated systematic uncertainties that are evaluated in Section 4.1.5.

3.4.1. Partially reconstructed background

B decays where a single daughter particle is missed in the invariant mass sum form a background at low reconstructed invariant mass (below the nominal $B^\pm$ mass of 5279 MeV/c^2). Contributions from six such partially reconstructed decays are considered in this analysis, namely:

- $B^- \to (D^{*0} \to D^0[\pi^0])h^-$
- $B^- \to (D^{*0} \to D^0[\gamma])h^-$
- $B^0 \to (D^{*+} \to D^0[\pi^+])h^-$
- $B^- \to D^0 h^-[\pi^0]$
- $B^0 \to D^0 h^-[\pi^+]$
- $B_s^0 \to [K^-\pi^+(\pi^-\pi^+)]_D K^+[\pi^-]$

where the particle in square brackets denotes the particle missed in the invariant mass sum. The final background in this list is relevant only to the suppressed $B \to [\pi K(\pi\pi)]_D K$ decay, where the charges of the D daughter kaon and the bachelor kaon are opposite. An approach has been developed whereby the invariant mass distributions of these decays can be obtained by exploiting the particular decay kinematics of partially reconstructed $B \to DhX$ decays, where $X \in \{\pi^+, \pi^0, \gamma\}$.

One may define a helicity angle θ of the missing particle X, where θ is defined with respect to the boosted momentum direction of the bachelor h in the rest frame of Y, Y being the parent of the missing particle. This angle θ corresponds on a one-to-one basis with the momentum carried away by the missing particle, as illustrated in Figure 3.10. In this example, the missing particle X is a neutral pion. Larger quantities of missing

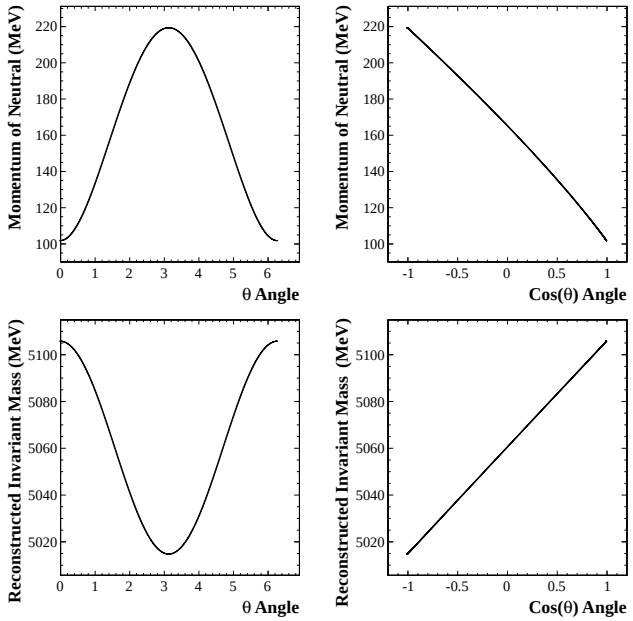

Figure 3.10.: Relationship between the missing particle helicity angle θ, the missing momentum, and the reconstructed invariant mass for the decay $B^- \to (D^{*0} \to D^0[\pi^0])h^-$, where a neutral pion is missed in the invariant mass sum. The characteristic parabolic shape (bottom left plot) is used to define the invariant mass distribution of this background in the signal extraction fit. The kinematic endpoints in the PDF definition, defined as a and b, relate to the trough and peak y-axis positions of this parabola, respectively.

momentum directly relate to lower reconstructed invariant masses, with the result that the helicity angle distribution fully defines the invariant mass distribution.

The helicity distribution is described by a characteristic parabola, with endpoints that are fully determined by the masses of the particles in the decay chain. This parabola forms the basis of an analytical Probability Density Function (PDF) that is used to describe such decays in the invariant mass fit (Section 4.1). In cases where the missing particle is a photon rather than a pion ($B^- \to (D^{*0} \to D^0[\gamma])h^-$), the parabola is inverted, with a single peak occurring at $\theta = \pi$ rather than two peaks at $\theta = 0, 2\pi$.

In the PDF definition, the parabolic shape is convolved with a resolution function to model the finite mass resolution of the detector, resulting in either a double-peaked structure (missing pion) or a sloped hill structure (missing photon). In the photon case, the parabola is turned on its head relative to the pion case. These two PDFs are defined within the `RooHORNSdini` and `RooHILLdini` classes, respectively, where the resolution function employed is a double Gaussian. The double Gaussian is chosen in order to accurately represent mass resolution effects in LHCb, where a single Gaussian is not

sufficient. The functions are of the form:

$$\texttt{RooHORNSdini}(x) = \int_a^b \left(x - \frac{a+b}{2}\right)^2 \left(\frac{1-\xi}{b-a}x + \frac{b\xi - a}{b-a}\right) e^{-\frac{(x-\mu)^2}{2\sigma^2}} \mathrm{d}x \tag{3.60}$$

$$\texttt{RooHILLdini}(x) = \int_a^b -(x-a)(x-b) \left(\frac{1-\xi}{b-a}x + \frac{b\xi - a}{b-a}\right) e^{-\frac{(x-\mu)^2}{2\sigma^2}} \mathrm{d}x \tag{3.61}$$

Each of the PDF parameters are briefly discussed below.

Partially reconstructed background parameterisation

The `RooHORNSdini` and `RooHILLdini` PDF classes used in this analysis to describe partially reconstructed backgrounds are parameterised using the following list of variables:

- x [MeV/c^2] - fit variable, in this case the reconstructed invariant mass $m(Dh)$.
- a [MeV/c^2] - lower kinematic endpoint. Fully determined by the specific particle masses in the decay chain.
- b [MeV/c^2] - upper kinematic endpoint, also fully determined by the specific particle masses in the decay chain.
- ξ - relative height of the two peaks, allowing for invariant mass dependent selection effects that remove more of one peak than the other. When $\xi = 1$, both peaks are of equal height. When $\xi > (<)1$, the lower (upper) peak is largest.
- σ [MeV/c^2] - width of the core resolution Gaussian. The core Gaussian is the Gaussian of narrowest width in the overall double Gaussian convolution.
- f_σ - fraction of yield contained in the core Gaussian.
- R_σ - ratio of wide Gaussian and core Gaussian widths in the double Gaussian resolution function.
- s [MeV/c^2] - rigid shift of the entire shape along x, allowing for differences between the analytical endpoints and the reconstructed endpoints.

The kinematic endpoints, a and b, are calculated analytically using the nominal masses for each particle in the chain, taken from [12]. In cases where the missing particle originates from a wide resonance however, such as in the $B^- \to D^0\pi^-[\pi^0]$ decay where a $\rho^- \to \pi^-\pi^0$ resonance dominates, the analytical solution is not precise. In these cases, values for a and b are taken from fits to simulation as described below. The relative height of

the peaks, ξ, is fixed to a value of 1 in the fit to data for all partially reconstructed background modes, as only the uppermost peaks are considered within the $5079 - 5899$ MeV/c^2 fit range.

The double Gaussian parameters σ, R_σ and f_σ are determined from fits to simulated events, but the value of σ is allowed to float freely in the fit to data for the $B^- \to (D^{*0} \to D^0[\pi^0])h^-$ decay in order to improve the low mass fit residuals. The rigid shift s can in principal be different in decays involving kaon or pion bachelors, and in decays involving different D final states. In the fit to data, the value of s is allowed to be different in each $B \to [hh]_D h$ and $B \to [hhhh]_D h$ mode, but all partially reconstructed decays for a given mode share the same value of s.

Determining background shape parameters from Monte Carlo fits

In order to determine values for each of the shape parameters listed above, dedicated MC samples for each of the six partially reconstructed decay modes have been generated. The analysis selection cuts detailed in Section 3.3 are applied to each sample, and invariant mass fits performed to each mode using the specialised `RooHORNSdini` and `RooHILLdini` PDFs. In the case of the two strongly double-peaked modes, (a) $B^- \to (D^{*0} \to D^0[\pi^0])h^-$ and (c) $B^- \to (D^{*+} \to D^0[\pi^+])h^-$, the sum of two `RooHORNSdini` PDFs is employed in order to model radiative tail effects. The radiative tail contribution (red) is small (4%) and is required to be the same for both of these modes[6]. In the fit to data, the radiative tail parameters are fixed to the values found in simulation. The modes illustrated in (d)−(f) also exhibit a double peaked structure, but their second peak is at an invariant mass much lower than the range considered due to the larger phase space available to the missing particle.

Fits to each of the partially reconstructed modes using the `RooHORNSdini` and `RooHILLdini` PDFs are shown in Figure 3.11. The custom PDFs inspired by the parabolic shape of the helicity distribution are shown to model the invariant mass distributions excellently. Systematic uncertainties will be assigned in Section 4.1.5 to account for the use of fixed shape parameters from these fits in the final fit to data. The fits shown here are performed over a wide invariant mass range of $4900 - 5300$ MeV/c^2 in order to constrain the shapes as well as possible. Only the portion of the PDFs above 5079 MeV/c^2 are considered in the fit to data, however.

[6] Radiative effects are modelled using PHOTOS [72].

In all of the fits detailed here, MC samples have been weighted with the PID efficiencies determined in Section 3.3.3, to account for the PID cuts applied to the bachelor. PID cuts are never applied directly to the MC samples, as the $\Delta LL_{K/\pi}$ distributions in simulation are not representative of those found in data. By performing this weighting procedure, changes in the invariant mass distribution as a result of the application of bachelor PID requirements are correctly accounted for.

Application in the data fit

With the exception of the $B^0 \to (D^{*+} \to D^0[\pi^+])h^-$ decay, the yield of each partially reconstructed mode floats freely in the data fit. The contribution from $B^0 \to (D^{*+} \to D^0[\pi^+])h^-$ is fixed relative to the fully reconstructed $B^\pm \to D\pi^\pm$ signal yield using branching fraction relations [12]. This fixing is required because the $B^0 \to (D^{*+} \to D^0[\pi^+])\pi^-$ and $B^- \to (D^{*0} \to D^0[\pi^0])h^-$ decays have such similar invariant mass distributions[7] that they cannot be accurately discriminated. The values of $R_{K/\pi}$ for each low mass mode float freely, but are required to be the same across each of the D modes.

A visual representation of the contribution from each partially reconstructed mode in the fit to the favoured $B \to [K\pi]_D h$ data is shown in Figure 3.12, where the individual contributions have been highlighted in a different colour. In the top plot, $B^\pm \to DK^\pm$ decays are shown, with fully reconstructed signal decays drawn with a solid red line. In the bottom plot, $B^\pm \to D\pi^\pm$ decays are shown, with fully reconstructed signal decays drawn with a solid green line. The contribution from misidentified $B^\pm \to D\pi^\pm$ decays in the $B^\pm \to DK^\pm$ sample is also visible as the solid green line to the right of the main $B^\pm \to DK^\pm$ peak. The PDFs describing these fully reconstructed decays are discussed in Section 4.1.1.

In dark blue, the contribution from $B^- \to (D^{*0} \to D^0[\pi^0])h^-$ decays is shown, whereas the contribution from the very similar $B^0 \to (D^{*+} \to D^0[\pi^+])h^-$ decays is shown in magenta. The wide contribution from $B^- \to (D^{*0} \to D^0[\gamma])h^-$ decays is shown in cyan; this is the only mode to be fit with a `RooHILLdini` PDF, since it involves a massless vector photon that is missed in the invariant mass sum. In light (dark) orange, the contribution from $B^- \to D^0 h^-[\pi^0]$ ($B^0 \to D^0 h^-[\pi^+]$) decays is shown. Together, each of these partially reconstructed modes describe the region at low invariant mass well.

[7] The difference between the charged and neutral pion masses is only 5 MeV/c^2.

Partially reconstructed and misidentified backgrounds

An additional component is also present in Figure 3.12, arising from partially reconstructed $B \to D\pi X$ decay modes where the bachelor pion has been misidentified as a kaon. This contribution is shown by the small and wide solid grey region at low values of invariant mass, which sits underneath each of the $B \to DKX$ modes in the top plot. Decays of this type cannot be described analytically using the `RooHORNSdini` and `RooHILLdini` PDFs, due to mass shift and smearing introduced by the incorrect mass hypothesis for the bachelor.

Such decays are modelled using a semi-empirical approach, where kernel estimation [73] is performed in fits to simulated events to determine a shape. The shape parameters used in the fit to data to model this background are taken from the fits shown in Figure 3.13, where partially reconstructed $B^- \to (D^{*0} \to D^0[\pi^0])\pi^-$ and $B^- \to (D^{*0} \to D^0[\gamma])\pi^-$ decays are plotted with the bachelor pion assigned the kaon mass hypothesis. An upward shift in invariant mass is evident relative to the distributions shown in Figure 3.11, due to the artificially high mass of the pion. The rate of this contribution is greatly reduced in the data fit due to the PID cut applied to the bachelor kaon in $B^{\pm} \to DK^{\pm}$.

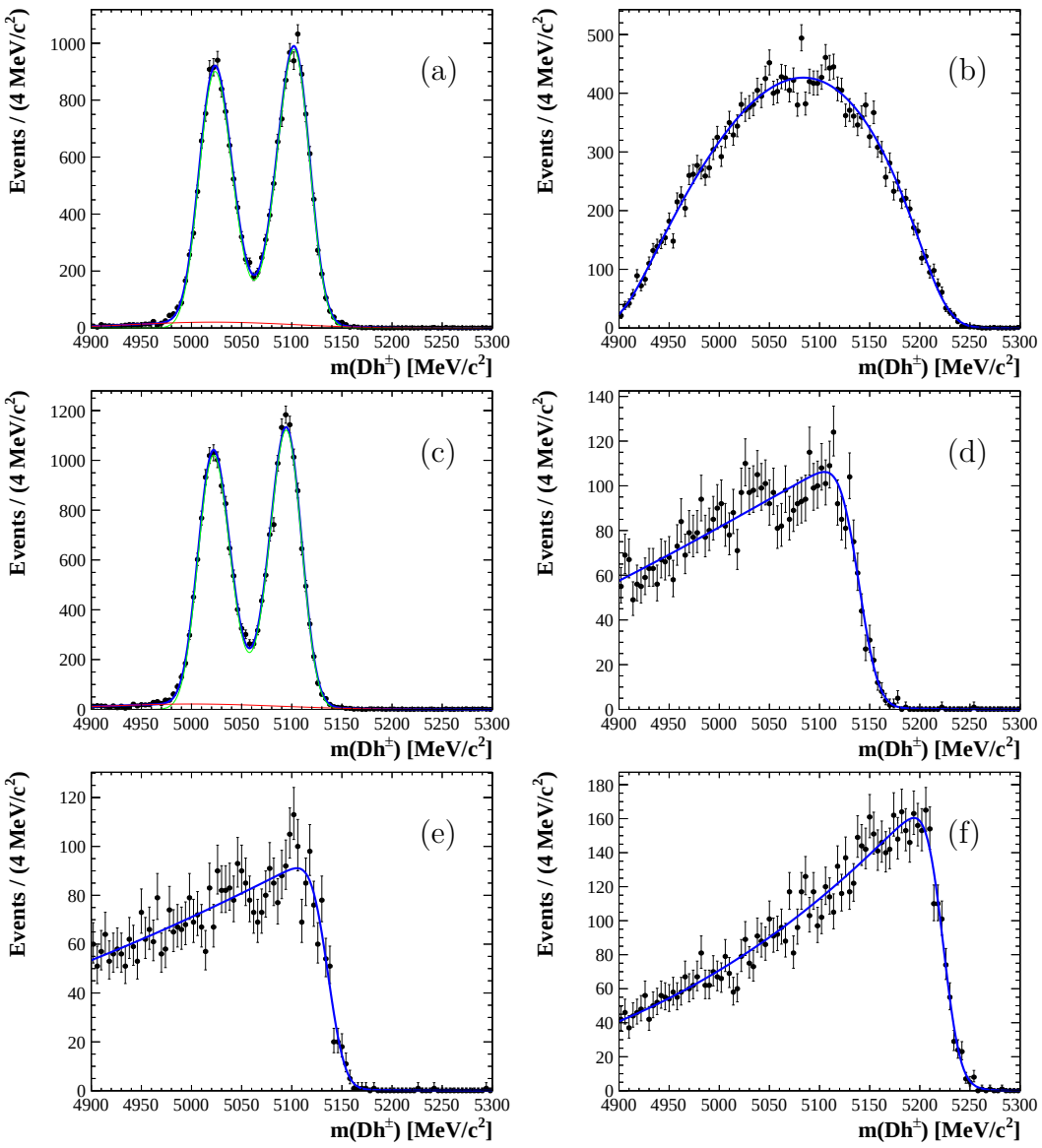

Figure 3.11.: Invariant mass fits to each of the partially reconstructed background contributions in MC: (a) $B^- \to (D^{*0} \to D^0[\pi^0])\pi^-$, (b) $B^- \to (D^{*0} \to D^0[\gamma])\pi^-$, (c) $B^0 \to (D^{*+} \to D^0[\pi^+])\pi^-$, (d) $B^- \to D^0 h^-[\pi^0]$, (e) $B^0 \to D^0 h^-[\pi^+]$ and (f) $B_s^0 \to [K^-\pi^+(\pi^-\pi^+)]_D K^+[\pi^-]$. The same shapes are applicable in the case where the bachelor is a kaon rather than a pion. Shape parameters from these fits are used in the fit to data as fixed terms with associated systematic uncertainties. Only those portions of the PDFs beyond 5079 MeV/c^2 are relevant to the final data fit. In (a) and (c), an additional small component shown in red is included to describe the radiative tail on the lower edge of the distribution. This component has the same functional form as the main green PDF, but has a freely floating uniform shift parameter s, enabling it to sit at lower mass values.

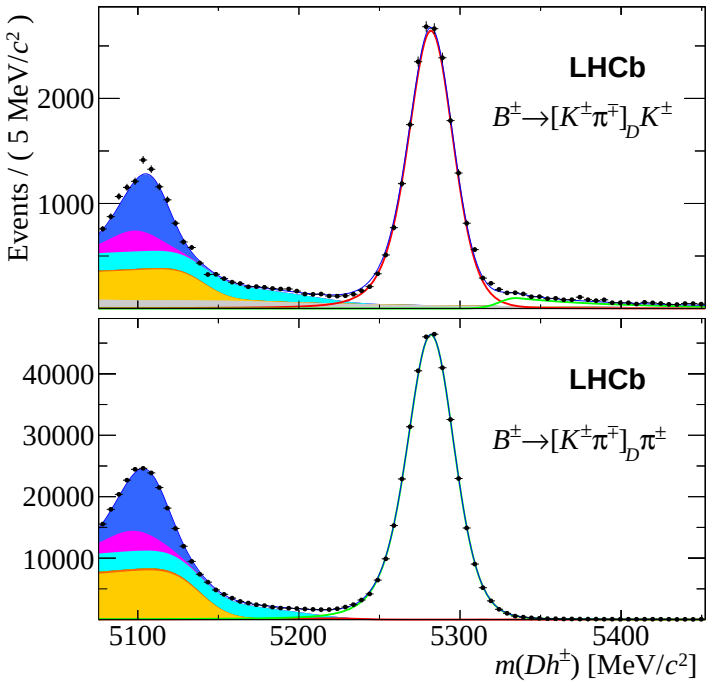

Figure 3.12.: Invariant mass fit to $B \to [K\pi]_D h$ events in data, where each of the low mass contributions has been highlighted in a different colour. The contribution from $B^{\pm} \to (D^{*0} \to D^0\pi^0)h^{\pm}$ decays is shown in dark blue, while the contribution from $B^0 \to (D^{*-} \to D^0\pi^-)h^+$ decays is shown in pink. The contribution from $B^{\pm} \to (D^{*0} \to D^0\gamma)h^{\pm}$ decays is plotted in cyan, while the contribution from $B^{\pm} \to D^0 h^{\pm}\pi^0$ decays is shown in orange. The small grey region to the left of the $B^{\pm} \to DK^{\pm}$ peak (top plot) is from partially reconstructed and misidentified $B \to D\pi X$ decays. The rate of this contribution is substantially reduced in the data fit due to the PID cut applied to the bachelor kaon in $B^{\pm} \to DK^{\pm}$.

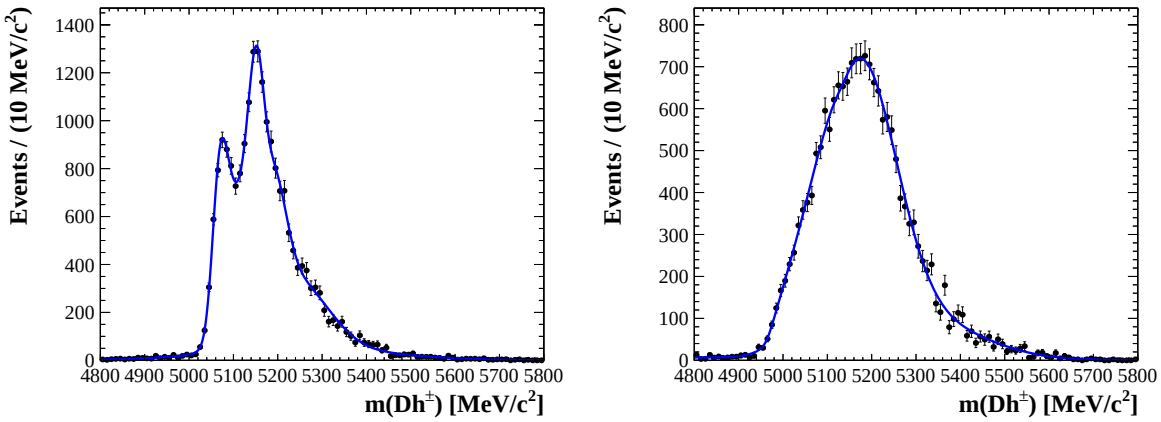

Figure 3.13.: Invariant mass fits to partially reconstructed and misidentified $B^- \to (D^{*0} \to D^0[\pi^0])\pi^-$ (left) and $B^- \to (D^{*0} \to D^0[\gamma])\pi^-$ (right) decays, where the bachelor pion has been assigned the kaon mass. Shape parameters from these MC fits are used in the fit to data as fixed terms with associated systematic uncertainties.

3.4.2. Charmless $B \to 3h$ and $B \to 5h$ backgrounds

In addition to the partially reconstructed backgrounds detailed in Section 3.4.1, there are potential peaking backgrounds from fully reconstructed $B \to hhh(hh)$ decays, where no D meson is involved. These so-called *charmless* decays are estimated using a data-driven approach, where the $m(Dh)$ invariant mass distribution is studied in the D sideband regions, well away from any true signal contributions. The charmless contributions that are expected to be present in the $B \to [hh]_D h$ data, purely from branching fraction arguments [12], are listed in Table 3.10; a similar hierarchy is anticipated in the $B \to [hhhh]_D h$ data, where the only difference is the production of two additional pions.

Charmless mode	$\mathcal{B}$
$B^- \to K^-\pi^+\pi^-$	5.1×10^{-5}
$B^- \to K^-K^+K^-$	3.4×10^{-5}
$B^- \to \pi^-\pi^+\pi^-$	1.5×10^{-5}
$B^- \to K^-K^+\pi^-$	5.0×10^{-6}

Table 3.10.: List of expected charmless contributions in $B \to [hh]_D h$, ordered by branching fraction magnitude [12]; a similar hierarchy is expected for the $B \to [hhhh]_D h$ case. A search for charmless contributions is performed within the D sidebands in data, in order to estimate their contribution in the signal extraction fit.

Any charmless B decays present in the D sidebands should peak at the nominal B mass in $m(Dh)$, since they involve no charmed meson. This allows the rate of any charmless contributions to be measured directly in the sidebands using invariant mass fits to $m(Dh)$. By choosing a sideband of 50 MeV/c^2 width (equivalent to the D mass window used in the main selection, as illustrated in Figure 3.5), the charmless yields measured in the sideband can be directly related to the expected charmless contributions in the fit to data. For this study, the following lower and upper sideband regions are defined:

- **Lower sideband:** The D candidate invariant mass must be between 45 and 95 MeV/c^2 below the nominal D^0 mass.
- **Upper sideband:** The D candidate invariant mass must be between 45 and 95 MeV/c^2 above the nominal D^0 mass.

A fit to the D candidate invariant mass in $B \to [K\pi]_D h$ data is shown in Figure 3.14, where the D peak has been fit using a double Gaussian function. From this fit, performed

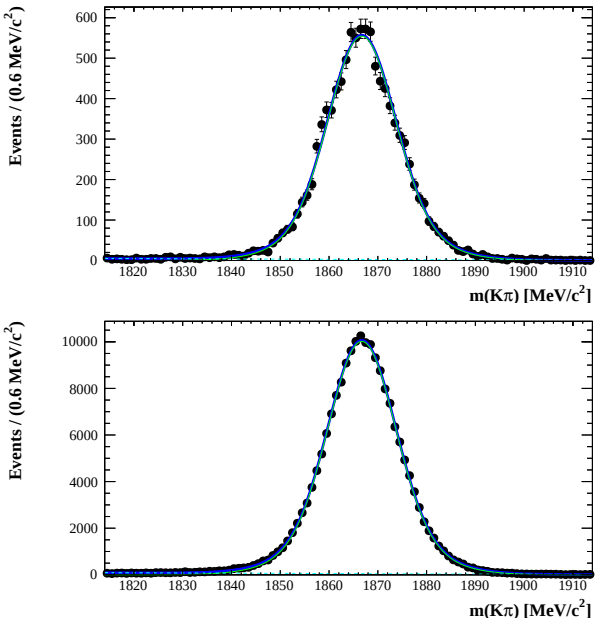

Figure 3.14.: D candidate invariant mass fit in $B \to [K\pi]_D h$ data, where a simultaneous fit to $B^{\pm} \to DK^{\pm}$ (top plot) and $B^{\pm} \to D\pi^{\pm}$ (bottom plot) data is performed. The upper (lower) D sideband used in the evaluation of charmless yields is chosen to be well away from the true D signal contribution present, at $45 - 90$ MeV/c^2 above (below) the nominal D^0 mass.

over a ± 50 MeV/c^2 window, it is evident that the $45 - 90$ MeV/c^2 charmless sidebands fall well away from the region containing true D candidates.

Mass fits to determine charmless yields

In this study, the sidebands of $D \to \pi^- K^+ (\pi^- \pi^+)$, $D \to K^- K^+$ and $D \to \pi^- \pi^+ (\pi^- \pi^+)$ are investigated for any charmless contributions. Only the sidebands corresponding to a charmless final state listed in Table 3.10 are considered in $B \to [hh]_D h$ (as well as the equivalent decays with two additional pions for $B \to [hhhh]_D h$), as any potential contributions from other lower branching fraction charmless decays are negligible. The favoured $D \to K^- \pi^+ (\pi^- \pi^+)$ sidebands are not used in the study, as the charmless rates are negligible relative to the very large favoured signal yields.

As a first step, invariant mass fits to $m(Dh)$ are performed for each sideband region in the *absence* of any D flight distance z significance cut. As described in Section 3.3.2, this cut is applied in the analysis specifically to suppress charmless decays, by selecting those B candidates that contain a flying D meson. As charmless decays involve no flying

Decay mode	Sideband	Charmless mode	$(N^{B^-} - N^{B^+})/(N^{B^-} + N^{B^+})(\%)$
$B^- \to [\pi^+\pi^-]_D K^-$	upper	$B^- \to K^-\pi^+\pi^-$	-3.6 ± 2.6
$B^- \to [K^+K^-]_D K^-$	lower	$B^- \to K^-K^+K^-$	-0.8 ± 3.5
$B^- \to [\pi^+\pi^-]_D \pi^-$	upper	$B^- \to \pi^-\pi^+\pi^-$	4.9 ± 4.2
$B^- \to [\pi^-K^+]_D K^-$	lower	$B^- \to \pi^-K^+K^-$	-17.8 ± 13.6
$B^- \to [\pi^-K^+]_D K^-$	upper	$B^- \to \pi^-K^+K^-$	-4.3 ± 11.5
$B^- \to [\pi^-K^+]_D K^-$	lower	Mis-ID $B^- \to K^-\pi^+\pi^-$	3.1 ± 6.3
$B^- \to [\pi^+\pi^-\pi^+\pi^-]_D K^-$	upper	$B^- \to K^-\pi^+\pi^-\pi^+\pi^-$	8.0 ± 1.5
$B^- \to [\pi^+\pi^-\pi^+\pi^-]_D \pi^-$	upper	$B^- \to \pi^-\pi^+\pi^-\pi^+\pi^-$	4.0 ± 1.6

Table 3.11.: Charmless asymmetries as measured in data sidebands, with no D flight distance z significance cut applied (charge conjugation implied). These asymmetries are later fixed, along with all shape parameters, when determining charmless yields in the presence of a D flight distance z significance cut. The asymmetries listed are also employed in the fit to data as fixed terms.

intermediate, this cut should effectively reduce the rate of any charmless decays present in the data.

This first fit in the absence of any cut is performed in order to establish baseline charmless yields and charge asymmetries; the latter are measured by performing the invariant mass fits simultaneously on separate samples of B^+ and B^- candidates. The asymmetries measured in these baseline fits are then fixed in subsequent sideband fits. They are also employed as fixed terms in the fit to data in Section 4.1, to describe the asymmetry of any charmless contributions. The asymmetries measured for each observed charmless mode are summarised in Table 3.11.

After the baseline fit is performed, the charmless suppression cut (subsequently referred to as $\sigma^z_{\rm FD}$) is applied at successively tighter cut values of $\sigma^z_{\rm FD} > 0$, $\sigma^z_{\rm FD} > 2$ and $\sigma^z_{\rm FD} > 4$, and the fit performed again at each cut value. This allows the charmless yields to be monitored as a function of the cut applied, and provides an estimate for the charmless yield at the analysis cut of $\sigma^z_{\rm FD} > 2$. The charmless yields measured at this cut value are employed as fixed terms in the fit to data in Section 4.1, along with the asymmetries described above. The use of fixed charmless yields and asymmetries in the fit is assigned a systematic uncertainty in Section 4.1.5.

The *non-zero*[8] charmless yields measured in the considered sidebands are summarised in Table 3.12. All of the expected charmless modes listed in Table 3.10 are observed in the $B \to [hh]_D h$ sidebands. In addition, charmless contributions from $B^\pm \to \pi^\pm\pi^\mp\pi^\pm\pi^\mp\pi^\pm$ and $B^\pm \to K^\pm\pi^\mp\pi^\pm\pi^\mp\pi^\pm$ are observed in the $B \to [\pi\pi\pi\pi]_D h$ sidebands, aligning with the two largest charmless yields seen in $B \to [hh]_D h$. All charmless contributions are effectively suppressed by the application of the $\sigma^z_{\text{FD}} > 2$ requirement.

Decay mode	Sideband	Charmless mode	N (no σ^z_{FD})	N ($\sigma^z_{\text{FD}} > 0$)	N ($\sigma^z_{\text{FD}} > 2$)	N ($\sigma^z_{\text{FD}} > 4$)
$B^- \to \left[\pi^+\pi^-\right]_D K^-$	upper	$B^- \to K^-\pi^+\pi^-$	1746 ± 49	639 ± 27	**83 ± 11**	17 ± 7
$B^- \to \left[K^+K^-\right]_D K^-$	lower	$B^- \to K^-K^+K^-$	1144 ± 41	567 ± 29	**49 ± 14**	0 ± 10
$B^- \to \left[\pi^+\pi^-\right]_D \pi^-$	upper	$B^- \to \pi^-\pi^+\pi^-$	1159 ± 60	572 ± 32	**66 ± 18**	-4 ± 14
$B^- \to \left[\pi^-K^+\right]_D K^-$	lower	$B^- \to \pi^-K^+K^-$	224 ± 50	91 ± 21	**19 ± 12**	4 ± 8
$B^- \to \left[\pi^-K^+\right]_D K^-$	upper	$B^- \to \pi^-K^+K^-$	197 ± 31	71 ± 16	**5 ± 9**	3 ± 7
$B^- \to \left[\pi^-K^+\right]_D K^-$	lower	Mis-ID $B^- \to K^-\pi^+\pi^-$	695 ± 62	255 ± 32	**55 ± 19**	0 ± 14
$B^- \to \left[\pi^+\pi^-\pi^+\pi^-\right]_D \pi^-$	lower	$B^- \to \pi^-\pi^+\pi^-\pi^+\pi^-$	607 ± 57	377 ± 45	**119 ± 32**	11 ± 8
$B^- \to \left[\pi^+\pi^-\pi^+\pi^-\right]_D \pi^-$	upper	$B^- \to \pi^-\pi^+\pi^-\pi^+\pi^-$	665 ± 56	367 ± 43	**96 ± 30**	9 ± 8
$B^- \to \left[\pi^+\pi^-\pi^+\pi^-\right]_D K^-$	lower	$B^- \to K^-\pi^+\pi^-\pi^+\pi^-$	1557 ± 47	731 ± 32	**110 ± 15**	10 ± 9
$B^- \to \left[\pi^+\pi^-\pi^+\pi^-\right]_D K^-$	lower	$B^- \to K^-\pi^+\pi^-\pi^+\pi^-$	1288 ± 44	596 ± 30	**120 ± 15**	11 ± 9

Table 3.12.: Charmless yields as measured in data sidebands under a range of D flight distance z significance cuts. All charmless rates are suppressed by the cut, and the yields measured with the analysis cut of $\sigma^z_{\text{FD}} > 2$ (column in bold) are employed in the fit as fixed PDF yields. In cases where charmless yields are measured in both the lower and upper sidebands, a weighted average yield is computed. In the row labelled "mis-ID", the measured yield of misidentified $B^- \to K^-\pi^+\pi^-$ decays that enter the suppressed $B^- \to \left[\pi^-K^+\right]_D K^-$ fit is listed. This yield is further adjusted by a factor 0.2/2.2 to account for the relative misidentification rates with and without a PID cut applied to the D daughter kaon (see Section 3.4.3).

An example of the charmless estimation procedure is illustrated in Figure 3.15, where the upper sideband fit for the $B \to [\pi\pi]_D K$ mode are shown. The charmless contribution here is the largest observed across the $B \to [hh]_D h$ modes (in line with the expectation from Table 3.10), and is seen to reduce with the application of successively tighter σ^z_{FD} cuts. In all sideband fits, charmless decays are modelled with a Crystal Ball PDF [74]. The combinatoric background is modelled using an exponential function, while partially reconstructed decays at low values of invariant mass are modelled using a single Gaussian

[8] Some sidebands were examined for charmless contributions and found to contain none, such as those of the suppressed modes $B \to [\pi K]\pi$, $B \to [\pi K\pi\pi]\pi$ and $B \to [\pi K\pi\pi]_D K$. In Chapter 4, the charmless background yield is fixed to zero for each of these modes with an associated systematic uncertainty.

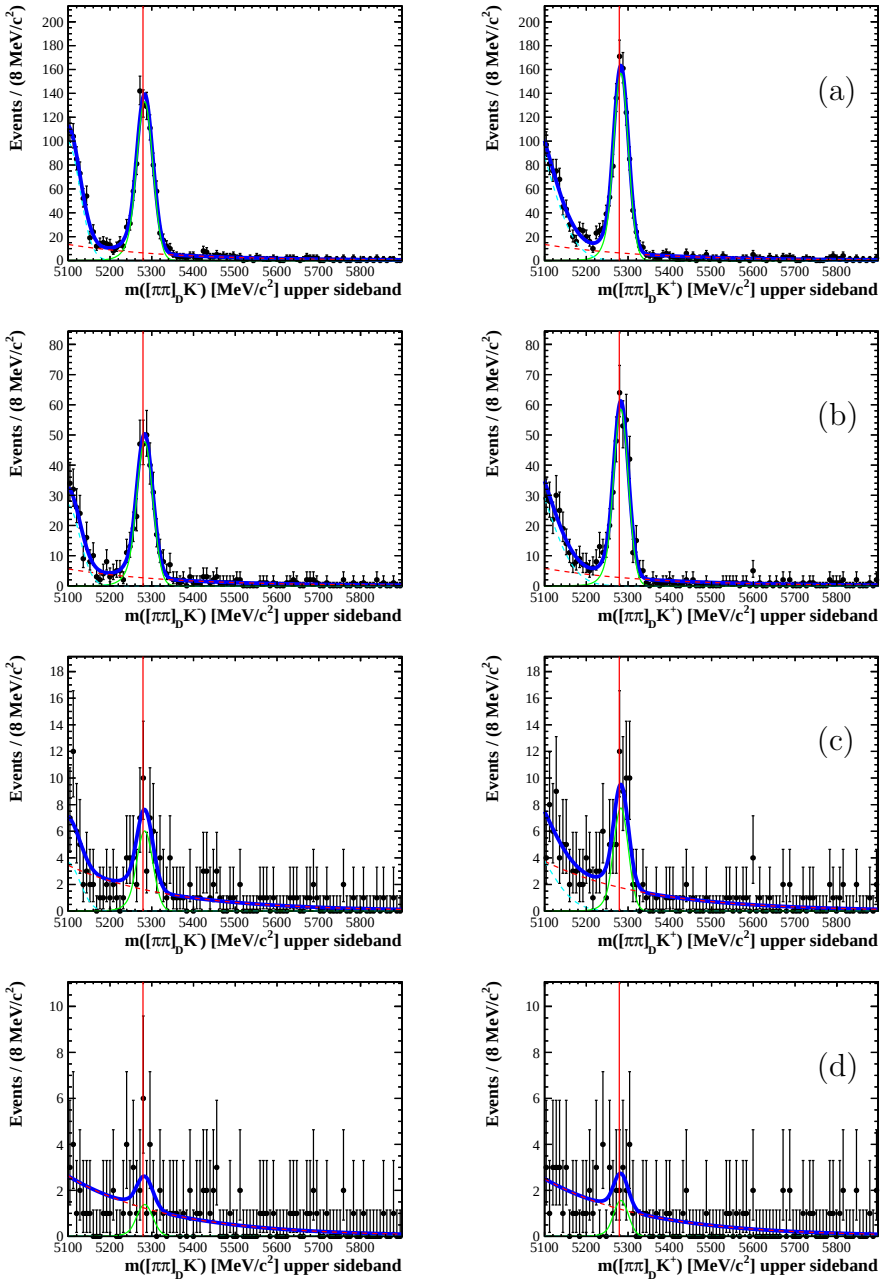

Figure 3.15.: Invariant mass fit to $m(DK)$ in the upper D sideband of $B^{\pm} \to [\pi^{\pm}\pi^{\mp}]_D K^{\pm}$ data. In the leftmost column, B^- events are shown, with B^+ events shown on the right. The nominal $B^{\pm}$ mass is indicated by a red vertical line. In (a), no D flight distance z significance cut has been applied - a clear contribution from charmless decays is evident. This contribution is suppressed with the application of successively tighter D flight distance z significance requirements, where a cut has been applied at (b) > 0, (c) > 2 (analysis cut) and (d) > 4.

function. The shape parameters for all components are floated freely in the baseline fits used to determine charmless asymmetries, and are subsequently fixed in all further fits.

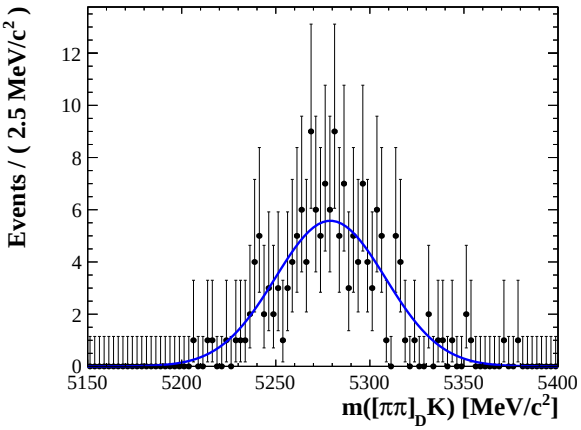

Figure 3.16.: Invariant mass fit to simulated $B^- \to K^-\pi^+\pi^-$ decays that have passed the full selection, with the exception of the D flight distance z significance cut. The distribution has been fit with a single Gaussian of width (29 ± 2) MeV/c^2, which is used in the fit to data as a fixed term for each of the charmless PDFs in the $B \to [hh]_D h$ fit; an identical procedure is carried out for the $B \to [hhhh]_D h$ case, using simulated $B^- \to K^-\pi^+\pi^-\pi^+\pi^-$ decays.

Charmless line shape

All charmless contributions in the fit to data (Section 4.1) are described by single Gaussians. The Gaussian mean is required to be the same as that of the main $B^{\pm} \to Dh^{\pm}$ signal PDF, whereas the width is taken from a fit to simulated charmless $B^- \to K^-\pi^+\pi^-(\pi^+\pi^-)$ decays, as shown in Figure 3.16. In this fit, simulated $B^- \to K^-\pi^+\pi^-$ events are required to pass the full selection with the exception of the D flight distance z significance cut; with this cut applied, not enough MC events remain to determine a shape.

The fitted width is (29 ± 2) MeV/c^2 for $B^- \to K^-\pi^+\pi^-$ and (25 ± 2) MeV/c^2 for $B^- \to K^-\pi^+\pi^-\pi^+\pi^-$, both of which are scaled by the observed width difference between data and simulation for $B \to [K\pi(\pi\pi)]_D\pi$ decays. The $B^- \to K^-\pi^+\pi^-(\pi^+\pi^-)$ mode was chosen to determine the charmless PDF shape, as it contributes most in the fit to data (see Table 3.12). The fixing of charmless widths is considered as a source of systematic uncertainty in Section 4.1.5.

3.4.3. Favoured decays entering the suppressed mode samples

Another potential source of peaking background exists for the suppressed $B \to [\pi K(\pi\pi)]_D h$ modes, arising from the misidentification of D daughters in favoured $B \to [K\pi(\pi\pi)]_D h$ decays. In cases where the D daughter kaon from a favoured decay is misidentified as

a pion, while a pion from the D of opposite charge is simultaneously misidentified as a kaon, the favoured decay is placed in the suppressed sample. This occurs because of the difference in signature of favoured and suppressed decays, namely the charge of the D daughter kaon relative to the bachelor being either the same (favoured) or opposite (suppressed).

Because of the much higher rate of favoured decays relative to their suppressed counterparts, this double misidentification (subsequently referred to as *crossfeed*) poses a potentially serious background to the suppressed mode samples. Three selection requirements, initially detailed in Section 3.3.2, are applied to reduce the crossfeed contribution:

- PID cuts are applied to D daughters.
- A mass window of ± 25 MeV/c^2 around the nominal D^0 mass is applied to D candidates.
- A veto window is applied around the D mass calculated when daughter mass hypotheses are swapped. This mass must fall further than 15 MeV/c^2 away from the PDG D^0 mass in order for the candidate to be retained.

Each of these requirements are now detailed, and an overall estimate of the surviving crossfeed contribution determined for both $B \to [hh]_D h$ and $B \to [hhhh]_D h$.

D daughter PID cuts

In $B \to [K\pi]_D h$ and $B \to [\pi K]_D h$, D daughter kaons are required to have $\Delta LL_{K/\pi} > x$, while D daughter pions are required to have $\Delta LL_{K/\pi} < y$. This requirement minimises the rate of doubly misidentified favoured decays in the suppressed sample for sufficiently tight x and y cuts. To determine the efficiency of this requirement (and the corresponding misidentification rate), fits to the D invariant mass in $B \to [K\pi]_D h$ data are performed. Fits are first performed in the absence of any PID cuts to determine baseline yields, N. The same fit is then performed across a range of x and y values, and yields $N(K > x, \pi < y)$ measured in each case. The efficiency of a certain $(K > x, \pi < y)$ PID requirement is given by $N(K > x, \pi < y)/N$. The efficiencies across a range of cuts are shown in Table 3.13, where the efficiency of the analysis cuts, $x = 2$ and $y = -2$, are highlighted in bold.

%	$y <$ 200	$y <$ 0	$y <$ -2	$y <$ -4	$y <$ -6
$x >$ -200	100	86.75 ± 0.05	80.19 ± 0.06	74.46 ± 0.06	69.22 ± 0.06
$x > 0$	94.37 ± 0.03	82.05 ± 0.05	75.99 ± 0.06	70.61 ± 0.06	65.68 ± 0.07
$x > 2$	88.86 ± 0.04	77.52 ± 0.06	**72.02 ± 0.06**	67.01 ± 0.07	62.41 ± 0.07
$x > 4$	84.29 ± 0.05	73.65 ± 0.06	68.55 ± 0.06	63.82 ± 0.07	59.48 ± 0.07
$x > 6$	80.09 ± 0.06	70.07 ± 0.06	65.29 ± 0.07	60.84 ± 0.07	56.71 ± 0.07

Table 3.13.: The efficiencies of various D daughter PID cuts as measured using a fit to the D invariant mass in $B \to [K\pi]_D h$ data, where the uncertainties quoted are statistical. The $y <$ cuts are applied to pions and the $x >$ cuts are applied to kaons. The value highlighted in bold corresponds to the efficiency of the PID cuts applied in the analysis.

%	$x <$ 200	$x <$ 0	$x <$ -2	$x <$ -4	$x <$ -6
$y >$ -200	100	5.59 ± 0.03	2.20 ± 0.02	0.94 ± 0.01	0.45 ± 0.01
$y > 0$	13.15 ± 0.05	0.86 ± 0.01	0.33 ± 0.01	0.14 ± 0.01	0.07 ± 0.00
$y > 2$	7.74 ± 0.04	0.46 ± 0.01	**0.20 ± 0.01**	0.08 ± 0.00	0.04 ± 0.00
$y > 4$	4.62 ± 0.03	0.25 ± 0.01	0.11 ± 0.00	0.05 ± 0.00	0.03 ± 0.00
$y > 6$	2.82 ± 0.02	0.16 ± 0.01	0.07 ± 0.00	0.03 ± 0.00	0.02 ± 0.00

Table 3.14.: The misidentification (mis-ID) rates for various D daughter PID cuts, as measured using a fit to the D invariant mass in $B \to [K\pi]_D h$ data, where the uncertainties quoted are statistical. The $x <$ cuts are applied to kaons and the $y >$ cuts are applied to pions. The value highlighted in bold corresponds to the mis-ID rate of the PID cuts applied in the analysis.

To determine the corresponding misidentification rates, the same procedure is performed where the opposite PID requirements are applied to the D daughters; kaons are required to have $\Delta LL_{K/\pi} < x$ while pions must have $\Delta LL_{K/\pi} > y$. Fits are performed under a range of values of x and y, and yields $N(K < x, \pi > y)$ determined. The misidentification rate for a given $(K < x, \pi > y)$ PID requirement is given by $N(K < x, \pi > y)/N$. The misidentification (mis-ID) rates for a range of cuts are listed in Table 3.14, where the mis-ID rate of the analysis cuts are again highlighted in bold. The combined mis-ID rate is 0.20%, indicating that doubly misidentified favoured decays in the suppressed sample are reduced to 0.2% of their nominal rate as a result of the PID requirements.

In $B \to [K\pi\pi\pi]_D h$ and $B \to [\pi K\pi\pi]_D h$, D daughter kaons are required to have $\Delta LL_{K/\pi} > x$, while the two D daughter pions of *opposite* charge to this kaon are required to have $\Delta LL_{K/\pi} < y$. An identical procedure to that used for $B \to [hh]_D h$ is employed to determine the efficiencies and mis-ID rates of these cuts, where all values are summarised in Tables 3.15 and 3.16. The analysis cuts of $x = 2$ and $y = -2$ are once more highlighted in bold, where the mis-ID rate is found to be 0.06%.

%	$y <$ 200	$y <$ 0	$y <$ -2	$y <$ -4	$y <$ -6
> -200	100	69.01 ± 0.08	60.29 ± 0.08	51.88 ± 0.08	44.22 ± 0.08
> 0	94.65 ± 0.04	65.30 ± 0.08	57.04 ± 0.08	49.08 ± 0.08	41.82 ± 0.08
> 2	91.32 ± 0.05	62.96 ± 0.08	**55.06 ± 0.08**	47.41 ± 0.08	40.41 ± 0.08
> 4	87.78 ± 0.06	60.57 ± 0.08	53.00 ± 0.08	45.63 ± 0.08	38.85 ± 0.08
> 6	84.25 ± 0.06	58.11 ± 0.08	50.78 ± 0.08	43.75 ± 0.08	37.26 ± 0.08

Table 3.15.: The efficiencies of various D daughter PID cuts as measured using a fit to the D invariant mass in $B \to [K\pi\pi\pi]_D h$ data. The $y <$ cuts are applied to pions and the $x >$ cuts are applied to kaons. The value highlighted in bold corresponds to the efficiency of the PID cuts applied in the analysis.

%	$x <$ 200	$x <$ 0	$x <$ -2	$x <$ -4	$x <$ -6
> -200	0	3.64 ± 0.03	1.88 ± 0.02	0.87 ± 0.02	0.39 ± 0.01
> 0	5.49 ± 0.04	0.21 ± 0.01	0.10 ± 0.01	0.04 ± 0.00	0.02 ± 0.00
> 2	3.21 ± 0.03	0.12 ± 0.01	**0.06 ± 0.00**	0.02 ± 0.00	0.01 ± 0.00
> 4	2.13 ± 0.02	0.08 ± 0.00	0.04 ± 0.00	0.02 ± 0.00	0.01 ± 0.00
> 6	1.55 ± 0.02	0.06 ± 0.00	0.03 ± 0.00	0.02 ± 0.00	0.01 ± 0.00

Table 3.16.: The misidentification (mis-ID) rates for various D daughter PID cuts, as measured using a fit to the D invariant mass in $B \to [K\pi\pi\pi]_D h$ data. The $x <$ cuts are applied to kaons and the $y >$ cuts are applied to pions. The value highlighted in bold corresponds to the mis-ID rate of the PID cuts applied in the analysis.

D candidate invariant mass window

In order to calculate the efficiency of the ± 25 MeV/c^2 selection window around the nominal D^0 mass applied to all D candidates, fits are performed to the D invariant mass distributions in $B \to [K\pi]_D\pi$ data (top plot in Figure 3.17) and $B \to [K\pi\pi\pi]_D\pi$ data (top plot in Figure 3.18). The D peaks are described by a modified Gaussian function like the one described by Equation 4.1, and the combinatoric background is described by a first order polynomial. The fitted width is (6.98 ± 0.04) MeV/c^2 in the 2-body case, and (6.84 ± 0.02) MeV/c^2 in the 4-body case. The efficiency of the ± 25 MeV/c^2 window selection is determined by integrating the signal PDF yield within this region. It is found to be $(97.98 \pm 0.02)\%$ for the 2-body case, and $(94.56 \pm 0.04)\%$ for 4-body case.

The D signal components from these fits are then isolated using the sWeighting technique [75]. This method uses the fit PDFs to assign signal weights to each event, depending on the relative values of the signal and background PDFs at a given value of $m(D)$. The invariant mass of the sWeighted events are then plotted in the case where the D daughter kaon has been assigned the pion mass while one of the negative D daughter pions is simultaneously assigned the kaon mass (bottom plot in Figure 3.17, and bottom two plots in Figure 3.18). This distribution, $m(D)^{\text{swap}}$, represents what the D invariant mass of favoured $B \to [K\pi(\pi\pi)]_D\pi$ events looks like when they are doubly misidentified, ending up in the suppressed $B \to [\pi K(\pi\pi)]_D\pi$ sample.

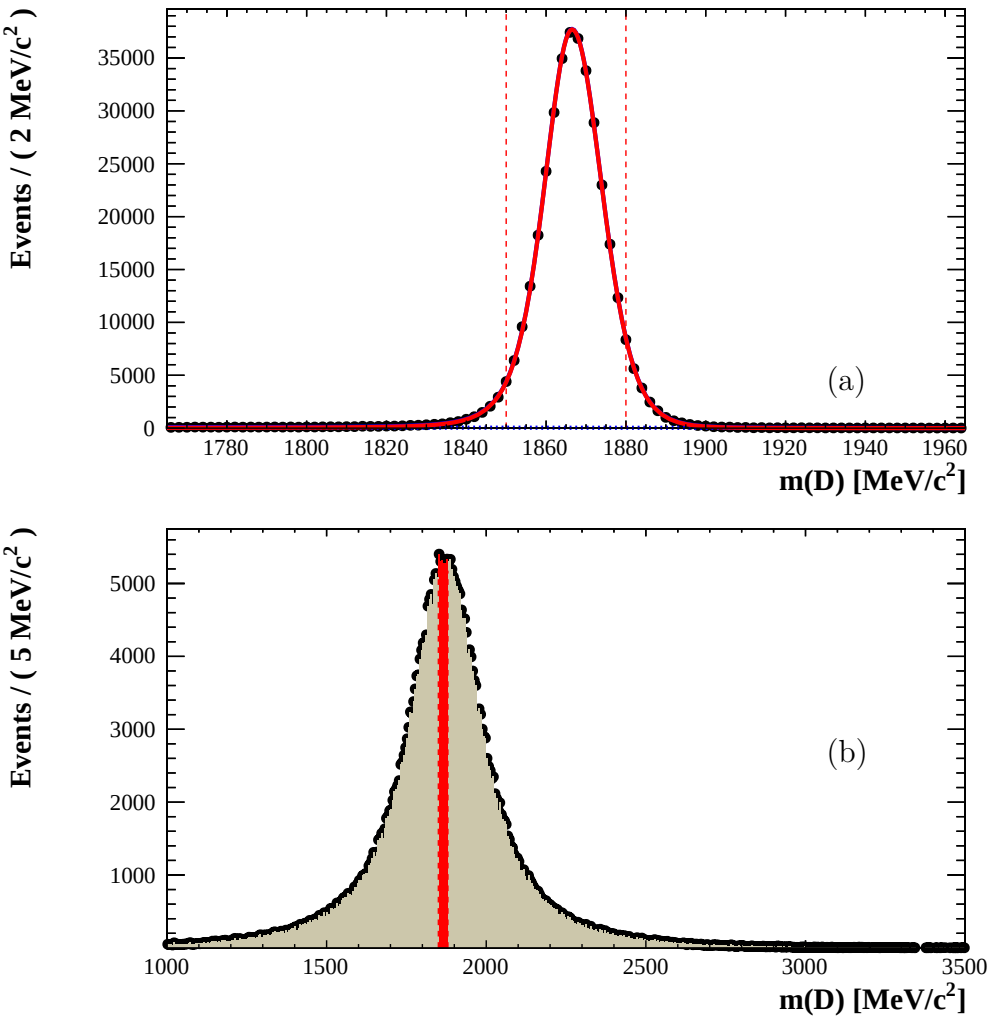

Figure 3.17.: (a) Invariant mass fit to $m(D)$ for $B \to [K\pi]_D\pi$ events in data. This fit is used to extract signal weights using the sPlot [75] method. The D invariant mass distribution where the mass hypotheses of the D daughter kaon and pion have been swapped, $m(D)^{\text{swap}}$, is shown in (b); the signal weights extracted from (a) have been used in plotting the distribution. The dotted red lines represent the veto window used to remove favoured $B \to [K\pi]_D h$ events from the suppressed $B \to [\pi K]_D h$ fit. Misidentified favoured decays removed from the suppressed sample are shown by the brown filled region in (b); correctly reconstructed favoured events also removed by the veto reside below and above the red dotted lines in (a).

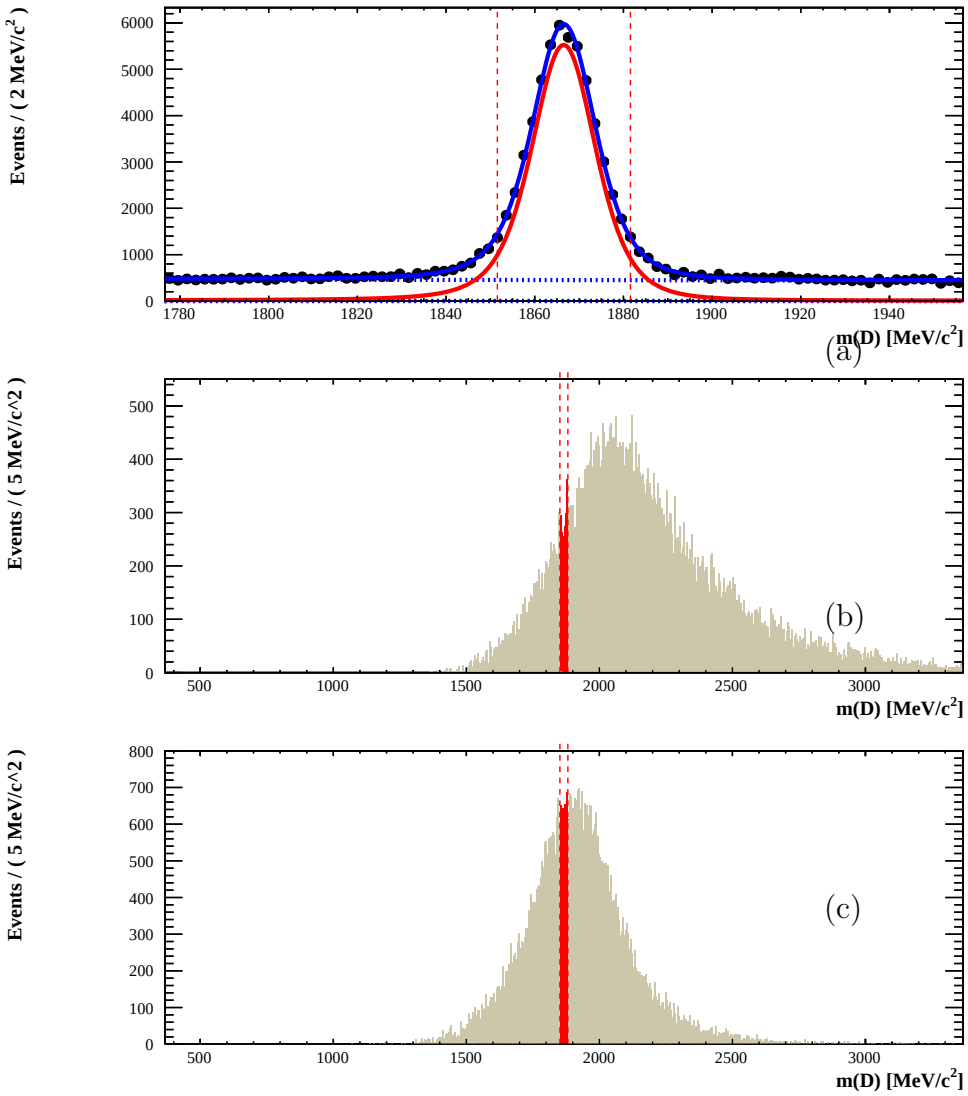

Figure 3.18.: (a) Invariant mass fit to $m(D)$ for $B \to [K\pi\pi\pi]_D\pi$ events in data. The D invariant mass distribution where the mass hypotheses of the D daughter kaon and opposite charge pion of highest momentum have been swapped, $m(D)^{\text{swap}}$, is shown in (b); the equivalent distribution for the lowest momentum opposite charge pion is shown in (c). See caption of Figure 3.17 for full details.

Applying the ± 25 MeV/c^2 D mass selection window to $m(D)^{\text{swap}}$ rather than $m(D)$ results in a lower selection efficiency, due to the spread in invariant mass caused by both particle misidentifications. In the case of favoured $B \to [K\pi]_D\pi$ decays that are doubly misidentified as suppressed $B \to [\pi K]_D\pi$, the mass window is only $(14.34 \pm 0.06)\%$ efficient, compared to the much higher efficiency for correctly identified favoured decays. This indicates that the crossfeed from favoured decays in the suppressed sample is further reduced by the ± 25 MeV/c^2 D mass window.

The same picture emerges for favoured $B \to [K\pi\pi\pi]_D\pi$ decays doubly misidentified as suppressed $B \to [\pi K\pi\pi]_D\pi$. Here, there are two possible $m(D)^{\text{swap}}$ distributions, corresponding to the two pions of opposite charge to the kaon that can be misidentified. The ± 25 MeV/c^2 window is $(4.47 \pm 0.03)\%$ and $(11.22 \pm 0.05)\%$ efficient on the two possible $m(D)^{\text{swap}}$ distributions.

Crossfeed veto

The final cut applied to reduce the contribution from misidentified favoured decays in the suppressed samples is an explicit mass window veto. Doubly misidentified favoured decays present in the suppressed samples should peak near the nominal D^0 mass in their $m(D)^{\text{swap}}$ distribution, since in the construction of $m(D)^{\text{swap}}$ both of the particle misidentifications will be undone.

In order to reject crossfeed events, the difference between the $m(D)^{\text{swap}}$ value for a candidate and the nominal D^0 mass is required to exceed 15 MeV/c^2. This veto is $(91.33 \pm 0.05)\%$ efficient on correctly reconstructed favoured $B \to [K\pi]_D\pi$ decays, but only $(9.64 \pm 0.05)\%$ efficient on doubly misidentified favoured decays i.e. those that would enter the suppressed sample.

In $B \to [K\pi\pi\pi]_D\pi$, the veto is $(93.29 \pm 0.04)\%$ efficient on correctly reconstructed decays. The efficiency on doubly misidentified decays is only $(14.36 \pm 0.36)\%$, while the efficiency on the distribution where the *other* pion was misidentified is $(95.30 \pm 2.10)\%$. Doubly misidentified favoured events removed by the veto are indicated by the brown shaded regions in Figures 3.17 and 3.18; the correctly reconstructed events removed by the same veto correspond to those falling above and below the dotted red lines in the top plots.

Overall crossfeed rejection

To determine the overall crossfeed contamination in the suppressed modes, the combined efficiency of the D daughter PID cuts, D mass window and crossfeed veto window must be evaluated. In the 2-body case, the efficiency of the combined selection on correctly reconstructed favoured events, $\epsilon(B \to [K_K\pi_\pi]_D h)$, is compared to the efficiency for doubly misidentified favoured events, $\epsilon(B \to [K_\pi\pi_K]_D h)$. The ratio:

$$r_{\rm CF}^{\pi K} = \frac{\epsilon(B \to [K_\pi\pi_K]_D h)}{\epsilon(B \to [K_K\pi_\pi]_D h)} \tag{3.62}$$

provides an estimate of the crossfeed rate in the suppressed modes.

The values of $\epsilon(B \to [K_K\pi_\pi]_D h)$ and $\epsilon(B \to [K_\pi\pi_K]_D h)$ are computed in Table 3.17, where the estimated crossfeed contribution is found to be $r_{\rm CF}^{\pi K} = (4.29 \pm 0.22) \times 10^{-5}$. This number represents the proportion of favoured $B \to [K\pi]_D h$ events expected to enter the suppressed modes $B \to [\pi K]_D h$, and is employed in the fit to data in Section 4.1 as a fixed term. The rate of suppressed decays relative to favoured decays is embodied by the observable $R_{\rm ADS(\pi)}^{\pi K}$, which has previously been measured to have a value of $(4.1 \pm 0.3) \times 10^{-3}$ [62]; the surviving crossfeed rate expected is thus only $\sim 1\%$ of the total expected suppressed signal yield.

In the 4-body case, there are two double misidentification efficiencies, $\epsilon(B \to [K_\pi\pi_K\pi_\pi\pi_\pi]_D h)$ and $\epsilon(B \to [K_\pi\pi_\pi\pi_\pi\pi_K]_D h)$, corresponding to the cases where each of the pions of opposite charge to the kaon are misidentified. The values for $\epsilon(B \to [K_K\pi_\pi\pi_\pi\pi_\pi]_D h)$, $\epsilon(B \to [K_\pi\pi_K\pi_\pi\pi_\pi]_D h)$ and $\epsilon(B \to [K_\pi\pi_\pi\pi_\pi\pi_K]_D h)$ are calculated in Table 3.18. In this case, an estimate for the expected crossfeed rate is given by the ratio:

$$r_{\rm CF}^{\pi K\pi\pi} = \frac{\epsilon(B \to [K_\pi\pi_K\pi_\pi\pi_\pi]_D h) + \epsilon(B \to [K_\pi\pi_\pi\pi_\pi\pi_K]_D h)}{\epsilon(B \to [K_K\pi_\pi\pi_\pi\pi_\pi]_D h)} \tag{3.63}$$

and is found to be $r_{\rm CF}^{\pi K\pi\pi} = (2.7 \pm 0.1) \times 10^{-5}$, which is around 0.7% of the previously measured vale of $R_{\rm ADS(\pi)}^{\pi K\pi\pi} = (3.69 \pm 0.36) \times 10^{-3}$ [63].

Crossfeed line shape

The crossfeed PDF shape is derived from $B \to [K\pi(\pi\pi)]_D\pi$ simulated events, where the mass hypotheses of the kaon and opposite charge pion D daughters have been swapped[9].

[9] In the case of $B \to [K\pi\pi\pi]_D\pi$, the mass swap with the highest momentum pion of opposite charge to the kaon is arbitrarily chosen.

Selection cut	$\epsilon(B \to [K_K\pi_\pi]_D h)$ (%)	$\epsilon(B \to [K_\pi\pi_K]_D h)$ (%)
D mass window : ± 25 MeV/c^2	97.98 $\pm$ 0.02	14.34 $\pm$ 0.06
Crossfeed veto window : ± 15 MeV/c^2	91.33 $\pm$ 0.05	9.64 $\pm$ 0.05
PID : $\Delta LL_{K/\pi}(K) > 2$, $\Delta LL_{K/\pi}(\pi) < -2$	72.02 $\pm$ 0.06	0.20 $\pm$ 0.01
Total	64.4 $\pm$ 0.07	(2.76 $\pm$ 0.14) $\times 10^{-3}$

Table 3.17.: Efficiencies of the D mass window, crossfeed veto window and D daughter PID cuts for $B \to [K\pi]_D h$ data events. Values are quoted for events reconstructed both with the D daughters given the correct ($[K_K\pi_\pi]_D$) and swapped ($[K_\pi\pi_K]_D$) mass hypotheses. The three selection cuts are orthogonal, and as such the total efficiency is given by the product of the individual efficiencies. The proportion of crossfeed events from the favoured $B \to [K\pi]_D h$ mode expected in the suppressed $B \to [\pi K]_D h$ mode is $r_{\rm CF}^{\pi K} = (4.29 \pm 0.22) \times 10^{-5}$. This number is employed as a fixed term in the fit to data.

Selection cut	$\epsilon(B \to [K_K\pi_\pi\pi_\pi\pi_\pi]_D h)$ (%)	$\epsilon(B \to [K_\pi\pi_K\pi_\pi\pi_\pi]_D h)$ (%)	$\epsilon(B \to [K_\pi\pi_\pi\pi_\pi\pi_K]_D h)$ (%)
D mass window : ± 25 MeV/c^2	94.56 $\pm$ 0.04	4.47 $\pm$ 0.03	11.22 $\pm$ 0.05
First pion crossfeed veto : ± 15 MeV/c^2	97.32 $\pm$ 0.03	14.36 $\pm$ 0.06	95.30 $\pm$ 2.10
Second pion crossfeed veto : ± 15 MeV/c^2	93.29 $\pm$ 0.04	95.30 $\pm$ 2.10	14.36 $\pm$ 0.06
PID : $\Delta LL_{K/\pi}(K^{\pm}) > 2$, $\Delta LL_{K/\pi}(\pi^{\mp}) < -2$	55.06 $\pm$ 0.16	0.06 $\pm$ 0.01	0.06 $\pm$ 0.01
Total	47.27 $\pm$ 0.08	(3.7 $\pm$ 0.1) $\times 10^{-4}$	(9.2 $\pm$ 0.2) $\times 10^{-4}$

Table 3.18.: Efficiencies of the D mass window, crossfeed veto window and D daughter PID cuts for $B \to [K\pi\pi\pi]_D h$ data events. Values are quoted for events reconstructed both with the D daughters given the correct ($[K_K\pi_\pi\pi_\pi\pi_\pi]_D$) and swapped ($[K_\pi\pi_K\pi_\pi\pi_\pi]_D$ and $[K_\pi\pi_\pi\pi_\pi\pi_K]_D$) mass hypotheses. The proportion of crossfeed events from the favoured $B \to [K\pi\pi\pi]_D h$ mode expected in the suppressed $B \to [\pi K\pi\pi]_D h$ mode is $r_{\rm CF}^{\pi K\pi\pi} = (2.7 \pm 0.1) \times 10^{-5}$. This number is employed as a fixed term in the fit to data.

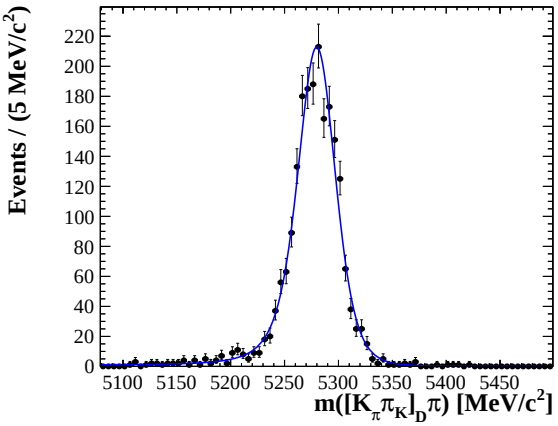

Figure 3.19.: Invariant mass fit to simulated $B \to [K\pi]_D\pi$ events, where the D daughter kaon and pion mass hypotheses have been swapped. Events plotted have passed the full selection, including the crossfeed requirements listed in the previous discussion. The fitted width is 17 MeV/c^2, which is wider than the corresponding width for correctly reconstructed events due to the double misidentification of the D daughters. A similar width of 23 MeV/c^2 is found in the case $B \to [K\pi\pi\pi]_D\pi$. Both widths are scaled to account for the difference in mass resolution between data and simulation, and are fixed in the fit to data.

The crossfeed events surviving the selection cuts detailed above are seen to have a peak similar to data (details of the main signal PDF are given in Section 4.1.1), but with a larger width. This larger width in $m(Dh)$ arises due to the spread of invariant mass introduced in the D system from to the double misidentification. Only a narrow region of this wider $m(D)$ distribution is eventually selected, resulting in a wider B invariant mass distribution.

A fit to simulated crossfeed $B \to [K_\pi\pi_K]_D\pi$ events is shown in Figure 3.19, where the crossfeed component has been fit with a Crystal Ball function. A Gaussian function is used in the final fit to data, as the additional yield in the Crystal Ball tail is negligible due to the very small crossfeed rates measured. The crossfeed widths as measured in simulation are 17 MeV/c^2 for $B \to [K_\pi\pi_K]_D\pi$ and 23 MeV/c^2 for $B \to [K_\pi\pi_K\pi_\pi\pi_\pi]_D\pi$, both of which are scaled in the fit to data to account for differences in the invariant mass resolution between data and simulation.

3.4.4. $\Lambda_b \to \Lambda_c h$ background in $B \to [KK]_D h$

An additional source of background in the $B \to [KK]_D h$ modes comes from $\Lambda_b \to \Lambda_c h$ decays where $\Lambda_c \to pK\pi$. When the pion from the Λ_c decay is missed in the invariant

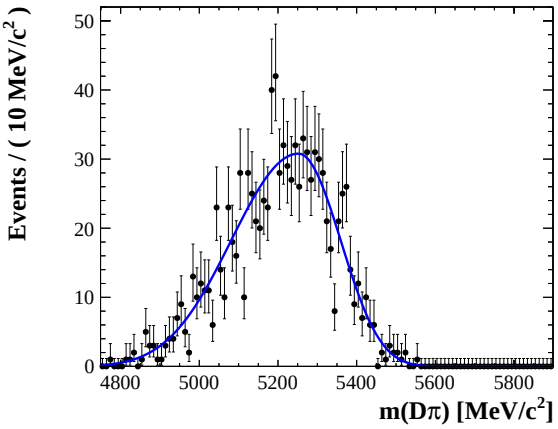

Figure 3.20.: Invariant mass fit to simulated $\Lambda_b \to [pK\pi]_{\Lambda_c}\pi$ decays reconstructed as $B \to [KK]_D\pi$. The distribution is fit with a modified Gaussian PDF, the parameters of which are listed in Table 3.19 and fixed in the fit to data.

mass sum, and the proton is misidentified as a kaon, such events can enter the invariant mass range considered in the fit to data ($5079 - 5899$ MeV/c^2). This contribution is described using a modified Gaussian PDF like the one described by Equation 4.1, with shape parameters taken from a fit to simulated $\Lambda_b \to [pK\pi]_{\Lambda_c}h$ decays reconstructed as $B^\pm \to Dh^\pm$, as shown in Figure 3.20.

The rate of this contribution in the $B^\pm \to D\pi^\pm$ fit sample, $N(\Lambda_b \to \Lambda_c\pi)$, floats freely. In the $B^\pm \to DK^\pm$ sample however, the yield $N(\Lambda_b \to \Lambda_c K)$ is fixed to the value:

$$N(\Lambda_b \to \Lambda_c K) = \frac{\mathcal{B}(\Lambda_b \to \Lambda_c K)}{\mathcal{B}(\Lambda_b \to \Lambda_c \pi)} \times N(\Lambda_b \to \Lambda_c \pi) = \mathcal{R}_{\Lambda_b} \times N(\Lambda_b \to \Lambda_c \pi) \tag{3.64}$$

where $\mathcal{R}_{\Lambda_b} = 0.073 \pm 0.002$, as measured by LHCb [76]. The shape parameters from simulation are listed in Table 3.19, and are fixed in the fit along with $\mathcal{R}_{\Lambda_b}$. A systematic uncertainty for this choice is assigned in Section 4.1.5.

3.4.5. Combinatoric background

Even after the application of the full selection, including both BDTs, some level of combinatoric background remains in the data. The remaining combinatoric contributions are described in the fit to data by first order polynomial PDFs, with gradient parameters that float freely in the $B^\pm \to DK^\pm$ and $B^\pm \to D\pi^\pm$ samples. The combinatoric yields for $B^\pm \to DK^\pm$ and $B^\pm \to D\pi^\pm$ also float freely, and can take different values for each D final state considered.

Parameter	Value
μ	5252.2 $\pm$ 14.7 MeV/c^2
σ_{L}	168.5 $\pm$ 16.8 MeV/c^2
σ_{R}	106.5 $\pm$ 14.0 MeV/c^2
α_{L}	-0.03 $\pm$ 0.06
α_{R}	-0.05 $\pm$ 0.06

Table 3.19.: Shape parameters from a fit to simulated $\Lambda_b \to \Lambda_c \pi$ decays using a modified Gaussian PDF, which are employed in the fit to data as fixed terms with an associated systematic uncertainty. The parameter μ denotes the mean, while σ_L, α_L and σ_R, α_R denote the left and right widths and tail parameters, respectively.

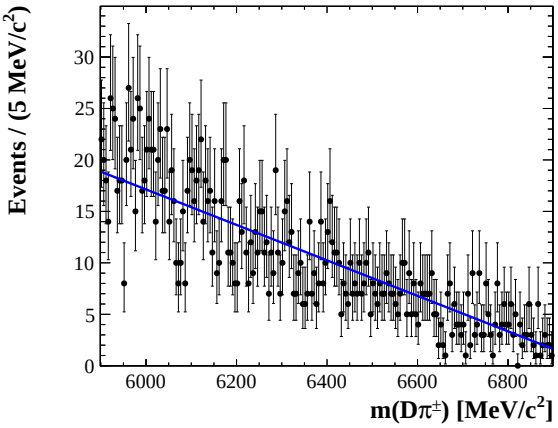

Figure 3.21.: Invariant mass fit to combinatoric events in upper sideband region of favoured $B \to [K\pi]_D \pi$. A first order polynomial function describes the data well in this region, justifying the use of this PDF in the fit to data to describe combinatoric background.

The choice of a first order polynomial to describe the combinatoric background is motivated by a fit to the upper $m(Dh)$ sideband in the highest statistics favoured $B \to [K\pi]_D \pi$ mode, as shown in Figure 3.21. The BDT2 cut has been removed to increase the number of remaining combinatoric events. A linear PDF describes the data well in this region, which is well separated from the signal region and contains no contributions from physics backgrounds.

3.4.6. Backgrounds from particle misidentification

It is possible to misidentify $B^\pm \to D\pi^\pm$ decays as $B^\pm \to DK^\pm$, in cases where the bachelor pion is misidentified as a kaon. By the same token, it is possible to misidentify $B^\pm \to DK^\pm$ decays as $B^\pm \to D\pi^\pm$, where the bachelor kaon is incorrectly assigned the pion mass hypothesis. The rate at which this misidentification process occurs for a bachelor $h \in \{\pi, K\}$ is given by $(1 - \epsilon^h_{\rm PID})$, where $\epsilon^h_{\rm PID}$ is the PID efficiency as defined in Section 3.3.3.

Due to the tight ($\Delta LL_{K/\pi} > 12$) requirement placed on bachelor kaons in the analysis, the number of $B^\pm \to D\pi^\pm$ decays that are incorrectly reconstructed as $B^\pm \to DK^\pm$ is very small, with a misidentification rate of less than 0.5%. Nevertheless, misidentified $B^\pm \to D\pi^\pm$ decays are still accounted for in the $B^\pm \to DK^\pm$ sample, with a yield that is fixed to be $(1 - \epsilon^\pi_{\rm PID})$ of the total $B^\pm \to D\pi^\pm$ yield in the fit. Since the pion is artificially given too much mass under the kaon hypothesis, the $B^\pm \to D\pi^\pm$ events appearing in the $B^\pm \to DK^\pm$ sample are shifted up from the nominal $B^\pm$ mass, as well as being spread out in invariant mass.

The shape of misidentified $B^\pm \to D\pi^\pm$ decays is taken from simulation, where favoured $B \to [K\pi]_D\pi$ MC events are reconstructed as $B \to [K\pi]_D K$ and weighted to account for the PID requirement applied to the bachelor. The resulting distribution is fit with a double Crystal Ball function as shown in Figure 3.22 (left plot), in order to model the tails in the distribution; the tail parameters are subsequently fixed in the fit to data. A tail extending to high invariant mass is evident, arising from the bachelor misidentification. The same shape is used to describe misidentified $B^\pm \to D\pi^\pm$ events in all other D modes, including the 4-body final states.

$B^\pm \to DK^\pm$ events that end up in the $B^\pm \to D\pi^\pm$ sample due to misidentification of the bachelor kaon are also included in the fit. They account for $(1 - \epsilon^K_{\rm PID})$ of the total $B^\pm \to DK^\pm$ yield in the fit, and are again modelled with a double Crystal Ball function in order to describe the tails in the distribution arising from particle misidentification. The shape is taken from a fit to simulated $B \to [K\pi]_D K$ events reconstructed as $B \to [K\pi]_D\pi$, as illustrated in Figure 3.22 (right plot). All shape parameters for this contribution, listed in Table 3.20, are fixed in the fit to data. This fixing is necessary, as the shape resides close to the much larger $B^\pm \to D\pi^\pm$ peak. The same shape is used to describe misidentified $B^\pm \to DK^\pm$ events for all D modes, including the 4-body final states.

Parameter	Value
$B^{\pm} \to D\pi^{\pm}$ as $B^{\pm} \to DK^{\pm}$	
α_L	1.62 ± 0.15
n_L	1.53 ± 0.37
α_R	-0.38 ± 0.03
n_R	7.20 ± 0.71
$B^{\pm} \to DK^{\pm}$ as $B^{\pm} \to D\pi^{\pm}$	
α_L	0.70 ± 0.03
n_L	3.80 ± 0.15
α_R	-2.73 ± 0.10
n_R	1.88 ± 0.31
σ_L	(22.8 ± 0.9) MeV/c^2
σ_R	(17.0 ± 0.3) MeV/c^2
μ	(5234.9 ± 0.5) MeV/c^2

Table 3.20.: Shape parameters from fits to $B \to [K\pi]_D\pi$ and $B \to [K\pi]_D K$ simulated events that have been reconstructed under the wrong bachelor mass hypothesis. All of the parameters listed are employed in the fit to data as fixed terms, with associated systematic uncertainties. The parameters α_L, n_L and α_R, n_R refer to the left and right tail parameters of the double Crystal Ball function, whereas σ_L and σ_R refer to the left and right widths. The parameter μ refers to the mean of the double Crystal Ball.

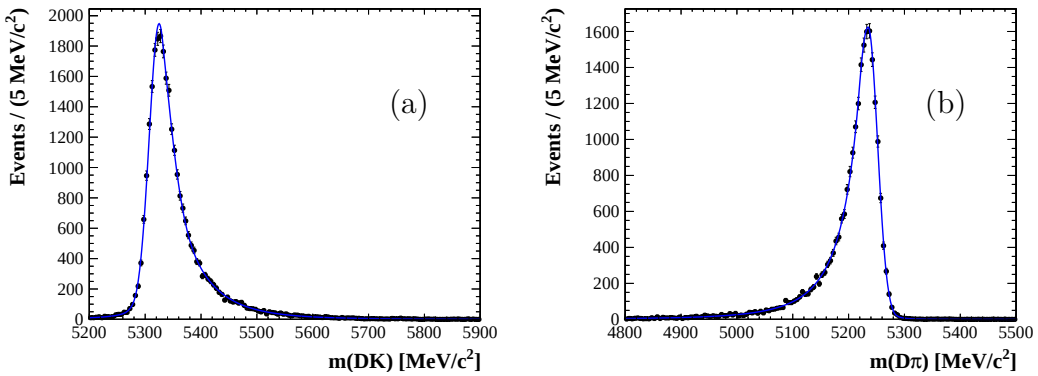

Figure 3.22.: Invariant mass fit to simulated (a) $B \to [K\pi]_D\pi$ events reconstructed as $B \to [K\pi]_D K$ and (b) $B \to [K\pi]_D K$ events reconstructed as $B \to [K\pi]_D\pi$. Shape parameters from these fits are employed in the fit to data as fixed terms with associated systematic uncertainties. Tails extending to higher and lower masses are evident in (a) and (b) respectively, due to the bachelor misidentification.

3.4.7. Summary of background components

A summary of the PDFs used to describe each of the background contributions in the invariant mass fit is provided in Table 3.21.

Background	PDF
Partially reconstructed	`RooHORNSdini` and `RooHILLdini` fit to MC
Charmless	Gaussian fit to MC, width scaled for data/MC differences
Crossfeed	Gaussian fit to MC, width scaled for data/MC differences
$\Lambda_b \to \Lambda_c h$	Modified Gaussian fit to MC
Combinatoric	First order polynomial, freely floating gradient parameter
Fully reconstructed with particle misidentification	Modified Gaussian, fixed tail parameters from MC
Partially reconstructed with particle misidentification	Kernel estimation from MC

Table 3.21.: The PDFs employed to describe each background component in the invariant mass fit.

Chapter 4.

Invariant mass fit to measure $\mathcal{CP}$ observables

In this Chapter, the invariant mass fit used to measure the ADS/GLW $\mathcal{CP}$ observables is presented. The strategy used to determine signal yields is discussed in Section 4.1, where a description of the Probability Density Functions (PDFs) employed to model signal and background components is given. The systematic uncertainties affecting each of the $\mathcal{CP}$ observables are quantified, and final numerical results presented, in Section 4.2.

4.1. Fit to data

In this Section, the fit strategy used to measure the $\mathcal{CP}$ observables is outlined. The PDF used to describe signal events is detailed in Section 4.1.1, with validation of the shape provided by fits to simulated events; all background PDFs used in the fit are discussed in Section 3.4. The concept of a simultaneous fit is introduced, and its application in the fitting of $B^{\pm} \to D\pi^{\pm}$ and $B^{\pm} \to DK^{\pm}$ events discussed, in Section 4.1.2. Separate, but almost identical, fits are performed to the $B \to [hh]_D h$ and $B \to [hhhh]_D h$ modes, due to differences in their underlying momentum spectra. Toy Monte Carlo studies, used to validate the fit method, are discussed in Section 4.1.4. To conclude, descriptions of the various systematic uncertainties affecting the measurement of each $\mathcal{CP}$ observable are given in Section 4.1.5.

4.1.1. Signal PDF

Correctly reconstructed $B^\pm \to Dh^\pm$ signal candidates are expected to peak at the nominal $B^\pm$ mass. All signal peaks in the fit to data are modelled with the sum of a modified Gaussian PDF and a wide Gaussian PDF. The functional form of the signal PDF is:

$$f(x) \propto A\text{exp}\left(\frac{-(x-\mu)^2}{2\sigma^2+(x-\mu)^2\alpha_{L,R}}\right) + (1-A)\text{exp}\left(\frac{-(x-\mu)^2}{2\sigma_w^2}\right) \tag{4.1}$$

where x is the B candidate invariant mass, μ is the mean of the function and σ is the width. The non-Gaussian tails of the distribution are described by a combination of the $\alpha_L(x < \mu)$ and $\alpha_R(x > \mu)$ factors and a wide Gaussian of mean μ and width σ_w, where σ_w is required to exceed 50 MeV/c^2 and floats freely to values $\sim$80 MeV/c^2. The fraction of the total yield contained within the main peak is denoted by A, which floats freely to values $\sim$99%. In general the tail parameters can also be floated freely, but they are fixed to the values found in simulation (see below) to increase fit stability. A systematic uncertainty for this choice is assigned in Section 4.1.5. The values of A, σ_w, α_L and α_R are shared across $B^\pm \to DK^\pm$ and $B^\pm \to D\pi^\pm$ and across all D final states in the 2-body and 4-body fits, respectively[1].

The mean μ can be different in the B^+ and B^- subsamples of the fit[2], as well as for each D final state, but is required to be the same in $B^\pm \to DK^\pm$ and $B^\pm \to D\pi^\pm$ in all cases. The width σ is required to be the same for B^+ and B^- events, but can be different for each D mode due to differences in the invariant mass resolution caused by having greater or fewer kaons in the final state. The signal width in $B^\pm \to DK^\pm$ is related to the corresponding width in $B^\pm \to D\pi^\pm$ by a freely floating ratio $\sigma(DK)/\sigma(D\pi)$; this ratio is shared across all D final states in the 2-body and 4-body fits, respectively.

Shape validation in simulation

The choice of signal PDF is motivated from fits performed to simulated $B \to [K\pi]_D h$ events, as shown in Figure 4.1. In this fit, the small contribution from the wide Gaussian PDF is ignored, as the effect that it models in the data is not reproduced by the lower statistics MC samples. $B \to [K\pi]_D K$ events are displayed in the top plot (red), and in

[1] The 2-body and 4-body D modes are fit separately due to differences in their underlying momentum distributions, which results in a difference in invariant mass resolution.

[2] The specific mechanics of the fit, including the splits made into various sub-samples, is detailed in full in Section 4.1.2.

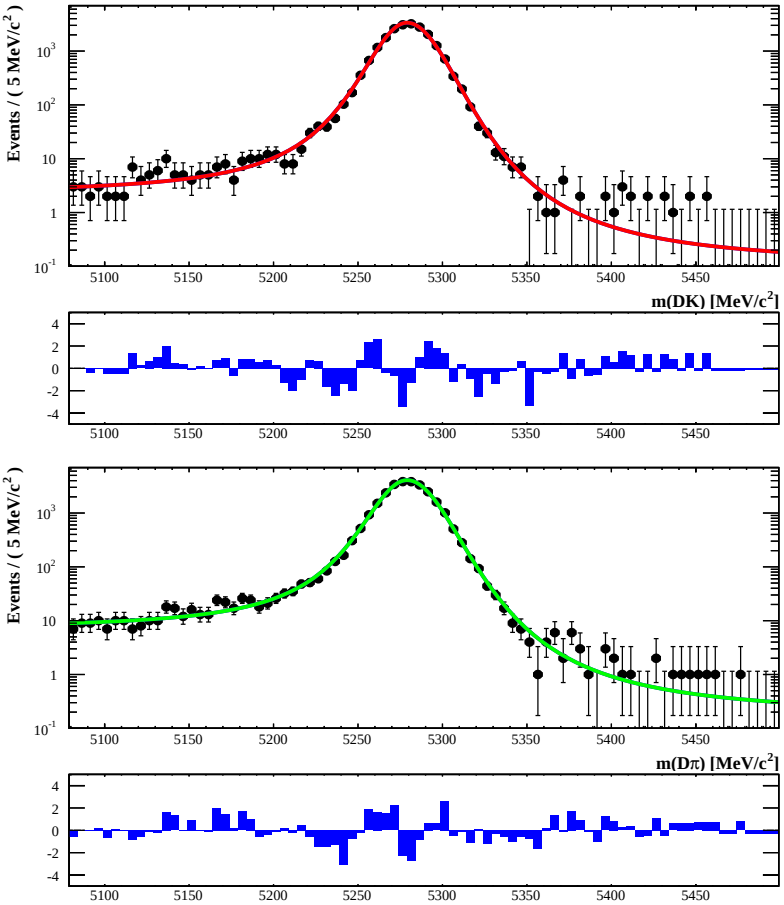

Figure 4.1.: Invariant mass fit to simulated $B \to [K\pi]_D\pi$ (bottom, green) and $B \to [K\pi]_D K$ (top, red) events passing the full selection. The distributions are fit simultaneously using a modified Gaussian function (first term in Equation 4.1), with tail parameters used in the fit to data. All D final states are well described by this function.

the bottom plot $B \to [K\pi]_D\pi$ events are shown (green); the two distributions have been fit simultaneously, sharing parameters as detailed above. The residual histograms in blue indicate that the modified Gaussian PDF reproduces the tails of the distribution well; the same behaviour is exhibited by all other 2-body and 4-body D final states considered.

The tail parameters from this fit are employed in the fit to $B \to [hh]_D h$ data as fixed terms, as are the corresponding parameters from fits to simulated $B \to [hhhh]_D h$ events. The values of all tail parameters are listed in Table 4.1. All other shape parameters float freely in the $B \to [hh]_D h$ and $B \to [hhhh]_D h$ fits.

Parameter	Value
$\boldsymbol{B \to [hh]_D h}$	
α_L	0.104 ± 0.002
α_R	0.072 ± 0.002
$\boldsymbol{B \to [hhhh]_D h}$	
α_L	0.107 ± 0.003
α_R	0.072 ± 0.003

Table 4.1.: Signal tail parameters from fits to simulated $B \to [K\pi]_D h$ and $B \to [K\pi\pi\pi]_D h$ events. These parameters are employed as fixed terms in the fit to data.

4.1.2. Simultaneous fit strategy

The observables of interest, as defined in Section 3.1.3, are measured with extended binned maximum likelihood fits to the invariant mass distributions of selected B candidates. Two fits are performed in an identical manner: one for the $D \to hh$ modes in the analysis, and one for the $D \to hhhh$ modes. Both of these fits operate in an identical fashion with respect to the observables being measured.

Sensitivity to $\mathcal{CP}$ asymmetries is achieved by separating the candidates by charge into $\boldsymbol{B^+}$ and $\boldsymbol{B^-}$ samples. For all of the D modes studied, the $B^\pm \to DK^\pm$ and $B^\pm \to D\pi^\pm$ decays can be separated with high purity by a $\Delta LL_{K/\pi} > 12$ requirement on the bachelor track, as discussed in Section 3.3.3. Events that **pass** this cut are deemed **kaon-like**, and are reconstructed as $B^\pm \to DK^\pm$. These events are placed in the **PASS** subsample. Events that **fail** the PID cut are deemed **pion-like** and are reconstructed in the $B^\pm \to D\pi^\pm$ final state; they are placed in the **FAIL** subsample.

As the PID requirement has an associated misidentification rate, some $B^\pm \to DK^\pm$ ($B \to D\pi^\pm$) events still end up in the **FAIL** (**PASS**) sample, but no candidate is explicitly rejected; they are placed in either the **PASS** or **FAIL** samples, depending on which side of the $\Delta LL_{K/\pi}$ cut they fall. The $B \to [hh]_D h$ and $B \to [hhhh]_D h$ fits both consist of four subsamples:

$$(B^+, B^-) \times (\text{PASS,FAIL})$$

for each of the D modes considered, where all of the subsamples are fitted simultaneously with a common set of parameters. The four subsamples are illustrated in Figure 4.2, where a toy sample of favoured $B \to [K\pi]_D h$ events generated from the total data fit PDF

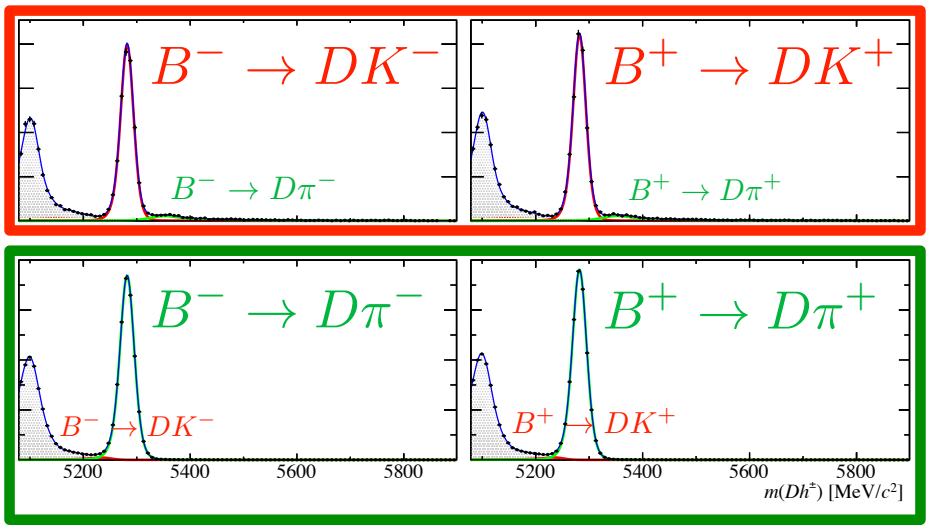

Figure 4.2.: The four subsamples of the fit : (B^+, B^-) $\times$ (PASS, FAIL). Each D mode in the analysis is split into the four subsamples shown, and the subsamples for all D modes are then fit simultaneously. This procedure is carried out in separate fits to the $B \to [hh]_D h$ and $B \to [hhhh]_D h$ modes. In the top row (red), the **PASS** slice is shown. This corresponds to events passing the bachelor PID requirement, where events are reconstructed as $B^\pm \to DK^\pm$. In the bottom row (green), the **FAIL** slice is plotted. Events in this sample fail the bachelor PID cut, and are reconstructed as $B^\pm \to D\pi^\pm$. Events are either placed in the **PASS** or **FAIL** samples, but *not* both. B^- candidates are shown on the left, and B^+ candidates on the right. The grey shaded region at low reconstructed invariant mass is from partially reconstructed B decays.

is plotted. $B^\pm \to DK^\pm$ decays are shown in red, while $B^\pm \to D\pi^\pm$ decays are shown in green. The **PASS** slice is shown in the top row, corresponding to events reconstructed as $B^\pm \to DK^\pm$, while the **FAIL** slice corresponding to $B^\pm \to D\pi^\pm$ events is shown in the bottom row. B^- candidates are shown on the left, while B^+ candidates are shown on the right.

A binned fit is preferred as it offers a significant speed improvement over the unbinned version, while degrading the measured fit errors in only their third significant figure. Bins of 5 MeV/c^2 width are chosen to cover an invariant mass range of $5079 - 5899$ MeV/c^2, 164 bins in total.

Components

The signal and background component PDFs have been described in detail in Section 3.4 and 4.1.1. The total PDF model is built from several components in each D subsample, each of which represent a different source of events in data.

1. **Correctly reconstructed $\boldsymbol{B \to [hh(hh)]_D h}$ events:** Described by the PDF defined in Equation 4.1 and illustrated in Figure 4.1, these events constitute a fraction $\epsilon_{\text{PID}}^{h'}$ of the total $B \to [hh(hh)]_D h'$ yield, where h' denotes the bachelor in this instance ($h' \in \{\pi, K\}$).

2. **Misidentified $\boldsymbol{B \to [hh(hh)]_D h}$ events:** Described by double Crystal Ball functions as illustrated in Figure 3.22, these events correspond to signal decays where the bachelor pion (kaon) h' has been misidentified as a kaon (pion). They account for a fraction $(1 - \epsilon_{\text{PID}}^{h'})$ of the total $B \to [hh(hh)]_D h'$ yield.

3. **Combinatoric background:** Arising from combinations of signal tracks and random tracks, the rate of these events is greatly reduced by the two-stage BDT selection. The surviving contributions are described by linear functions, as illustrated in Figure 3.21.

4. **Partially reconstructed background:** Decays of the type $B \to DhX$, where the particle $X \in \{\pi^{\pm}, \pi^0, \gamma\}$ is missed in the invariant mass sum, form a background at low invariant mass. Events of this type are described by the analytical `RooHORNSdini` and `RooHILLdini` PDFs as shown in Figure 3.11, where five contributions are common to all D modes. The B^+ and B^- yields vary independently, but a common charge asymmetry representing the net effect of any CP, production and detection asymmetry effects is shared across all partially reconstructed modes and D final states.

5. **$\boldsymbol{B_s^0 \to D^0 K\pi}$:** In the suppressed $B \to [\pi K(\pi\pi)]_D K$ modes, an additional partially reconstructed background from $B_s^0 \to D^0 K[\pi]$ decays also contributes; this component is also described using a `RooHORNSdini` PDF. The $\mathcal{CP}$ asymmetry of this background is assumed from physics to be zero, since it is a neutral B meson and thus exhibits no direct $\mathcal{CP}$-violation.

6. **$\boldsymbol{\Lambda_b \to \Lambda_c h}$:** In the specific case of $B \to [KK]_D h$, the background from partially reconstructed $\Lambda_b \to [pK\pi]_{\Lambda_c} h$ decays (where the pion from the Λ_c decay is missed, and the proton is misidentified as a kaon) is described using a modified Gaussian

PDF, as illustrated in Figure 3.20. The $\mathcal{CP}$ asymmetry of this background is also assumed to be zero.

Yields

B^+ and B^- yields for each component are floated independently, with the exception of the combinatoric background yields and the yields of the partially reconstructed $B_s^0 \to D^0 K\pi$ and $\Lambda_b \to \Lambda_c h$ backgrounds. The number of $B^\pm \to Dh^\pm$ signal events for a given D mode is defined as:

$$n_{\rm TOT}(B^\pm \to D\pi^\pm) = n_{\rm PASS}(B^\pm \to D\pi^\pm) + n_{\rm FAIL}(B^\pm \to D\pi^\pm) \tag{4.2}$$
$$n_{\rm TOT}(B^\pm \to DK^\pm) = n_{\rm PASS}(B^\pm \to DK^\pm) + n_{\rm FAIL}(B^\pm \to DK^\pm) \tag{4.3}$$
$$\tag{4.4}$$

Equivalently, the yields in the **PASS** and **FAIL** samples can be defined in terms of the total yield:

$$n_{\rm PASS}(B^\pm \to D\pi^\pm) = (1 - \epsilon^\pi_{\rm PID}) \times n_{\rm TOT}(B^\pm \to D\pi^\pm) \tag{4.5}$$
$$n_{\rm FAIL}(B^\pm \to D\pi^\pm) = \epsilon^\pi_{\rm PID} \times n_{\rm TOT}(B^\pm \to D\pi^\pm) \tag{4.6}$$
$$n_{\rm PASS}(B^\pm \to DK^\pm) = \epsilon^K_{\rm PID} \times n_{\rm TOT}(B^\pm \to DK^\pm) \tag{4.7}$$
$$n_{\rm FAIL}(B^\pm \to DK^\pm) = (1 - \epsilon^K_{\rm PID}) \times n_{\rm TOT}(B^\pm \to DK^\pm) \tag{4.8}$$

The $n(B^+)$ and $n(B^-)$ signal yields are then combined to construct the $\mathcal{CP}$ observables, as defined in Section 3.1.3. The total $B \to [hh(hh)]_D\pi$ yield, $n(B^+)+n(B^-)$, is a floating parameter of the fit for each D mode, while the following ratios are measured directly:

$$R^{K\pi(\pi\pi)}_{K/\pi} = \frac{n_{\rm TOT}(B^\pm \to [K\pi(\pi\pi)]_D K^\pm)}{n_{\rm TOT}(B^\pm \to [K\pi(\pi\pi)]_D \pi^\pm)} \tag{4.9}$$
$$R^{KK}_{CP} = \frac{n_{\rm TOT}(B^\pm \to [KK]_D K^\pm)}{n_{\rm TOT}(B^\pm \to [KK]_D \pi^\pm)} \times \frac{1}{R^{K\pi}_{K/\pi}} \tag{4.10}$$
$$R^{\pi\pi(\pi\pi)}_{CP} = \frac{n_{\rm TOT}(B^\pm \to [\pi\pi(\pi\pi)]_D K^\pm)}{n_{\rm TOT}(B^\pm \to [\pi\pi(\pi\pi)]_D \pi^\pm)} \times \frac{1}{R^{K\pi(\pi\pi)}_{K/\pi}} \tag{4.11}$$
$$\tag{4.12}$$

Charge asymmetries

The raw charge asymmetries measured in each of the $B \to [hh(hh)]_D h$ signal modes are defined experimentally as:

$$A_{\text{raw}} = \frac{n(B^-) - n(B^+)}{n(B^-) + n(B^+)} \tag{4.13}$$

where $n(B^+)$ and $n(B^-)$ are the measured signal yields in each sample of B charge. All asymmetries are normalised to be within the range $[-1, +1]$, with positive symmetries indicating an excess of B^- mesons. There are two classes of contributing asymmetry in the fit: the asymmetry from $\mathcal{CP}$ violation, A_{CP}, and other charge asymmetries introduced due to experimental factors. There are several contributing asymmetries in the latter case:

- **Production asymmetry A_{B_u}:** This is the production asymmetry of $B^\pm$ mesons in pp collisions at $\sqrt{s} = 7(8)$ TeV in 2011 (2012). It is easier to produce B^+ mesons than B^- mesons in pp collisions ($\bar{u}$ quarks needed for a B^- must be taken from the proton sea), and thus a small negative asymmetry is expected. A_{B_u} is a free parameter of the fit, and is shared across all signal modes. It can be measured by assuming zero A_{CP} for the highest statistics favoured $B \to [K\pi(\pi\pi)]_D\pi$ modes in the analysis, and is measured independently in the $B \to [hh]_D h$ and $B \to [hhhh]_D h$ fits as $A_{B_u}^{hh}$ and $A_{B_u}^{hhhh}$. A dedicated measurement of A_{B_u} is performed in Chapter 5.

- **Kaon and pion detection asymmetries, A_K^{det} and A_π^{det} :** Due to the different quark content of K^+ and K^- mesons, their interaction probabilities with the detector material are slightly different, resulting in a small detection asymmetry. The equivalent asymmetry for pions is much smaller, and is assumed to be zero with an associated systematic uncertainty, $A_\pi^{\text{det}} = (0.0 \pm 0.3)\%$. A dedicated measurement of $A_K^{\text{det}} - A_\pi^{\text{det}}$ has been performed at LHCb, where $A_K^{\text{det}} - A_\pi^{\text{det}} = (-1.1 \pm 0.3)\%$ [77], giving access to A_K^{det} when combined with the knowledge of A_π^{det}. Both values are employed as fixed terms in the fit to data, and are considered as a source of systematic uncertainty in Section 4.1.5.

- **Left/Right detector asymmetry $A_{L,R}$:** The left/right asymmetry is defined as the difference in the data collection efficiency between the left and right sections of LHCb. Due to the use of approximately equal samples of opposite magnet polarity data, this effect cancels in the analysis. Any residual effect is accounted for by the systematic uncertainties on A_K^{det} and A_π^{det}.

The production asymmetry contribution is common to all $B \to [hh(hh)]_D h$ modes, but the degree to which $A_K^{\rm det}$ and $A_K^{\rm det}$ influence the specific asymmetry measurements depends upon the number of kaons and pions in the reconstructed final state.

The asymmetries measured in the analysis are then defined as:

$$A_{B_u}^{hh(hh)} = A_{\rm raw}(B \to [K\pi(\pi\pi)]_D\pi) - A_\pi^{K\pi(\pi\pi)} - A_K^{\rm det} \tag{4.14}$$
$$A_K^{K\pi(\pi\pi)} = A_{\rm raw}(B \to [K\pi(\pi\pi)]_D K) - A_{B_u}^{hh(hh)} - 2A_K^{\rm det} + A_\pi^{\rm det} \tag{4.15}$$
$$A_\pi^{KK} = A_{\rm raw}(B \to [KK]_D\pi) - A_{B_u}^{hh} - A_\pi^{\rm det} \tag{4.16}$$
$$A_K^{KK} = A_{\rm raw}(B \to [KK]_D K) - A_{B_u}^{hh} - A_K^{\rm det} \tag{4.17}$$
$$A_\pi^{\pi\pi(\pi\pi)} = A_{\rm raw}(B \to [\pi\pi(\pi\pi)]_D\pi) - A_{B_u}^{hh(hh)} - A_\pi^{\rm det} \tag{4.18}$$
$$A_K^{\pi\pi(\pi\pi)} = A_{\rm raw}(B \to [\pi\pi(\pi\pi)]_D K) - A_{B_u}^{hh(hh)} - A_K^{\rm det} \tag{4.19}$$
$$A_{\rm ADS(\pi)}^{\pi K(\pi\pi)} = A_{\rm raw}(B \to [\pi K(\pi\pi)]_D\pi) - A_{B_u}^{hh(hh)} - 2A_\pi^{\rm det} + A_K^{\rm det} \tag{4.20}$$
$$A_{\rm ADS(K)}^{\pi K(\pi\pi)} = A_{\rm raw}(B \to [\pi K(\pi\pi)]_D K) - A_{B_u}^{hh(hh)} - A_\pi^{\rm det} \tag{4.21}$$
$$\tag{4.22}$$

where $A_\pi^{K\pi(\pi\pi)}$ is assumed to be zero to enable the measurement of $A_{B_u}^{hh(hh)}$[3], and the detection asymmetries $A_K^{\rm det}$ and $A_\pi^{\rm det}$ are fixed to the measured LHCb value and zero, respectively. The presence of a track $h^\pm$ in the final state, in the absence of an oppositely charged track $h^\mp$, contributes a factor $\pm A_h^{\rm det}$ to the asymmetry definitions above.

4.1.3. Summary of fit components

A visual summary of the various fit components is presented in Figure 4.3, where an invariant mass fit to $B^\pm \to [\pi\pi]_D h^\pm$ candidates in 3 fb^{-1} data is shown on a logarithmic scale.[4] $B^\pm \to D\pi^\pm$ decays reconstructed under the pion bachelor mass hypothesis are shown by a green solid line in the **FAIL** sample (bottom plots). The contribution from misidentified $B^\pm \to D\pi^\pm$ decays in the **PASS** sample (top plots) are also shown in green, where the PDF is displaced to higher invariant mass values due to the bachelor misidentification.

$B^\pm \to DK^\pm$ decays reconstructed under the kaon bachelor mass hypothesis are shown by a red solid line in the **PASS** sample. The corresponding contribution from misidentified $B^\pm \to DK^\pm$ decays in the **FAIL** sample is also shown in red. The contribution

[3] By construction, the same A_{B_u} is shared by all modes in the fit to data.
[4] This mode is chosen for ease of visualisation, as it contains the largest charmless contribution.

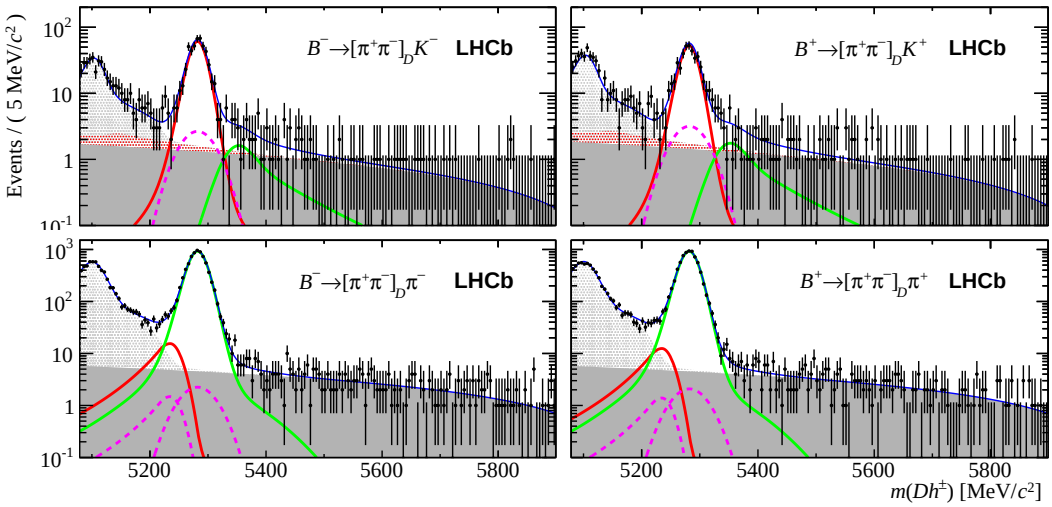

Figure 4.3.: Invariant mass fit to $B^\pm \to [\pi\pi]_D h^\pm$ candidates in 3 fb^{-1} data, for the purpose of illustration. The distributions are plotted on a logarithmic scale to aid visibility. In the bottom row of plots (FAIL slice), $B^\pm \to [\pi\pi]_D \pi^\pm$ are shown by the green solid line; B^- candidates appear in the leftmost plot, with B^+ candidates on the right. In the top row of plots (PASS slice), $B^\pm \to [\pi\pi]_D K^\pm$ are shown by the red solid line. The corresponding misidentification components for each of these modes are shown by solid lines of the same colour. The dotted grey region at low invariant mass shows the contribution from partially reconstructed B decays, while the dotted red region in the PASS slice shows the contribution from partially reconstructed and misidentified $B \to D\pi X$ decays. The solid grey region indicates the combinatoric background contribution, while he dashed pink lines represent the contributions from charmless B decays. The total fit PDF is shown by the solid blue line.

from charmless $B^\pm \to K^\pm\pi^\pm\pi^\pm$ decays in the **PASS** sample are shown by the pink dashed line. Misidentified $B^\pm \to K^\pm\pi^\pm\pi^\pm$ decays entering the **FAIL** sample are also plotted in pink, where the PDF is displaced to lower invariant mass values due to the misidentification of a kaon as a pion. The contribution from charmless $B^\pm \to \pi^\pm\pi^\pm\pi^\pm$ decays in the **FAIL** sample is also shown in pink.

The combinatoric background contribution is shown by the solid filled grey region in both the **PASS** and **FAIL** samples. Partially reconstructed background events are shown by the filled light grey regions at low invariant mass in both the **PASS** and **FAIL** samples. The contribution from partially reconstructed $B \to D\pi X$ decays, where the pion is misidentified as a kaon, are shown by the filled red region in the **PASS** sample.

4.1.4. Validation with toy Monte Carlo fits

The performance and stability of the fit procedure is evaluated using toy experiments. As a first step, the $B \to [hh]_D h$ and $B \to [hhhh]_D h$ fits to data (results presented in Section 4.2) are performed, providing a final set of values for each floating fit parameter. The fit PDF is then used to generate toy Monte Carlo datasets, initialising all PDF parameters to the final values found in the fit to data. A fit to this generated toy dataset is then performed using the data fit PDF, where all parameters are this time initialised to their *starting positions* in the fit to data. With this procedure, it is possible to check the robustness of the fit, its rate of convergence and its ability to accurately measure the $\mathcal{CP}$ observable parameter values and their uncertainties without bias.

Pull distributions $P(x)$ for each observable of the fit x can be constructed by running many such iterations of generation and fitting. The pull for a given parameter is defined as:

$$P(x) = \frac{x^{\text{fit}} - x^{\text{gen}}}{\sigma^{\text{fit}}} \tag{4.23}$$

where x^{fit} is the parameter value as measured in the toy fit, x^{gen} is the generated parameter value in the toy dataset (this is always equal to the parameter value as measured in the fit to data), and σ^{fit} is the parameter uncertainty in the toy fit. If the fit is unbiased in its estimation of x, this distribution should exhibit a Gaussian structure with a mean of zero and a width of unity, for sufficiently large numbers of generated toys. An increase (decrease) from unity in the width suggests an underestimation (overestimation) of the parameter uncertainty, while a shift in the mean away from zero suggests a bias in the central value. Gaussian behaviour is exhibited by all of the fit observables measured in this thesis, indicating that the fit procedure is free from any inherent bias.

The pull distributions for all of the physics observables in the analysis are presented in Figures 4.4 and 4.5 for the $B \to [hh]_D h$ and $B \to [hhhh]_D h$ fits, respectively. Gaussian behaviour is exhibited in all cases, with no significant deviations from the unit Gaussian observed. This indicates that the fit procedure is free from any inherent bias.

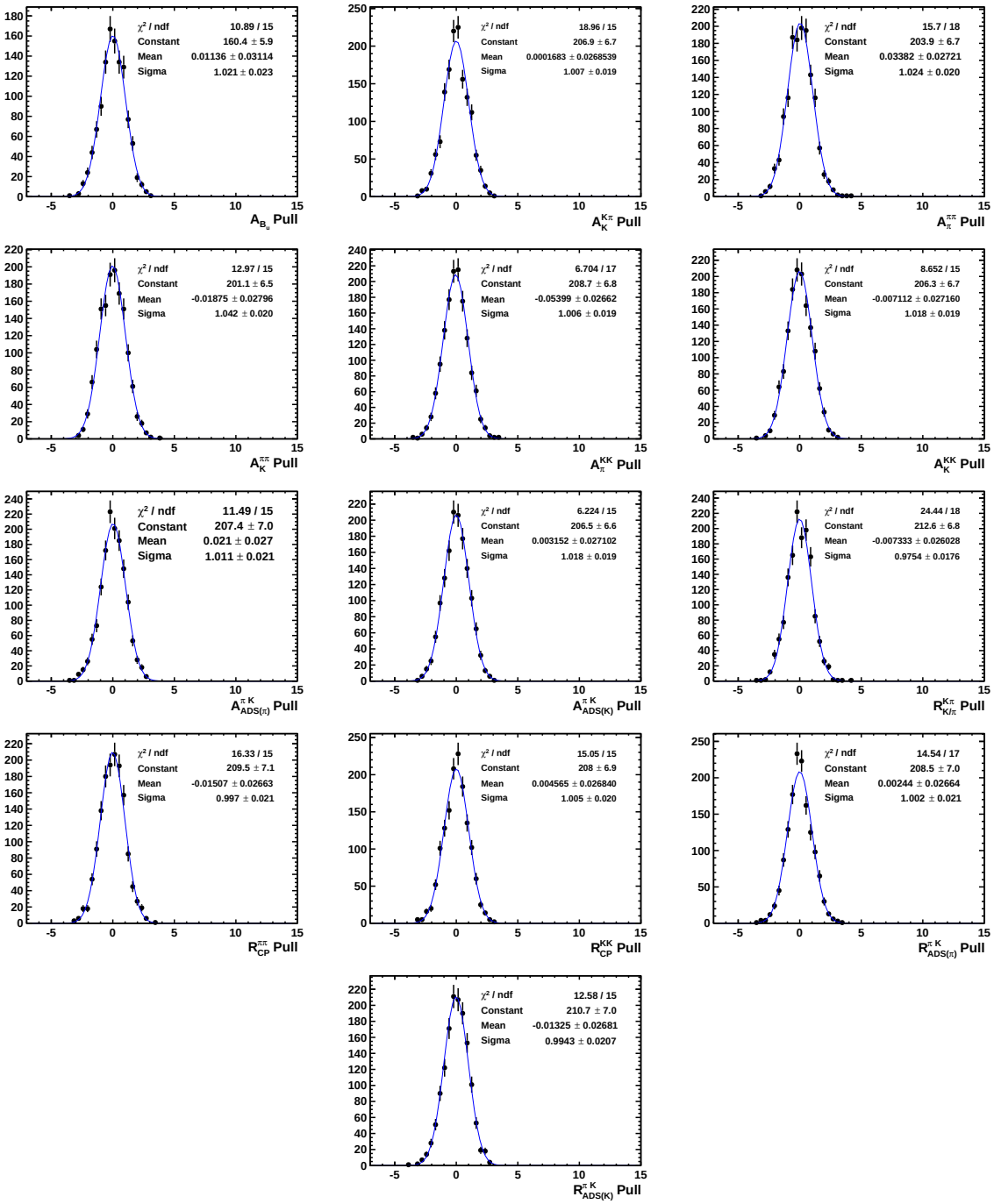

Figure 4.4.: Pull distributions for each of the observables in the $B \to [hh]_D h$ fit, from toy Monte Carlo fits. All pulls exhibit Gaussian behaviour with means close to zero and widths close to unity, indicating no underlying bias in the fit procedure.

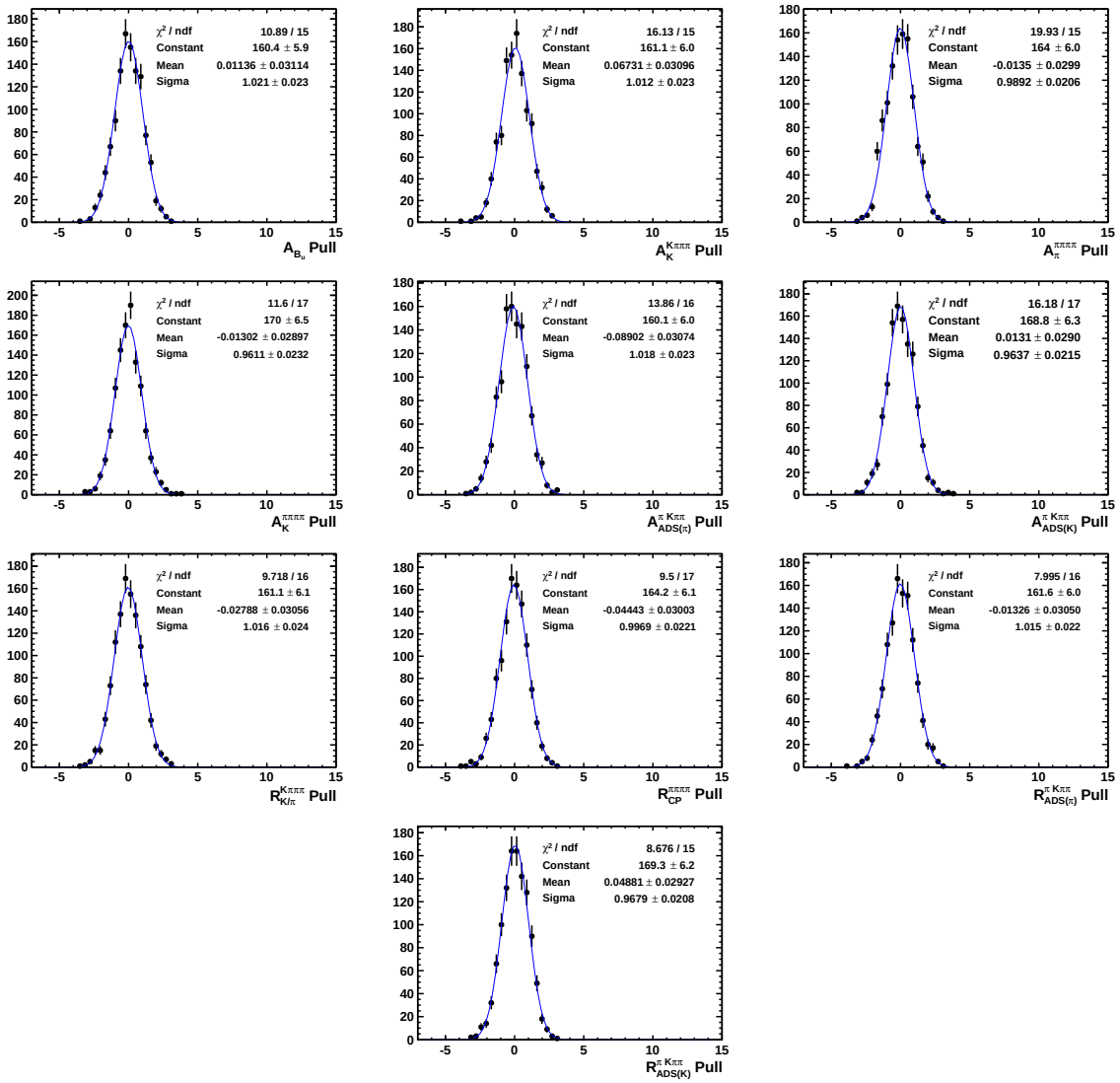

Figure 4.5.: Pull distributions for each of the observables in the $B \to [hhhh]_D h$ fit, from toy Monte Carlo fits. All pulls exhibit Gaussian behaviour with means close to zero and widths close to unity, indicating no underlying bias in the fit procedure.

4.1.5. Systematic uncertainties

As the analysis is constructed to measure ratios between final states with highly similar topologies, many systematic uncertainties cancel completely. Residual systematic uncertainties from several sources remain however, each of which can be traced to an assumption made within the fit by the use of a fixed parameter. In this Section, each source of systematic uncertainty is discussed in turn, and the total systematic uncertainty for each observable evaluated.

Using the fit to determine systematics

The fits to data are implemented with various fixed parameters[5], each of which carries an associated systematic uncertainty. What is of interest is how these fixed parameter uncertainties relate to the systematic uncertainty on each physics observable. To determine the systematic uncertainty arising from the use of fixed terms, the fit to data is repeated N times. For each run i of the fit, a specific fixed parameter p of the fit is randomly varied from its nominal fixed value. The variation δ_p introduced in p is in accordance with a Gaussian distribution of width σ_p, where σ_p is the prescribed uncertainty on the fixed term p. In instances where there are several correlated fixed terms employed in the mass fit, all of the terms are varied at the same time, taking into account their correlations.

By performing the fit N times[6], each time with a slightly different value of p, distributions in the physics observables O can be built up. The RMS of these distributions then provide a measure of the systematic uncertainties relating to using a fixed value of p in the fit. This procedure is carried out for various fixed parameters, and the sum in quadrature of the individual RMS values taken to represent the total systematic uncertainty on the observables. In this way, the uncertainties σ_p on the fixed parameters p are propagated through the fit, providing a direct measure of the corresponding systematic uncertainties on the observables O. A general assumption of this method is that the different sources of systematic uncertainty considered are uncorrelated.

[5] Fixed parameters are those that are given no freedom to float in the fit, such as various PDF shape parameters and background yields taken from the data-driven studies in Chapter 3.

[6] Only the subset of fits with fully accurate error matrices (`covQual` = 3), proper convergence (`MIGRAD` = 0 status) and small estimated distances to the minimum (`EDM` < 0.1) are retained. These correspond to the fits that would be deemed acceptable to an analyst, and typically comprise over 90% of the N systematic fits.

Kaon PID efficiency $\epsilon^{K}_{\rm PID}$

In the simultaneous invariant mass fit to $B^\pm \to DK^\pm$ and $B^\pm \to D\pi^\pm$ events, the relative rate of $B^\pm \to DK^\pm$ events in the **PASS** and **FAIL** samples is fixed using the value of $\epsilon^{K}_{\rm PID}$ determined in Section 3.3.3. The systematic uncertainty on this efficiency varies from 0.3% in the favoured $B \to [K\pi(\pi\pi)]_D h$ modes, to 1.5% in the lower statistics $B \to [\pi\pi(\pi\pi)]_D h$ modes. This uncertainty is driven by the size of the reference sample of signal tracks used in the calibration procedure, explaining why it increases for the lower statistics modes. A small contribution from the weighting procedure is also accounted for in the quoted uncertainty, but it comprises less that 10% of the total uncertainty. The $\epsilon^{K}_{\rm PID}$ values for each D mode are varied independently within their prescribed uncertainties in order to determine the systematic uncertainty from this source.

Shape parameters for misidentified $B^\pm \to D\pi^\pm$ events entering the PASS sample

The contribution from misidentified $B^\pm \to D\pi^\pm$ events in the **PASS** sample is modelled using a double Crystal Ball PDF. The tail parameters of this shape are fixed to the values found in a fit to simulated events, and varied within their MC fit uncertainties to determine the systematic uncertainty. The fixed values used in the fit, and their corresponding uncertainties, are listed in Table 3.20.

The rate of this contribution in the **PASS** sample is small, and is allowed to float freely in the fit; the yield found agrees fully with the expected contribution of $(1 - \epsilon^{\pi}_{\rm PID}) \times N_{\rm TOT}(B^\pm \to D\pi^\pm)$.

Shape parameters for misidentified $B^\pm \to DK^\pm$ events entering the FAIL sample

Misidentified $B^\pm \to DK^\pm$ events entering the **FAIL** sample are also modelled using a double Crystal Ball PDF, with each shape parameter taken from a fit to simulated events. The systematic arising from the fully fixed shape is determined by varying the fixed shape parameters within their MC fit errors. The fixed shape parameters and their corresponding uncertainties are listed in Table 3.20.

The rate of this contribution is fixed to be $(1 - \epsilon^K_{\rm PID})$ of the total $B^\pm \to DK^\pm$ yield, where the systematic uncertainty from this choice is determined by varying $\epsilon^K_{\rm PID}$ as described above.

Charmless yields and asymmetries

As detailed in Section 3.4.2, all charmless contributions in the fit are estimated using a data-driven approach, where the upper and lower D sidebands are studied. The yields and asymmetries measured in the sidebands are employed as fixed terms in the fit to data, and varied within their sideband fit uncertainties as a source of systematic uncertainty. The charmless asymmetries and their corresponding uncertainties are listed in Table 3.11, while the yields are listed in Table 3.12.

Charmless shape

The line shape describing charmless decays in the fit to data is taken from fits to simulated $B \to K^-\pi^+\pi^-(\pi^+\pi^-)$ events. A Gaussian PDF is used, with a mean equal to the main signal peak mean and a width taken from simulation. The width is scaled according to the difference in mass resolution between data and simulation, and varied within its MC fit uncertainty to determine the systematic uncertainty from this source.

Crossfeed from favoured $B \to [K\pi(\pi\pi)]_D h$ decays in the suppressed $B \to [\pi K(\pi\pi)]_D h$ samples

The contamination of the suppressed modes resulting from double misidentification of favoured decays is determined using a data-driven approach, as detailed in Section 3.4.3. The crossfeed rate is estimated to be small at around 1% of $R^{\pi K(\pi\pi)}_{\rm ADS(\pi)}$, and is fixed in the fit to data. The crossfeed rates used in the $B \to [hh]_D h$ and $B \to [hhhh]_D h$ fits, and their associated systematic uncertainties, can be found in Tables 3.17 and 3.17.

All crossfeed contributions are described using Gaussian PDFs in the fit to data, with widths taken from fits to simulated $B \to [K\pi(\pi\pi)]_D\pi$ events that have been doubly misidentified as suppressed $B \to [\pi K(\pi\pi)]_D\pi$. This width is varied within its MC fit uncertainty to determine the systematic uncertainty due to this choice.

Instrumentation asymmetries A_K^{det} and A_π^{det}

The kaon and pion detection asymmetries are fixed to the values $A_\pi^{\text{det}} = (0.0 \pm 0.3)\%$ and $A_K^{\text{det}} - A_\pi^{\text{det}} = (-1.1 \pm 0.3)\%$, respectively. Both values are varied within their associated uncertainties to determine the systematic uncertainty.

Efficiency corrections

The selection efficiencies for $B^\pm \to DK^\pm$ and $B^\pm \to D\pi^\pm$ decays are slightly different, owing to the different bachelor type. The efficiencies for selecting both types of decay are evaluated using samples of simulated favoured $B \to [K\pi(\pi\pi)]_D h$ events as detailed in Section 3.3.4, and the efficiency ratios $R_\epsilon^{K\pi(\pi\pi)}$ employed in the fits to correct the measured yield ratios where appropriate.

The values of $R_\epsilon^{K\pi(\pi\pi)}$ are varied within their associated uncertainties to determine the systematic uncertainty from this source, where the uncertainties on $R_\epsilon^{K\pi(\pi\pi)}$ arise from the use of finite samples of simulated events in determining efficiencies. The systematic uncertainty on $R_{K/\pi}^{K\pi(\pi\pi)}$ is dominated by this contribution, whereas the systematic uncertainties on $R_{CP}^{\pi\pi(\pi\pi)}$ and R_{CP}^{KK} from this source are minimal due to their construction as double ratios.

$\Lambda_b \to \Lambda_c h$ background in $B \to [KK]_D h$

The contribution from partially reconstructed $\Lambda_b \to [pK\pi]_{\Lambda_c} h$ decays in the $B \to [KK]_D h$ modes is described using a modified Gaussian PDF, with shape parameter values taken from a fit to simulated events. The fixed values used, and their corresponding systematic uncertainties, are listed in Table 3.19. All shape parameters are varied within their MC fit uncertainties to determine the systematic uncertainty.

$B_s^0 \to D^0 K\pi$ background shape

An important background to the suppressed $B \to [\pi K(\pi\pi)]_D K$ modes comes from partially reconstructed $B_s^0 \to D^0 K[\pi]$ decays, which are modelled in the fit to data using a `RooHORNSdini` PDF, as detailed in Section 3.4.1. The key parameters of the shape are its width σ and the upper kinematic endpoint b, the latter of which is determined from fits to simulated events. The width of this component is fixed to the width measured in data

for fully reconstructed $B \to [\pi K(\pi\pi)]_D K$ decays, as the MC fit width underestimates the true width in data.

The upper endpoint b is varied by ± 1 MeV/c^2 on its MC fit value of 5224 MeV/c^2, while the width σ is also varied by ± 1 MeV/c^2. The width variation introduced is conservative (relative to the width uncertainty measured in $B \to [\pi K(\pi\pi)]_D K$ data of 0.03 (0.04) MeV/c^2), due to the proximity of this background to the suppressed $B \to [\pi K(\pi\pi)]_D K$ signal peaks. This mode sits closer to the signal region than the other partially reconstructed backgrounds, because of the higher mass of B_s^0 mesons relative to the $B^\pm$ mesons.

Other partially reconstructed background shapes

All remaining partially reconstructed backgrounds are modelled using the `RooHORNSdini` and `RooHILLdini` PDFs, with shape parameter values taken from fits to simulated events as detailed in Section 3.4.1. In order to determine the systematic uncertainty from the fixing of low mass background parameters, the widths of each partially reconstructed background component are varied within their MC fit uncertainties. This excludes the mode $B^\pm \to (D^{*0} \to D^0[\pi^0])h^\pm$, which has a freely floating width in the fit to data in order to improve the residuals.

The kinematic endpoints, a and b, of the low mass contributions are calculable analytically from the particle masses in the decay chain (which are well known), and as such no systematic uncertainty arises from this source. For wider modes such as $B^\pm \to D^0\pi^\pm[\pi^0]$[7], where analytical widths are not precise, the endpoints are fixed to the values found in fits to simulated events and varied within their MC fit uncertainties to determine the systematic uncertainty.

All partially reconstructed modes (including the $B_s^0 \to D^0 K\pi$ contribution in the suppressed $B \to [\pi K(\pi\pi)]_D K$ modes) share a freely floating uniform shift in invariant mass, such that no systematic uncertainty is incurred. Only the upper regions of each partially reconstructed distribution enter the $5079 - 5899$ MeV/c^2 fit region, such that the lower peaks of any double-peaking structures are ignored. The relative peak height parameters for each shape are fixed to unity (equal peak height) with no systematic uncertainty, since only one of the peaks features in the invariant mass fit range considered.

[7] Such modes are wider due to the larger phase space available to the missing particle, which is produced via an intermediate ρ resonance.

The contributions from partially reconstructed $B^0 \to D^{*+}\pi^-$ decays have fixed yields in the fit, where branching fractions are used to fix the yields relative to the fully reconstructed $B^\pm \to D\pi^\pm$ signal yield for each D mode. Branching fraction uncertainties from [12] are used to determine the systematic uncertainty due to this assumption, by varying the $B^0 \to D^{*+}\pi^-$ yields in the fit accordingly.

Additional uncertainty in the low mass description arises from the use of semi-empirical shapes to model partially reconstructed and misidentified $B \to D\pi X$ decays entering the **PASS** sample. A 10% variation in each parameter of the semi-empirical shapes is introduced in order to determine the systemic uncertainty from this source. The choice of tight bachelor PID cut in the **PASS** sample ($\Delta LL_{K/\pi} > 12$) helps to minimise the systematic contribution from this source.

$\mathcal{CP}$-violation in partially reconstructed background

All partially reconstructed modes share a freely floating charge asymmetry in the fit to data. This assumption ignores the potential for some of the partially reconstructed modes to exhibit greater degrees of $\mathcal{CP}$-violation, in particular the $B^\pm \to D^{*0}h^\pm$ modes. To determine a systematic uncertainty for this choice, the fit to data is performed many times, each time introducing random degrees of $\mathcal{CP}$-violation for each of the low mass contributions independently. The degree of $\mathcal{CP}$-violation introduced depends upon the specific D final state, aligning with the amount of $\mathcal{CP}$-violation previously observed in the 1fb^{-1} analysis of $B^\pm \to Dh^\pm$ decays.

Total systematic uncertainties

In Tables 4.2 and 4.3, each contribution to the total systematic uncertainty for all observables in the $B \to [hh]_D h$ and $B \to [hhhh]_D h$ fits are listed. To help visualise which of the systematics are most important and which variables are systematically limited, all systematics have been quoted as a percentage of the measured statistical uncertainty for each observable; when the systematic uncertainty and statistical uncertainty are equal for instance, the systematic uncertainty is quoted as 100%.

It is clear that only two observables are systematically limited, namely $R_{K/\pi}^{K\pi(\pi\pi)}$ and A_{B_u}. In the former case, the efficiency correction $R_\epsilon^{K\pi(\pi\pi)}$ contributes most to the systematic uncertainty. The uncertainty on this correction arises from the use of finite

samples of simulated events, but is sufficiently large to cover other ignored systematic effects such as the reliability of the L0 trigger emulation in the simulation.

In the case of A_{B_u}, the systematic uncertainty is vastly dominated by the kaon and pion detection asymmetries, A_K^{det} and A_π^{det}. This is expected, since each raw asymmetry in the fit is corrected with A_{B_u}, and the detection asymmetries enter at several points in the definition of each $\mathcal{CP}$ asymmetry (Equations 4.14– 4.21). The value of A_{B_u} measured in this Chapter represents an effective value; a dedicated measurement is presented in Chapter 5.

Table 4.2.: Systematic uncertainties for each observable in the $B \to [hh]_D h$ fit. Each uncertainty is quoted as a percentage of the statistical uncertainty for a given observable. In the final row, the total systematic uncertainties for each observable are listed. These are given by the sum in quadrature of each systematic contribution.

(%)	$A_K^{K\pi}$	A_{B_u}	$R_{K/\pi}^{K\pi}$	A_K^{KK}	A_π^{KK}	R_{CP}^{KK}	$A_K^{\pi\pi}$	$A_\pi^{\pi\pi}$	$R_{CP}^{\pi\pi}$	$R_{ADS(\pi)}^{\pi K}$	$R_{ADS(K)}^{\pi K}$	$A_{ADS(\pi)}^{\pi K}$	$A_{ADS(K)}^{\pi K}$
Kaon PID cut	2.1	2.6	62.9	20.8	0.4	34.3	1.5	1.7	33.5	6.0	6.8	3.5	6.8
$B^\pm \to D\pi^\pm$ as $B^\pm \to DK^\pm$ shape	2.8	1.9	61.2	19.1	0.6	16.9	2.3	2.0	10.0	9.0	13.2	3.0	8.2
Charmless yields and asymmetries	3.9	3.8	32.7	18.0	0.1	25.5	8.2	3.8	31.1	8.3	23.1	3.4	11.3
Crossfeed	0.6	0.5	2.2	6.2	0.0	2.4	0.2	0.4	0.8	2.0	1.4	0.5	1.5
Instrumentation asymmetries	42.9	254.1	19.5	18.7	55.3	14.4	2.7	35.2	7.8	7.2	5.4	18.7	8.6
$B^\pm \to DK^\pm$ as $B^\pm \to D\pi^\pm$ shape	3.0	2.5	38.8	20.0	0.4	18.6	1.6	2.1	11.9	9.8	14.5	5.7	6.6
Charmless shape	1.1	1.3	15.3	13.4	5.1	8.7	1.2	1.1	6.8	4.6	5.1	1.9	4.5
$\Lambda_b \to \Lambda_c h$ shape	3.0	1.9	37.0	10.2	3.1	62.8	2.0	1.7	9.6	10.8	10.9	5.2	5.8
Efficiency correction	8.7	4.5	239.4	19.1	0.1	14.4	1.3	2.2	7.8	8.5	7.5	4.3	9.0
$B_s^0 \to D^0 K\pi$ shape	1.8	2.8	27.9	21.5	9.9	17.2	1.3	1.6	9.5	6.8	11.5	2.7	8.4
Low mass background	10.4	4.2	31.4	21.8	0.1	36.1	4.8	4.3	18.6	20.3	37.2	17.6	1.0
Signal peak tails	4.0	2.4	34.2	17.7	8.2	18.3	2.4	2.4	11.0	7.6	12.1	5.6	7.1
CPV in low mass background	3.3	6.0	32.4	19.7	2.1	17.2	4.2	2.0	10.1	8.0	8.2	3.6	11.1
Total	45.8	254.3	271.2	64.8	57.1	95.5	11.8	36.1	57.0	33.6	54.1	28.7	27.2

Table 4.3.: Systematic uncertainties for each observable in the $B \to [hhhh]_D h$ fit. Each uncertainty is quoted as a percentage of the statistical uncertainty for a given observable. In the final row the, total systematic uncertainties for each observable are listed. These are given by the sum in quadrature of each contributing source of systematic uncertainty.

(%)	$R_{K/\pi}^{K\pi\pi\pi}$	$R_{CP}^{\pi\pi\pi\pi}$	$R_{ADS(K)}^{\pi K\pi\pi}$	$R_{ADS(\pi)}^{\pi K\pi\pi}$	A_{B_u}	$A_K^{K\pi\pi\pi}$	$A_{ADS(K)}^{\pi K\pi\pi}$	$A_{ADS(\pi)}^{\pi K\pi\pi}$	$A_K^{\pi\pi\pi\pi}$	$A_\pi^{\pi\pi\pi\pi}$
Kaon PID cut	37.1	1.4	0.3	3.5	0.2	0.3	0.8	2.6	0.5	0.2
$B^\pm \to D\pi^\pm$ as $B^\pm \to DK^\pm$ shape	39.4	4.6	13.4	9.3	0.4	1.1	13.9	2.0	1.7	0.3
Charmless yields and asymmetries	1.1	19.7	22.3	15.4	0.1	0.0	13.7	1.5	21.7	6.8
Crossfeed	0.1	0.2	0.6	13.4	0.0	0.0	0.3	0.4	0.0	0.0
Instrumentation asymmetries	1.5	0.3	0.3	0.1	156.3	25.8	2.9	14.1	1.8	37.9
$B^\pm \to DK^\pm$ as $B^\pm \to D\pi^\pm$ shape	34.7	1.2	1.9	6.6	0.5	1.3	2.8	3.0	0.5	1.2
Charmless shape	0.3	6.1	0.2	0.1	0.0	0.0	0.1	0.2	0.8	0.0
Efficiency correction	190.9	5.0	0.6	11.9	0.1	0.3	1.7	0.7	0.2	0.2
$B_s^0 \to D^0 K\pi$ shape	21.3	1.5	13.6	17.7	8.8	1.1	2.2	3.8	9.0	11.6
Low mass background	33.2	2.7	14.1	11.2	0.2	0.4	6.7	0.6	1.6	0.1
Signal peak tails	39.5	16.0	3.0	1.3	0.5	0.5	3.1	0.4	3.0	2.8
CPV in low mass background	20.0	10.8	6.7	5.6	3.7	1.7	6.1	2.3	5.9	2.1
Total	210.0	29.3	33.5	34.2	156.6	25.9	22.3	15.5	24.6	40.4

4.2. Results

4.2.1. $B \to [hh]_D h$ results

Invariant mass fits to $m(Dh)$ for each of the $D \to hh$ modes are shown in Figures 4.6-4.9. The plots follow the layout detailed in Figure 4.2, with the **PASS** sample (events reconstructed as $B^\pm \to DK^\pm$) shown in the top row and the **FAIL** sample (events reconstructed as $B^\pm \to D\pi^\pm$) shown in the bottom row. B^- candidates are plotted on the left and B^+ on the right in all cases. Events reconstructed as $B^\pm \to DK^\pm (B^\pm \to D\pi^\pm)$ are indicated with solid red (green) lines, while partially reconstructed background events are plotted as a grey filled region at low invariant mass. Specific physics backgrounds in each mode are shown by dashed pink lines, and are individually described in the captions.

The final results for each of the $B \to [hh]_D h$ $\mathcal{CP}$ observables, including systematic uncertainties, are:

Decay mode	Yield
$B^\pm \to [K^\pm\pi^\mp]_D \pi^\pm$	378,120 $\pm$ 652
$B^\pm \to [K^\pm\pi^\mp]_D K^\pm$	29,409 $\pm$ 233
$B^\pm \to [K^\pm K^\mp]_D \pi^\pm$	50,151 $\pm$ 265
$B^\pm \to [K^\pm K^\mp]_D K^\pm$	3818 $\pm$ 92
$B^\pm \to [\pi^\pm\pi^\mp]_D \pi^\pm$	14,682 $\pm$ 125
$B^\pm \to [\pi^\pm\pi^\mp]_D K^\pm$	1162 $\pm$ 48
$B^\pm \to [\pi^\pm K^\mp]_D \pi^\pm$	1361 $\pm$ 44
$B^\pm \to [\pi^\pm K^\mp]_D K^\pm$	551 $\pm$ 34

Table 4.4.: Signal yields measured in the $B \to [hh]_D h$ fit. Values are quoted for $B^\pm \to DK^\pm$ and $B^\pm \to D\pi^\pm$ in each of the four D final states considered. The uncertainties quoted are statistical only.

$R^{K\pi}_{K/\pi}$	=	0.0778	$\pm$ 0.0006 (stat.)	$\pm$ 0.0016 (syst.)
R^{KK}_{CP}	=	0.979	$\pm$ 0.022 (stat.)	$\pm$ 0.021 (syst.)
$R^{\pi\pi}_{\mathrm{CP}}$	=	1.018	$\pm$ 0.040 (stat.)	$\pm$ 0.023 (syst.)
A_{B_u}	=	$-$ 0.0033	$\pm$ 0.0017 (stat.)	$\pm$ 0.0042 (syst.)
$A^{K\pi}_{K}$	=	$-$ 0.0169	$\pm$ 0.0072 (stat.)	$\pm$ 0.0033 (syst.)
A^{KK}_{π}	=	$-$ 0.0160	$\pm$ 0.0050 (stat.)	$\pm$ 0.0028 (syst.)
A^{KK}_{K}	=	0.0855	$\pm$ 0.0201 (stat.)	$\pm$ 0.0130 (syst.)
$A^{\pi\pi}_{\pi}$	=	0.00291	$\pm$ 0.00860 (stat.)	$\pm$ 0.00311 (syst.)
$A^{\pi\pi}_{K}$	=	0.123	$\pm$ 0.037 (stat.)	$\pm$ 0.004 (syst.)
$R^{\pi K}_{ADS(K)}$	=	0.0187	$\pm$ 0.0011 (stat.)	$\pm$ 0.0006 (syst.)
$A^{\pi K}_{ADS(K)}$	=	$-$ 0.4044	$\pm$ 0.0563 (stat.)	$\pm$ 0.0153 (syst.)
$R^{\pi K}_{ADS(\pi)}$	=	0.00360	$\pm$ 0.00012 (stat.)	$\pm$ 0.00004 (syst.)
$A^{\pi K}_{ADS(\pi)}$	=	0.0971	$\pm$ 0.0314 (stat.)	$\pm$ 0.0090 (syst.)

where each of these values are floating parameters of the fit. The corresponding yields for each signal mode are listed in Table 4.4, which are derived from the observables using the formalism outlined in Section 4.1.2. These results represent the most precise measurements of $\mathcal{CP}$ violating observables in $B \to [hh]_D h$ decays to date, and agree with the published 1fb^{-1} results. A combination measurement of A_{B_u} using both the $B \to [hh]_D h$ and $B \to [hhhh]_D h$ modes is presented in Chapter 5.

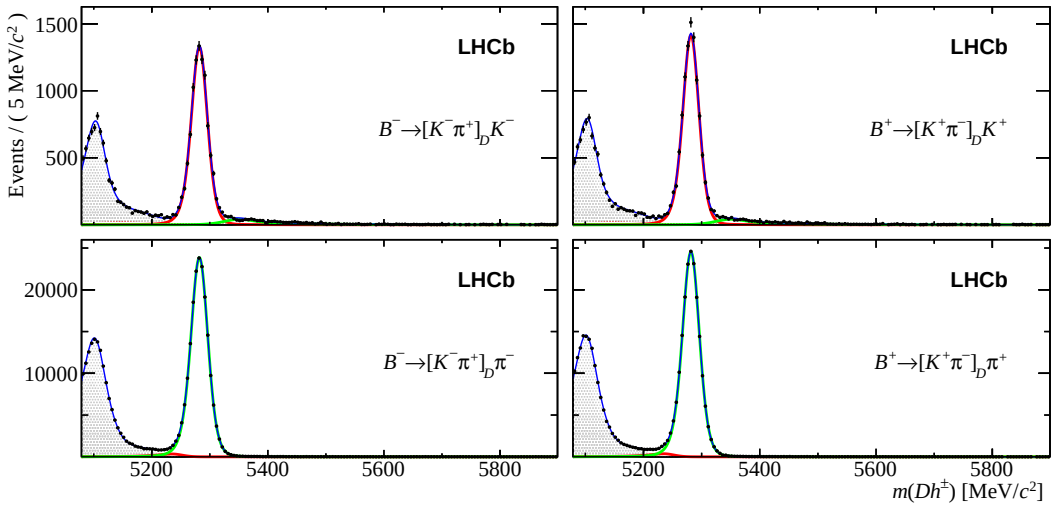

Figure 4.6.: Invariant mass fit to favoured $B^\pm \to [K^\pm\pi^\mp]_D h^\pm$ events in 3 fb^{-1} of data. $B^\pm \to D\pi^\pm$ events are shown in the bottom row of plots, and $B^\pm \to DK^\pm$ events in the top row. B^- events are displayed on the left, and B^+ events on the right. The red (green) solid lines indicate $B^\pm \to DK^\pm$ ($B^\pm \to D\pi^\pm$) signal events, and the shaded grey region at low invariant mass shows the contribution from partially reconstructed decays. The combinatoric background contribution is also plotted, but is not visible on the linear scale. The total PDF is plotted as a solid blue line.

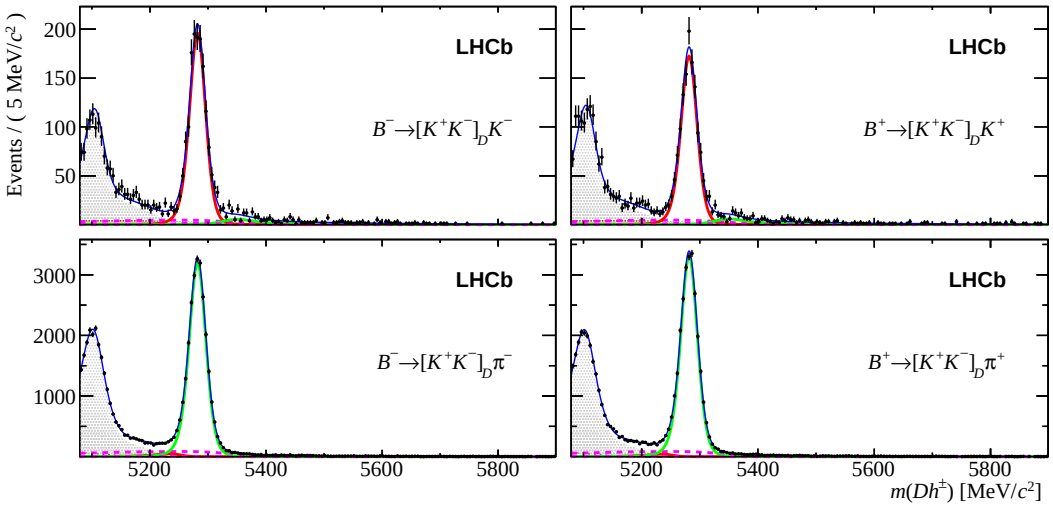

Figure 4.7.: Invariant mass fit to $B^\pm \to [K^\pm K^\mp]_D h^\pm$ events in 3 fb^{-1} of data. $B^\pm \to D\pi^\pm$ events are shown in the bottom row of plots, and $B^\pm \to DK^\pm$ events in the top row. B^- events are displayed on the left, and B^+ events on the right. The red (green) solid lines indicate $B^\pm \to DK^\pm$ ($B^\pm \to D\pi^\pm$) signal events, and the shaded grey region at low invariant mass shows the contribution from partially reconstructed decays. The combinatoric background contribution is also plotted, but is not visible on the linear scale. The dashed pink line shows the contribution from partially reconstructed $\Lambda_b \to \Lambda_c h$ decays, which affects only the $D \to KK$ modes in the analysis. The total PDF is plotted as a solid blue line.

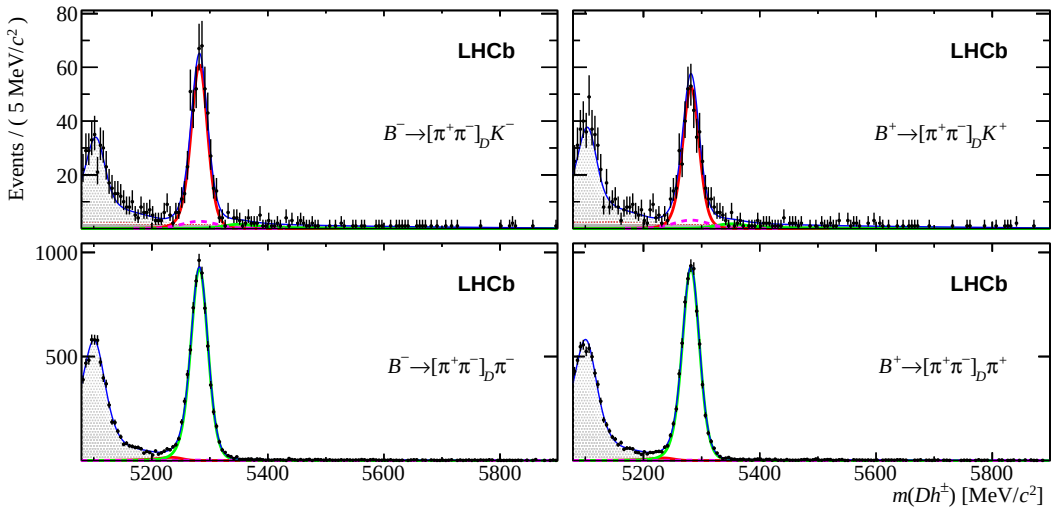

Figure 4.8.: Invariant mass fit to $B^\pm \to [\pi^\pm\pi^\mp]_D\, h^\pm$ events in 3 fb^{-1} of data. $B^\pm \to D\pi^\pm$ events are shown in the bottom row of plots, and $B^\pm \to DK^\pm$ events in the top row. B^- events are displayed on the left, and B^+ events on the right. The red (green) solid lines indicate $B^\pm \to DK^\pm$ ($B^\pm \to D\pi^\pm$) signal events, and the shaded grey region at low invariant mass shows the contribution from partially reconstructed decays. The combinatoric background contribution is also plotted, but is not visible on the linear scale. The dashed pink line in the top row of plots shows the largest charmless contribution in the $B \to [hh]_D h$ data, from $B^\pm \to K^\pm\pi^\mp\pi^\pm$ decays. Charmless modes are also present elsewhere in the data fit as described in Section 3.4.2, but are not visible on the linear scale. The total PDF is plotted as a solid blue line.

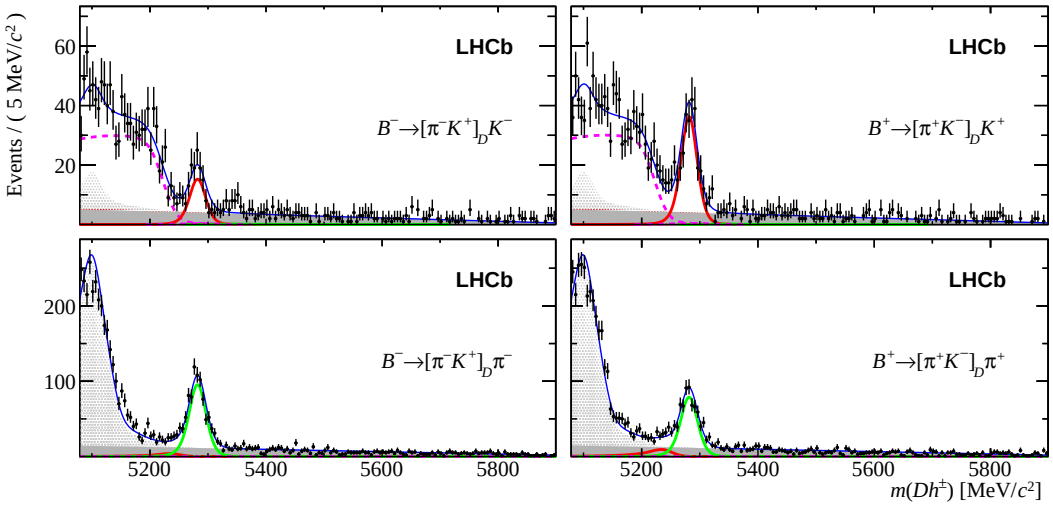

Figure 4.9.: Invariant mass fit to suppressed $B^\pm \to [\pi^\pm K^\mp]_D\, h^\pm$ events in 3 fb^{-1} of data. $B^\pm \to D\pi^\pm$ events are shown in the bottom row of plots, and $B^\pm \to DK^\pm$ events in the top row. B^- events are displayed on the left, and B^+ events on the right. The red (green) solid lines indicate $B^\pm \to DK^\pm$ ($B^\pm \to D\pi^\pm$) signal events, and the shaded grey region at low invariant mass shows the contribution from partially reconstructed decays. The contribution from combinatoric events is shown as a filled grey region across the entire fit range; this component is present in each fit, but is most visible in the low statistics suppressed modes. The contribution from partially reconstructed $B_s^0 \to D^0 K\pi$ decays in the PASS sample is shown by a dotted pink line below the main signal peak. This background sits closer to the signal region than the other partially reconstructed backgrounds, due to the larger mass of the B_s^0 meson. The total PDF is plotted as a solid blue line.

4.2.2. $B \to [hhhh]_D h$ results

The invariant mass fits to $m(Dh)$ for each $D \to hhhh$ mode are shown in Figures 4.10-4.12; all plots adopt the same convention as the $B \to [hh]_D h$ fits previously shown. Signal yields for each of the $B \to [hhhh]_D h$ modes are listed in Table 4.5. The final results for the $B \to [hhhh]_D h$ $\mathcal{CP}$ observables are:

$R_{K/\pi}^{K\pi\pi\pi}$	=	0.0793	$\pm$ 0.0010 (stat.)	$\pm$ 0.0020 (syst.)
A_{B_u}	=	$-$ 0.0054	$\pm$ 0.0027 (stat.)	$\pm$ 0.0039 (syst.)
$A_K^{K\pi\pi\pi}$	=	0.0010	$\pm$ 0.0119 (stat.)	$\pm$ 0.0030 (syst.)
$R_{CP}^{\pi\pi\pi\pi}$	=	0.975	$\pm$ 0.037 (stat.)	$\pm$ 0.010 (syst.)
$A_\pi^{\pi\pi\pi\pi}$	=	$-$ 0.00552	$\pm$ 0.00791 (stat.)	$\pm$ 0.0032 (syst.)
$A_K^{\pi\pi\pi\pi}$	=	0.1004	$\pm$ 0.0336 (stat.)	$\pm$ 0.0079 (syst.)
$R_{ADS(\pi)}^{\pi K\pi\pi}$	=	0.00377	$\pm$ 0.00018 (stat.)	$\pm$ 0.00005 (syst.)
$R_{ADS(K)}^{\pi K\pi\pi}$	=	0.01399	$\pm$ 0.00149 (stat.)	$\pm$ 0.00041 (syst.)
$A_{ADS(\pi)}^{\pi K\pi\pi}$	=	0.0205	$\pm$ 0.0481 (stat.)	$\pm$ 0.0068 (syst.)
$A_{ADS(K)}^{\pi K\pi\pi}$	=	$-$ 0.316	$\pm$ 0.102 (stat.)	$\pm$ 0.015 (syst.)

which represent the most accurate determination of $\mathcal{CP}$ violating observables in such decays to date. The value of A_{B_u} is measured independently in the $B \to [hh]_D h$ and $B \to [hhhh]_D h$ fits; a dedicated measurement of A_{B_u} as a function of $B^\pm$ kinematics is presented in Chapter 5, alongside a complementary measurement of the $\mathcal{CP}$ asymmetry in $B^\pm \to J/\psi K^\pm$ decays. Although the $B^\pm \to [hh(hh)]_D h^\pm$ modes studied in this thesis cannot alone resolve the trigonometric ambiguities in γ, they are highly powerful when combined with other LHCb measurements. The results presented in this thesis will be used in combination with other LHCb measurements to perform a dedicated measurement of the CKM phase γ in 2015.

4.2.3. Correlation matrices

The statistical and systematic correlation matrices for the observables in the $2h$ and $4h$ fits are provided in Tables 4.6 - 4.9.

Decay mode	Yield
$B^\pm \to [K^\pm\pi^\mp\pi^\pm\pi^\mp]_D\pi^\pm$	$142,910 \pm 389$
$B^\pm \to [K^\pm\pi^\mp\pi^\pm\pi^\mp]_D K^\pm$	$11,334 \pm 143$
$B^\pm \to [\pi^\pm K^\mp\pi^\pm\pi^\mp]_D\pi^\pm$	539 ± 26
$B^\pm \to [\pi^\pm K^\mp\pi^\pm\pi^\mp]_D K^\pm$	159 ± 17
$B^\pm \to [\pi^\pm\pi^\mp\pi^\pm\pi^\mp]_D\pi^\pm$	$19,356 \pm 146$
$B^\pm \to [\pi^\pm\pi^\mp\pi^\pm\pi^\mp]_D K^\pm$	1497 ± 60

Table 4.5.: Measured yields in the $B \to [hhhh]_D h$ fit. Values are quoted for $B^\pm \to DK^\pm$ and $B^\pm \to D\pi^\pm$ in each of the three D final states considered. The uncertainties quoted are statistical only.

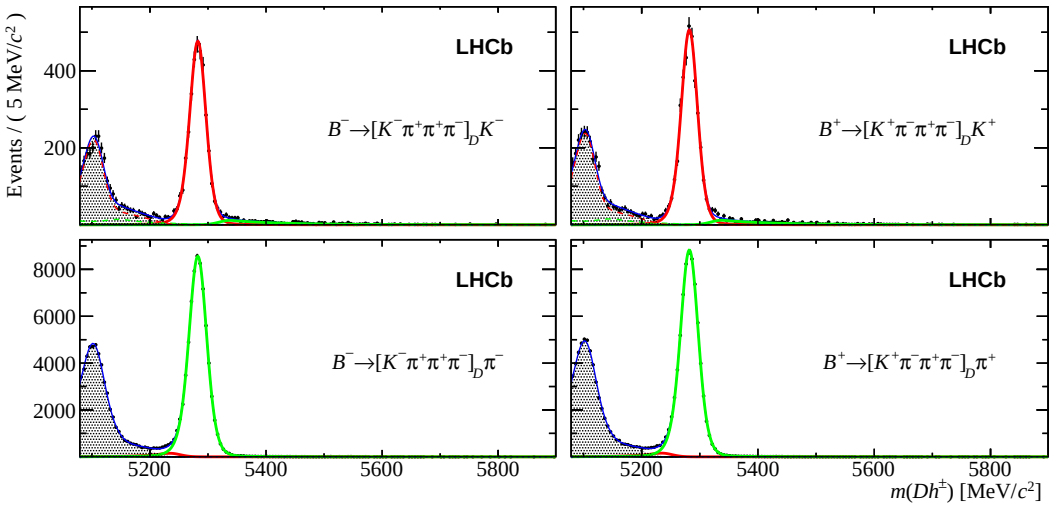

Figure 4.10.: Invariant mass fit to favoured $B^\pm \to [K^\pm\pi^\mp\pi^\pm\pi^\mp]_D\, h^\pm$ events in 3 fb^{-1} of data. $B^\pm \to D\pi^\pm$ events are shown in the bottom row of plots, and $B^\pm \to DK^\pm$ events in the top row. B^- events are displayed on the left, and B^+ events on the right. The red (green) solid lines indicate $B^\pm \to DK^\pm$ ($B^\pm \to D\pi^\pm$) signal events, and the shaded grey region at low invariant mass shows the contribution from partially reconstructed decays. The combinatoric background contribution is also plotted, but is not visible on the linear scale. The total PDF is plotted as a solid blue line.

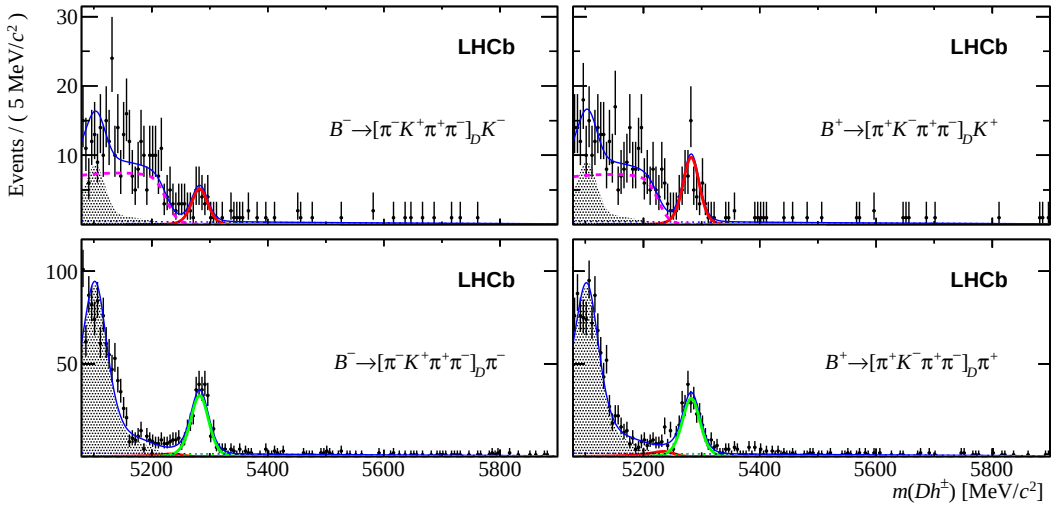

Figure 4.11.: Invariant mass fit to suppressed $B^\pm \to [\pi^\pm K^\mp \pi^\pm \pi^\mp]_D h^\pm$ events in 3 fb^{-1} of data. $B^\pm \to D\pi^\pm$ events are shown in the bottom row of plots, and $B^\pm \to DK^\pm$ events in the top row. B^- events are displayed on the left, and B^+ events on the right. The red (green) solid lines indicate $B^\pm \to DK^\pm$ ($B^\pm \to D\pi^\pm$) signal events, and the shaded grey region at low invariant mass shows the contribution from partially reconstructed decays. The contribution from partially reconstructed $B_s^0 \to D^0 K\pi$ decays in the PASS sample is shown by a dotted pink line below the main signal peak. This background sits closer to the signal region than the other partially reconstructed backgrounds, due to the larger mass of the B_s^0 meson. The total PDF is plotted as a solid blue line.

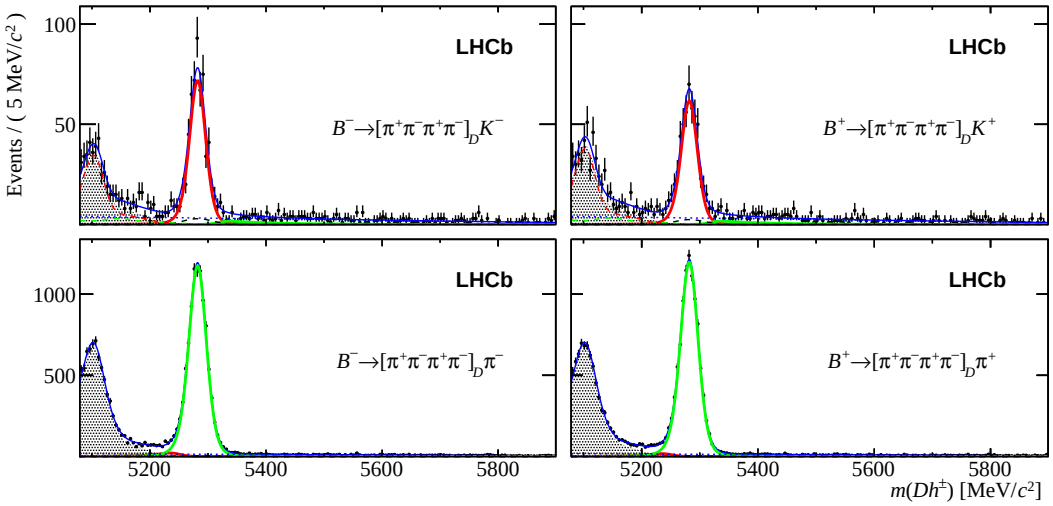

Figure 4.12.: Invariant mass fit to $B^\pm \to [\pi^\pm\pi^\mp\pi^\pm\pi^\mp]_D\, h^\pm$ events in 3 fb^{-1} of data. $B^\pm \to D\pi^\pm$ events are shown in the bottom row of plots, and $B^\pm \to DK^\pm$ events in the top row. B^- events are displayed on the left, and B^+ events on the right. The red (green) solid lines indicate $B^\pm \to DK^\pm$ ($B^\pm \to D\pi^\pm$) signal events, and the shaded grey region at low invariant mass shows the contribution from partially reconstructed decays. The combinatoric background contribution is also plotted, but is not visible on the linear scale. The dashed line in the top row of plots shows the largest charmless contribution in the $B \to [hhhh]_D h$ data, from $B^\pm \to K^\pm\pi^\mp\pi^\pm\pi^\mp\pi^\pm$ decays. Charmless modes are also present elsewhere in the data fit as described in Section 3.4.2, but are not visible on the linear scale. The total PDF is plotted as a solid blue line.

Table 4.6.: Statistical correlation matrix from MINUIT for the thirteen physics observables in the 2-body fit.

	$R(DK/D\pi)^{K\pi}$	A_{Prod}	$A_K^{K\pi}$	$R_{CP}^{\pi\pi}$	R_{CP}^{KK}	$A_\pi^{\pi\pi}$	$A_K^{\pi\pi}$	A_π^{KK}	A_K^{KK}	$R_{ADS(K)}^{\pi K}$	$R_{ADS(\pi)}^{\pi K}$	$A_{ADS(K)}^{\pi K}$	$A_{ADS(\pi)}^{\pi K}$
A_{Prod}	1.0	-0.0279	-0.0522	-0.0827	-0.0483	-0.3325	-0.1921	-0.2765	0.0008	0.0004	-0.0005	0.0001	0.0024
$A_{ADS(K)}^{\pi K}$	-0.0279	1.0	-0.0474	0.0023	0.0012	0.0093	0.0053	0.0078	0.1024	-0.0032	0.0006	0.0009	0.0003
$A_{ADS(\pi)}^{\pi K}$	-0.0522	-0.0474	1.0	0.0043	0.0025	0.0174	0.01	0.0144	0.0155	-0.0431	0.0002	0.0001	0.0
A_K^{KK}	-0.0827	0.0023	0.0043	1.0	0.0043	-0.0069	0.0158	0.0243	-0.0003	0.0001	-0.0144	-0.0001	-0.001
$A_K^{\pi\pi}$	-0.0483	0.0012	0.0025	0.0043	1.0	0.016	-0.0359	0.0143	-0.001	-0.0	-0.0002	-0.0382	-0.0021
A_π^{KK}	-0.3325	0.0093	0.0174	-0.0069	0.016	1.0	0.0639	0.0917	-0.0002	-0.0002	-0.0013	0.0	-0.0011
$A_\pi^{\pi\pi}$	-0.1921	0.0053	0.01	0.0158	-0.0359	0.0639	1.0	0.053	-0.0001	-0.0001	0.0001	-0.0029	-0.0005
$A_K^{K\pi}$	-0.2765	0.0078	0.0144	0.0243	0.0143	0.0917	0.053	1.0	-0.0001	-0.0001	0.0002	0.0	-0.0004
$R_{ADS(K)}^{\pi K}$	0.0008	0.1024	0.0155	-0.0003	-0.001	-0.0002	-0.0001	-0.0001	1.0	-0.0219	0.0399	0.0245	-0.1136
$R_{ADS(\pi)}^{\pi K}$	0.0004	-0.0032	-0.0431	0.0001	-0.0	-0.0002	-0.0001	-0.0001	-0.0219	1.0	-0.0055	-0.0025	0.0114
R_{CP}^{KK}	-0.0005	0.0006	0.0002	-0.0144	-0.0002	-0.0013	0.0001	0.0002	0.0399	-0.0055	1.0	0.0597	-0.3165
$R_{CP}^{\pi\pi}$	0.0001	0.0009	0.0001	-0.0001	-0.0382	0.0	-0.0029	0.0	0.0245	-0.0025	0.0597	1.0	-0.1756
$R(DK/D\pi)^{K\pi}$	0.0024	0.0003	0.0	-0.001	-0.0021	-0.0011	-0.0005	-0.0004	-0.1136	0.0114	-0.3165	-0.1756	1.0

Table 4.7.: Statistical correlation matrix from MINUIT for the ten physics observables in the 4-body fit.

	$R^{K\pi\pi\pi}_{K/\pi}$	A_{B_u}	$A^{K\pi\pi\pi}_{K}$	$R^{\pi\pi\pi\pi}_{CP}$	$A^{\pi\pi\pi\pi}_{\pi}$	$A^{\pi\pi\pi\pi}_{K}$	$R^{\pi K\pi\pi}_{ADS(K)}$	$R^{\pi K\pi\pi}_{ADS(\pi)}$	$A^{\pi K\pi\pi}_{ADS(K)}$	$A^{\pi K\pi\pi}_{ADS(\pi)}$
$R^{K\pi\pi\pi}_{K/\pi}$	1.0	0.0012	0.0012	-0.308	-0.0004	-0.0023	-0.099	0.0116	0.0028	0.0005
A_{B_u}	0.0012	1.0	-0.2836	0.0004	-0.3413	-0.084	0.0005	0.0004	-0.0256	-0.0593
$A^{K\pi\pi\pi}_{K}$	0.0012	-0.2836	1.0	-0.0009	0.0968	0.0239	-0.0005	-0.0001	0.0064	0.0166
$R^{\pi\pi\pi\pi}_{CP}$	-0.308	0.0004	-0.0009	1.0	-0.0041	-0.0182	0.0409	-0.0041	0.002	-0.0001
$A^{\pi\pi\pi\pi}_{\pi}$	-0.0004	-0.3413	0.0968	-0.0041	1.0	-0.0197	-0.0001	-0.0001	0.0088	0.0202
$A^{\pi\pi\pi\pi}_{K}$	-0.0023	-0.084	0.0239	-0.0182	-0.0197	1.0	-0.0011	0.0	0.0018	0.005
$R^{\pi K\pi\pi}_{ADS(K)}$	-0.099	0.0005	-0.0005	0.0409	-0.0001	-0.0011	1.0	-0.0464	0.0821	0.0135
$R^{\pi K\pi\pi}_{ADS(\pi)}$	0.0116	0.0004	-0.0001	-0.0041	-0.0001	0.0	-0.0464	1.0	-0.004	-0.0218
$A^{\pi K\pi\pi}_{ADS(K)}$	0.0028	-0.0256	0.0064	0.002	0.0088	0.0018	0.0821	-0.004	1.0	-0.0618
$A^{\pi K\pi\pi}_{ADS(\pi)}$	0.0005	-0.0593	0.0166	-0.0001	0.0202	0.005	0.0135	-0.0218	-0.0618	1.0

Table 4.8.: Systematic correlation matrix for the thirteen physics observables in the 2-body fit.

	A_K^{KK}	$A_K^{\pi\pi}$	A_π^{KK}	$A_\pi^{\pi\pi}$	$A_K^{K\pi}$	A_{B_u}	$R_{K/\pi}^{K\pi}$	$R_{CP}^{\pi\pi}$	R_{CP}^{KK}	$A_{ADS(K)}$	$A_{ADS(\pi)}$	$R_{ADS(K)}$	$R_{ADS(\pi)}$
A_K^{KK}	1.00	-0.02	-0.80	0.09	0.09	-0.10	0.07	0.03	-0.28	-0.06	-0.03	-0.10	-0.06
$A_K^{\pi\pi}$	-0.02	1.00	0.19	-0.42	-0.01	-0.09	-0.07	-0.22	0.11	0.27	0.31	0.35	-0.28
A_π^{KK}	-0.80	0.19	1.00	0.11	0.09	-0.25	-0.13	-0.16	0.20	0.30	0.22	0.37	-0.21
$A_\pi^{\pi\pi}$	0.09	-0.42	0.11	1.00	0.30	-0.39	-0.09	-0.08	-0.03	0.04	-0.06	-0.03	0.06
$A_K^{K\pi}$	0.09	-0.01	0.09	0.30	1.00	-0.31	-0.02	-0.01	-0.02	0.09	-0.55	-0.11	0.05
A_{B_u}	-0.10	-0.09	-0.25	-0.39	-0.31	1.00	0.00	0.05	-0.01	-0.12	-0.05	-0.02	0.10
$R_{K/\pi}^{K\pi}$	0.07	-0.07	-0.13	-0.09	-0.02	0.00	1.00	0.21	-0.11	-0.14	-0.04	-0.22	0.02
$R_{CP}^{\pi\pi}$	0.03	-0.22	-0.16	-0.08	-0.01	0.05	0.21	1.00	0.17	-0.04	-0.01	-0.14	0.19
R_{CP}^{KK}	-0.28	0.11	0.20	-0.03	-0.02	-0.01	-0.11	0.17	1.00	0.23	0.12	0.33	0.10
$A_{ADS(K)}$	-0.06	0.27	0.30	0.04	0.09	-0.12	-0.14	-0.04	0.23	1.00	0.36	0.78	-0.43
$A_{ADS(\pi)}$	-0.03	0.31	0.22	-0.06	-0.55	-0.05	-0.04	-0.01	0.12	0.36	1.00	0.59	-0.47
$R_{ADS(K)}$	-0.10	0.35	0.37	-0.03	-0.11	-0.02	-0.22	-0.14	0.33	0.78	0.59	1.00	-0.57
$R_{ADS(\pi)}$	-0.06	-0.28	-0.21	0.06	0.05	0.10	0.02	0.19	0.10	-0.43	-0.47	-0.57	1.00

Table 4.9.: Systematic correlation matrix for the ten physics observables in the 4-body fit.

	$R^{K\pi\pi\pi}_{K/\pi}$	$R^{\pi\pi\pi\pi}_{CP}$	$R^{\pi K\pi\pi}_{ADS(K)}$	$R^{\pi K\pi\pi}_{ADS(\pi)}$	A_{B_u}	$A^{K\pi\pi\pi}_{K}$	$A^{\pi K\pi\pi}_{ADS(K)}$	$A^{\pi K\pi\pi}_{ADS(\pi)}$	$A^{\pi\pi\pi\pi}_{DK}$	$A^{\pi\pi\pi\pi}_{D\pi}$
$R^{K\pi\pi\pi}_{K/\pi}$	1.00	0.11	-0.04	0.13	-0.01	0.00	-0.13	0.17	-0.14	0.08
$R^{\pi\pi\pi\pi}_{CP}$	0.11	1.00	0.04	-0.06	0.01	0.02	-0.04	-0.04	0.07	-0.07
$R^{\pi K\pi\pi}_{ADS(K)}$	-0.04	0.04	1.00	0.14	-0.00	0.02	0.87	0.10	0.03	0.01
$R^{\pi K\pi\pi}_{ADS(\pi)}$	0.13	-0.06	0.14	1.00	-0.04	-0.02	0.05	0.46	-0.35	0.24
A_{B_u}	-0.01	0.01	-0.00	-0.04	1.00	-0.36	-0.05	-0.42	-0.03	-0.64
$A^{K\pi\pi\pi}_{K}$	0.00	0.02	0.02	-0.02	-0.36	1.00	0.02	0.05	0.09	0.32
$A^{\pi K\pi\pi}_{ADS(K)}$	-0.13	-0.04	0.87	0.05	-0.05	0.02	1.00	-0.09	-0.04	0.02
$A^{\pi K\pi\pi}_{ADS(\pi)}$	0.17	-0.04	0.10	0.46	-0.42	0.05	-0.09	1.00	-0.34	0.43
$A^{\pi\pi\pi\pi}_{DK}$	-0.14	0.07	0.03	-0.35	-0.03	0.09	-0.04	-0.34	1.00	0.31
$A^{\pi\pi\pi\pi}_{D\pi}$	0.08	-0.07	0.01	0.24	-0.64	0.32	0.02	0.43	0.31	1.00

Chapter 5.

Measurement of the phase-space dependent $B^{\pm}$ production asymmetry, and the $\mathcal{CP}$ asymmetry in $B^{\pm} \to J/\psi K^{\pm}$ decays

In this Chapter, a measurement of the $B^{\pm}$ production asymmetry A_{B_u} is performed using the $B^{\pm} \to [K^{\pm}\pi^{\mp}(\pi^{\pm}\pi^{\mp})]_D\pi^{\pm}$ final state. The measurement is motivated by the importance of A_{B_u} as a contributing uncertainty in $\mathcal{CP}$-violation analyses, as detailed in Section 1.2.1. In Section 5.2, the invariant mass fit strategy first detailed in Section 4.1 is employed in order to measure a series of raw asymmetries $A_{Raw}^{D\pi}$ in seven bins of $B^{\pm}$ kinematics. These raw asymmetries are corrected for instrumentation asymmetry effects (described in Section 5.3) in order to measure A_{B_u} as a function of $B^{\pm}$ transverse momentum and pseudorapidity in Section 5.4. The measurement is performed both on the full Run I dataset and on the $\sqrt{s} = 7$ TeV and $\sqrt{s} = 8$ TeV component datasets, in order to investigate any dependence on the centre of mass collision energy. Using the knowledge of raw asymmetries in $B^{\pm} \to D\pi^{\pm}$ decays, a complementary measurement of the $\mathcal{CP}$ asymmetry in $B^{\pm} \to J/\psi K^{\pm}$ decays is performed in Section 5.6.

5.1. Advantages of using $B^{\pm} \to D\pi^{\pm}$ decays to measure A_{B_u}

In this thesis, the first measurement of A_{B_u} using the $B^{\pm} \to D\pi^{\pm}$ final state is performed. Being both colour and Cabibbo favoured, this decay represents a high statistics sample that is free from any significant $\mathcal{CP}$ asymmetry. This feature enables A_{B_u} to be measured with improved precision relative to previous attempts using $B^{\pm} \to J/\psi K^{\pm}$ decays. In addition, knowledge of the raw asymmetry in $B^{\pm} \to D\pi^{\pm}$ can be used to measure $A_{CP}^{J/\psi K}$ with improved precision (see Section 5.6).

5.2. Measuring the raw asymmetry in $B^{\pm} \to D\pi^{\pm}$ decays

In Chapter 3, a simultaneous fit strategy was adopted in order to measure several $\mathcal{CP}$ observables. As part of this approach, the favoured decay modes $B^{\pm} \to [K^{\pm}\pi^{\mp}(\pi^{\pm}\pi^{\mp})]_D h^{\pm}$ were included to provide high statistics samples with which PDF shapes could be accurately determined. The raw charge asymmetry measured in $B^{\pm} \to D\pi^{\pm}$ is defined as:

$$A_{Raw}^{D\pi} = A_{B_u} + A_{CP}^{D\pi} + A_{det}^{K\pi} + A_{det}^{\pi} + A_{L0} \tag{5.1}$$

The various asymmetries involved are:

- $\boldsymbol{A_{CP}^{D\pi}}$: $\mathcal{CP}$ asymmetry in favoured $B^{\pm} \to D\pi^{\pm}$ decays. Using current knowledge on the fundamental parameters r_B^{π}, δ_B and γ, the assumption can be made that zero $\mathcal{CP}$-violation occurs in $B^{\pm} \to [K^{\pm}\pi^{\mp}(\pi^{\pm}\pi^{\mp})]_D h^{\pm}$ decays, such that $A_{CP}^{D\pi} = 0$. This assumption is made throughout the analysis, with an associated systematic uncertainty.
- $\boldsymbol{A_{det}^{K\pi}}$ **and** $\boldsymbol{A_{det}^{\pi}}$: detection asymmetries associated with measuring a $K^{\pm}\pi^{\mp}$ pair and a pion, respectively (see Section 4.1.2).
- $\boldsymbol{A_{L0}}$: asymmetry introduced by the L0 trigger. Dedicated approaches to measuring the various instrumentation asymmetries $A_{det}^{K\pi}$, A_{det}^{π} and A_{L0} have been developed at LHCb, the salient features of which are detailed in Section 5.3.

Using this information, the production asymmetry can be constructed from the raw charge asymmetry measured in fits to $B^{\pm} \to D\pi^{\pm}$ data.

In order to measure the raw charge asymmetry, a simultaneous invariant mass fit to $B^{\pm} \to D\pi^{\pm}$ and $B^{\pm} \to DK^{\pm}$ decays is performed.[1] The $B^{\pm} \to DK^{\pm}$ data does not contribute to the raw asymmetry measurement, but is included in order to accurately define the amount of background from particle misidentification in the $B^{\pm} \to D\pi^{\pm}$ sample.

The data sample and fit procedure used is identical to that detailed in Section 4.1, with the following important distinctions:

- Only the favoured modes $B^{\pm} \to [K^{\pm}\pi^{\mp}(\pi^{\pm}\pi^{\mp})]_D\pi^{\pm}$ and $B^{\pm} \to [K^{\pm}\pi^{\mp}(\pi^{\pm}\pi^{\mp})]_D K^{\pm}$ are considered. The additional modes presented in Chapter 3 have much lower statistics, and do not contribute significantly to the precision on A_{B_u}.
- Only those candidates passing the L0 TIS trigger are used. In Chapter 3, $B^{\pm}$ candidates passing the L0 hadron TOS trigger were also used, but are removed from the A_{B_u} analysis to enable the precise determination of the trigger asymmetry A_{L0}. The potential asymmetries introduced by the L0 hadron TOS trigger are not yet fully understood.
- In Chapter 3, the detection asymmetries were employed as fixed values in the fit with associated systematic uncertainties. These values adjusted the raw asymmetry being measured within the fit, such that the fit returned an effective A_{B_u} value. In the present case, no fixed asymmetry correction terms are employed in the fit, such that the fit result returned is a pure measure of $A_{Raw}^{D\pi}$. In Section 5.4, these raw asymmetries will be corrected in order to measure A_{B_u}.
- The D^0 flight distance requirement, defined in Equation 3.58, is relaxed relative to the cut applied in Chapter 3. This cut is designed to suppress the contributions from charmless $B^{\pm}$ decays, which are important in the lower statistics modes but negligible in the case of favoured $B^{\pm} \to Dh^{\pm}$ decays. The cut applied is relaxed from > 2 to > 0, thus boosting the fit statistics by around 20%.
- Fiducial cuts are applied to the sample, to remove regions of large positive and negative charge asymmetry near the LHCb angular acceptance edge (see Section 5.2.1).

[1] As was the case in Chapter 3, the 2-body and 4-body decays are measured using separate invariant mass fits.

- The fit is performed independently in seven bins of $B^{\pm}$ kinematics (See Section 5.2.2).

5.2.1. Fiducial cuts

At large angles in the $x - z$ plane within LHCb, charged tracks of a given charge are more likely to remain within the horizontal acceptance than those of opposite charge. This effect arises due to the bending of low momentum tracks through angles comparable to the angular acceptance of LHCb. This results in regions of large positive and negative asymmetry near the acceptance edge of LHCb, where the assumption that such effects cancel when summing over magnet polarity is no longer valid.

To investigate this effect, the distribution of bachelor pion momentum in the $x - z$ plane has been studied in $B^{\pm} \to [K^{\pm}\pi^{\mp}]_D\pi^{\pm}$ decays, splitting by both bachelor charge and magnet polarity. The distributions are shown in Figure 5.1, where the corresponding charge asymmetries are shown in Figure 5.2. The regions of large positive (negative) asymmetry near the acceptance edge are visible as the red (blue) regions to the left of the red lines.

The choice is made to remove these regions from the analysis. A fiducial cut of the form:

$$|p_x| \leq \alpha(p_z - p_0)$$

is applied to all candidates, where $\alpha = 0.294$ and $p_0 = 2$ GeV/c. The vetoed region corresponds to those events falling to the left of the red lines drawn in Figures 5.1 and 5.2; 98.3% of offline selected candidates survive the veto.

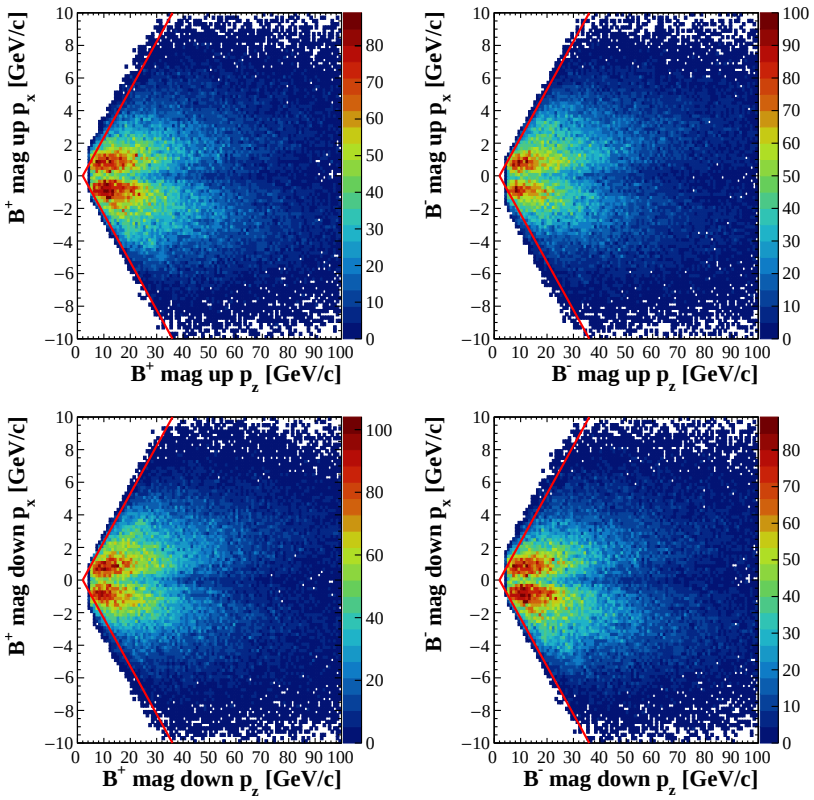

Figure 5.1.: Bachelor momentum distribution in the $x-z$ plane, for B^+ magnet up (top left), B^+ magnet down (bottom left), B^- magnet up (top right) and B^- magnet down (bottom right). The fiducial cut applied to remove regions of large positive and negative asymmetry is indicated by the red line, where vetoed candidates fall to the left of the line. The colour scale denotes the number of events in each bin.

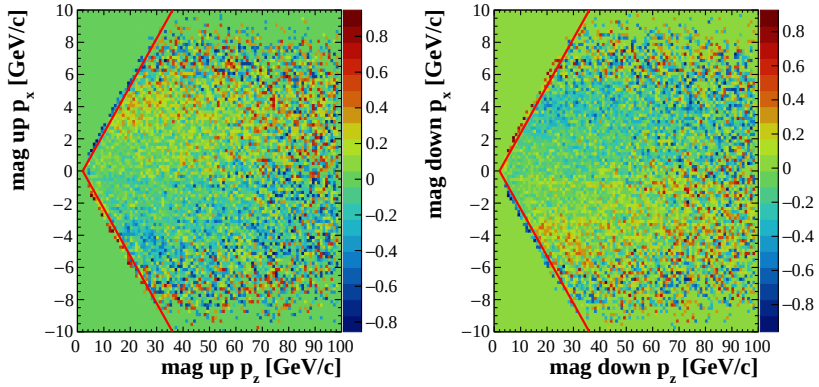

Figure 5.2.: Raw charge asymmetry in the $x-z$ plane of bachelor momentum, for magnet up (left) and magnet down (right) data. The z-axis scale denotes the value of the charge asymmetry in a given bin. Regions of large positive and negative asymmetry are indicated by the red and blue areas to the left of the red lines, and are removed by application of a fiducial cut. The cut is highly efficient, removing only 1.7% of candidates.

5.2.2. Measuring $A_{Raw}^{D\pi}$ in bins of $B^\pm$ kinematics

In order to investigate the dependence of A_{B_u} on $B^\pm$ kinematics, measurements of the raw charge asymmetry are made in seven independent bins of $B^\pm$ kinematics. The bins are defined in two dimensions [78], across rectangular regions of $B^\pm$ candidate transverse momentum (p_T) and pseudorapidity (η), as illustrated in Figure 5.3; only $B^\pm$ candidates falling within a ± 50 MeV/c^2 window around the nominal $B^\pm$ mass are shown. Separate invariant mass fits are performed for each bin, allowing the floating shape parameters to find values appropriate for each region of $B^\pm$ kinematics. The fits are identical in structure to those presented in Chapter 3, and exhibit high quality residuals and fully accurate covariance matrices in each bin.

The $B^\pm \to D\pi^\pm$ signal yields measured in each bin are recorded in Table 5.1, for both the 2-body and 4-body fits; in Table 5.2, the corresponding raw asymmetries measured in each bin are listed. For illustration, the invariant mass fits to $B^\pm \to [K^\pm\pi^\mp]_D h^\pm$ and $B^\pm \to [K^\pm\pi^\mp\pi^\pm\pi^\pm]_D h^\pm$ candidates residing in the ($1 < p_T < 6$ GeV/c, $3.3 < \eta < 4.2$) bin are shown in Figures 5.4 and 5.5, respectively. These fits are representative of those for each of the kinematic bins considered. Within each bin, weighted average values of $A_{Raw}^{D\pi}$ are calculated using the 2-body and 4-body results and their statistical uncertainties;

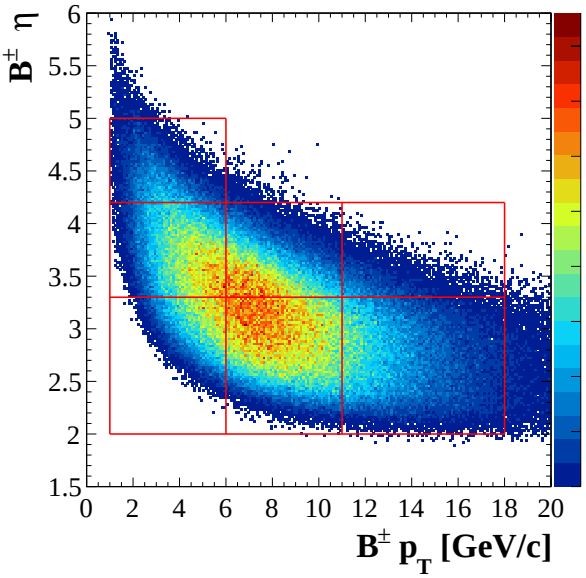

Figure 5.3.: Kinematic bins employed in the measurement of A_{B_u}, where selected $B^\pm \to D\pi^\pm$ candidates falling within a ± 50 MeV/c^2 window around the nominal $B^\pm$ mass are plotted. The same binning scheme will later be employed for the measurement of $A_{CP}^{J/\psi K}$ in $B^\pm \to J/\psi K^\pm$ decays.

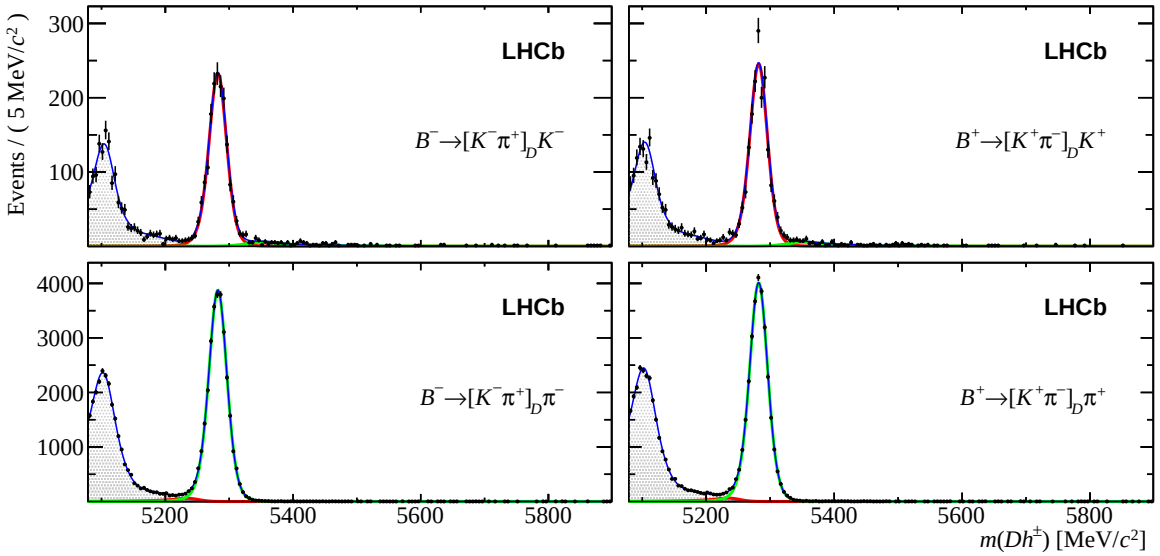

Figure 5.4.: Invariant mass distributions of selected $B^{\pm} \to [K^{\pm}\pi^{\mp}]_D h^{\pm}$ candidates, where the $B^{\pm}$ candidates residing in the ($1 < p_T < 6$ GeV/c, $3.3 < \eta < 4.2$) kinematic bin are displayed for illustration. B^- candidates are shown in the leftmost plots, with B^+ candidates displayed on the right. In the top row of plots, the bachelor track passes the PID cut, and the $B^{\pm}$ candidates are reconstructed by assigning this track the kaon mass. The remaining candidates are placed in the sample displayed in the bottom plots, and are reconstructed with a pion bachelor mass hypothesis. The red and green curves represent the fitted $B^{\pm} \to DK^{\pm}$ and $B^{\pm} \to D\pi^{\pm}$ components, respectively. The shaded contribution indicates partially reconstructed decays, and the total PDF includes the combinatorial background component.

$B^{\pm}(p_T[GeV/c], \eta)$	$\mathcal{N}(B^{\pm} \to [K^{\pm}\pi^{\mp}]_D \pi^{\pm})$	$\mathcal{N}(B^{\pm} \to [K^{\pm}\pi^{\mp}\pi^{\pm}\pi^{\mp}]_D \pi^{\pm})$
$1-6, 2.2-3.3$	24,992 $\pm$ 162	5020 $\pm$ 76
$1-6, 3.3-4.2$	59,394 $\pm$ 259	19,134 $\pm$ 151
$1-6, 4.2-5.0$	13,202 $\pm$ 126	24,015 $\pm$ 197
$6-11, 2.2-3.3$	65,916 $\pm$ 294	24,206 $\pm$ 268
$6-11, 3.3-4.2$	35,149 $\pm$ 211	28,740 $\pm$ 166
$11-18, 2.2-3.3$	30,371 $\pm$ 172	25,274 $\pm$ 166
$11-18, 3.3-4.2$	3200 $\pm$ 60	6385 $\pm$ 79

Table 5.1.: Signal yields measured in $B^{\pm} \to [K^{\pm}\pi^{\mp}]_D \pi^{\pm}$ and $B^{\pm} \to [K^{\pm}\pi^{\mp}\pi^{\pm}\pi^{\mp}]_D \pi^{\pm}$, within each bin of $B^{\pm}$ kinematics. The uncertainties quoted are statistical only. The corresponding raw asymmetries measured in each bin are listed in Table 5.2.

these averages will later be employed to measure A_{B_u} within each bin (Section 5.4), and to measure the $\mathcal{CP}$ asymmetry in $B^{\pm} \to J/\psi K^{\pm}$ decays (Section 5.6).

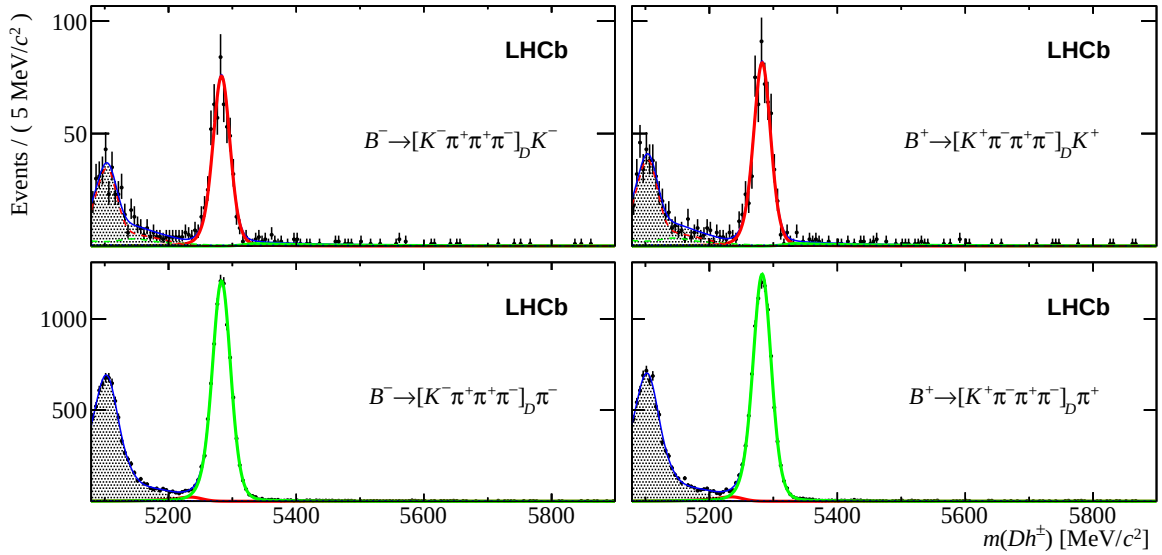

Figure 5.5.: Invariant mass distributions of selected $B^{\pm} \to [K^{\pm}\pi^{\mp}\pi^{\pm}\pi^{\mp}]_D h^{\pm}$ candidates, where $B^{\pm}$ candidates from the ($1 < p_T < 6$ GeV/c, $3.3 < \eta < 4.2$) kinematic bin are shown. See the caption of Figure 5.4 for a full description.

$(p_T[GeV/c], \eta)$	$A_{Raw}^{[K\pi]\pi}$ [%]	$A_{Raw}^{[K\pi\pi\pi]\pi}$ [%]	Weighted average [%]
$1-6, 2.2-3.3$	-1.10 ± 0.64	-2.84 ± 1.43	-1.39 ± 0.58
$1-6, 3.3-4.2$	-1.65 ± 0.42	-1.54 ± 0.74	-1.62 ± 0.36
$1-6, 4.2-5.0$	-1.41 ± 0.88	-0.32 ± 1.57	-1.15 ± 0.77
$6-11, 2.2-3.3$	-1.42 ± 0.39	-1.48 ± 0.58	-1.44 ± 0.32
$6-11, 3.3-4.2$	-1.14 ± 0.54	-1.34 ± 0.60	-1.23 ± 0.40
$11-18, 2.2-3.3$	-1.52 ± 0.55	-1.33 ± 0.64	-1.44 ± 0.42
$11-18, 3.3-4.2$	-2.63 ± 1.80	0.71 ± 1.27	-0.40 ± 1.04

Table 5.2.: Raw asymmetries measured in $B^{\pm} \to [K^{\pm}\pi^{\mp}]_D\pi^{\pm}$ and $B^{\pm} \to [K^{\pm}\pi^{\mp}\pi^{\pm}\pi^{\mp}]_D\pi^{\pm}$, with their weighted average computed in each kinematic bin. The uncertainties quoted are statistical only. The weighted averages will be used in Section 5.4 to measure the $B^{\pm}$ production asymmetry, and later in Section 5.6 as input to a measurement of $A_{CP}^{J/\psi K}$.

5.3. Measuring the detection asymmetries $A_{det}^{K\pi}$, A_{det}^{π} and $A_{L0|TIS}$

To measure the production asymmetry, various instrumentation asymmetries must be unfolded from the raw asymmetries measured in Section 5.2. The procedures developed to measure each contributing detection asymmetry are now discussed.

5.3.1. Determining $A_{det}^{K\pi}$ using prompt charm decays

The dominant source of detection asymmetry arises from nuclear interactions with the detector material, which affect the single charged kaon in the final state. This detection asymmetry, denoted as $A_{det}^{K\pi}$ throughout, is determined using decays of promptly produced $D^{\pm}$ mesons, where $A_{det}^{K\pi}$ is equivalent to:

$$A_{det}^{K\pi} = \frac{\epsilon(K^-\pi^+) - \epsilon(K^+\pi^-)}{\epsilon(K^-\pi^+) + \epsilon(K^+\pi^-)} \tag{5.2}$$

It is possible to determine this asymmetry by subtracting the raw asymmetries measured in two separate $D^{\pm}$ decay channels, namely $D^- \to K^+\pi^-\pi^-$ and $D^- \to K_s^0\pi^-$:

$$A_{det}^{K\pi} = A_{Raw}^{K\pi\pi} - A_{Raw}^{K_s^0\pi} + A_{det}^{K_s^0} \tag{5.3}$$

where the detection asymmetry of K_s^0 mesons, a calculable quantity[2], is accounted for. The raw asymmetries are measured in both $D^{\pm}$ decay channels using fits to the $D^{\pm}$ invariant mass, where a split by D charge is implemented.

Prior to fitting, a re-weighting procedure is performed to ensure that the kinematic distributions of the $D^{\pm}$ daughters (in p_T and η) match those of the $B^{\pm}$ daughters from the $A_{Raw}^{D\pi}$ measurement (Section 5.2). The re-weighting is applied to both the $D^- \to K^+\pi^-\pi^-$ and $D^- \to K_s^0\pi^-$ samples, and ensures that the measured raw asymmetries are consistent with the kinematics of $B^{\pm} \to D\pi^{\pm}$ decays. The $A_{det}^{K\pi}$ values are measured in each of the seven bins of $B^{\pm}$ kinematics, and will be employed in Section 5.4 in to measure A_{B_u}. The values of $A_{det}^{K\pi}$ measured in each bin are listed in Table 5.3, and show no strong dependence on $B^{\pm}$ kinematics.

[2] The time evolution of the LHCb material map can be used to calculate $A_{det}^{K_s^0}$ [78].

5.3.2. Tag-and-probe J/ψ method to measure A^{π}_{det}

If one assumes that the nuclear interaction asymmetry for pions is negligible, the detection asymmetry associated with the bachelor pion in $B^\pm \to D\pi^\pm$ reduces to the asymmetry introduced by the tracking system. The tracking asymmetry in LHCb is measured using a tag-and-probe method with $J/\psi \to \mu^+\mu^-$ decays, where one of the muons acts as the tag particle and the other as a probe. The kinematics of the tag muon are re-weighted to match the kinematics of the bachelor pion in $B^\pm \to D\pi^\pm$, and the asymmetry A^{π}_{det} determined in each bin of $B^\pm$ kinematics. The asymmetries measured are smaller than the corresponding $A^{K\pi}_{det}$ values in each bin, and are listed in Table 5.3.

5.3.3. Trigger asymmetry A_{L0}

All $B^\pm$ candidates considered in the measurement of A_{B_u} are required to pass the L0 TIS (Triggered Independent of Signal, see Section 3.3.1) trigger. The asymmetry of this trigger requirement is assessed using the semileptonic $B^\pm \to [K^\pm\pi^\mp]_D\mu^\pm\nu X$ decay. The efficiency of the TIS requirement is determined by evaluating the ratio:

$$\epsilon_{\text{TIS}} = \frac{\mathcal{N}(\text{Global TIS})}{\mathcal{N}} \tag{5.4}$$

where $\mathcal{N}$(Global TIS) represents the number of events that were triggered at L0 by some other activity in the event, and $\mathcal{N}$ represents the total number of L0 triggered events. This efficiency is evaluated for B^+ and B^- candidates separately, and the asymmetry measured using:

$$A_{L0|TIS} = \frac{\epsilon_{\text{TIS}}(B^-) - \epsilon_{\text{TIS}}(B^+)}{\epsilon_{\text{TIS}}(B^-) + \epsilon_{\text{TIS}}(B^+)} \tag{5.5}$$

As the TIS trigger requirement is independent of the signal $B^\pm$ by definition, the value of $A_{L0|TIS}$ applies equally well to the $B^\pm \to D\pi^\pm$ mode and indeed to all $B^\pm$ kinematic bins. The TIS trigger asymmetry is measured to be $A_{L0|TIS} = (0.03 \pm 0.11)\%$, and is thus consistent with zero. This value will be used in the measurement of A_{B_u} in Section 5.4.

5.4. From $A_{Raw}^{D\pi}$ to A_{B_u}

In order to translate the measured raw asymmetries from Table 5.2 into production asymmetries, Equation 5.1 is used along with the detection asymmetries described in Section 5.3. The production asymmetry values obtained for each bin of $B^\pm$ kinematics are listed in Table 5.3, along with their corresponding raw asymmetries and detection asymmetries. The first uncertainty quoted on each A_{B_u} value is statistical, arising from the statistics of the $B^\pm \to [K^\pm\pi^\mp(\pi^\pm\pi^\mp)]_D\pi^\pm$ samples in a given bin (see Table 5.1). The second uncertainty is systematic, and contains contributions from:

- The assumption that there is no $\mathcal{CP}$-violation in favoured $B \to D\pi$ decays (**0.16%** in each bin)
- The uncertainties on the detection asymmetries $A_{det}^{K\pi}$ and A_{det}^{π} (varies from **0.06%** to **0.25%** across bins) and the TIS trigger asymmetry (**0.11%** in each bin)
- Uncertainties arising due to the use of fixed PDF parameters in the $B^\pm \to Dh^\pm$ invariant mass fits (**0.02%** in each bin, as evaluated in Section 4.1.5)

5.4.1. Zero $\mathcal{CP}$-violation in $B^\pm \to D\pi^\pm$ decays

The uncertainty arising from assuming zero $\mathcal{CP}$-violation in favoured $B^\pm \to D\pi^\pm$ decays has been evaluated using current knowledge on the fundamental parameters $r_B^\pi = 0.025$ and $\gamma = 70°$, including the most recent measurements from LHCb. Assuming perfect knowledge of these parameters, no knowledge of the strong phase δ_B^π, and using the following definition of the $\mathcal{CP}$ asymmetry[3]:

$$A_\pi^{K\pi(\pi\pi)} = \frac{2\kappa^{K\pi(\pi\pi)} r_B^\pi r_D^{K\pi(\pi\pi)} \sin\left(\delta_B^\pi - \delta_D^{K\pi(\pi\pi)}\right)\sin\gamma}{1 + \left(r_B^\pi r_D^{K\pi(\pi\pi)}\right)^2 + 2\kappa^{K\pi(\pi\pi)} r_B^\pi r_D^{K\pi(\pi\pi)} \cos\left(\delta_B^\pi - \delta_D^{K\pi(\pi\pi)}\right)\cos\gamma} \tag{5.6}$$

$$\tag{5.7}$$

a range of possible $A_\pi^{K\pi(\pi\pi)}$ values are calculated across the full range of possible δ_B^π values, as illustrated in Figure 5.6. The standard deviation of these values, 0.16%, is taken as the systemic uncertainty.

[3] This definition follows the formalism adopted in Chapter 3, where the $\mathcal{CP}$ observables in the ADS/GLW analysis were defined.

$(p_T[GeV/c], \eta)$	$A^{D\pi}_{Raw}$	$A^{D\pi}_{CP}$	$A^{K\pi}_{det}$	A^{π}_{det}	$A_{L0\vert TIS}$	A_{B_u}
$1-6, 2.2-3.3$	-1.39 $\pm$ 0.58	0.00 $\pm$ 0.16	-1.33 $\pm$ 0.16	-0.14 $\pm$ 0.08	0.03 $\pm$ 0.11	0.05 $\pm$ 0.58 $\pm$ 0.26
$1-6, 3.3-4.2$	-1.62 $\pm$ 0.36	0.00 $\pm$ 0.16	-1.27 $\pm$ 0.06	-0.10 $\pm$ 0.06	0.03 $\pm$ 0.11	-0.28 $\pm$ 0.36 $\pm$ 0.21
$1-6, 4.2-5.0$	-1.15 $\pm$ 0.77	0.00 $\pm$ 0.16	-0.92 $\pm$ 0.15	-0.04 $\pm$ 0.07	0.03 $\pm$ 0.11	-0.22 $\pm$ 0.77 $\pm$ 0.26
$6-11, 2.2-3.3$	-1.44 $\pm$ 0.32	0.00 $\pm$ 0.16	-1.35 $\pm$ 0.10	-0.27 $\pm$ 0.14	0.03 $\pm$ 0.11	0.15 $\pm$ 0.32 $\pm$ 0.26
$6-11, 3.3-4.2$	-1.23 $\pm$ 0.40	0.00 $\pm$ 0.16	-1.17 $\pm$ 0.11	-0.16 $\pm$ 0.14	0.03 $\pm$ 0.11	0.07 $\pm$ 0.40 $\pm$ 0.26
$11-18, 2.2-3.3$	-1.44 $\pm$ 0.42	0.00 $\pm$ 0.16	-1.19 $\pm$ 0.15	-0.47 $\pm$ 0.24	0.03 $\pm$ 0.11	0.19 $\pm$ 0.42 $\pm$ 0.34
$11-18, 3.3-4.2$	-0.40 $\pm$ 1.04	0.00 $\pm$ 0.16	-1.69 $\pm$ 0.16	-0.16 $\pm$ 0.28	0.03 $\pm$ 0.11	1.42 $\pm$ 1.04 $\pm$ 0.38

Table 5.3.: $B^{\pm}$ production asymmetry A_{B_u} (%), measured in seven bins of $B^{\pm}$ kinematics. All values are quoted in percent. The raw asymmetries A_{Raw} measured in $B^{\pm} \to [K^{\pm}\pi^{\mp}(\pi^{\pm}\pi^{\mp})]_{D}\pi^{\pm}$ are corrected by the detection asymmetries $A^{K\pi}_{det}$ and A^{π}_{det} as well as the TIS trigger asymmetry $A_{L0|TIS}$. The first uncertainty quoted on each $A^{B^+}_{\mathcal{P}}$ is statistical, arising from the statistics of the $B^{\pm} \to [K^{\pm}\pi^{\mp}(\pi^{\pm}\pi^{\mp})]_{D}\pi^{\pm}$ sample in a given bin. The second uncertainty is systematic, arising from the assumption of zero $\mathcal{CP}$-violation in $B \to D\pi$ decays and the use of fixed detection asymmetries.

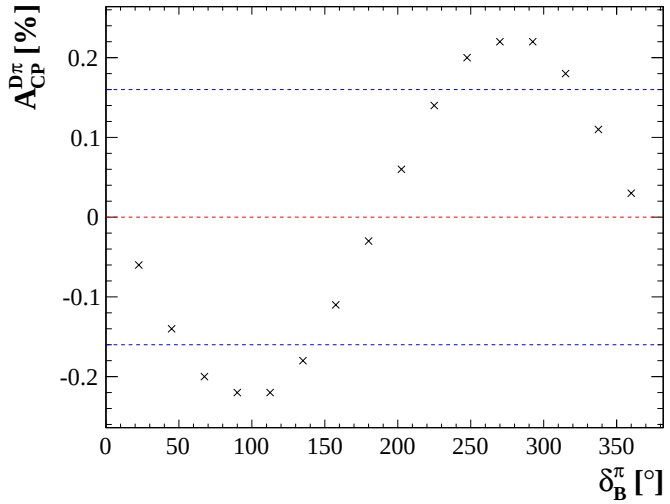

Figure 5.6.: Variation in $A_{CP}^{D\pi}$ with strong phase δ_B^{π}, assuming $r_B^{\pi} = 2.5\%$. The standard deviation of the values shown, as indicated by the blue lines, is taken as a systematic uncertainty on the assumption of zero $\mathcal{CP}$-violation in $B^{\pm} \to D\pi^{\pm}$ decays.

5.4.2. Phase space integrated result

Graphical representations of the A_{B_u} values measured in each bin are presented in Section 5.7. The phase space integrated value of A_{B_u}, determined from a single fit for $A_{Raw}^{D\pi}$ across all bins of $B^{\pm}$ kinematics[4], is:

$$A_{B_u} = (+0.02 \pm 0.17 \pm 0.23)\%$$

which is consistent with zero asymmetry given the current level of statistical precision.

Data	$A_{Raw}^{D\pi}$	$A_{CP}^{D\pi}$	$A_{det}^{K\pi}$	A_{det}^{π}	$A_{L0\|TIS}$	A_{B_u}
2011	-1.35 ± 0.31	0.00 ± 0.16	-1.31 ± 0.22	-0.24 ± 0.19	0.03 ± 0.11	0.17 ± 0.31 ± 0.35
2012	-1.37 ± 0.20	0.00 ± 0.16	-0.96 ± 0.12	-0.22 ± 0.13	0.03 ± 0.11	-0.22 ± 0.20 ± 0.26

Table 5.4.: Phase space integrated $B^{\pm}$ production asymmetries measured in 2011 and 2012 data. All values are quoted in percent.

5.5. Dependence of A_{B_u} on the centre of mass collision energy

The production asymmetry may exhibit some dependence on the centre of mass collision energy, which was different during 2011 ($\sqrt{s} = 7$ TeV) and 2012 ($\sqrt{s} = 8$ TeV) data taking. To investigate any dependence, the production asymmetry measurement has been performed separately on 2011 and 2012 data, with results listed in Tables 5.5 and 5.6 for each bin of $B^{\pm}$ kinematics. The phase space integrated production asymmetries measured in 2011 and 2012 data are:

$$A_{B_u}^{7\text{ TeV}} = (+0.17 \pm 0.31 \pm 0.35)\% \tag{5.8}$$

$$A_{B_u}^{8\text{ TeV}} = (-0.22 \pm 0.20 \pm 0.26)\% \tag{5.9}$$

where both results are consistent with zero asymmetry. The asymmetries contributing to these phase space integrated measurements are listed in Table 5.4, where the contributing systematic uncertainties from the use of fixed $A_{CP}^{D\pi}$, $A_{det}^{K\pi}$, A_{det}^{π} and $A_{L0|TIS}$ values are indicated. It is not possible to conclude whether the production asymmetry exhibits any dependence on the centre of mass collision energy given the current level of statistical precision.

[4] The phase space integrated detection asymmetries are also used in constructing A_{B_u} in this instance.

$(p_T[GeV/c], \eta)$	$A_{Raw}^{D\pi}$	$A_{CP}^{D\pi}$	$A_{det}^{K\pi}$	A_{det}^{π}	$A_{L0\|TIS}$	A_{B_u}
$1-6, 2.2-3.3$	-0.73 ± 1.1	0.00 ± 0.16	-1.9 ± 0.37	-0.19 ± 0.17	0.03 ± 0.11	1.3 ± 1.1 ± 0.41
$1-6, 3.3-4.2$	-1.3 ± 0.74	0.00 ± 0.16	-1.3 ± 0.21	-0.11 ± 0.098	0.03 ± 0.11	0.1 ± 0.74 ± 0.23
$1-6, 4.2-5.0$	-0.83 ± 1.2	0.00 ± 0.16	-0.74 ± 0.17	-0.012 ± 0.13	0.03 ± 0.11	-0.074 ± 1.2 ± 0.22
$6-11, 2.2-3.3$	-1.7 ± 0.61	0.00 ± 0.16	-1.2 ± 0.28	-0.29 ± 0.25	0.03 ± 0.11	-0.15 ± 0.61 ± 0.37
$6-11, 3.3-4.2$	-0.39 ± 0.67	0.00 ± 0.16	-0.97 ± 0.2	-0.075 ± 0.25	0.03 ± 0.11	0.65 ± 0.67 ± 0.33
$11-18, 2.2-3.3$	-1.6 ± 0.79	0.00 ± 0.16	-1.3 ± 0.39	-0.58 ± 0.48	0.03 ± 0.11	0.37 ± 0.79 ± 0.62
$11-18, 3.3-4.2$	-0.74 ± 1.9	0.00 ± 0.16	-2 ± 0.3	-0.22 ± 0.63	0.03 ± 0.11	1.4 ± 1.9 ± 0.69

Table 5.5: $B^{\pm}$ production asymmetry A_{B_u}, measured in seven bins of $B^{\pm}$ kinematics in 2011 data. The first uncertainties quoted are statistical only, while the second uncertainties quoted on each A_{B_u} are systematic.

$(p_T[GeV/c], \eta)$	$A_{Raw}^{D\pi}$	$A_{CP}^{D\pi}$	$A_{det}^{K\pi}$	A_{det}^{π}	$A_{L0\|TIS}$	A_{B_u}
$1-6, 2.2-3.3$	-1.7 ± 0.69	0.00 ± 0.16	-1.6 ± 0.049	-0.2 ± 0.11	0.03 ± 0.11	0.18 ± 0.69 ± 0.12
$1-6, 3.3-4.2$	-1.6 ± 0.43	0.00 ± 0.16	-1.3 ± 0.14	-0.086 ± 0.067	0.03 ± 0.11	-0.22 ± 0.43 ± 0.16
$1-6, 4.2-5.0$	-1.5 ± 0.92	0.00 ± 0.16	-0.45 ± 0.05	-0.035 ± 0.092	0.03 ± 0.11	-0.97 ± 0.92 ± 0.11
$6-11, 2.2-3.3$	-1.1 ± 0.36	0.00 ± 0.16	-0.85 ± 0.2	-0.25 ± 0.17	0.03 ± 0.11	-0.0064 ± 0.36 ± 0.26
$6-11, 3.3-4.2$	-1.5 ± 0.47	0.00 ± 0.16	-0.85 ± 0.16	-0.2 ± 0.17	0.03 ± 0.11	-0.43 ± 0.47 ± 0.23
$11-18, 2.2-3.3$	-1.4 ± 0.51	0.00 ± 0.16	-0.85 ± 0.29	-0.4 ± 0.28	0.03 ± 0.11	-0.14 ± 0.51 ± 0.4
$11-18, 3.3-4.2$	-2.4 ± 1.4	0.00 ± 0.16	-1.2 ± 0.18	-0.13 ± 0.31	0.03 ± 0.11	-1.1 ± 1.4 ± 0.36

Table 5.6.: $B^{\pm}$ production asymmetry A_{B_u}, measured in seven bins of $B^{\pm}$ kinematics in 2012 data. The first uncertainties quoted are statistical only, while the second uncertainties quoted on each A_{B_u} are systematic.

5.6. Using $A_{Raw}^{D\pi}$ to measure the $\mathcal{CP}$ asymmetry in $B^{\pm} \to J/\psi K^{\pm}$ decays

The $B^{\pm} \to J/\psi K^{\pm}$ decay is expected to exhibit very small direct $\mathcal{CP}$-violation, since the tree and penguin contributions for $b \to sc\bar{c}$ decays have the same weak phase within the SM. Estimates of the effect of penguin loops show that there could be a small amount of direct $\mathcal{CP}$-violation in $B^{\pm} \to J/\psi K^{\pm}$ decays, up to $\mathcal{O}(0.3\%)$ [79]. A measurement of a relatively large charge asymmetry would indicate the existence of physics beyond the SM, thus motivating a precise measurement of $A_{CP}^{J/\psi K}$.

The world average CP asymmetry $A_{CP}^{J/\psi K} = (0.3 \pm 0.6)\%$ [12] is consistent with zero. Using the same convention as Equation 5.1, the raw asymmetry measured in $B^{\pm} \to J/\psi K^{\pm}$ can be expressed as:

$$A_{Raw}^{J/\psi K} = A_{B_u} + A_{CP}^{J/\psi K} + A_{det}^{K\pi} + A_{det}^{\pi} + A_{L0|TIS} \tag{5.10}$$

If one assumes that the production asymmetry, pion detection asymmetry and L0 TIS asymmetry are identical in $B^{\pm} \to J/\psi K^{\pm}$ and $B^{\pm} \to D\pi^{\pm}$ decays (with some associated systematic uncertainty), a ΔA_{CP} can be constructed from the raw asymmetries measured in both modes:

$$\Delta A_{CP} = A_{CP}^{J/\psi K} - A_{CP}^{D\pi} = A_{Raw}^{J/\psi K} - A_{Raw}^{D\pi} + \delta A_{det}^{K\pi} \tag{5.11}$$

where $\delta A_{det}^{K\pi}$ represents the difference in $K^{\pm}\pi^{\mp}$ detection asymmetry between the $B^{\pm} \to J/\psi K^{\pm}$ and $B^{\pm} \to D\pi^{\pm}$ modes. These are determined by repeating the procedure outlined in Section 5.3.1 using $B^{\pm} \to J/\psi K^{\pm}$ decays. The values of $\delta A_{det}^{K\pi}$ found in each bin of $B^{\pm}$ kinematics are listed in Table 5.7.

As the assumption that $A_{CP}^{D\pi} = 0$ was made in the measurement of $A_{Raw}^{D\pi}$ in Section 5.2, this expression reduces to a direct measurement of the $\mathcal{CP}$ asymmetry $A_{CP}^{J/\psi K}$. A measurement of $A_{CP}^{J/\psi K}$ in the $B^{\pm} \to [\mu^+\mu^-]_D K^{\pm}$ final state, using the $A_{Raw}^{D\pi}$ and $\delta A_{det}^{K\pi}$ values measured across seven bins of $B^{\pm}$ kinematics, is now presented.

$(p_T[GeV/c], \eta)$	$A_{det}^{K\pi}(B^\pm \to D\pi^\pm)$ [%]	$A_{det}^{K\pi}(B^\pm \to J/\psi K^\pm)$ [%]	$\delta A_{det}^{K\pi}$ [%]
$1-6, 2.2-3.3$	-1.41 $\pm$ 0.05	-1.15 $\pm$ 0.20	0.26 $\pm$ 0.21
$1-6, 3.3-4.2$	-1.27 $\pm$ 0.12	-1.10 $\pm$ 0.07	0.17 $\pm$ 0.14
$1-6, 4.2-5.0$	-0.78 $\pm$ 0.05	-0.21 $\pm$ 0.13	0.57 $\pm$ 0.14
$6-11, 2.2-3.3$	-1.29 $\pm$ 0.16	-0.90 $\pm$ 0.16	0.39 $\pm$ 0.23
$6-11, 3.3-4.2$	-1.04 $\pm$ 0.12	-0.71 $\pm$ 0.12	0.33 $\pm$ 0.17
$11-18, 2.2-3.3$	-1.13 $\pm$ 0.23	-1.05 $\pm$ 0.14	0.08 $\pm$ 0.27
$11-18, 3.3-4.2$	-1.20 $\pm$ 0.15	-1.02 $\pm$ 0.19	0.18 $\pm$ 0.24

Table 5.7.: Values of $A_{det}^{K\pi}$ in each bin of $B^\pm$ kinematics, as measured by re-weighting to the bachelor kinematics in $B \to J/\psi K$ and the D daughter kaon kinematics in $B \to D\pi$. The differences $\delta A_{det}^{K\pi}$ between both modes are used as input in the measurement of $A_{CP}^{J/\psi K}$.

5.6.1. $B^\pm \to [\mu^+\mu^-]_{J/\psi} K^\pm$ candidate selection

Stripping and trigger

The $B^\pm \to J/\psi K^\pm$ candidates pass both stripping and trigger selections prior to offline analysis, in a similar manner to that described in Section 3.3.1 for $B^\pm \to D\pi^\pm$ decays. All candidates are selected from the `BetaSBu2JpsiKNoPIDDetachedLine` stripping stream, and are required to have passed the following set of triggers:

- L0 Global TIS only (`Bu_L0Global_TIS`, to align with the TIS only measurement of $A_{Raw}^{D\pi}$ in Section 5.2)
- Hlt1 Track TOS or Hlt1 Track Muon TOS or Hlt1 DiMuon TOS (`Bu_Hlt1TrackAllL0Decision_TOS` || `Bu_Hlt1TrackMuonDecision_TOS` || `Bu_Hlt1DiMuon(LowMass,HighMass,Deteched)Decision_TOS`)
- Hlt2 DiMuon TOS (`Bu_Hlt2DiMuon(Deteched,DetachedHeavy,DetachedJPsi, JPsi,JPsiHighPT)Decision_TOS`)

The HLT triggers differ from those required in the $B^\pm \to D\pi^\pm$ case, by virtue of having a J/ψ in the final state. The presence of two muons in the final state enables clean triggering of the event.

Multivariate BDT selection

A single stage BDT is used to select $B^{\pm} \to [\mu^+\mu^-]_{J/\psi}K^{\pm}$ decays. Training of the BDT is performed using a sample of $B^{\pm} \to [\mu^+\mu^-]_{J/\psi}K^{\pm}$ simulated events, while background events are taken from the upper sideband in data with $m(B^{\pm}) > 5500$ MeV/c^2. This region is well isolated from the signal region, and consists of combinatoric events where fake bachelor tracks are combined with J/ψ candidates.

The training is performed using the gradient boost method (the same method as was used in the ADS/GLW selection detailed in Section 3.3.2), and employs a number of discriminating variables including:

- Cosine of the angle between the B momentum and the vector from the primary to the secondary vertex (DIRA), B decay vertex χ^2, cylindrical coordinate distance from the B decay vertex to the primary vertex, and minimum impact parameter of the B candidate with respect to the primary vertex.
- J/ψ decay vertex χ^2.
- Muon track χ^2 per degree of freedom, momentum, transverse momentum and impact parameter χ^2 with respect to J/ψ decay vertex.
- Bachelor kaon track χ^2 per degree of freedom and impact parameter with respect to the $B^{\pm}$ decay vertex.

As was the case for the $B \to D\pi$ BDTs described in Section 3.3.2, the primary function of this BDT is to reduce the level of combinatoric background, providing a high purity sample of $B^{\pm} \to J/\psi K^{\pm}$ decays with which to measure $A_{CP}^{J/\psi K}$. The BDT exhibits a high level of background rejection and high signal efficiency, as demonstrated by the output classifier distribution in Figure 5.7; signal events (blue) appear peaked towards 1, while background events (red) peak towards -1. A cut at > 0.5 in the BDT response was chosen, as it reduced the level of background to an acceptable level for the $B^{\pm} \to [\mu^+\mu^-]_{J/\psi}K^{\pm}$ invariant mass fit (see Section 5.6.2), while retaining 74% of all signal decays.

Additional cuts

In addition to the BDT selection, a small number of further cuts are applied. The invariant mass of J/ψ candidates are required to fall within the range (3057 - 3127) MeV/c^2, while all bachelor kaons are required to have $\mathrm{DLL}_{K\pi} > -5$. The fiducial cuts

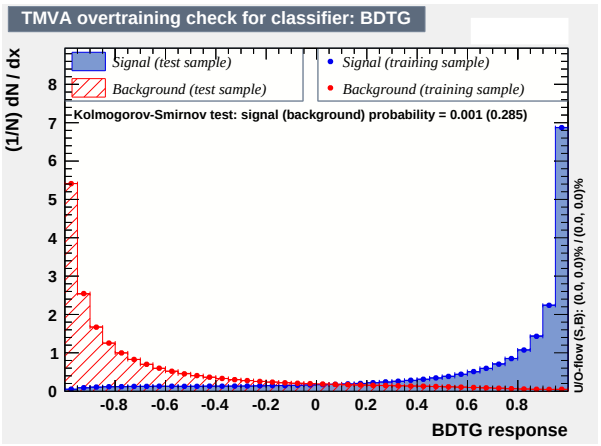

Figure 5.7.: BDT output classifier distribution for $B^{\pm} \to J/\psi K^{\pm}$. The BDT exhibits a high degree of separation, with a signal efficiency of 74% at the response cut of > 0.5 chosen for the analysis.

detailed in Section 5.2.1 are also applied to all $B^{\pm} \to [\mu^+\mu^-]_{J/\psi} K^{\pm}$ candidates, to remove the regions of high positive and negative charge asymmetry. This cut retains 98.4% of signal decays passing all previous selection requirements. As was the case for the $B^{\pm} \to D\pi^{\pm}$ selection, only one $B^{\pm}$ signal candidate is retained per event.

5.6.2. Simultaneous invariant mass fit to $m(J/\psi K)$ in seven bins of $B^{\pm}$ kinematics

To correctly measure $A_{CP}^{J/\psi K}$, one must correct for the combined asymmetries in $B^{\pm}$ production, charged particle detection and L0 triggering. This is achieved by subtracting the raw asymmetry measured in $B^{\pm} \to D\pi^{\pm}$ decays from the raw asymmetry measured in $B^{\pm} \to J/\psi K^{\pm}$ decays, with a correction $\delta A_{det}^{K\pi}$ included to account for the difference in $K^{\pm}\pi^{\pm}$ detection asymmetry in $B^{\pm} \to D\pi^{\pm}$ and $B^{\pm} \to J/\psi K^{\pm}$ decays. The assumption that no $\mathcal{CP}$-violation occurs in $B^{\pm} \to D\pi^{\pm}$ is also made, where all assumptions are assigned systematic uncertainties in Section 5.6.3.

The strategy adopted to measure $A_{CP}^{J/\psi K}$ is a binned maximum-likelihood fit to the invariant mass of selected $B^{\pm} \to J/\psi K^{\pm}$ candidates, where the fit is performed simultaneously across fourteen bins - seven bins of $B^{\pm}$ kinematics for each B candidate charge. The kinematic bins are chosen to be identical to those used in Section 5.2.2 for the measurement of $A_{Raw}^{D\pi}$, allowing each raw asymmetry from Table 5.2 to be used as direct input to the fit.

Within a given bin of $B^\pm$ kinematics, the raw charge symmetry measured in $B^\pm \to J/\psi K^\pm$ ($A_{Raw}^{J/\psi K}$) is corrected by the corresponding raw asymmetry in $B^\pm \to D\pi^\pm$ ($A_{Raw}^{D\pi}$) and the difference in $K^\pm\pi^\pm$ detection asymmetry between $B^\pm \to D\pi^\pm$ and $B^\pm \to J/\psi K^\pm$ ($\delta A_{det}^{K\pi}$). The statistical uncertainties on each $A_{Raw}^{D\pi}$ and $\delta A_{det}^{K/\pi}$ are propagated through the $B^\pm \to J/\psi K^\pm$ fit by means of Gaussian constraints, which are applied to each of the individual values of $A_{Raw}^{D\pi}$ and $\delta A_{det}^{K/\pi}$. The constraint Gaussians are centred at the measured values of each $A_{Raw}^{D\pi}$ and $\delta A_{det}^{K\pi}$, with widths equal to the measured uncertainties listed in Tables 5.2 and 5.7, respectively.

A single floating parameter describes $A_{CP}^{J/\psi K}$ in the fit, and is shared across all seven bins. The statistical uncertainty on this parameter is determined by the total number of $B^\pm \to J/\psi K^\pm$ candidates across all seven bins, as well as the statistical uncertainty on each $A_{Raw}^{D\pi}$ and $\delta A_{det}^{K\pi}$. The statistics in $B^\pm \to J/\psi K^\pm$ and $B^\pm \to D\pi^\pm$ are similar, with both modes contributing around a 0.2% uncertainty to the total statistical uncertainty. The total number of $B^\pm \to J/\psi K^\pm$ candidates measured in the fit is $\mathcal{N}(B^\pm \to J/\psi K^\pm) = 217,780 \pm 650$, while the total number of $B^\pm \to D\pi^\pm$ candidates (from Table 5.1) is $\mathcal{N}(B^\pm \to D\pi^\pm) = 364,998 \pm 688$.

Signal and background PDFs

The PDF used to describe signal decays is identical to that used in the $B \to D\pi$ mass fit (see Equation 4.1), with the exception of the small Gaussian component which is not required in the case of $B^\pm \to J/\psi K^\pm$. The peak mean floats freely and is shared across all bins of $B^\pm$ kinematics, but can be different is the B^+ and B^- samples. The peak widths float freely in each of the fourteen bins, as do the tail parameters. The fractional yields in the seven kinematic bins float freely, comprising the total signal yield $\mathcal{N}(B^\pm \to J/\psi K^\pm)$. A single charge asymmetry representing $A_{CP}^{J/\psi K}$ is shared across all seven kinematic bins, where the raw asymmetries $A_{Raw}^{J/\psi K}$ in each bin are corrected by the corresponding $A_{Raw}^{D\pi}$ values from Table 5.2, as well as the $\delta A_{det}^{K\pi}$ values from Table 5.7.

The contributions from combinatoric background events are described by first order polynomial PDFs, which share a common freely floating gradient in B^+ and B^-. The gradient is allowed to be different in each bin of $B^\pm$ kinematics, allowing for potential variation in the background distribution with $B^\pm$ candidate kinematics. The combinatoric yields in each of the fourteen bins also float freely.

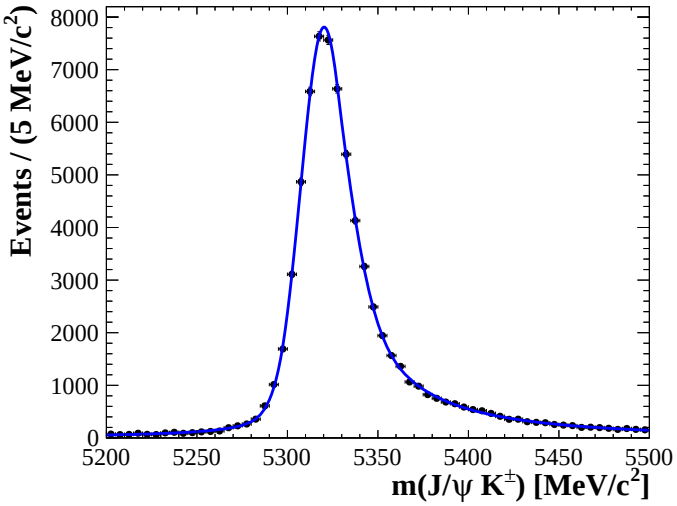

Figure 5.8.: Invariant mass fit to simulated $B^{\pm} \to J/\psi\pi^{\pm}$ decays reconstructed under the kaon bachelor mass hypothesis. Shape parameters from this fit are employed as fixed terms in the $A_{CP}^{J/\psi K}$ fit, with an associated systematic uncertainty.

The final fit component describes misidentified $B^{\pm} \to J/\psi\pi^{\pm}$ decays, and is modelled using the sum of two modified Gaussian PDFs in an identical manner to the contribution from misidentified $B^{\pm} \to D\pi^{\pm}$ decays in the $B^{\pm} \to DK^{\pm}$ fit (see Section 3.4.6). The yield of this component floats freely in each bin of $B^{\pm}$ kinematics, but the charge asymmetry is required to be the same in all bins and floats freely. The parameters of this shape are fully fixed from a fit performed to $B^{\pm} \to J/\psi\pi^{\pm}$ simulated events reconstructed under the kaon bachelor mass hypothesis. The fit is shown in Figure 5.8, with the shape parameters and their corresponding fit uncertainties listed in Table 5.8. The use of a fully fixed shape contributes a small systematic uncertainty which is evaluated in Section 5.6.3. With the exception of this PDF, all other shape parameters float freely in the fit. The reported uncertainty on $A_{CP}^{J/\psi K}$ thus contains a small component from the PDF uncertainties.

Parameter	Value
α_L	1.45 ± 0.08
α_R	-0.61 ± 0.04
n_L	1.28 ± 0.10
n_R	2.14 ± 0.12
μ	5232.0 ± 0.2 MeV/c^2
σ_L	14.9 ± 0.5 MeV/c^2
σ_R	12.4 ± 0.3 MeV/c^2
f	0.29 ± 0.03

Table 5.8.: Shape parameter values from a fit to simulated $B^{\pm} \to J/\psi\pi^{\pm}$ decays reconstructed under the kaon bachelor mass hypothesis. The parameters $\alpha_{L,R}$ and $n_{L,R}$ describe the tails, while the parameters $\sigma_{L,R}$ and μ describe the widths and mean, respectively. The parameter f describes the fractional contribution to the total PDF from the modified Gaussian of width σ_L. All of these parameters are employed as fixed terms in the fit to $B^{\pm} \to J/\psi K^{\pm}$ data, with an associated systematic uncertainty (see Section 5.6.3).

5.6.3. Fit results and systematic uncertainties

The invariant mass distributions in each bin of $B^{\pm}$ kinematics are very similar. To illustrate their general structure, the invariant mass fit for the kinematic bin ($1 < p_T < 6\text{GeV}/c, 2.2 < \eta < 3.3$) is plotted in Figure 5.9. The low level of combinatoric background is evident, and the small contribution from misidentified $B^{\pm} \to J/\psi\pi^{\pm}$ events visible to the right of the main signal peak. The signal yields measured in each bin of $B^{\pm}$ kinematics are summarised in Table 5.9.

$B^{\pm}(p_T[GeV/c], \eta)$	$\mathcal{N}(B^{\pm} \to J/\psi K^{\pm})$
$1-6, 2.2-3.3$	15,875 $\pm$ 144
$1-6, 3.3-4.2$	55,410 $\pm$ 313
$1-6, 4.2-5.0$	32,804 $\pm$ 372
$6-11, 2.2-3.3$	39,732 $\pm$ 247
$6-11, 3.3-4.2$	37,578 $\pm$ 247
$11-18, 2.2-3.3$	24,278 $\pm$ 190
$11-18, 3.3-4.2$	12,103 $\pm$ 224

Table 5.9.: Signal yields measured in $B^{\pm} \to J/\psi K^{\pm}$ within each bin of $B^{\pm}$ kinematics.

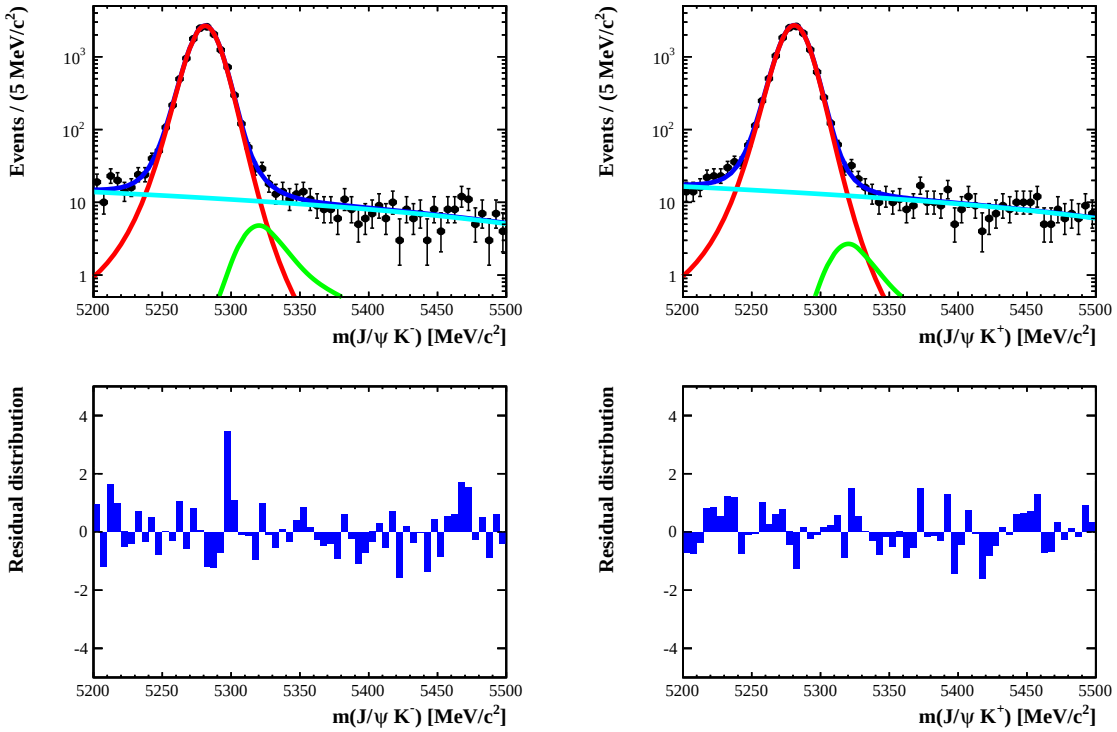

Figure 5.9.: Invariant mass fit to $B^{\pm} \to J/\psi K^{\pm}$ decays in the $(1 < p_T < 6\ \mathrm{GeV}/c, 2.2 < \eta < 3.3)$ bin of $B^{\pm}$ kinematics. Signal decays are shown by the red line, while combinatoric background events are drawn in cyan. The contribution from misidentified $B^{\pm} \to J/\psi \pi^{\pm}$ decays is shown by the green line. B^{-} candidates are plotted on the left, and B^{+} candidates on the right. The fit residuals are excellent, and this behaviour is reproduced in each of the seven bins of $B^{\pm}$ kinematics.

The $\mathcal{CP}$ asymmetry in $B^\pm \to J/\psi K^\pm$ decays is measured to be:

$$A_{CP}^{J/\psi K} = (+0.10 \pm 0.30)\%$$

where the uncertainty reported is statistical, and accounts for the statistics in the $B^\pm \to J/\psi K^\pm$ and $B^\pm \to D\pi^\pm$ fits, as well as the uncertainties on each $\delta A_{det}^{K\pi}$ correction. The statistical precision of this result improves upon the current world average [12] by a factor of two. There are two sources of systematic uncertainty that must be considered, both of which are discussed below.

Zero $\mathcal{CP}$-violation in $B^\pm \to D\pi^\pm$ decays

In making the assumption of zero $\mathcal{CP}$-violation in $B^\pm \to D\pi^\pm$ decays, a measurement of $A_{CP}^{J/\psi K}$ is performed rather than a measurement of ΔA_{CP}. A systematic uncertainty of **0.16%** on $A_{CP}^{J/\psi K}$ is assigned in an identical fashion to the measurement of A_{B_u}.

Use of fixed shape parameters in the $B^\pm \to D\pi^\pm$ and $B^\pm \to J/\psi K^\pm$ fits

To determine the systematic uncertainty from this source, the fits to data are performed many times. Each time a fit is performed, the fixed PDF shape parameters are randomly varied within their assigned systematic uncertainties, and the values of $A_{Raw}^{D\pi}$ and $A_{CP}^{J/\psi K}$ measured. The RMS spread in the fit results under this variation is taken as a measure of the systematic uncertainty.

In the case of the $B^\pm \to D\pi^\pm$ fit, the overall systematic uncertainty from this source is 0.02%. In the case of the $B^\pm \to J/\psi K^\pm$ fit, where only the small $B^\pm \to J/\psi \pi^\pm$ contribution is described by a fixed shape, the systematic uncertainty is 0.001%. The total systematic uncertainty is thus **0.02%**, and is equal in each bin of $B^\pm$ kinematics due to the sharing of PDFs across each bin.

The final result including systematic uncertainties is:

$$A_{CP}^{J/\psi K} = (+0.10 \pm 0.30 \pm 0.16)\%$$

where the first uncertainty is statistical and the second is systematic. This result is consistent with, and improves upon, the current world average value of $A_{CP}^{J/\psi K}$, and is testament to the high statistics data samples collected by LHCb during Run I.

5.7. Asymmetries measured in each bin of $B^{\pm}$ kinematics

In Figure 5.10, a graphical summary of the various asymmetries featured in this Chapter ($A_{Raw}^{D\pi}$, $A_{det}^{K\pi}$, A_{det}^{π}, $A_{L0|TIS}$, A_{B_u}, $A_{CP}^{D\pi}$ and $A_{CP}^{J/\psi K}$) is presented. The raw asymmetry measured in each bin of $B^{\pm}$ kinematics is visible on the far left (shown in black), and is corrected by $A_{det}^{K\pi}$, A_{det}^{π} and $A_{L0|TIS}$ (all plotted in blue) in order to measure A_{B_u} (plotted in red). The solid error bar represents the statistical uncertainty on A_{B_u}, and the dotted error bar represents the total uncertainty including systematics. The systematic uncertainty on A_{B_u} is composed of contributions from the use of fixed detection and trigger asymmetries, the assumption of zero $\mathcal{CP}$-violation in favoured $B^{\pm} \to D\pi^{\pm}$ decays, and the use of fixed PDF shape parameters in the $B^{\pm} \to D\pi^{\pm}$ fit.

The raw asymmetries $A_{Raw}^{D\pi}$ and the detection asymmetry differences $\delta A_{det}^{K\pi}$ correct the raw asymmetries measured in $B^{\pm} \to J/\psi K^{\pm}$, enabling a value of $A_{CP}^{J/\psi K}$ to be measured across all bins of $B^{\pm}$ kinematics. The measurement of $A_{CP}^{J/\psi K}$ is shown by rightmost red point, and is the same in each bin of $B^{\pm}$ kinematics by construction. This measurement is subject to the assumption of zero $\mathcal{CP}$-violation in $B \to D\pi$ decays (plotted in blue with its associated systematic uncertainty), and the use of fixed shape parameters in the $B^{\pm} \to D\pi^{\pm}$ and $B^{\pm} \to J/\psi K^{\pm}$ invariant mass fits. The statistical uncertainty on $A_{CP}^{J/\psi K}$ is shown by the solid error bar, and the total uncertainty including systematics is shown by the dotted line.

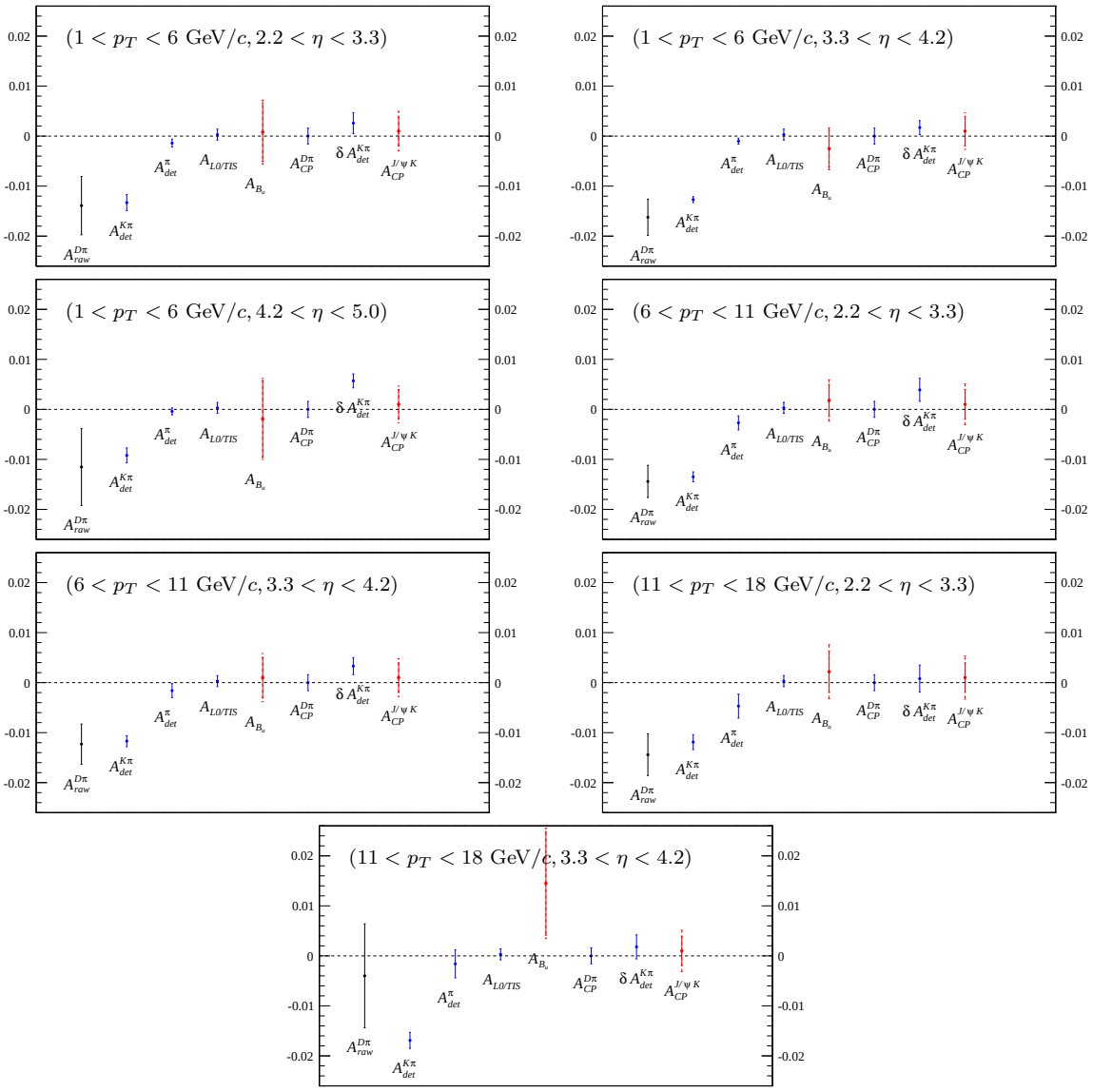

Figure 5.10.: Asymmetries measured in each bin of $B^{\pm}$ kinematics. The value of $A_{CP}^{J\psi K}$ is common to all bins by construction. The uncertainties shown by the solid error bars are statistical only, while the dotted error bars show the total uncertainty including systematics.

5.8. Conclusion

In this Chapter, the production asymmetry of $B^{\pm}$ mesons at LHCb was measured using the $B^{\pm} \to D\pi^{\pm}$ final state, where raw asymmetries were corrected for detection asymmetry effects in seven bins of $B^{\pm}$ kinematics. The phase space averaged production

asymmetry was measured to be:

$$A_{B_u} = (+0.02 \pm 0.17 \pm 0.23)\% \tag{5.12}$$

which is consistent with zero given the current level of statistics. No strong dependence of A_{B_u} on $B^\pm$ kinematics is evident. The production asymmetries measured at $\sqrt{s} = 7$ TeV and $\sqrt{s} = 8$ TeV are:

$$A_{B_u}^{7\text{ TeV}} = (+0.17 \pm 0.31 \pm 0.35)\% \tag{5.13}$$

$$A_{B_u}^{8\text{ TeV}} = (-0.22 \pm 0.20 \pm 0.26)\% \tag{5.14}$$

both of which are consistent with zero asymmetry. These measurements represent the first use of the $B^\pm \to D\pi^\pm$ final state in measuring the production asymmetry.

Using the raw asymmetries measured in $B^\pm \to D\pi^\pm$, the $\mathcal{CP}$ asymmetry in $B^\pm \to J/\psi K^\pm$ decays was measured under the assumption that zero $\mathcal{CP}$-violation occurs in favoured $B^\pm \to D\pi^\pm$ decays. The $\mathcal{CP}$ asymmetry was measured to be:

$$A_{CP}^{J/\psi K} = (+0.10 \pm 0.30 \pm 0.16)\% \tag{5.15}$$

which is consistent with zero as expected, but with a statistical precision that improves upon the current world average by a factor of two.

Chapter 6.

Search for $B_c \to D^{(*)}h$ decays

In this Chapter, an exploratory search for $B_c^- \to \bar{D}^{(*)}h^-$ decays is performed, where $h \in \{\pi, K\}$ and charge conjugation is implied. The analysis makes use of the upper sideband regions of the suppressed ADS modes $B^\pm \to [K^\mp\pi^\pm(\pi^\mp\pi^\pm)]_D h^\pm$ to search for fully reconstructed and partially reconstructed B_c decays, and employs the favoured $B^\pm \to [K^\pm\pi^\mp(\pi^\mp\pi^\pm)]_D\pi^\pm$ mode as a normalisation channel. The theoretical motivation for this study is outlined in Section 6.1, while the event selection and signal extraction fits are detailed in Sections 6.2 and 6.3, respectively. An analysis using the CLs method is performed in Section 6.4 to assess the potential significance of any observed signals.

6.1. Motivation

In the Standard Model, B_c mesons are the only bound states consisting of two heavy quarks of different flavour, namely the $\bar{b}$ and c quarks. Their formation requires the production of both a $b\bar{b}$ and a $c\bar{c}$ pair, which is suppressed by a significant factor relative to the lighter B mesons.

This analysis searches for $B_c^- \to \bar{D}^0\pi^-$ and $B_c^- \to \bar{D}^0K^-$ decays in the 3.0 fb^{-1} Run I dataset, where the $\bar{D}^0$ is reconstructed in the two Cabibbo-favoured final states from Chapter 3 that yield highest statistics: $\bar{D}^0 \to K^+\pi^-$ and $\bar{D}^0 \to K^+\pi^-\pi^+\pi^-$. This search is extended to include the partially reconstructed $B_c \to (\bar{D}^{*0} \to \bar{D}^0\{\pi^0, \gamma\})\pi^-$ and $B_c^- \to (\bar{D}^{*0} \to \bar{D}^0\{\pi^0, \gamma\})K^-$ decays, where the neutral particle from the D^{*0} decay (indicated in braces) is missed in the invariant mass sum.

These decays are of interest because they proceed via suppressed $b \to u$, penguin or annihilation transitions (see Figure 6.1), none of which have been observed in a B_c decay.

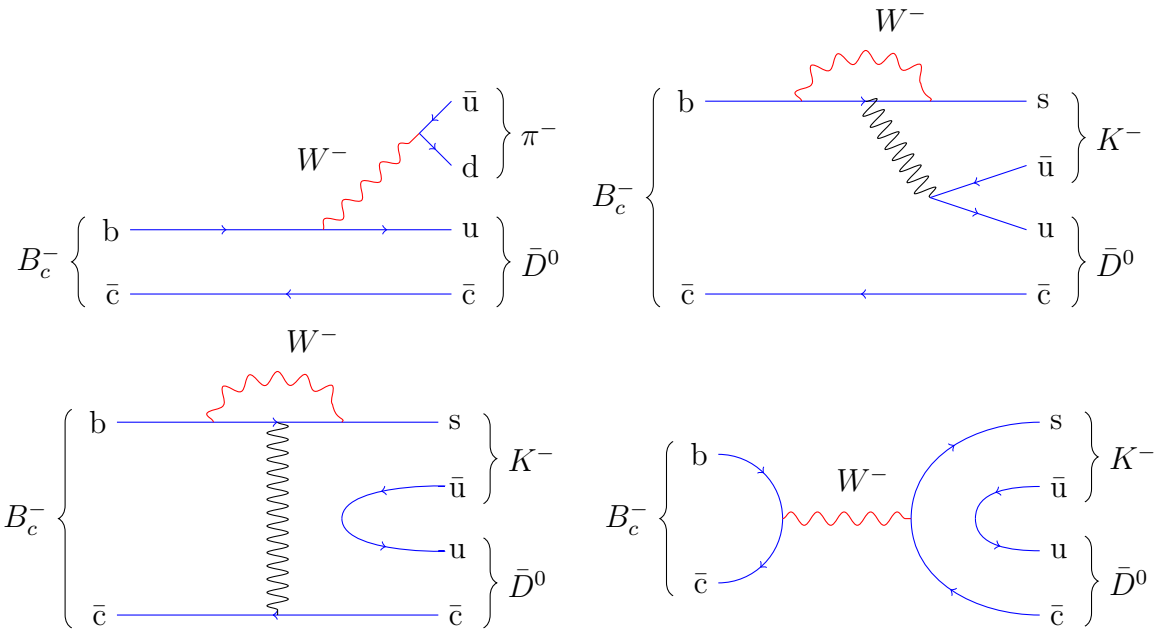

Figure 6.1.: Tree (top left), time-like penguin (top right), space-like penguin (bottom left) and annihilation (bottom right) diagrams for the decays studied within this Chapter. Only the rare $b \to u$ tree process is favoured for the $B_c^- \to \bar{D}^0\pi^-$ final state. By their topology, the other three processes favour $B_c^- \to \bar{D}^0 K^-$ decays.

An estimate of the expected $B_c \to \bar{D}^0\pi$ yield may be taken from the recent LHCb measurement of the B_c lifetime [18], where 2886 $B_c^- \to J/\psi\pi^-$ decays and 586,000 $B^- \to J/\psi K^-$ decays were measured in 3 fb^{-1}. The normalisation mode for the search presented in this Chapter is $B^- \to D^0\pi^-$, in which around 300,000 events are reconstructed (see Section 6.2). The $B^- \to J/\psi K^-$ mode has also been studied in Chapter 5, obtaining a high purity signal sample of 780,000 events.[1] From these four yields, an approximate value for the ratio of efficiencies can be determined:

$$\frac{\eta_{J/\psi K}}{\eta_{\bar{D}\pi}} = \frac{N(B^- \to J/\psi K^-)}{N(B^- \to D^0\pi^-)} \times \frac{\mathcal{B}(B^- \to D^0\pi^-)}{\mathcal{B}(B^- \to J/\psi K^-)} \approx 3 \times 5 = 15 \tag{6.1}$$

The leading Feynman diagrams for $B_c^- \to J/\psi\pi^-$ and the signal mode $B_c \to \bar{D}^0\pi^-$ are identical. Assuming QCD factors are similar in both cases, the dominant difference is the

[1] This yield is larger than the one quoted in Chapter 5, as it contains events that pass either the TIS or TOS triggers at L0. For the $A_{CP}^{J/\psi K}$ measurement, only TIS events were selected.

Cabibbo vertex factor, $|V_{ub}|/|V_{cb}| = 0.00355/0.04117$. As will be detailed in Section 6.2, the analysis selection is approximately three times less efficient for B_c decays relative to B_u decays, a factor that one can conservatively assume is unity in the J/ψ-based analysis. Overall, this gives:

$$N(B_c^- \to \bar{D}^0\pi^-) \approx N(B_c^- \to J/\psi\pi^-) \times \left(\frac{0.00355}{0.04117}\right)^2 \times \frac{\eta_{\bar{D}\pi}}{\eta_{J/\psi K}} \times \tfrac{1}{3} \approx 1 \text{ event.} \qquad (6.2)$$

However, this expectation may be enhanced by penguin amplitudes if they are dominant. This is the case in charmless B_u decays, which share an identical set of diagrams to those in Figure 6.1 with only the spectator quark changed. If such amplitudes dominate, they will be seen predominantly in the $B_c^- \to \bar{D}^0 K^-$ mode, which is Cabibbo-favoured (compared to $B_c^- \to \bar{D}^0\pi^-$) for all diagrams in Figure 6.1, aside from the tree amplitude.

It is also noted that, unlike B_u decays, the annihilation contribution is expected to be significant in B_c decays. This process will also favour the $\bar{D}^0 K^-$ final state rather than $\bar{D}^0\pi^-$. As such, a search for these final states in the current 3fb^{-1} dataset is well motivated. The branching fraction estimates in the literature vary considerably; a selection are recorded in Table 6.1 for reference.

	Final state, X	$\mathcal{B}(B_c \to X)$	reference	relative to decay (1)
(1)	$J/\psi\pi^-$	1.3×10^{-3}	[80]	1
(2)	$J/\psi D_s^-$	1.7×10^{-3}	[80]	~ 1
(3)	$J/\psi D_s^-$	2.4×10^{-3}	[81]	~ 1
(4)	$\bar{D}^0\pi^-$	2.3×10^{-7}	[81]	$\sim 2 \times 10^{-4}$
(5)	$\bar{D}^0 K^-$	1.3×10^{-7}	[81]	$\sim 1 \times 10^{-4}$
(6)	$\bar{D}^0\pi^-$	2.3×10^{-6}	[82]	$\sim 2 \times 10^{-3}$
(7)	$\bar{D}^0 K^-$	4.8×10^{-5}	[82]	$\sim 4 \times 10^{-2}$

Table 6.1.: Branching fraction estimates from the literature. It is noted that (4) and (6), as well as (5) and (7), are quite inconsistent, and that neither align with the naive Cabibbo factor scaling, $(|V_{ub}|/|V_{cb}|)^2 \approx 7 \times 10^{-3}$, described in the text.

The observables of interest in this search are:

$$r_{B_c}^{D^{(*)}h} = \frac{f_c}{f_u} \times \mathcal{B}(B_c^+ \to D^{(*)}h^+) \qquad (6.3)$$

where $h \in \{\pi, K\}$, f_c/f_u represents the ratio of fragmentation fractions for c and u quarks, and $\mathcal{B}(B_c^\pm \to D^{(*)}h^\pm)$ represents the branching fraction for the B_c decay. Using

the branching fraction estimate for decay (1) in Table 6.1, and the measurement of the production ratio [17],

$$\frac{f_c}{f_u} \times \frac{\mathcal{B}(B_c \to J/\psi\pi^-)}{\mathcal{B}(B_u \to J/\psi K^-)} = (6.83 \pm 0.18 \pm 0.09) \times 10^{-3} \tag{6.4}$$

one can deduce that $\frac{f_c}{f_u} \approx \frac{1}{200}$. Using decay (7) in Table 6.1, this suggests that $r_{B_c}^{DK} \approx 2.5 \times 10^{-7}$, which falls around the limit of sensitivity in this analysis.

The final states of both fully reconstructed $B_c \to Dh$ decays are identical to the suppressed ADS $B^\pm \to [\pi^\pm K^\mp(\pi^\pm\pi^\mp)]_D h^\pm$ modes, which have been studied in detail in Chapter 3. As a reminder, the signature of suppressed ADS decays is that the kaon from the D decay is of opposite charge to the bachelor particle from the B decay. In contrast, the favoured counterpart $B^\pm \to [K^\pm\pi^\mp(\pi^\pm\pi^\mp)]_D h^\pm$ decays have a kaon and a bachelor with the same charge. To perform a search for $B_c^\pm \to D^{(*)}\pi^\pm$ and $B_c^\pm \to D^{(*)}K^\pm$ decays, suppressed ADS $B^\pm \to [\pi^\pm K^\mp(\pi^\pm\pi^\mp)]_D\pi^\pm$ and $B^\pm \to [\pi^\pm K^\mp(\pi^\pm\pi^\mp)]_D K^\pm$ candidates are studied in the invariant mass region $[5799 - 6899]$ MeV/c^2, using the favoured $B^\pm \to [K^\pm\pi^\mp(\pi^\pm\pi^\mp)]_D\pi^\pm$ decays as a normalisation mode in order to measure:

$$r_{B_c}^{D^{(*)}h} = \frac{\mathcal{N}(B_c^\pm \to D^{(*)}h^\pm)}{\mathcal{N}(B^\pm \to D^0\pi^\pm)} \times \mathcal{B}(B^\pm \to D^0\pi^\pm) \times \eta \tag{6.5}$$

where $\mathcal{N}(B_c^\pm \to D^{(*)}h^\pm)$ represents the number of $B_c^\pm \to D^{(*)}h^\pm$ decays observed, $\mathcal{N}(B^\pm \to D^0\pi^\pm)$ represents the number of favoured $B^\pm \to D^0\pi^\pm$ normalisation decays observed in the same sample, $\mathcal{B}(B^\pm \to D^0\pi^\pm)$ represents the normalisation mode branching fraction and η represents the relative efficiency of reconstructing and selecting B_c and B_u mesons decaying to the same final state. The relative efficiency term η is evaluated in Section 6.2, while the signal and normalisation yields are evaluated in Section 6.3.

6.2. Event selection

The selection strategy used to select both $B_c \to D^{(*)}h$ signal decays and $B_u \to D\pi$ normalisation decays closely resembles the ADS/GLW selection strategy described in Section 3.3.2, adopting a two-stage BDT selection with additional rectangular cuts to reduce the combinatorial background rate. The B_c search is performed on $B^\pm \to [K^\mp\pi^\pm(\pi^\mp\pi^\pm)]_D h^\pm$ candidates falling within an invariant mass window $[5799 - 6899]$ MeV/c^2, while the normalisation mode is selected with the same invariant mass window used in Chapter 3, namely $[5079 - 5899]$ MeV/c^2.

6.2.1. BDT training and cut optimisation

As was the case in Section 3.3.2, two BDTs are trained for both the $D \to 2h$ and $D \to 4h$ modes. The variables employed in the B_c selection BDTs are identical to those used in the ADS/GLW selection (Table 3.2), but the training is performed using samples of simulated $B_c \to Dh$ signal decays instead of $B_u \to Dh$ signal decays in order to increase the B_c signal efficiency. The background samples are taken from the *favoured* mode sidebands, as illustrated in Figure 3.5; it is important to note that the suppressed mode sidebands are not used in the BDT training, since they contain the B_c signal region being studied.

Loose cuts at > -0.9 are applied to the output classifier responses of BDT1($2h$) and BDT1($4h$) prior to the training of BDT2($2h$) and BDT2($4h$), in an identical manner to the ADS/GLW selection. The B_c BDTs exhibit a high degree of separation, as evidenced by their output classifier distributions in Figure 6.2. To determine the optimal BDT2 cuts to apply, a 2-dimensional optimisation procedure is carried out across a range of BDT2($2h$) and BDT2($4h$) values.

For this exercise, an imagined signal yield of $B_c^\pm \to D\pi^\pm$ events, corresponding to a measurement of $r_{B_c}^{D\pi} = 10^{-7}$, is considered. For a range of cuts on the 2-body and 4-body second stage BDTs, the B_c signal extraction fit (later described in Section 6.3) is performed with the signal yields blinded. A value of the background level **B** is calculated for each pair of BDT cuts using the integrated background yield within $\pm 3\sigma$ of the $B_c \to D\pi$ signal PDF mean, where σ is the width of the B_c signal component.[2]

[2] Both the mean and width of the B_c signal shape are fully fixed at all points in this analysis, as is described in Section 6.3.

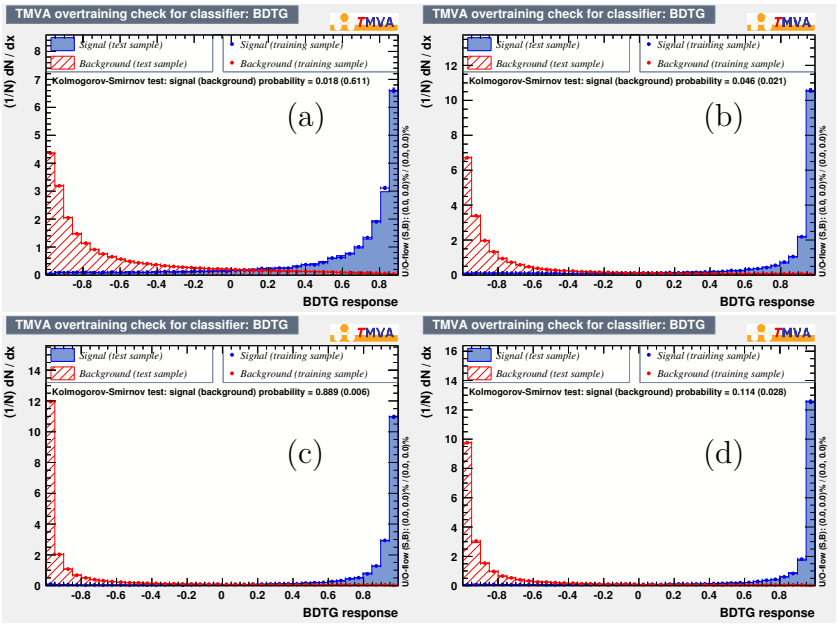

Figure 6.2.: BDT1 and BDT2 output classifier distributions for the B_c search. In (a), the first stage BDT response for the $D^0 \to \pi^\pm K^\mp$ case is shown, with the second stage response shown in (b). The corresponding distributions for the $D^0 \to \pi^\pm K^\mp \pi^\pm \pi^\mp$ case are shown in (c) and (d), respectively.

The imagined signal yield **S** for the same pair of BDT cuts is then calculated using the corresponding normalisation yield $\mathcal{N}(B^\pm \to D^0\pi^\pm)$ as input to Equation 6.5, along with $r_{B_c}^{D\pi} = 10^{-7}$, $\mathcal{B}(B^\pm \to D^0\pi^\pm) = 4.81 \times 10^{-3}$ [12] and $\eta = 1$.[3] The signal significance is then determined using a Punzi figure of merit $\mathbf{S}/(\sqrt{\mathbf{B}} + a/2)$, which is calculated for each pair of BDT cuts considered using $a = 3$ [83].

The values of $\mathbf{S}/(\sqrt{\mathbf{B}} + a/2)$ for each pair of BDT cuts are shown in Figure 6.3, where the colour of a given bin represents the signal significance as indicated by the z-axis scale. The bin with optimal significance corresponds to cuts of > 0.95 on the 2-body BDT and > 0.99 on the 4-body BDT; these cuts are applied to both the signal and normalisation channels as part of the offline selection procedure, along with the > -0.9 cuts applied to the 2-body and 4-body first stage BDTs.

An important input to each $r_{B_c}^{D^{(*)}h}$ measurement is the normalisation yield of favoured $B^\pm \to D\pi^\pm$ decays. The invariant mass fit used to determine the normalisation yield is identical to that used in both Chapters 3 and 5, and the yield values measured at the chosen BDT cuts (BDT2($2h$) > 0.95 and BDT2($4h$) > 0.99, as detailed above) are

[3] The use of $\eta = 1$ aligns with the $r_{B_c}^{DK} \approx 10^{-7}$ estimate made in Section 6.1, where the same reconstruction and selection efficiency for B_c and B_u decays is assumed.

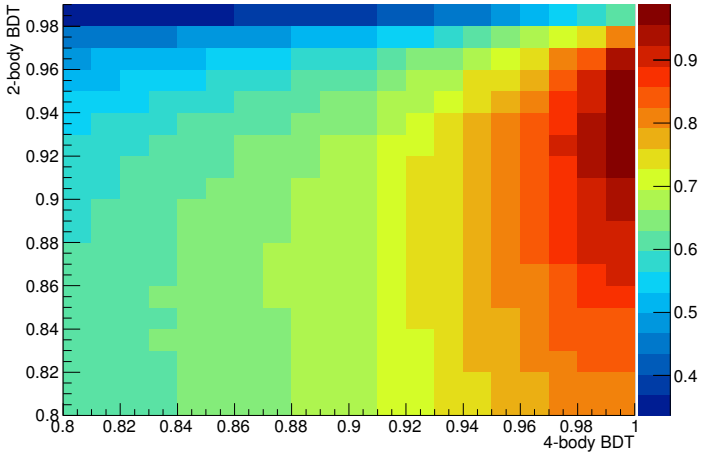

Figure 6.3.: Imagined $B_c \to D\pi$ signal significance for a range of cuts on the second stage 2-body and 4-body BDTs. The bin with the highest signal significance corresponds to cuts of > 0.95 on the 2-body BDT and > 0.99 on the 4-body BDT. The efficiency of this pair of cuts on both B_c and B_u decays is evaluated in Section 6.2.4.

listed in Table 6.2. The yields are measured separately for $B^\pm \to [K^\pm\pi^\mp]_D\pi^\pm$ and $B^\pm \to [K^\pm\pi^\mp\pi^\pm\pi^\mp]_D\pi^\pm$ decays, and their sum employed in the determination of each $r_{B_c}^{D^{(*)}h}$.

Decay mode	Yield
$B^\pm \to [K^\pm\pi^\mp]_D\pi^\pm$	$213,650 \pm 450$
$B^\pm \to [K^\pm\pi^\mp\pi^\pm\pi^\mp]_D\pi^\pm$	$95,812 \pm 316$
Total	$309,462 \pm 550$

Table 6.2.: $B^\pm \to [K^\pm\pi^\mp(\pi^\pm\pi^\mp)]_D\pi^\pm$ normalisation yield, as measured at the BDT cut values chosen for the analysis. The invariant mass fit used to measure the normalisation yield is identical to the one employed in Chapters 3 and 5.

6.2.2. Rectangular cuts

In addition to the two-stage BDT selection, a series of rectangular cuts are applied to both the signal and normalisation modes to further reduce the combinatoric background rate. The cuts applied are identical to those applied to the favoured and suppressed modes in the ADS/GLW analysis, with the exception of the D^0 flight distance requirement defined by Equation 3.58. The cut applied is loosened from > 2 to > 0, since the charmless

contributions in the normalisation mode are negligible and no significant charmless contributions are expected in the B_c search window.

6.2.3. Particle identification requirements

In the B_c search, the D^0 daughter PID requirements applied are identical to those applied in both Chapters 3 and 5. The bachelor PID requirements applied to the normalisation mode also mirror those applied previously, where $B_u \to Dh$ decays containing a kaon are isolated using a $\mathrm{DLL}_{K\pi} > 12$ requirement. Candidates failing this requirement are placed in the sample composed predominantly of $B \to D\pi$ decays. Both samples are fit simultaneously in order to determine the total $B \to D\pi$ normalisation yield. The efficiencies of the PID requirements on the bachelor are determined using a data-driven approach, as detailed in Section 3.3.3.

The bachelor PID requirement in the B_c signal search is chosen such that the efficiencies for kaons and pions are highly similar. This ensures that the analysis is sensitive to observing both the $B_c \to D^{(*)}\pi$ and $B_c \to D^{(*)}K$ signal modes. Decays involving a bachelor kaon are selected by requiring $\mathrm{DLL}_{K\pi} > 2$, while decays involving a pion bachelor are selected by requiring $\mathrm{DLL}_{K\pi} < 2$. Both samples are fit simultaneously, such that no events are explicitly rejected by the bachelor PID requirement. The efficiencies of the bachelor PID requirements are listed in Table 6.3, and are evaluated using the procedure detailed in Section 3.3.3, with $B^\pm \to D\pi^\pm$ decays employed as a reference signal sample.

Bachelor PID requirement	2011, B^+(%)	2011, B^-(%)	2012, B^+(%)	2012, B^-(%)
$\epsilon^K_{\mathrm{PID}}$, $\Delta LL_{K/\pi} > 2$	93.42	93.48	93.71	93.68
$\epsilon^\pi_{\mathrm{PID}}$, $\Delta LL_{K/\pi} < 2$	91.95	91.93	91.59	91.51

Table 6.3.: PID efficiencies for the bachelor in $B \to Dh$ decays, for both B^+ and B^- candidates in 2011 and 2012 data. These efficiencies are taken to represent $B_c \to Dh$ decays, with an associated systematic uncertainty that is assigned in Section 6.4.

The assumption is made that the B_c bachelor particle identification efficiencies are well described by the B_u efficiencies. It is well known that the PID efficiency in LHCb varies as a function of track momentum, pseudorapidity and number of tracks in the underlying event. As such, it is possible for the B_c and B_u PID efficiencies to differ, as a result of the additional phase space available to the bachelor in B_c decays. Inspecting the bachelor

momentum distributions in simulated $B_c \to D\pi$ and $B_u \to D\pi$ decays (Figure 6.4) does not reveal a large difference, however. A systematic uncertainty for the use of B_u PID efficiencies to describe B_c decays is nevertheless assigned in Section 6.4.

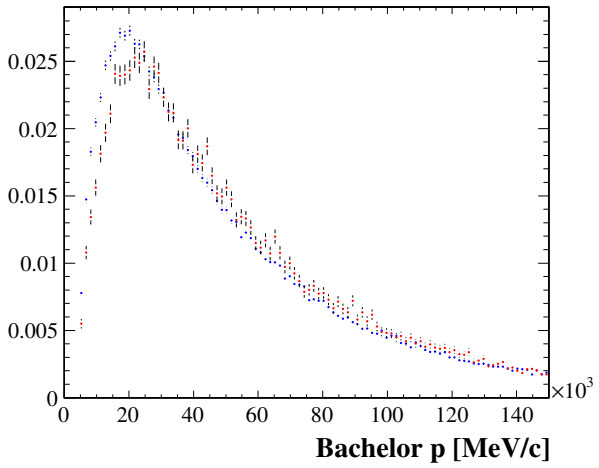

Figure 6.4.: Comparison of bachelor momentum distributions in fully selected $B_c \to D\pi$ (red) and $B_u \to D\pi$ (blue) simulated events. Both distributions have been normalised to unit integral. The assumption of identical bachelor PID efficiencies in B_c and B_u decays is supported by the agreement shown between the distributions.

6.2.4. Relative efficiency for B_c and B_u decays

To evaluate the relative efficiency for selecting B_c and B_u decays, samples of simulated $B_c^\pm \to [\pi^\pm K^\mp(\pi^\pm\pi^\mp)]_D\pi^\pm$ and $B_u^\pm \to [K^\pm\pi^\mp(\pi^\pm\pi^\mp)]_D\pi^\pm$ decays are used. These modes are also taken to represent cases where the bachelor is a kaon. This assumption has been tested by calculating the relative efficiency using simulated samples of $B_c^\pm \to [\pi^\pm K^\mp(\pi^\pm\pi^\mp)]_D K^\pm$ decays, where the values found are fully consistent with those determined using the $B_c \to D\pi$ samples.

The relative efficiency ratio is defined as:

$$\eta = \frac{\epsilon_{\rm acc}(B_u^\pm \to Dh^\pm)}{\epsilon_{\rm acc}(B_c^\pm \to Dh^\pm)} \times \frac{\epsilon_{\rm strip}(B_u^\pm \to Dh^\pm)}{\epsilon_{\rm strip}(B_c^\pm \to Dh^\pm)} \times \frac{\epsilon_{\rm sel}(B_u^\pm \to Dh^\pm)}{\epsilon_{\rm sel}(B_c^\pm \to Dh^\pm)} \times \frac{\epsilon_{\rm trig}(B_u^\pm \to Dh^\pm)}{\epsilon_{\rm trig}(B_c^\pm \to Dh^\pm)}$$

where $\epsilon_{\rm acc}$ denotes the LHCb acceptance efficiency, $\epsilon_{\rm strip}$ represents the stripping efficiency for fully reconstructed events falling within the acceptance, $\epsilon_{\rm sel}$ represents the offline selection efficiency for stripped candidates and $\epsilon_{\rm trig}$ represents the efficiency for offline selected events to pass the trigger requirements. The values for each efficiency component are listed in Table 6.4, and correspond to an overall correction of $\boldsymbol{\eta = 3.23 \pm 0.07}$ for

the 2-body case and $\boldsymbol{\eta = 3.10 \pm 0.10}$ for the 4-body case. The larger selection efficiency for B_u decays largely arises due to the smaller lifetime of B_c mesons, where fewer B_c decays are retained by a lifetime cut of > 0.2 ps applied to all candidates during the stripping phase (see Section 3.3.1).

The uncertainties quoted are at the $2-3\%$ level, and arise from the use of finite simulated samples; they are considered as a source of systematic uncertainty in Section 6.4. Additional uncertainty may arise from mis-modelling of the L0 trigger in simulation, resulting in an incorrect estimate of the trigger efficiency. Such effects largely cancel in construction of the ratio η, but the average difference between the B_c and B_u trigger efficiencies across the 2-body and 4-body modes is nevertheless taken as a source of systematic uncertainty. From Table 6.4, the difference in trigger efficiency is 3.2% for the 2-body case, while the corresponding difference is 1.4% in the 4-body case. The average difference, 2.3%, is assigned as a systematic uncertainty.

Mode	ϵ_{acc}	ϵ_{strip}	ϵ_{sel}	ϵ_{trig}	$\epsilon_{\text{tot}} \times 10^{-3}$
$B_c^{\pm} \to [\pi^{\pm} K^{\mp}]_D \pi^{\pm}$	0.134 ± 0.002	0.0288 ± 0.0001	0.310 ± 0.002	0.925 ± 0.002	1.11 ± 0.02
$B^{\pm} \to [\pi^{\pm} K^{\mp}]_D \pi^{\pm}$	0.171 ± 0.002	0.0765 ± 0.0002	0.286 ± 0.001	0.957 ± 0.001	3.58 ± 0.04
$B_c^{\pm} \to [\pi^{\pm} K^{\mp} \pi^{\pm} \pi^{\mp}]_D \pi^{\pm}$	0.124 ± 0.002	0.0111 ± 0.0001	0.218 ± 0.004	0.948 ± 0.004	0.285 ± 0.007
$B^{\pm} \to [\pi^{\pm} K^{\mp} \pi^{\pm} \pi^{\mp}]_D \pi^{\pm}$	0.158 ± 0.002	0.0255 ± 0.0002	0.228 ± 0.003	0.962 ± 0.002	0.883 ± 0.016

Table 6.4.: Acceptance and selection efficiencies for $B_c^{\pm} \to Dh^{\pm}$ and $B_u^{\pm} \to Dh^{\pm}$ decays, taken from samples of simulated $B_c^{\pm} \to [\pi^{\pm} K^{\mp} (\pi^{\pm} \pi^{\mp})]_D \pi^{\pm}$ and $B_u^{\pm} \to [K^{\pm} \pi^{\mp} (\pi^{\pm} \pi^{\mp})]_D \pi^{\pm}$ decays. The efficiencies listed correspond to overall corrections of $\eta = 3.23 \pm 0.07$ for the 2-body case, and $\eta = 3.10 \pm 0.10$ for the 4-body case.

6.2.5. Mis-modelling of B_c spectra in simulation

It is possible that the simulation does not correctly reproduce the B_c kinematic spectra, leading to an incorrect estimate of the efficiency corrections η as calculated above. To test the robustness of the efficiency estimates, three highly discriminating variables in the BDT training have been studied: bachelor p_T, the p_T asymmetry variable A_{p_T}, and the log of the cylindrical coordinate separation of the B_c from the primary vertex, $\log(\Delta\rho)$. For this study, simulated $B_c \to [\pi K]_D \pi$ decays have been used.

The distributions of each parameter P are altered such that they sit $\pm 0.1 \mu_{\text{P}}$ away from the nominal distributions, where μ_{P} represents the mean of the nominal parameter distribution. These shifts are illustrated in Figure 6.5, where the nominal parameter

distributions are displayed in blue. The distributions that have been shifted by $+0.1\mu_{\mathrm{P}}$ and $-0.1\mu_{\mathrm{P}}$ are displayed in red and magenta, respectively.

The full selection is applied to the events after shifting the distributions, and the efficiency corrections η re-evaluated. This procedure is performed independently for each of the three parameters considered. The values of η determined in each instance are listed in Table 6.5. The spread in η is determined for each parameter as the difference between the η values calculated using the red and magenta distributions; the average spread across the three variables is found to be 0.24. Half of this average, 0.12, is taken as a source of systematic uncertainty due to possible mis-modelling of the B_c spectra in simulation, corresponding to a 3.7% uncertainty on the correction term η.

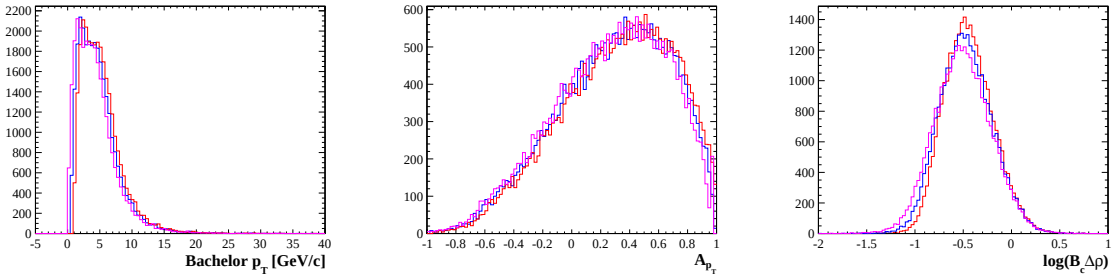

Figure 6.5.: Distribution of highly ranked BDT variables in $B_c \to D\pi$ simulation. The blue histograms represent the nominal distributions, whereas the red and magenta histograms represent the shifted distributions which have been moved away from the nominal distributions by $\pm 0.1\mu_{\mathrm{P}}$, respectively (μ_{P} is the mean of the nominal distribution for a given parameter P). The red and magenta distributions are used to determine alternative efficiency corrections η, in order to determine the systematic uncertainty arising from mis-modelling of the B_c spectra in simulation.

Variable	$\eta(-0.1\mu_{\mathrm{P}})$	$\eta(+0.1\mu_{\mathrm{P}})$	Difference
Bachelor p_T	3.49 ± 0.07	3.11 ± 0.06	0.37
A_{p_T}	3.35 ± 0.07	3.19 ± 0.07	0.16
$\log(\Delta\rho)$	3.36 ± 0.07	3.19 ± 0.06	0.18
		Average/2	0.12

Table 6.5.: Shift in efficiency corrections due to variation in highly ranked BDT variable distributions in B_c simulation. The efficiencies have been calculated using the red ($+0.1\mu_{\mathrm{P}}$) and magenta ($-0.1\mu_{\mathrm{P}}$) distributions illustrated in Figure 6.5. Half of the average spread in η values, 0.12, is taken as a source of systematic uncertainty on the η corrections, corresponding to an uncertainty of 3.7%.

6.2.6. B_c lifetime correction

The B_c lifetime employed in EvtGen was $\tau_{\text{gen}} = 0.454$ ps, whereas the current HFAG world average value is $\tau_{\text{HFAG}} = 0.507 \pm 0.009$ ps [84]. As a lifetime cut of > 0.2 ps is applied to all B candidates in the stripping, this difference has the potential to bias the efficiency estimates from the simulation, reporting a lower B_c efficiency than expected.

A lifetime correction has been determined by evaluating exponential integrals above 0.2 ps for both τ_{gen} and τ_{HFAG}, as shown in Figure 6.6. The lifetime distribution corresponding to the generated simulated events is shown in red, while the distribution corresponding to the HFAG world average is shown in blue. The stripping cut is shown by the vertical dotted line at 0.2 ps.

The ratio of PDF integrals in the region above 0.2 ps is determined to be $I_{\text{HFAG}}/I_{\text{gen}} = 1.049$, indicating that a larger proportion of events in the HFAG distribution pass the stripping requirement, as expected. This ratio is applied as a correction to the values of η determined in Section 6.2.4, where the HFAG uncertainty is taken as a source of systematic uncertainty. The validity of this correction is justified by the flatness of the total efficiency as a function of B_c decay time, as illustrated by Figure 6.7.

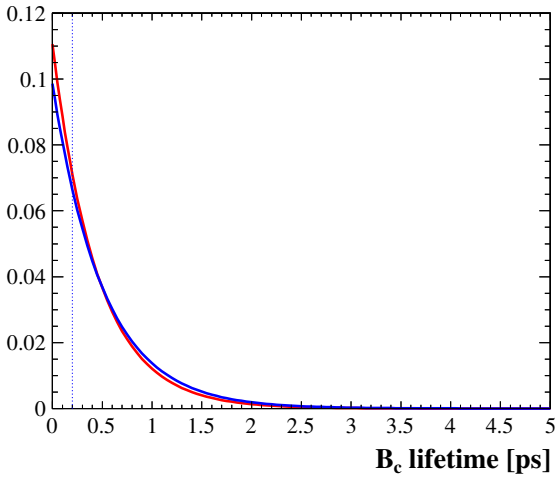

Figure 6.6.: Lifetime PDFs corresponding to the B_c lifetime used in MC generation (red curve, 0.454 ps), and the current HFAG world average B_c lifetime (blue curve, 0.507 ps). The ratio of PDF integrals above the stripping cut of 0.2 ps, $I_{\text{HFAG}}/I_{\text{gen}} = 1.049$, is used to correct the measured efficiency ratios η from Section 6.2.4.

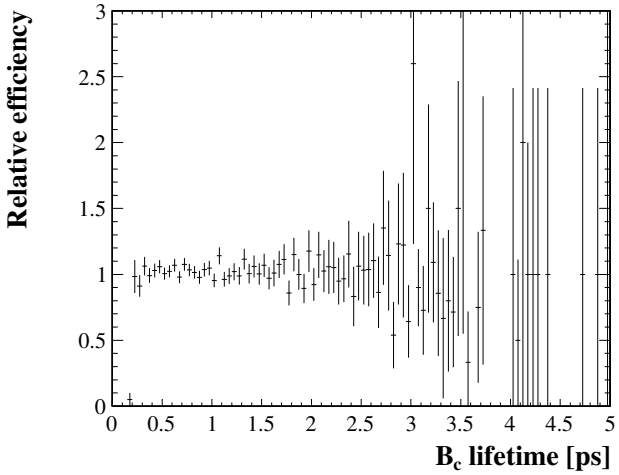

Figure 6.7.: Relative efficiency of the selection, reconstruction and acceptance as a function of B_c lifetime for simulated $B_c \to D\pi$ decays. The stripping cut applied at 0.2 ps is evident, and the full selection is shown to be unbiased with respect to the lifetime of B_c candidates due to the flatness of the observed distribution.

6.2.7. Summary of Monte Carlo correction systematics

The analysis relies upon simulation to determine the efficiency corrections η. In calculating these corrections, several sources of systematic uncertainty are considered:

- Finite simulated samples $(2 - 3\%)$
- Mis-modelling of the L0 trigger (2.3%)
- B_c lifetime correction (1.8%)
- Mis-modelling of B_c spectra (3.7%)

The total uncertainty from the use of simulation to determine efficiencies is thus 5.6%, which will be considered in Section 6.4 as a source of systematic uncertainty.

6.3. Invariant mass fits

Two invariant mass fits feature in this analysis, both of which are described below.

6.3.1. $B^\pm \to D\pi^\pm$ normalisation fit

The first fit measures the normalisation yield of $B^\pm \to D\pi^\pm$ events, and employs an identical strategy to that detailed in Chapters 3 and 5, aside from the following differences:

- No split by B candidate charge is performed, as the measurement of the charge asymmetry is not applicable to the B_c search.
- The fit is performed only on favoured $B^\pm \to Dh^\pm$ decays, but adopts the familiar simultaneous fit to $B^\pm \to D\pi^\pm$ and $B^\pm \to DK^\pm$ candidates.
- $B^\pm$ candidates are required to pass the B_c selection requirements detailed in Section 6.2, with the exception of the invariant mass range which is maintained at $[5079 - 5899]$ MeV/c^2.

The total normalisation yield measured is $\mathcal{N}(B^\pm \to [K^\pm\pi^\mp(\pi^\pm\pi^\mp)]_D\pi^\pm) = 309,462 \pm 550$, as listed in Table 6.2. This yield is used as input into Equation 6.5, in order to construct the various $r_{B_c}^{D^{(*)}h}$ observables.

6.3.2. $B_c^\pm \to D^{(*)}h^\pm$ signal extraction fit

In order to measure $\mathcal{N}(B_c^\pm \to D^{(*)}\pi^\pm)$ and $\mathcal{N}(B_c^\pm \to D^{(*)}K^\pm)$, a simultaneous invariant mass fit to the $B^\pm \to D\pi^\pm$ and $B^\pm \to DK^\pm$ samples is performed in the region $[5799 - 6899]$ MeV/c^2. This mass range is chosen for the following reasons:

- The contributions from fully reconstructed $B_c \to Dh$ and partially reconstructed $B_c \to D^{*0}h$ signal decays are fully contained within this mass range.
- The fit has enough scope to accurately determine the level of combinatoric background.
- Extending the fit to lower invariant mass values requires the addition of PDFs for $B_c \to DhX$ decays, where X contains two or more missing particles. These backgrounds are poorly understood and their inclusion could potentially bias the combinatoric background level estimation.

Fully reconstructed signal PDF

The fit uses a fixed Gaussian PDF to describe the fully reconstructed B_c signal components. The mean of the signal Gaussian is fixed to the PDG B_c mass [12], and is required to be the same in the $D\pi$ and DK slices. The width of the $B_c \to D\pi$ signal shape is taken from a Gaussian fit to the suppressed ADS $B^\pm \to [\pi^\pm K^\mp]_D \pi^\pm$ peak, as shown in Figure 6.9.[4] The measured width from this fit is scaled according to the relative q values of the $B_c \to D\pi$ and $B_u \to D\pi$ decays, $q^\pi_{B_c}/q^\pi_{B_u} = (6276 - 1864 - 140)/(5279 - 1864 - 140) = 1.30$. The fitted width of the suppressed $B^\pm \to D\pi^\pm$ peak is $\sigma_{B_u} = 16.0 \pm 0.6$ MeV/c^2, such that the B_c signal peak width is fixed to be $\sigma^\pi_{B_c} = 20.8 \pm 0.8$ MeV/c^2.

The DK width $\sigma^K_{B_c}$ is related to $\sigma^\pi_{B_c}$ by a fixed ratio $\sigma(DK)/\sigma(D\pi) = 0.951 \pm 0.007$, taken from the normalisation mode fit. The ratio of q values for $B \to DK$ decays is $q^K_{B_c}/q^K_{B_u} = 1.34$, which is slightly larger due to the larger mass of the kaon bachelor. This is also taken into account in the fit.

Partially reconstructed decays

The same parameterisation as the normalisation fit is used to describe partially reconstructed decays where a particle is missed in the invariant mass sum (see Section 3.4.1), including the signal components $B_c \to D^* h$. An additional component at lowest invariant mass is also included to describe partially reconstructed B_c decays where two particles are missed in the invariant mass sum, with shape parameters taken from fits to $B^\pm \to D^{*0}\pi^\pm\pi^0$ simulated events (see Figure 6.8). The fit is performed using the `RooHORNSdini` and `RooHILLdini` PDFs described in Section 3.4.1. All partially reconstructed shape parameters are determined using $B^\pm$ simulated events, with widths scaled appropriately to account for the q^2 difference between B_c and B_u decays. A systematic uncertainty for the use of fixed shape parameters is assigned in Section 6.4.

Particle misidentification

The contributions from misidentified $B_c \to D\pi(K)$ decays in the $B_c \to DK(\pi)$ slice are modelled using the same PDFs employed in the normalisation mode fit, with widths and means scaled as appropriate for the higher invariant mass region begin considered.

[4] This fit differs from the ADS/GLW fit presented in Chapter 3, where the signal PDF is dictated by the high statistics favoured $B^\pm \to D\pi^\pm$ mode.

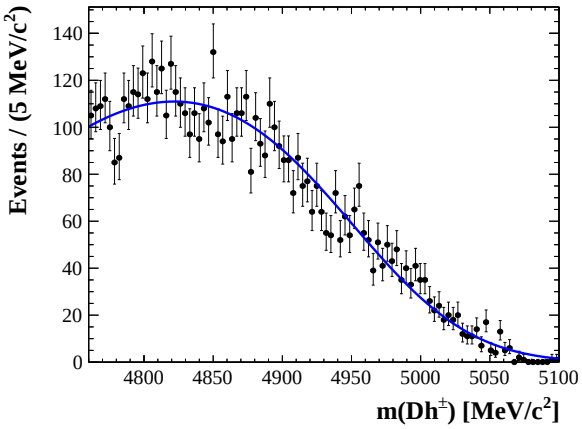

Figure 6.8.: Invariant mass fit to simulated $B^\pm \to D^{*0}\pi^\pm\pi^0$ events, which are used to describe $B_c^\pm \to D^{*0}\pi^\pm\pi^0$ events in the B_c signal extraction fit. The shape parameters are scaled according for the higher invariant mass region considered in the B_c mass fit.

These mis-ID shapes are fully fixed in the fit. The relative proportions of $D\pi$ and DK events in each fit slice (passing and failing the PID cut) are fixed using PID efficiencies for the $\mathrm{DLL}_{K\pi} > (<)2$ cut applied to the bachelor, as listed in Table 6.3. The efficiencies are determined using reference samples of $B^\pm \to D\pi^\pm$ signal events in data. The $\mathrm{DLL}_{K\pi} > (<)2$ cut was chosen to ensure that the pion and kaon PID efficiencies are as similar as possible, such that neither the $B_c \to D^{(*)}\pi$ nor $B_c \to D^{(*)}K$ modes suffer from a loss in potential signal significance. The assumption that the B_c bachelor PID efficiencies are identical to the B_u efficiencies is assigned a systematic uncertainty in Section 6.4.

Combinatoric background

An exponential function is used to describe the combinatoric background, with a freely floating exponential parameter λ that is allowed to be different in the $D\pi$ and DK slices. An exponential PDF, as opposed to the linear PDF used in the normalisation fit, is employed for the following reasons:

- The use of a linear shape in the high statistics normalisation fit gives the fit greater control over the increase in the combinatoric level when moving from higher to lower invariant masses.
- The parameterisation of the combinatoric background PDF is critical in the B_c search, as it influences the intervals determined in the CLs analysis (Section 6.4).

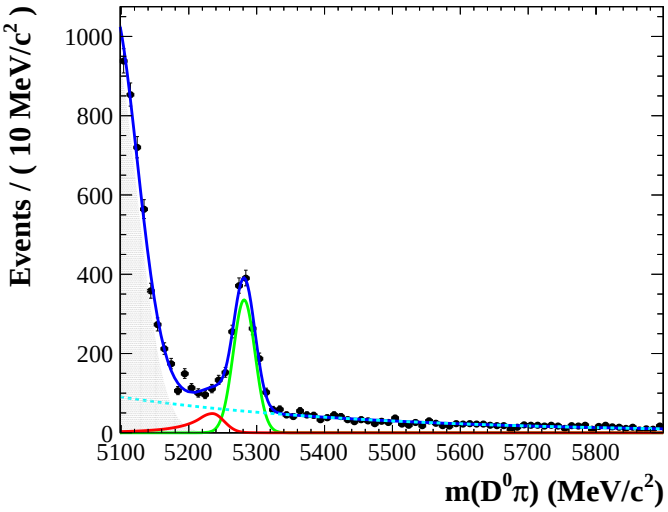

Figure 6.9.: Invariant mass fit to suppressed $B^{\pm} \to [\pi^{\mp} K^{\pm}]_D \pi^{\pm}$ decays using a Gaussian PDF for the signal component. The mean and width of this Gaussian determine the shape parameters of the Gaussian PDF used to describe fully reconstructed $B_c \to Dh$ decays.

An exponential is the most physically well motivated choice of PDF for describing the combinatoric background in the B_c signal extraction fit.

The combinatoric yields in the $D\pi$ and DK slices both float freely, as do the the fully reconstructed $B_c \to Dh$ and partially reconstructed $B_c \to D^*h$ signal yields. The signal yields are allowed to find large negative and positive values. The total partially reconstructed $B_c \to D^*\pi$ and $B_c \to D^*K$ signal yields both consist of two components, namely from the $D^{*0} \to D^0\pi^0$ and $D^{*0} \to D^0\gamma$ sub-decays that produce the missing particle. The π^0 yield relative to the γ yield is fixed using PDG branching fractions, and varied as a source of systematic uncertainty.

The yields of the additional partially reconstructed contributions from $B_c \to Dh\{\pi^0\}$ and $B_c \to D^*h\{\pi^0\}$ decays also float freely, with the requirement that their yields do not fall below -0.1. This restriction is imposed in order to achieve an acceptable level of fit stability with a small estimated distance to the minimum in MINUIT.

The fit to data is shown in Figure 6.10, and in Table 6.6 the yields and shape parameters of the fit are listed. To determine the significance of any $B_c \to D^{(*)}h$ signals, an analysis using the CLs method is performed.

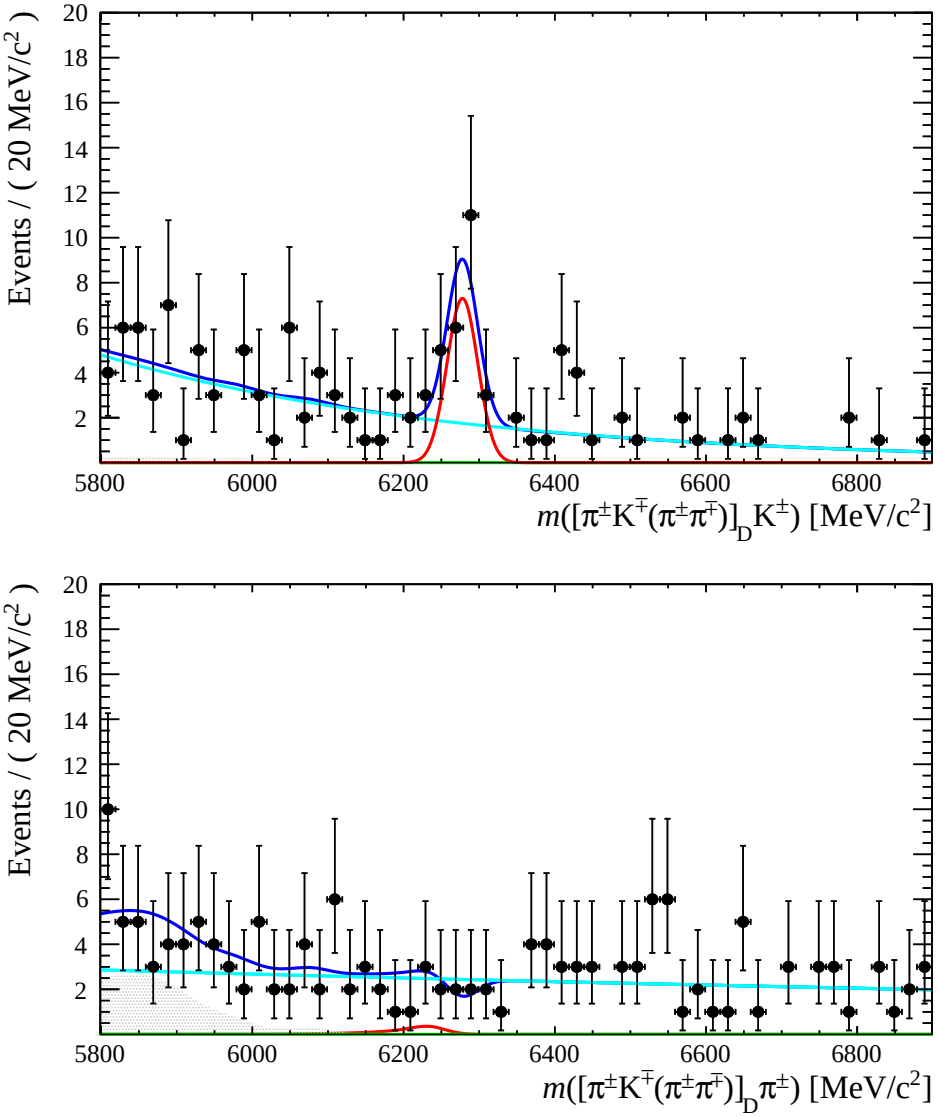

Figure 6.10.: Simultaneous invariant mass fit to $B_c^\pm \to D^{(*)}\pi^\pm$ (bottom plot) and $B_c^\pm \to D^{(*)}K^\pm$ (top plot) candidates in data, in both the $D^0 \to \pi^\pm K^\mp$ and $D^0 \to \pi^\pm K^\mp \pi^\pm \pi^\mp$ final states. The $B_c \to DK$ signal component is plotted in red, with $B_c \to D\pi$ decays indicated in green. Partially reconstructed $B_c \to DhX$ decays are shown by the grey filled regions at low invariant mass. The contribution from combinatoric background events is plotted in cyan, while the total fit PDF is plotted in dark blue.

6.4. Upper limit setting using the CLs method

To determine the significance of any measured signals, the CLs method implemented within the `RooStats` framework [85] is employed. In this method, hypothesis tests are

Parameter	Value
μ	6276 MeV/c^2 (fixed)
$\sigma^{\pi}_{B_c}$	20.8 MeV/c^2 (fixed)
$\sigma(DK)/\sigma(D\pi)$	0.951 (fixed)
$\epsilon^{\pi}_{\mathrm{PID}}$	93.6% (fixed)
$\epsilon^{K}_{\mathrm{PID}}$	91.6% (fixed)
$\lambda^{D\pi}$	-0.0003 ± 0.0006 (floating)
λ^{DK}	-0.0018 ± 0.0035 (floating)
$\mathcal{N}(B_c^{\pm} \to D\pi^{\pm})$	-2 ± 3 (floating)
$\mathcal{N}(B_c^{\pm} \to DK^{\pm})$	20 ± 6 (floating)
$\mathcal{N}(B_c^{\pm} \to D^*\pi^{\pm})$	2 ± 10 (floating)
$\mathcal{N}(B_c^{\pm} \to D^*K^{\pm})$	1 ± 12 (floating)
$\mathcal{N}^{\pi}_{\mathrm{com}}$	132 ± 24 (floating)
$\mathcal{N}^{K}_{\mathrm{com}}$	102 ± 27 (floating)
$\mathcal{N}^{D\pi\{\pi^0\}}$	0 ± 23 (floating)
$\mathcal{N}^{DK\{\pi^0\}}$	9 ± 17 (floating)
$\mathcal{N}^{D^*\pi\{\pi^0\}}$	18 ± 11 (floating)
$\mathcal{N}^{D^*K\{\pi^0\}}$	2 ± 30 (floating)

Table 6.6.: Parameters of the B_c invariant mass fit, as shown in Figure 6.10. The significance of the observed signals are evaluated in Section 6.4.

performed by scanning over a range of $r^{D^{(*)}h}_{B_c}$ values[5], evaluating the p-value at each point.

To compute upper limits on each $r^{D^{(*)}h}_{B_c}$, the $S+B$ hypothesis (signal plus background) is compared to the B hypothesis (background only) at each point, where in the latter instance the signal yield is fixed to zero. Upper limits are then interpreted as the point at which the p-value falls below 5%, corresponding to 95% confidence level. In measuring upper limits for a given $r^{D^{(*)}h}_{B_c}$ observable, all of the other floating variables in the fit are considered as nuisance parameters, including the other three signal yields.

The p-value distributions for each $r^{D^{(*)}h}_{B_c}$ are shown in Figure 6.11, where the 1σ and 2σ contours are indicated by the green and yellow shaded regions, respectively. Upper limits are interpreted as the points at which the observed CLs p-values (black points)

[5] In scanning over $r^{D^{(*)}h}_{B_c}$ values, one is equivalently scanning over measured signal yields through the relationship embodied by Equation 6.5.

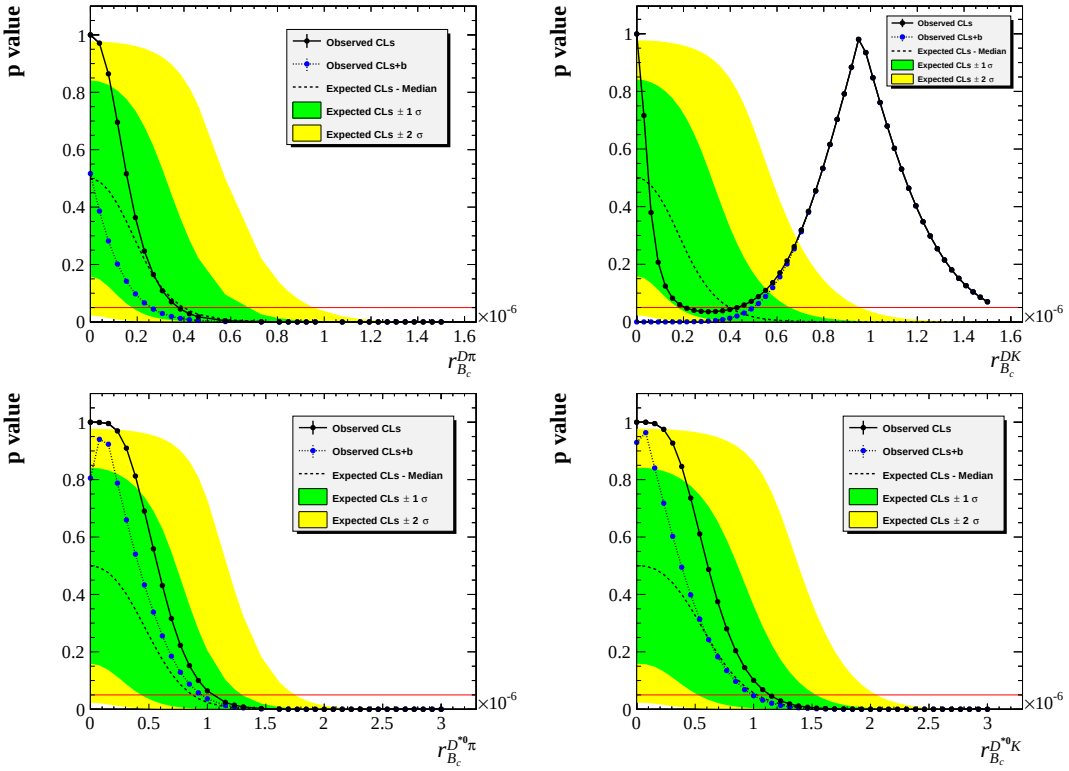

Figure 6.11.: CLs plots for each of the $r_{B_c}^{D^{(*)}h}$ observables. The 1σ and 2σ contours are indicated by the green and yellow shaded regions, respectively. Upper limits are interpreted as the points at which the observed CLs p-values (black points) fall below 5%, as indicated by the red horizontal lines in each plot. A dedicated procedure to determine two-sided uncertainties for $r_{B_c}^{DK}$ is performed, given the significance of the peak observed.

fall below 5%, as indicated by the red horizontal lines in each plot. In the case of $r_{B_c}^{D\pi}$, $r_{B_c}^{D^*\pi}$ and $r_{B_c}^{D^*K}$, the p-value distributions are seen to fall below 5% within the coloured bands, indicating that their significances are all below the threshold for evidence. The upper limits calculated using the CLs method for each of these observables are:

$$r_{B_c}^{D\pi} < 4.0 \times 10^{-7} \text{ at } 95\% \text{ C.L.}$$
$$r_{B_c}^{D^*\pi} < 1.1 \times 10^{-6} \text{ at } 95\% \text{ C.L.}$$
$$r_{B_c}^{D^*K} < 1.1 \times 10^{-6} \text{ at } 95\% \text{ C.L.}$$

where the upper limits quoted correspond to 95% confidence level. In the case of $r_{B_c}^{DK}$, it is clear that the observed signal is of much higher significance, as indicated by the peak in p-value well beyond the 1σ and 2σ contours. As such, a formal procedure to determine two-sided uncertainties for this observable is carried out.

6.4.1. Systematic uncertainties on $r_{B_c}^{DK}$

To determine two-sided uncertainties for $r_{B_c}^{DK}$, the systematic uncertainties affecting the measurement must be taken into account. These uncertainties are much smaller than the statistical uncertainty, and as such do not influence the upper limits set for the other observables. There are two categories of systematic uncertainty considered, both of which are now discussed.

Fixed parameters in the fit to data

There are various fixed terms used in the signal extraction fit shown in Figure 6.10, each of which contribute some uncertainty to the measurement of $r_{B_c}^{DK}$. To assess the systemic uncertainty from the use of fixed terms in the fit to data, each of the fixed terms are varied randomly within their prescribed uncertainties. Each time some variation is introduced, the fit to data is repeated, building up a distribution of measured $r_{B_c}^{DK}$ values under the systematic variation of fixed parameters.

The fixed parameters are each varied according to Gaussians, within the following prescribed uncertainties:

- Signal peak mean μ - varied by ± 1 MeV/c^2.
- Signal peak width σ - varied by ± 0.8 MeV/c^2.
- Mis-ID means - varied by ± 1 MeV/c^2.
- Mis-ID widths - varied by ± 0.8 MeV/c^2.
- Upper endpoints of partially reconstructed shapes - varied by ± 1 MeV/c^2.
- PID efficiencies $\epsilon_{\text{PID}}^{\pi}$ and $\epsilon_{\text{PID}}^{K}$ - varied by $\pm 1\%$ on their nominal values (see Table 6.3).
- Relative rate of π^0 and γ contributions in $B_c \to D^{*0}h$ modes - varied by PDG uncertainty of 2.9% [12].

The distribution of measured $r_{B_c}^{DK}$ values under the variations described is shown in Figure 6.12. The RMS of this distribution, $\mathbf{1.1 \times 10^{-8}}$, is taken to represent the total systematic uncertainty arising from the use of fixed parameters in the fit to data. This systematic uncertainty is at the $\mathcal{O}(1\%)$ level, and is taken into account in Section 6.4.2, where a likelihood scan is performed to assess the $B_c \to DK$ signal significance.

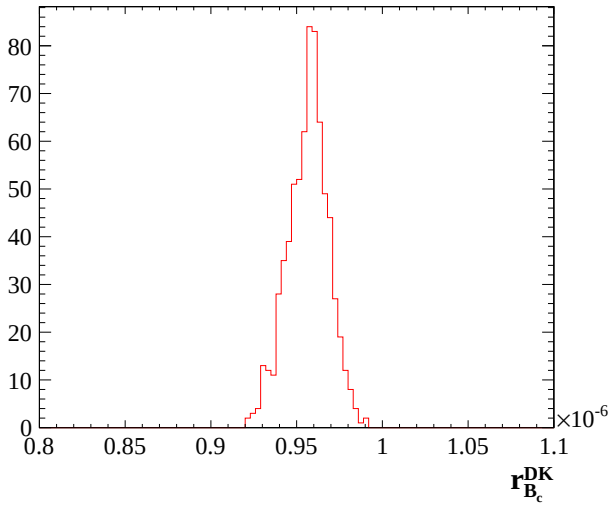

Figure 6.12.: Variation in the measured value of $r_{B_c}^{DK}$ under systematic variations of fixed parameters in the fit to data. The RMS of this distribution, 1.1×10^{-8}, is taken as the total systematic uncertainty from the use of fixed parameters, and is considered in Section 6.4.2 when determining the significance of the observed $B_c \to DK$ signal.

Other sources of uncertainty that do not affect the significance

In constructing $r_{B_c}^{DK}$, various terms with associated uncertainties (quoted in brackets below) multiply the measured signal yield:

- Efficiency correction term η, as determined in Section 6.2.4 (5.6%)
- Favoured $B^\pm \to D\pi^\pm$ branching fraction, $\mathcal{B}(B^\pm \to D\pi^\pm) = (4.81 \pm 0.15) \times 10^{-3}$ (3.1%)
- Normalisation yield $\mathcal{N}(B^\pm \to D\pi^\pm)$, as determined in Section 6.3.1 (0.2%)

The total uncertainty is 6.4%, and will be quoted as part of the total systematic uncertainty on $r_{B_c}^{DK}$. The use of these fixed terms does not affect the significance of the result in any way, since they are purely multiplicative factors which transform the measured $B_c \to DK$ yield into a value of $r_{B_c}^{DK}$.

6.4.2. Likelihood scan to assess $r_{B_c}^{DK}$ significance

The change in likelihood with respect to the data fit shown in Figure 6.10 has been evaluated by repeating the fit to data for a number of fixed $r_{B_c}^{DK}$ values. The change

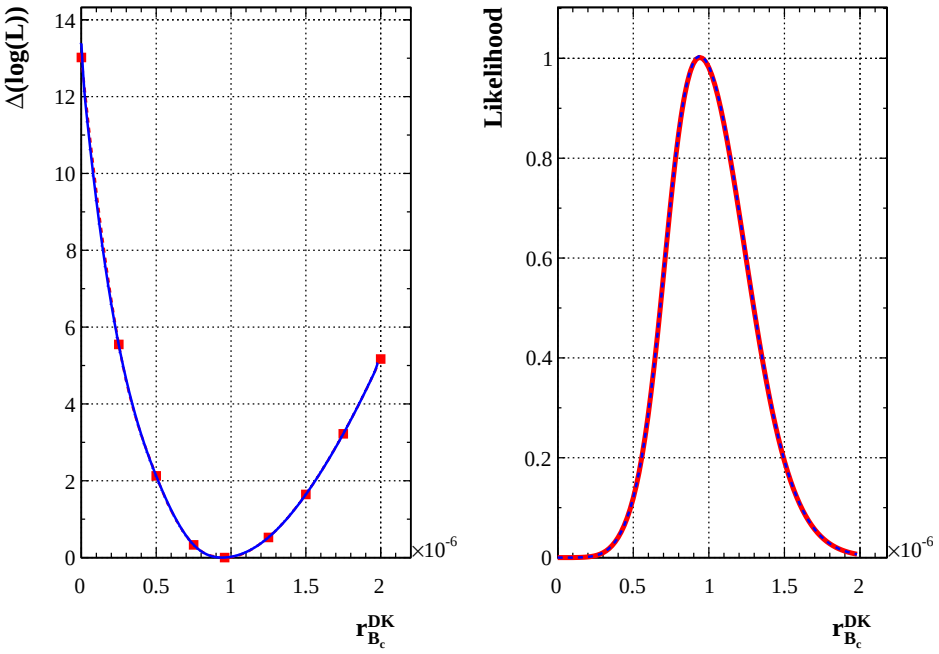

Figure 6.13.: Likelihood scan for $r_{B_c}^{DK}$, indicating a signal significance of $S = 5.1\sigma$ when systematic uncertainties are considered.

in likelihood with respect to the nominal fit result is shown in Figure 6.13, where the change in log likelihood $\Delta(\log(L))$ at each fixed value of $r_{B_c}^{DK}$ is shown by the red points (left plot). This likelihood scan does not account for the systematic uncertainty due to the used of fixed terms in the signal extraction fit, which was determined to be 1.1×10^{-8} (around 1% of the result central value) in Section 6.4.1.

To account for this systematic uncertainty, the likelihood difference is translated into a Gaussian likelihood distribution, as illustrated by the red curve in Figure 6.13 (right plot). This distribution is convolved with a Gaussian of width 1.1×10^{-8} (corresponding to the systematic uncertainty), resulting in the dashed blue curve (right plot). Since the systematic uncertainty is small, the convolution does not visibly alter the distribution. Finally, the convolved distribution is translated back to a $\Delta(\log(L))$ distribution, appearing on the left of Figure 6.13 as a blue curve, which intersects the y-axis at a slightly lower value than the default $\Delta(\log(L))$ distribution. The reduction in y-axis intercept embodies the reduction in significance as a result of including the systematic uncertainty.

The significance of the observed $B_c^- \to \bar{D}^0 K^-$ signal is determined using $S = \sqrt{2y}$, where $y = 13.0$ is the y intercept discussed above. The significance is measured to be $S = 5.1\sigma$; an observation of the $B_c^- \to \bar{D}^0 K^-$ decay is thus made.

6.4.3. Final result

The final result, including systematic uncertainties, is:

$$r_{B_c}^{DK} = (9.6 \pm 2.7 \pm 0.6) \times 10^{-7}$$

where the first uncertainty quoted is statistical (as measured by the fit in Figure 6.10) and the second is systematic, including each of the systematic uncertainty contributions discussed above. A first observation of the $B_c^- \to \bar{D}^0 K^-$ decay is made with a significance of 5.1σ.

6.5. Conclusions

In this Chapter, an exploratory search for $B_c^- \to \bar{D}^{(*)} h^-$ decays was performed in the invariant mass region $[5799 - 6899]$ MeV/c^2. Upper limits have been placed on the branching fractions of the $B_c^- \to \bar{D}^0 \pi^-$, $B_c^- \to \bar{D}^{*0} \pi^-$ and $B_c^- \to \bar{D}^{*0} K^-$ decays, while a first observation of the $B_c^- \to \bar{D}^0 K^-$ decay has been made with a significance of 5.1σ. The final results are:

$$\begin{aligned} r_{B_c}^{DK} &= (9.6 \pm 2.7 \pm 0.6) \times 10^{-7} \\ r_{B_c}^{D\pi} &< 4.0 \times 10^{-7} \text{ at } 95\% \text{ C.L.} \\ r_{B_c}^{D^*\pi} &< 1.1 \times 10^{-6} \text{ at } 95\% \text{ C.L.} \\ r_{B_c}^{D^*K} &< 1.1 \times 10^{-6} \text{ at } 95\% \text{ C.L.} \end{aligned}$$

The observation of the $B_c^- \to \bar{D}^0 K^-$ decay is of particular note, as the value of $r_{B_c}^{DK}$ appears high relative to both theoretical predictions and a naive expectation based on the observed $B_c^- \to J/\psi \pi^-$ yield at LHCb [18]. A comparison with $B_c^- \to \bar{D}^0 \pi^-$ is also interesting; the absence of this mode strongly indicates that the amplitude driving the DK signal is not a tree process, as illustrated in Figure 6.1. This result therefore constitutes the first observation of a non-tree amplitude in the decay of a B_c meson.

Chapter 7.

Conclusions

In this thesis, three analysis have been performed using $B^{\pm} \to Dh^{\pm}$ decays from the Run I LHCb data. In Chapter 4, $\mathcal{CP}$ observables were measured in several D meson final states, building upon the previous 1fb^{-1} LHCb measurements with improved analysis techniques and greater statistical precision. The observables measured are:

3fb^{-1} $B^{\pm} \to [hh]_D h^{\pm}$ results

$R^{K\pi}_{K/\pi}$	=	0.0778	$\pm$ 0.0006 (stat.)	$\pm$ 0.0016 (syst.)
$R^{KK}_{\rm CP}$	=	0.979	$\pm$ 0.022 (stat.)	$\pm$ 0.021 (syst.)
$R^{\pi\pi}_{\rm CP}$	=	1.018	$\pm$ 0.040 (stat.)	$\pm$ 0.023 (syst.)
A_{B_u}	=	$-$ 0.0033	$\pm$ 0.0017 (stat.)	$\pm$ 0.0042 (syst.)
$A^{K\pi}_{K}$	=	$-$ 0.0169	$\pm$ 0.0072 (stat.)	$\pm$ 0.0033 (syst.)
A^{KK}_{π}	=	$-$ 0.0160	$\pm$ 0.0050 (stat.)	$\pm$ 0.0028 (syst.)
A^{KK}_{K}	=	0.0855	$\pm$ 0.0201 (stat.)	$\pm$ 0.0130 (syst.)
$A^{\pi\pi}_{\pi}$	=	0.00291	$\pm$ 0.00860 (stat.)	$\pm$ 0.00311 (syst.)
$A^{\pi\pi}_{K}$	=	0.123	$\pm$ 0.037 (stat.)	$\pm$ 0.004 (syst.)
$R^{\pi K}_{ADS(K)}$	=	0.0187	$\pm$ 0.0011 (stat.)	$\pm$ 0.0006 (syst.)
$A^{\pi K}_{ADS(K)}$	=	$-$ 0.4044	$\pm$ 0.0563 (stat.)	$\pm$ 0.0153 (syst.)
$R^{\pi K}_{ADS(\pi)}$	=	0.00360	$\pm$ 0.00012 (stat.)	$\pm$ 0.00004 (syst.)
$A^{\pi K}_{ADS(\pi)}$	=	0.0971	$\pm$ 0.0314 (stat.)	$\pm$ 0.0090 (syst.)

3fb^{-1} $B^{\pm} \to [hhhh]_D h^{\pm}$ results

$R^{K\pi\pi\pi}_{K/\pi}$	=	0.0793	$\pm$ 0.0010 (stat.)	$\pm$ 0.0020 (syst.)
A_{B_u}	=	$-$ 0.0054	$\pm$ 0.0027 (stat.)	$\pm$ 0.0039 (syst.)
$A^{K\pi\pi\pi}_{K}$	=	0.0010	$\pm$ 0.0119 (stat.)	$\pm$ 0.0030 (syst.)
$R^{\pi\pi\pi\pi}_{CP}$	=	0.975	$\pm$ 0.037 (stat.)	$\pm$ 0.010 (syst.)
$A^{\pi\pi\pi\pi}_{\pi}$	=	$-$ 0.00552	$\pm$ 0.00791 (stat.)	$\pm$ 0.0032 (syst.)
$A^{\pi\pi\pi\pi}_{K}$	=	0.1004	$\pm$ 0.0336 (stat.)	$\pm$ 0.0079 (syst.)
$R^{\pi K\pi\pi}_{ADS(\pi)}$	=	0.00377	$\pm$ 0.00018 (stat.)	$\pm$ 0.00005 (syst.)
$R^{\pi K\pi\pi}_{ADS(K)}$	=	0.01399	$\pm$ 0.00149 (stat.)	$\pm$ 0.00041 (syst.)
$A^{\pi K\pi\pi}_{ADS(\pi)}$	=	0.0205	$\pm$ 0.0481 (stat.)	$\pm$ 0.0068 (syst.)
$A^{\pi K\pi\pi}_{ADS(K)}$	=	$-$ 0.316	$\pm$ 0.102 (stat.)	$\pm$ 0.015 (syst.)

The results quoted are consistent with[1], and improve upon, those measured in the previous 1 fb^{-1} publication. The improvement in precision achieved will help to reduce the uncertainty on the CKM phase γ. Good examples of the improvement shown are the statistical uncertainty on $R^{\pi K}_{\mathrm{ADS}(K)}$, which has reduced from 0.2% to 0.1%, and the statistical uncertainty on the corresponding asymmetry $A^{\pi K}_{\mathrm{ADS}(K)}$, which has improved considerably from 15% to 5.6%. These improvements are attributable to the higher statistics available, as well as advances in selection strategy, background description and fit procedure since the 1fb^{-1} publication.

In Chapter 5, the first dedicated measurement of the $B^{\pm}$ production asymmetry in proton-proton collisions at LHCb was performed using $B^{\pm} \to D\pi^{\pm}$ decays, where both the $D \to K^{\pm}\pi^{\mp}$ and $D \to K^{\pm}\pi^{\mp}\pi^{\pm}\pi^{\mp}$ final states were considered. The phase space integrated values of A_{B_u} measured at $\sqrt{s} = 7$ TeV and $\sqrt{s} = 8$ TeV are:

$$A_{B_u}^{7\ \mathrm{TeV}} = (+0.17 \pm 0.31 \pm 0.35)\%$$
$$A_{B_u}^{8\ \mathrm{TeV}} = (-0.22 \pm 0.20 \pm 0.26)\%$$

[1] The only exception to this is the A^{K}_{KK} observable, which exhibits tension at the 2σ level between the value presented within and the 1 fb^{-1} publication. This discrepancy has been extensively crosschecked and found to remain, and is likely to be the result of a downward statistical fluctuation in the 2012 data.

where both results are consistent with zero asymmetry given the current level of statistical precision. No strong dependence on $B^{\pm}$ kinematics was found. Using the raw charge asymmetries measured in $B^{\pm} \to D\pi^{\pm}$ decays, a measurement of the CP asymmetry in $B^{\pm} \to J/\psi K^{\pm}$ decays was also made:

$$A_{CP}^{J/\psi K} = (+0.10 \pm 0.30 \pm 0.21)\%$$

which represents the most precise determination of this quantity to date.

In Chapter 6, an exploratory search for the $B_c^- \to \bar{D}^{(*)}\pi^-$ and $B_c^- \to \bar{D}^{(*)}K^-$ decays was performed. The search was conducted in the invariant mass region $[5799 - 6899]$ MeV/c^2, employing the favoured $B^- \to D^0\pi^-$ mode as a normalisation channel. The following quantities are measured:

$$\begin{aligned} r_{B_c}^{DK} &= (9.6 \pm 2.7 \pm 0.6) \times 10^{-7} \\ r_{B_c}^{D\pi} &< 4.0 \times 10^{-7} \text{ at } 95\% \text{ C.L.} \\ r_{B_c}^{D^*\pi} &< 1.1 \times 10^{-6} \text{ at } 95\% \text{ C.L.} \\ r_{B_c}^{D^*K} &< 1.1 \times 10^{-6} \text{ at } 95\% \text{ C.L.} \end{aligned}$$

where a first observation of the $B_c^- \to \bar{D}^0 K^-$ decay is made with a significance of 5.1σ.

The use of $B^{\pm} \to Dh^{\pm}$ decays at LHCb has proved fruitful during Run I, as evidenced by the range of physics topics covered within this thesis. Continued study of these decays is thus well motivated during Run II and beyond.

Appendix A.

Study of $B^0 \to D^{*-}\pi^+\pi^-\pi^+$ and $B^0 \to D^{*-}K^+\pi^-\pi^+$ decays

During the course of my DPhil I completed an analysis of $B^0 \to D^{*-}\pi^+\pi^-\pi^+$ and $B^0 \to D^{*-}K^+\pi^-\pi^+$ decays, which was subsequently published. The analysis measured with improved precision the branching fraction $\mathcal{B}(B^0 \to D^{*-}\pi^+\pi^-\pi^+)$, and included a first observation of the $B^0 \to D^{*-}K^+\pi^-\pi^+$ decay. The publication is reproduced here for reference.

PHYSICAL REVIEW D **87,** 092001 (2013)

Study of $B^0 \to D^{*-}\pi^+\pi^-\pi^+$ and $B^0 \to D^{*-}K^+\pi^-\pi^+$ decays

R. Aaij *et al.**
(LHCb Collaboration)

(Received 2 April 2013; published 3 May 2013)

Using proton-proton collision data collected by the LHCb experiment at $\sqrt{s} = 7$ TeV, corresponding to an integrated luminosity of 1.0 fb^{-1}, the ratio of branching fractions of the $B^0 \to D^{*-}\pi^+\pi^-\pi^+$ decay relative to the $B^0 \to D^{*-}\pi^+$ decay is measured to be $\frac{\mathcal{B}(B^0\to D^{*-}\pi^+\pi^-\pi^+)}{\mathcal{B}(B^0\to D^{*-}\pi^+)} = 2.64 \pm 0.04(\text{stat}) \pm 0.13(\text{syst})$. The Cabibbo-suppressed decay $B^0 \to D^{*-}K^+\pi^-\pi^+$ is observed for the first time, and the measured ratio of branching fractions is $\frac{\mathcal{B}(B^0\to D^{*-}K^+\pi^-\pi^+)}{\mathcal{B}(B^0\to D^{*-}\pi^+\pi^-\pi^+)} = (6.47 \pm 0.37(\text{stat}) \pm 0.35(\text{syst})) \times 10^{-2}$. A search for orbital excitations of charm mesons contributing to the $B^0 \to D^{*-}\pi^+\pi^-\pi^+$ final state is also performed, and the first observation of the $B^0 \to \bar{D}_1(2420)^0\pi^+\pi^-$ decay is reported with the ratio of branching fractions $\frac{\mathcal{B}(B^0\to(\bar{D}_1(2420)^0\to D^{*-}\pi^+)\pi^-\pi^+)}{\mathcal{B}(B^0\to D^{*-}\pi^+\pi^-\pi^+)} = (2.04 \pm 0.42(\text{stat}) \pm 0.22(\text{syst})) \times 10^{-2}$, where the numerator represents a product of the branching fractions $\mathcal{B}(B^0 \to \bar{D}_1(2420)^0\pi^-\pi^+)$ and $\mathcal{B}(\bar{D}_1(2420)^0 \to D^{*-}\pi^+)$.

DOI: 10.1103/PhysRevD.87.092001 PACS numbers: 14.40.Nd, 13.25.Hw, 13.20.He

I. INTRODUCTION

Open charm decays of b hadrons offer a means by which both the electroweak and QCD sectors of the Standard Model (SM) may be tested. Beyond measurements of CP violation and the phases derived from the Cabibbo-Kobayashi-Maskawa matrix, rare $B \to DX$ decays may be used to search for new physics in decays mediated via annihilation or exchange processes. High-multiplicity $B \to DX$ decays are receiving increasing attention at LHCb [1–3], in part owing to the large samples that can be obtained as a result of the copious $b\bar{b}$ production at the LHC [4].

Improving knowledge of the $B^0 \to D^{(*)-}\pi^+\pi^-\pi^+$ decay is of interest because of its potential use as a normalization mode for the semileptonic decay $B^0 \to D^{(*)-}\tau^+\nu_\tau$ with $\tau^+ \to \pi^+\pi^-\pi^+\bar{\nu}_\tau$ [5]. Charge conjugation is implied throughout. The latter B decay has recently shown an excess over the SM branching fraction expectation [6], which could indicate the presence of physics beyond the SM.

In this work three measurements of ratios of branching fractions are described. The first measurement is of the Cabibbo-favored (CF) ratio

$$r_{3h} = \frac{\mathcal{B}(B^0 \to D^{*-}\pi^+\pi^-\pi^+)}{\mathcal{B}(B^0 \to D^{*-}\pi^+)},$$

from which a value for $\mathcal{B}(B^0 \to D^{*-}\pi^+\pi^-\pi^+)$ is obtained. The current world average value is $\mathcal{B}(B^0 \to D^{*-}\pi^+\pi^-\pi^+) = (7.0 \pm 0.8) \times 10^{-3}$ [7]. The subscript $3h$ denotes the three hadrons (or "bachelors") in the signal B^0 decay, which are produced along with the charmed meson. The second measurement is of the ratio of branching fractions of the Cabibbo-suppressed (CS) decay $B^0 \to D^{*-}K^+\pi^-\pi^+$ relative to its CF counterpart

$$r_{\text{CS}}^{K\pi\pi} = \frac{\mathcal{B}(B^0 \to D^{*-}K^+\pi^-\pi^+)}{\mathcal{B}(B^0 \to D^{*-}\pi^+\pi^-\pi^+)},$$

where the subscript denotes Cabibbo suppression of the signal decay. The third measurement is of the ratio of branching fractions of the CS decay $B^0 \to D^{*-}K^+$ relative to its CF counterpart

$$r_{\text{CS}}^{K} = \frac{\mathcal{B}(B^0 \to D^{*-}K^+)}{\mathcal{B}(B^0 \to D^{*-}\pi^+)}.$$

The superscripts in r_{CS}^{K} and $r_{\text{CS}}^{K\pi\pi}$ are used to differentiate the single- and triple-bachelor measurements, respectively. The rates of the CS processes are expected to be smaller than their CF counterparts by a factor of roughly $\tan^2(\theta_{\text{C}}) \sim 1/20$, where θ_{C} is the Cabibbo angle [7].

II. DETECTOR, SIGNAL SELECTION AND SIMULATION

The LHCb detector [8] is a single-arm forward spectrometer covering the pseudorapidity range $2 < \eta < 5$, designed for the study of particles containing b or c quarks. The detector includes a high-precision tracking system consisting of a silicon-strip vertex detector surrounding the pp interaction region, a large-area silicon-strip detector located upstream of a dipole magnet with a bending power of about 4 Tm, and three stations of silicon-strip detectors and straw drift tubes placed downstream. The combined tracking system has a momentum resolution $\Delta p/p$ that varies from 0.4% at 5 GeV/c to 0.6% at 100 GeV/c, and an impact parameter (IP) resolution of 20 μm for tracks with high transverse momentum (p_{T}). Charged hadrons are

*Full author list given at the end of the article.

identified using two ring-imaging Cherenkov (RICH) detectors, which provide a kaon identification efficiency of ~95% for a pion fake rate of a few percent, integrated over the momentum range from 3–100 GeV/c [9]. Photon, electron and hadron candidates are identified by a calorimeter system consisting of scintillating-pad and preshower detectors, an electromagnetic calorimeter and a hadronic calorimeter. Muons are identified by a system composed of alternating layers of iron and multiwire proportional chambers.

LHCb uses a two-level trigger system. The first level of the trigger consists of a hardware stage that searches for either a large transverse energy cluster ($E_{\rm T} > 3.6$ GeV) in the calorimeters, or a single high-$p_{\rm T}$ muon or dimuon pair in the muon stations. This is followed by a software stage that applies a full event reconstruction. The software trigger requires a two-, three- or four-track secondary vertex with a high sum of the $p_{\rm T}$ of the tracks and a significant displacement from the primary pp interaction vertices. At least one track should have $p_{\rm T} > 1.7$ GeV/c and IP χ^2 with respect to the primary interaction greater than 16. The IP χ^2 is defined as the difference between the χ^2's of the primary vertex (PV) reconstructed with and without the considered track. A multivariate algorithm is used for the identification of secondary vertices consistent with the decay of a b hadron [10]. The results presented in this paper use the full 2011 data set corresponding to an integrated luminosity of 1.0 fb^{-1} of pp collisions at $\sqrt{s} = 7$ TeV.

Candidate B^0 decays are formed by combining a $D^{*-} \to (\bar{D}^0 \to K^+\pi^-)\pi^-$ candidate with either a single-bachelor or triple-bachelor combination. All final state tracks are required to have $p_{\rm T}$ in excess of 500 MeV/c, except for the slow pion produced in the D^{*-} decay, which must have $p_{\rm T}$ in excess of 100 MeV/c. All tracks must be well separated from any reconstructed PV in the event. They must be identified as either a pion or a kaon using information from the RICH detectors. Particle identification likelihoods for several hypotheses (e.g., π^+, K^+, p) are formed, and the difference in the logarithms of these likelihoods, ΔLL, is used to differentiate between particle types. Candidate $\bar{D}^0$ mesons are required to have good vertex fit quality, be well displaced from the nearest PV and have an invariant mass $m(K^+\pi^-)$ within 50 MeV/c^2 of the $\bar{D}^0$ mass. Candidate D^{*-} decays are selected by requiring $140 < m(K^+\pi^-\pi^+) - m(K^+\pi^-) < 150$ MeV/c^2.

Candidate triple bachelors are formed from a $\pi^+\pi^-\pi^+$ or $K^+\pi^-\pi^+$ combination, where all invariant mass values up to 3 GeV/c^2 are accepted. The vertex of the combination must be well separated from the nearest PV. Backgrounds from $B^0 \to D^{*-}\pi^+(\pi^-\pi^+)$ decays for the CS modes $B^0 \to D^{*-}K^+(\pi^-\pi^+)$ are reduced by applying more stringent particle identification (PID) requirements to the bachelor kaon. To suppress backgrounds from $B^0 \to D^{*-}D_s^+$ decays where $D_s^+ \to K^+\pi^-\pi^+$ in the triple-bachelor decay $B^0 \to D^{*-}K^+\pi^-\pi^+$, it is required that $m(K^+\pi^-\pi^+)$ be more than 15 MeV/c^2 away from the D_s^+ mass. Reconstructed B^0 candidates are required to be well separated from the nearest PV, with decay time larger than 0.2 ps and good quality vertex fit. Candidates passing all selection requirements are refit with both $\bar{D}^0$ mass and vertex constraints to improve the B^0 mass resolution [11].

The selection efficiencies and trigger pass fractions defined below are evaluated using Monte Carlo simulation. In the simulation, pp collisions are generated using PYTHIA 6.4 [12] with a specific LHCb configuration [13]. Decays of hadronic particles are described by EVTGEN [14], in which final state radiation is generated using PHOTOS [15]. The interaction of the generated particles with the detector and its response are implemented using the GEANT4 toolkit [16] as described in Ref. [17].

The simulated events are passed through an emulation of the hardware trigger and then through the full software trigger as run on data. The total kinematic efficiency, $\epsilon_{\rm kin}$, is determined from the simulation as the fraction of events that pass all reconstruction and selection requirements and the trigger. The fraction of selected events that pass the particular trigger selection relative to the total number of selected events is taken to be the trigger pass fraction, $f_{\rm trig}$. This fraction does not represent the true trigger efficiency, since it is evaluated with respect to a sample of events that have all passed the trigger.

III. FITS TO DATA

The reconstructed invariant mass distributions for $B^0 \to D^{*-}h^+\pi^-\pi^+$ and $B^0 \to D^{*-}h^+$ decays are shown in Fig. 1. Simultaneous binned maximum-likelihood fits to the CF and CS decays are performed, where the probability density functions (PDFs) are composed of a signal component and several background components. The CF signal shapes are required to share parameters with their CS counterparts. The total CF (CS) signal yield $\mathcal{N}_{\rm CF}$ ($\mathcal{N}_{\rm CS}$) is given by the sum of the yield contained in the signal shape and the yield contained in the particle misidentification background from the CS (CF) sample. The values of $\mathcal{N}_{\rm CF}$ and the ratio $\mathcal{N}_{\rm CS}/\mathcal{N}_{\rm CF}$ vary freely in the fit.

The PDF of the signal decays is described by the sum of a Crystal Ball [18] and a Gaussian function, when all final state particles are assigned the correct mass hypothesis. This shape was chosen because it describes radiative loss and the non-Gaussian mass resolution. In the simultaneous fit to the CF and CS decays, the Crystal Ball widths vary freely and independently for both modes. A single freely varying peak position parameter is shared by all signal components in the fit to both modes. The Gaussian width is required to be equal to or greater than the Crystal Ball width, and this width is shared by the CF and CS signal shapes.

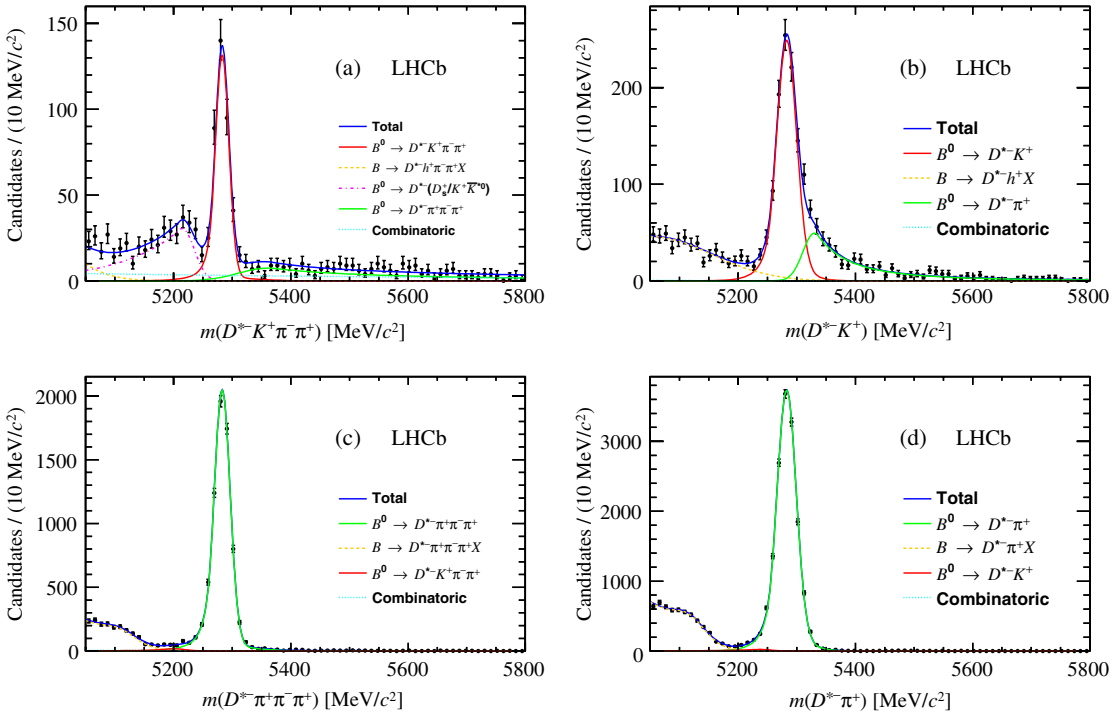

FIG. 1 (color online). Invariant mass distributions of selected (a) $B^0 \to D^{*-}K^+\pi^-\pi^+$, (b) $B^0 \to D^{*-}K^+$, (c) $B^0 \to D^{*-}\pi^+\pi^-\pi^+$ and (d) $B^0 \to D^{*-}\pi^+$ candidates. Green (red) solid lines represent the CF (CS) signal shapes and their respective particle misidentification backgrounds. Orange dashed lines at low invariant mass represent backgrounds from partially reconstructed decays. Cyan dotted lines represent combinatorial backgrounds. The pink dash-dotted line below the signal peak in the fit to $B^0 \to D^{*-}K^+\pi^-\pi^+$ candidates represents the background from misidentified $B^0 \to D^{*-}D_s^+$ and $B^0 \to D^{*-}K^+\bar{K}^{*0}$ decays.

All decay modes have background contributions from partially reconstructed decays of the type $B \to D^*X$, where X represents the final state bachelor(s) for the given decay plus an additional photon or pion that is not reconstructed. These backgrounds are parameterized by the sum of two single-sided Gaussian functions with a common mean and independent widths, all of which vary freely. A combinatorial background is present in all cases and is fit by an exponential function. The yields of the partially reconstructed and combinatorial backgrounds vary freely in all parts of the fit to data.

Misidentification of pions and kaons causes cross feed between the CF and CS signal decays. The simulation indicates that backgrounds of this type can be described by a PDF comprising two Crystal Ball functions that share a common mean but have independent widths. The absolute rate of a background from particle misidentification is fixed to be $(100 - \epsilon_{\rm PID})\%$ of the corresponding signal yield in the simultaneous fit, where $\epsilon_{\rm PID}$ represents the efficiency for all final-state hadrons in the signal decay to be correctly identified. For the single-bachelor decays, $\epsilon_{\rm PID}$ is determined by reweighting the $\Delta LL(K-\pi)$ distributions obtained from calibration events to match the properties of the signal bachelor. The reweighting is performed in bins of momentum, pseudorapidity and number of tracks in the event. Calibration tracks are taken from $D^{*+} \to D^0\pi^+$ decays with $D^0 \to K^-\pi^+$ [9]. For the triple-bachelor decays, a similar approach is used, but the kinematic correlations between each bachelor are also considered. A per-candidate particle identification efficiency is determined from the product of each bachelor PID efficiency, and $\epsilon_{\rm PID}$ is given by the weighted average of the per-candidate efficiencies.

Further backgrounds are present in the $B^0 \to D^{*-}K^+\pi^-\pi^+$ sample from the decays $B^0 \to D^{*-}D_s^+$ where $D_s^+ \to K^+K^-\pi^+$ and the K^- meson is misidentified as a π^-, and $B^0 \to D^{*-}K^+\bar{K}^{*0}$ where $\bar{K}^{*0} \to K^-\pi^+$ and the K^- is misidentified as a π^-. The backgrounds are modeled together using a Crystal Ball shape that peaks at a lower mass than the signal, with a peak position and

TABLE I. Selected candidate yields from fits to data that are used in the branching fraction calculations. The yield for a decay is given by the sum of the signal shape yield in the CF (CS) fit and the corresponding misidentification background yield in the CS (CF) fit. Uncertainties quoted are statistical only.

Decay	Yield
$B^0 \to D^{*-}\pi^+\pi^-\pi^+$	7228 ± 93
$B^0 \to D^{*-}\pi^+$	15 693 ± 136
$B^0 \to D^{*-}K^+\pi^-\pi^+$	519 ± 30
$B^0 \to D^{*-}K^+$	1241 ± 53

TABLE II. Kinematic efficiencies, trigger pass fractions and their products, taken from simulation. Quoted uncertainties come from the use of finite size samples to determine efficiencies and are accounted for as a source of systematic uncertainty.

Decay	$\epsilon_{\rm kin}$ (%)	$f_{\rm trig}$ (%)	$\epsilon_{\rm tot}$ (%)
$B^0 \to D^{*-}\pi^+\pi^-\pi^+$	0.037 ± 0.001	69.3 ± 0.5	0.0259 ± 0.0005
$B^0 \to D^{*-}\pi^+$	0.197 ± 0.002	75.4 ± 0.3	0.148 ± 0.002
$B^0 \to D^{*-}K^+\pi^-\pi^+$	0.044 ± 0.001	67.4 ± 0.9	0.0298 ± 0.0007
$B^0 \to D^{*-}K^+$	0.201 ± 0.003	75.4 ± 0.5	0.151 ± 0.002

width that vary freely in the fit. The Crystal Ball tail parameters are fixed to the values found in simulation. This background could be reduced by applying tighter particle identification requirements to the π^- bachelor, but this has not been applied in order to maintain symmetry between the CF and CS particle identification requirements. To eliminate the background from $B^0 \to D^{*-}D_s^+$ decays where $D_s^+ \to K^+\pi^-\pi^+$, the veto previously described is applied. The background from $B^0 \to D^{*-}D_s^+$ decays with $D_s^+ \to \pi^+\pi^-\pi^+$ does not contribute due to the tight particle identification requirement applied to the bachelor kaon in the $B^0 \to D^{*-}K^+\pi^-\pi^+$ decay.

The fits are superimposed on the data in Fig. 1, and the measured yields $\mathcal{N}$ for each decay are listed in Table I. The CF and CS ratios of branching fractions are obtained using

$$r_{3h} = f_{3h} \times \frac{\mathcal{N}(B^0 \to D^{*-}\pi^+\pi^-\pi^+)/\epsilon_{\rm tot}(B^0 \to D^{*-}\pi^+\pi^-\pi^+)}{\mathcal{N}(B^0 \to D^{*-}\pi^+)/\epsilon_{\rm tot}(B^0 \to D^{*-}\pi^+)},$$

$$r_{\rm CS}^{K\pi\pi} = f_{\rm CS}^{K\pi\pi} \times \frac{\mathcal{N}(B^0 \to D^{*-}K^+\pi^-\pi^+)/\epsilon_{\rm tot}(B^0 \to D^{*-}K^+\pi^-\pi^+)}{\mathcal{N}(B^0 \to D^{*-}\pi^+\pi^-\pi^+)/\epsilon_{\rm tot}(B^0 \to D^{*-}\pi^+\pi^-\pi^+)},$$

$$r_{\rm CS}^{K} = f_{\rm CS}^{K} \times \frac{\mathcal{N}(B^0 \to D^{*-}K^+)/\epsilon_{\rm tot}(B^0 \to D^{*-}K^+)}{\mathcal{N}(B^0 \to D^{*-}\pi^+)/\epsilon_{\rm tot}(B^0 \to D^{*-}\pi^+)}.$$

The values of $\epsilon_{\rm tot}$ are listed in Table II, and the f factors correct for systematic effects.

IV. SYSTEMATIC UNCERTAINTIES

When measuring ratios of branching fractions, many sources of systematic uncertainty cancel. The systematic uncertainties for the r_{3h}, $r_{\rm CS}^{K\pi\pi}$ and $r_{\rm CS}^{K}$ measurements will be discussed in turn. The primary sources of systematic uncertainty that remain in the r_{3h} measurement are due to the different topologies of the signal and normalization decays. Compared to the $B^0 \to D^{*-}\pi^+$ normalization mode, the triple-pion decay mode has two additional pions which must be reconstructed and selected. The tracking efficiency has been studied using a tag-and-probe method with $J/\psi \to \mu^+\mu^-$ decays [19], which leads to a correction in r_{3h} of 1.017 ± 0.035. In the $B^0 \to D^{*-}\pi^+\pi^-\pi^+$ decay, the three bachelor pions are required to have a common vertex. The IP resolution and vertex χ^2/ndf distributions are observed to be $\sim$15% broader in data relative to the simulation [1], resulting in a correction on r_{3h} of 0.982 ± 0.016.

Possible background from decays of the type $B^0 \to D^{*-}D_s^+$, where $D_s^+ \to \pi^+\pi^-\pi^+$, has been considered, and a correction of 0.990 ± 0.005 is applied to r_{3h}. The use of simulated events to determine trigger pass fractions has a residual systematic uncertainty arising from differences between data and simulation with respect to the emulation of the hardware trigger and trigger software. A correction of 1.009 ± 0.012 is applied to r_{3h} to account for this difference. The candidate selection is limited to the mass region $m(\pi^+\pi^-\pi^+) < 3\,{\rm GeV}/c^2$. The $m(\pi^+\pi^-\pi^+)$ distributions in data and simulation are in good agreement, such that the selection efficiency properly accounts for this choice. The fraction of events falling beyond 3 GeV/c^2 in simulation is 3.7%. Assuming 50% uncertainty on this value, a relative systematic uncertainty of 1.9% is assigned.

The methods used to determine $\epsilon_{\rm PID}$ have an uncertainty from which the systematic contribution is determined to be 0.8%. A systematic uncertainty of 0.6% arises from the specific choice of PDF shapes in the fit. Both of the CF simulated samples have a comparable number of events after selection requirements are imposed, from which a 2.1% systematic uncertainty due to finite simulated samples is incurred.

The CF and CS $B^0 \to D^{*-}h^+\pi^-\pi^+$ modes have identical selection requirements, apart from the particle identification requirements placed on the h^+ and the D_s^+ veto applied in the CS case. A systematic uncertainty of 3.4% is incurred as a result of the particle identification requirement placed on the bachelor kaon in the $B^0 \to D^{*-}K^+\pi^-\pi^+$ mode. This tight requirement is necessary in order to reduce the background from misidentified

$B^0 \to D^{*-}\pi^+\pi^-\pi^+$ decays. To evaluate the loss of signal events due to the D_s^+ veto in the CS selection, the fit to data is performed both with and without the veto applied. The measured CS signal yield decreases by 1% upon application of the veto, which is taken as an inefficiency with 50% uncertainty, and a correction of 1.010 ± 0.005 is applied to $r_{\rm CS}^{K\pi\pi}$.

The ratio of trigger pass fractions taken from simulation is $f_{\rm trig}(B^0 \to D^{*-}\pi^+\pi^-\pi^+)/f_{\rm trig}(B^0 \to D^{*-}K^+\pi^-\pi^+) = 1.03 \pm 0.02$, where the quoted uncertainty is derived from the size of the simulated samples. For such similar decay modes, this ratio should be close to unity. The ratio itself is already applied as part of the branching fraction calculation, but half of the difference in the ratio from unity (1.5%) is taken as an additional source of systematic uncertainty.

In a similar fashion to the CF measurement, the CS measurement has a systematic uncertainty of 1% from the specific choice of PDF shapes and 3.0% uncertainty from the use of finite simulated samples to determine efficiencies. The fraction of CS decays with $m(K^+\pi^-\pi^+)$ in the range 2.7–3.0 GeV/c^2 in data is 5.5%. The fraction of events falling beyond the analysis cut at 3 GeV/c^2 is estimated to be half of this value (2.8%) with 50% uncertainty. The value of $r_{\rm CS}^{K\pi\pi}$ is therefore corrected by a factor 1.028 ± 0.023, where the quoted uncertainty contains a 1.9% contribution from the corresponding systematic uncertainty in the CF decay. The choice of resonance model used to describe the $B^0 \to D^{*-}h^+\pi^-\pi^+$ decays in the simulation was found not to alter the measured efficiencies.

The $B^0 \to D^{*-}h^+$ modes have identical selection requirements apart from the particle identification requirements placed on the h^+ bachelor. A systematic uncertainty of 2.0% is incurred as a result of the particle identification requirements applied to the bachelors. Further systematic uncertainties of 0.7%, 1.7% and 2.0% arise from the specific choice of PDF shapes, the use of finite simulated samples and the trigger emulation [20], respectively.

TABLE III. Contributions to the relative systematic uncertainty for all measurements. The total uncertainty is obtained by adding the contributions from the individual sources in quadrature.

Source	Value (%) r_{3h}	$r_{\rm CS}^{K\pi\pi}$	$r_{\rm CS}^{K}$
Track reconstruction	3.4	...	...
Selection requirements	1.6	...	...
$B^0 \to D^{*-}D_s^+$ background	0.5	...	...
Trigger	1.2	1.5	2.0
$m(h^+\pi^-\pi^+) > 3$ GeV/c^2	1.9	2.2	...
Particle identification	0.8	3.4	2.0
Choice of PDFs	0.6	1.0	0.7
Simulated sample size	2.1	3.0	1.7
$D_s^+ \to K^+\pi^-\pi^+$ veto	...	0.5	...
Total	5.0	5.4	3.4

Each contribution to the systematic uncertainty is listed in Table III. The total systematic uncertainty is given by the sum in quadrature of all contributions. The overall systematic uncertainty for the CF measurement is 5.0%, with a factor $f_{3h} = 0.998$ that is applied as part of the calculation for r_{3h}. The CS triple- and single-bachelor measurements have overall systematic uncertainties of 5.4% and 3.4%, respectively. A factor $f_{\rm CS}^{K\pi\pi} = 1.038$ is applied to $r_{\rm CS}^{K\pi\pi}$, whereas $f_{\rm CS}^{K} = 1$.

V. RESULTS

The results for the ratios of branching fractions are

$$r_{3h} = 2.64 \pm 0.04(\text{stat}) \pm 0.13(\text{syst}),$$
$$r_{\rm CS}^{K\pi\pi} = (6.47 \pm 0.37(\text{stat}) \pm 0.35(\text{syst})) \times 10^{-2},$$
$$r_{\rm CS}^{K} = (7.76 \pm 0.34(\text{stat}) \pm 0.26(\text{syst})) \times 10^{-2},$$

where the first uncertainty is statistical and the second is absolute systematic. Using the world average value for $\mathcal{B}(B^0 \to D^{*-}\pi^+) = (2.76 \pm 0.13) \times 10^{-3}$ [7], the branching fractions are obtained:

$$\mathcal{B}(B^0 \to D^{*-}\pi^+\pi^-\pi^+) = (7.27 \pm 0.11(\text{stat}) \pm 0.36(\text{syst}) \pm 0.34(\text{norm})) \times 10^{-3},$$
$$\mathcal{B}(B^0 \to D^{*-}K^+) = (2.14 \pm 0.09(\text{stat}) \pm 0.08(\text{syst}) \pm 0.10(\text{norm})) \times 10^{-4},$$

where the final uncertainty is due to the normalization mode. Both results are consistent with and improve upon the precision of the current world average values, $\mathcal{B}(B^0 \to D^{*-}\pi^+\pi^-\pi^+) = (7.0 \pm 0.8) \times 10^{-3}$ and $\mathcal{B}(B^0 \to D^{*-}K^+) = (2.14 \pm 0.16) \times 10^{-4}$ [7]. Combining the CF result and the current world average, where both values are weighted according to their total uncertainty, gives $\mathcal{B}(B^0 \to D^{*-}\pi^+\pi^-\pi^+) = (7.19 \pm 0.43) \times 10^{-3}$. The measurement of $r_{\rm CS}^{K\pi\pi}$ represents a first observation of the decay $B^0 \to D^{*-}K^+\pi^-\pi^+$. The value of this ratio is similar to the related measurement of $\mathcal{B}(B^0 \to D^-K^+\pi^-\pi^+)/\mathcal{B}(B^0 \to D^-\pi^+\pi^-\pi^+) = (5.9 \pm 1.1(\text{stat}) \pm 0.5(\text{syst})) \times 10^{-2}$ [2]. Using the updated world average value for $\mathcal{B}(B^0 \to D^{*-}\pi^+\pi^-\pi^+)$, the branching fraction is obtained:

$$\mathcal{B}(B^0 \to D^{*-}K^+\pi^-\pi^+) = (4.65 \pm 0.26(\text{stat}) \pm 0.25(\text{syst}) \pm 0.28(\text{norm})) \times 10^{-4}.$$

VI. SEARCH FOR EXCITED CHARM RESONANCES

Using the same data set, a search for orbital excitations of charm resonances (D^{**}) contributing to the $B^0 \to D^{*-}\pi^+\pi^-\pi^+$ final state is performed. The selection is identical to that presented above, except the lower $p_{\rm T}$ cut on bachelors is reduced to 300 MeV/c. Events that have

been triggered via tracks not associated with the $B^0 \to D^{*-}\pi^+\pi^-\pi^+$ candidate are also included. The signal purity is only slightly reduced as a result of the looser selection.

The corrected mass $M(D^{*-}\pi^+) = m(D^{*-}\pi^+) - m(D^{*-}) + m(D^{*-})_{\rm PDG}$ MeV/c^2 is computed for each $D^{*-}\pi^+$ combination, in which the contribution to the mass resolution from the D^{*-} mass measurement is removed. To statistically subtract the background, each event is weighted using SWEIGHTS [21] obtained from the $B^0 \to D^{*-}\pi^+\pi^-\pi^+$ invariant mass fit. Figure 2 shows the resulting distribution of $M(D^{*-}\pi^+)$ for $B^0 \to D^{*-}\pi^+\pi^-\pi^+$ signal decays.

A peaking structure associated to the $\bar{D}_1(2420)^0$ resonance is observed, where ~90% of the candidates in the peaking structure originate from the combination with the softer π^+ meson. Other resonances, consistent with $D_2^*(2460)^0$, $D(2550)^0$, $D(2600)$ and $D(2750)$, are included in the fit but are not found to be significant. All resonances in the fit are described by Breit-Wigner functions. The $\bar{D}_1(2420)^0$ Breit-Wigner function is convolved with a Gaussian resolution function of 3 MeV/c^2 width. The means and natural widths of all peaking structures vary around their established values [22] with Gaussian constraints.

The background from $B^0 \to D^{*-}\pi^+\pi^-\pi^+$ decays that do not pass through an excited charm resonance is described by a function comprising the two-body phase space equation multiplied by an exponential acceptance function, $e^{-\alpha M(D^{*-}\pi^+)}$. The shape parameter α and all yields vary freely. The branching fraction ratio is calculated by comparing the fitted $\bar{D}_1(2420)^0 \to D^{*-}\pi^+$ yield with the total

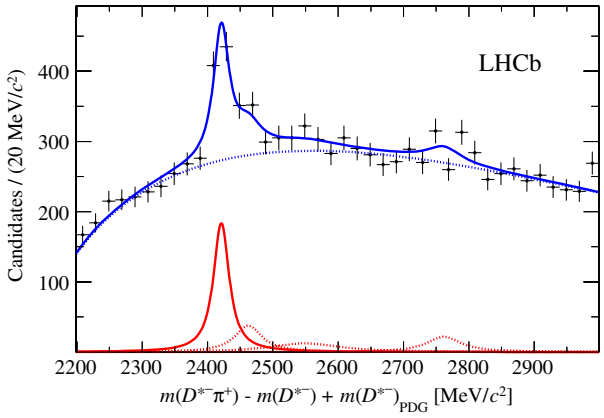

FIG. 2 (color online). Corrected mass $M(D^{*-}\pi^+) = m(D^{*-}\pi^+) - m(D^{*-}) + m(D^{*-})_{\rm PDG}$ MeV/c^2 distribution from background-subtracted $B^0 \to D^{*-}\pi^+\pi^-\pi^+$ candidates. The red solid line represents the contribution from $\bar{D}_1(2420)^0$; the red dashed lines represent contributions from the higher excited charm states $D_2^*(2460)^0$, $D(2550)^0$, $D(2600)$ and $D(2750)$, which are expected to be present [22] but are not significant in this dataset. The blue dashed line represents B^0 decays that have not passed through an excited charm resonance.

number of accepted $D^{*-}\pi^+\pi^-\pi^+$ events in the sample. A correction is taken from simulation to account for the acceptance, reconstruction and selection efficiency for events in the region close to $m(\bar{D}_1(2420)^0)$ relative to the efficiency averaged across the full phase space. The ratio of efficiencies is $f = 0.91 \pm 0.04$. A systematic uncertainty of 10% is assigned to the choice of background PDF, which is determined by remeasuring the $\bar{D}_1(2420)^0$ yield after shifting the fit range by ± 50 MeV/c^2.

The measured yield is $\mathcal{N}(B^0 \to \bar{D}_1(2420)^0\pi^+\pi^-) = 203 \pm 42$, and the total number of B^0 signal events after the looser selection is $\mathcal{N}(B^0 \to D^{*-}\pi^+\pi^-\pi^+) = 10939 \pm 105$. Using these values, the ratio of branching fractions is obtained:

$$\frac{\mathcal{B}(B^0 \to (\bar{D}_1(2420)^0 \to D^{*-}\pi^+)\pi^-\pi^+)}{\mathcal{B}(B^0 \to D^{*-}\pi^+\pi^-\pi^+)} = (2.04 \pm 0.42(\text{stat}) \pm 0.22(\text{syst})) \times 10^{-2},$$

where the numerator represents a product of the branching fractions $\mathcal{B}(B^0 \to \bar{D}_1(2420)^0\pi^-\pi^+)$ and $\mathcal{B}(\bar{D}_1(2420)^0 \to D^{*-}\pi^+)$. The Wilk's theorem statistical significance of the $\bar{D}_1(2420)^0$ peak is 5.9σ, which becomes 5.3σ when the systematic uncertainty is included. The significance is unchanged if a mass window is used to select signal decays instead of SWEIGHTS. This constitutes the first observation of the color-suppressed $B^0 \to \bar{D}_1(2420)^0\pi^+\pi^-$ decay.

VII. SUMMARY

In conclusion, $B^0 \to D^{*-}h^+\pi^-\pi^+$ decays have been studied using $B^0 \to D^{*-}h^+$ decays for normalization and verification. The branching fractions of $B^0 \to D^{*-}\pi^+\pi^-\pi^+$ and $B^0 \to D^{*-}K^+$ decays are measured, and the CS $B^0 \to D^{*-}K^+\pi^-\pi^+$ and color-suppressed $B^0 \to \bar{D}_1(2420)^0\pi^+\pi^-$ decays are observed. The final results are

$$\begin{aligned} r_{3h} &= 2.64 \pm 0.04(\text{stat}) \pm 0.13(\text{syst}), \\ r_{\rm CS}^{K\pi\pi} &= (6.47 \pm 0.37(\text{stat}) \pm 0.35(\text{syst})) \times 10^{-2}, \\ r_{\rm CS}^{K} &= (7.76 \pm 0.34(\text{stat}) \pm 0.26(\text{syst})) \times 10^{-2}, \\ \frac{\mathcal{B}(B^0 \to (\bar{D}_1(2420)^0 \to D^{*-}\pi^+)\pi^-\pi^+)}{\mathcal{B}(B^0 \to D^{*-}\pi^+\pi^-\pi^+)} &= (2.04 \pm 0.42(\text{stat}) \pm 0.22(\text{syst})) \times 10^{-2}. \end{aligned}$$

The results for r_{3h} and $r_{\rm CS}^K$ represent an improvement in precision, and the measurements of the decays $B^0 \to D^{*-}K^+\pi^-\pi^+$ and $B^0 \to (\bar{D}_1(2420)^0 \to D^{*-}\pi^+)\pi^-\pi^+$ both constitute first observations.

ACKNOWLEDGMENTS

We express our gratitude to our colleagues in the CERN accelerator departments for the excellent performance of the LHC. We thank the technical and administrative staff at the LHCb institutes. We acknowledge support from CERN

and from the national agencies: CAPES, CNPq, FAPERJ and FINEP (Brazil); NSFC (China); CNRS/IN2P3 and Region Auvergne (France); BMBF, DFG, HGF and MPG (Germany); SFI (Ireland); INFN (Italy); FOM and NWO (The Netherlands); SCSR (Poland); ANCS/IFA (Romania); MinES, Rosatom, RFBR and NRC "Kurchatov Institute" (Russia); MinECo, XuntaGal and GENCAT (Spain); SNSF and SER (Switzerland); NAS Ukraine (Ukraine); STFC (United Kingdom); NSF (USA). We also acknowledge the support received from the ERC under FP7. The Tier1 computing centres are supported by IN2P3 (France), KIT and BMBF (Germany), INFN (Italy), NWO and SURF (The Netherlands), PIC (Spain), GridPP (United Kingdom). We are thankful for the computing resources put at our disposal by Yandex LLC (Russia), as well as to the communities behind the multiple open source software packages that we depend on.

[1] R. Aaij *et al.* (LHCb Collaboration), Phys. Rev. D **84**, 092001 (2011).
[2] R. Aaij *et al.* (LHCb Collaboration), Phys. Rev. Lett. **108**, 161801 (2012).
[3] R. Aaij *et al.* (LHCb Collaboration), Phys. Rev. D **86**, 112005 (2012).
[4] R. Aaij *et al.* (LHCb Collaboration), Phys. Lett. B **694**, 209 (2010).
[5] A. Keune, Ph.D. thesis, EPFL, Switzerland, 2012.
[6] J. P. Lees *et al.* (*BABAR* Collaboration), Phys. Rev. Lett. **109**, 101802 (2012).
[7] J. Beringer *et al.* (Particle Data Group), Phys. Rev. D **86**, 010001 (2012).
[8] A. A. Alves, Jr. *et al.* (LHCb Collaboration), JINST **3**, S08005 (2008).
[9] M. Adinolfi *et al.*, arXiv:1211.6759.
[10] R. Aaij *et al.*, JINST **8**, P04022 (2013).
[11] W. D. Hulsbergen, Nucl. Instrum. Methods Phys. Res., Sect. A **552**, 566 (2005).
[12] T. Sjöstrand, S. Mrenna, and P. Skands, J. High Energy Phys. 05 (2006) 026.
[13] I. Belyaev *et al.*, *Nuclear Science Symposium Conference Record (NSS/MIC)* (IEEE, Knoxville, TN, 2010), p. 1155.
[14] D. J. Lange, Nucl. Instrum. Methods Phys. Res., Sect. A **462**, 152 (2001).
[15] P. Golonka and Z. Was, Eur. Phys. J. C **45**, 97 (2006).
[16] J. Allison *et al.* (GEANT4 Collaboration), IEEE Trans. Nucl. Sci. **53**, 270 (2006); S. Agostinelli *et al.* (GEANT4 Collaboration), Nucl. Instrum. Methods Phys. Res., Sect. A **506**, 250 (2003).
[17] M. Clemencic, G. Corti, S. Easo, C. R. Jones, S. Miglioranzi, M. Pappagallo, and P. Robbe, J. Phys. Conf. Ser. **331**, 032023 (2011).
[18] T. Skwarnicki, Ph.D. thesis, Institute of Nuclear Physics, Krakow, 1986 [DESY-F31-86-02].
[19] A. Jaeger *et al.*, Report No. LHCb-PUB-2011-025.
[20] R. Aaij *et al.* (LHCb Collaboration), J. High Energy Phys. 04 (2013) 001.
[21] M. Pivk and F. R. Le Diberder, Nucl. Instrum. Methods Phys. Res., Sect. A **555**, 356 (2005).
[22] P. del Amo Sanchez *et al.* (*BABAR* Collaboration), Phys. Rev. D **82**, 111101 (2010).

R. Aaij,[38] C. Abellan Beteta,[33,n] A. Adametz,[11] B. Adeva,[34] M. Adinolfi,[43] C. Adrover,[6] A. Affolder,[49] Z. Ajaltouni,[5] J. Albrecht,[9] F. Alessio,[35] M. Alexander,[48] S. Ali,[38] G. Alkhazov,[27] P. Alvarez Cartelle,[34] A. A. Alves, Jr.,[22,35] S. Amato,[2] Y. Amhis,[7] L. Anderlini,[17,f] J. Anderson,[37] R. Andreassen,[57] R. B. Appleby,[51] O. Aquines Gutierrez,[10] F. Archilli,[18] A. Artamonov,[32] M. Artuso,[53] E. Aslanides,[6] G. Auriemma,[22,m] S. Bachmann,[11] J. J. Back,[45] C. Baesso,[54] V. Balagura,[28] W. Baldini,[16] R. J. Barlow,[51] C. Barschel,[35] S. Barsuk,[7] W. Barter,[44] Th. Bauer,[38] A. Bay,[36] J. Beddow,[48] I. Bediaga,[1] S. Belogurov,[28] K. Belous,[32] I. Belyaev,[28] E. Ben-Haim,[8] M. Benayoun,[8] G. Bencivenni,[18] S. Benson,[47] J. Benton,[43] A. Berezhnoy,[29] R. Bernet,[37] M.-O. Bettler,[44] M. van Beuzekom,[38] A. Bien,[11] S. Bifani,[12] T. Bird,[51] A. Bizzeti,[17,h] P. M. Bjørnstad,[51] T. Blake,[35] F. Blanc,[36] C. Blanks,[50] J. Blouw,[11] S. Blusk,[53] A. Bobrov,[31] V. Bocci,[22] A. Bondar,[31] N. Bondar,[27] W. Bonivento,[15] S. Borghi,[51] A. Borgia,[53] T. J. V. Bowcock,[49] E. Bowen,[37] C. Bozzi,[16] T. Brambach,[9] J. van den Brand,[39] J. Bressieux,[36] D. Brett,[51] M. Britsch,[10] T. Britton,[53] N. H. Brook,[43] H. Brown,[49] I. Burducea,[26] A. Bursche,[37] J. Buytaert,[35] S. Cadeddu,[15] O. Callot,[7] M. Calvi,[20,j] M. Calvo Gomez,[33,n] A. Camboni,[33] P. Campana,[18,35] A. Carbone,[14,c] G. Carboni,[21,k] R. Cardinale,[19,i] A. Cardini,[15] H. Carranza-Mejia,[47] L. Carson,[50] K. Carvalho Akiba,[2] G. Casse,[49] M. Cattaneo,[35] Ch. Cauet,[9] M. Charles,[52] Ph. Charpentier,[35] P. Chen,[3,36] N. Chiapolini,[37] M. Chrzaszcz,[23] K. Ciba,[35] X. Cid Vidal,[34] G. Ciezarek,[50] P. E. L. Clarke,[47] M. Clemencic,[35] H. V. Cliff,[44] J. Closier,[35] C. Coca,[26] V. Coco,[38] J. Cogan,[6] E. Cogneras,[5] P. Collins,[35] A. Comerma-Montells,[33] A. Contu,[15,52] A. Cook,[43] M. Coombes,[43] S. Coquereau,[8] G. Corti,[35] B. Couturier,[35] G. A. Cowan,[36] D. Craik,[45] S. Cunliffe,[50] R. Currie,[47] C. D'Ambrosio,[35] P. David,[8] P. N. Y. David,[38] I. De Bonis,[4] K. De Bruyn,[38] S. De Capua,[51] M. De Cian,[37] J. M. De Miranda,[1] L. De Paula,[2]

W. De Silva,[57] P. De Simone,[18] D. Decamp,[4] M. Deckenhoff,[9] H. Degaudenzi,[36,35] L. Del Buono,[8] C. Deplano,[15] D. Derkach,[14] O. Deschamps,[5] F. Dettori,[39] A. Di Canto,[11] J. Dickens,[44] H. Dijkstra,[35] M. Dogaru,[26] F. Domingo Bonal,[33,n] S. Donleavy,[49] F. Dordei,[11] A. Dosil Suárez,[34] D. Dossett,[45] A. Dovbnya,[40] F. Dupertuis,[36] R. Dzhelyadin,[32] A. Dziurda,[23] A. Dzyuba,[27] S. Easo,[46,35] U. Egede,[50] V. Egorychev,[28] S. Eidelman,[31] D. van Eijk,[38] S. Eisenhardt,[47] U. Eitschberger,[9] R. Ekelhof,[9] L. Eklund,[48] I. El Rifai,[5] Ch. Elsasser,[37] D. Elsby,[42] A. Falabella,[14,e] C. Färber,[11] G. Fardell,[47] C. Farinelli,[38] S. Farry,[12] V. Fave,[36] D. Ferguson,[47] V. Fernandez Albor,[34] F. Ferreira Rodrigues,[1] M. Ferro-Luzzi,[35] S. Filippov,[30] C. Fitzpatrick,[35] M. Fontana,[10] F. Fontanelli,[19,i] R. Forty,[35] O. Francisco,[2] M. Frank,[35] C. Frei,[35] M. Frosini,[17,f] S. Furcas,[20] E. Furfaro,[21] A. Gallas Torreira,[34] D. Galli,[14,c] M. Gandelman,[2] P. Gandini,[52] Y. Gao,[3] J. Garofoli,[53] P. Garosi,[51] J. Garra Tico,[44] L. Garrido,[33] C. Gaspar,[35] R. Gauld,[52] E. Gersabeck,[11] M. Gersabeck,[51] T. Gershon,[45,35] Ph. Ghez,[4] V. Gibson,[44] V. V. Gligorov,[35] C. Göbel,[54] D. Golubkov,[28] A. Golutvin,[50,28,35] A. Gomes,[2] H. Gordon,[52] M. Grabalosa Gándara,[5] R. Graciani Diaz,[33] L. A. Granado Cardoso,[35] E. Graugés,[33] G. Graziani,[17] A. Grecu,[26] E. Greening,[52] S. Gregson,[44] O. Grünberg,[55] B. Gui,[53] E. Gushchin,[30] Yu. Guz,[32] T. Gys,[35] C. Hadjivasiliou,[53] G. Haefeli,[36] C. Haen,[35] S. C. Haines,[44] S. Hall,[50] T. Hampson,[43] S. Hansmann-Menzemer,[11] N. Harnew,[52] S. T. Harnew,[43] J. Harrison,[51] P. F. Harrison,[45] T. Hartmann,[55] J. He,[7] V. Heijne,[38] K. Hennessy,[49] P. Henrard,[5] J. A. Hernando Morata,[34] E. van Herwijnen,[35] E. Hicks,[49] D. Hill,[52] M. Hoballah,[5] C. Hombach,[51] P. Hopchev,[4] W. Hulsbergen,[38] P. Hunt,[52] T. Huse,[49] N. Hussain,[52] D. Hutchcroft,[49] D. Hynds,[48] V. Iakovenko,[41] P. Ilten,[12] R. Jacobsson,[35] A. Jaeger,[11] E. Jans,[38] F. Jansen,[38] P. Jaton,[36] F. Jing,[3] M. John,[52] D. Johnson,[52] C. R. Jones,[44] B. Jost,[35] M. Kaballo,[9] S. Kandybei,[40] M. Karacson,[35] T. M. Karbach,[35] I. R. Kenyon,[42] U. Kerzel,[35] T. Ketel,[39] A. Keune,[36] B. Khanji,[20] O. Kochebina,[7] I. Komarov,[36,29] R. F. Koopman,[39] P. Koppenburg,[38] M. Korolev,[29] A. Kozlinskiy,[38] L. Kravchuk,[30] K. Kreplin,[11] M. Kreps,[45] G. Krocker,[11] P. Krokovny,[31] F. Kruse,[9] M. Kucharczyk,[20,23,j] V. Kudryavtsev,[31] T. Kvaratskheliya,[28,35] V. N. La Thi,[36] D. Lacarrere,[35] G. Lafferty,[51] A. Lai,[15] D. Lambert,[47] R. W. Lambert,[39] E. Lanciotti,[35] G. Lanfranchi,[18,35] C. Langenbruch,[35] T. Latham,[45] C. Lazzeroni,[42] R. Le Gac,[6] J. van Leerdam,[38] J.-P. Lees,[4] R. Lefèvre,[5] A. Leflat,[29,35] J. Lefrançois,[7] O. Leroy,[6] Y. Li,[3] L. Li Gioi,[5] M. Liles,[49] R. Lindner,[35] C. Linn,[11] B. Liu,[3] G. Liu,[35] J. von Loeben,[20] J. H. Lopes,[2] E. Lopez Asamar,[33] N. Lopez-March,[36] H. Lu,[3] J. Luisier,[36] H. Luo,[47] F. Machefert,[7] I. V. Machikhiliyan,[4,28] F. Maciuc,[26] O. Maev,[27,35] S. Malde,[52] G. Manca,[15,d] G. Mancinelli,[6] N. Mangiafave,[44] U. Marconi,[14] R. Märki,[36] J. Marks,[11] G. Martellotti,[22] A. Martens,[8] L. Martin,[52] A. Martín Sánchez,[7] M. Martinelli,[38] D. Martinez Santos,[39] D. Martins Tostes,[2] A. Massafferri,[1] R. Matev,[35] Z. Mathe,[35] C. Matteuzzi,[20] M. Matveev,[27] E. Maurice,[6] A. Mazurov,[16,30,35,e] J. McCarthy,[42] R. McNulty,[12] B. Meadows,[57,52] F. Meier,[9] M. Meissner,[11] M. Merk,[38] D. A. Milanes,[8] M.-N. Minard,[4] J. Molina Rodriguez,[54] S. Monteil,[5] D. Moran,[51] P. Morawski,[23] R. Mountain,[53] I. Mous,[38] F. Muheim,[47] K. Müller,[37] R. Muresan,[26] B. Muryn,[24] B. Muster,[36] P. Naik,[43] T. Nakada,[36] R. Nandakumar,[46] I. Nasteva,[1] M. Needham,[47] N. Neufeld,[35] A. D. Nguyen,[36] T. D. Nguyen,[36] C. Nguyen-Mau,[36,o] M. Nicol,[7] V. Niess,[5] R. Niet,[9] N. Nikitin,[29] T. Nikodem,[11] S. Nisar,[56] A. Nomerotski,[52] A. Novoselov,[32] A. Oblakowska-Mucha,[24] V. Obraztsov,[32] S. Oggero,[38] S. Ogilvy,[48] O. Okhrimenko,[41] R. Oldeman,[15,35,d] M. Orlandea,[26] J. M. Otalora Goicochea,[2] P. Owen,[50] B. K. Pal,[53] A. Palano,[13,b] M. Palutan,[18] J. Panman,[35] A. Papanestis,[46] M. Pappagallo,[48] C. Parkes,[51] C. J. Parkinson,[50] G. Passaleva,[17] G. D. Patel,[49] M. Patel,[50] G. N. Patrick,[46] C. Patrignani,[19,i] C. Pavel-Nicorescu,[26] A. Pazos Alvarez,[34] A. Pellegrino,[38] G. Penso,[22,l] M. Pepe Altarelli,[35] S. Perazzini,[14,c] D. L. Perego,[20,j] E. Perez Trigo,[34] A. Pérez-Calero Yzquierdo,[33] P. Perret,[5] M. Perrin-Terrin,[6] G. Pessina,[20] K. Petridis,[50] A. Petrolini,[19,i] A. Phan,[53] E. Picatoste Olloqui,[33] B. Pietrzyk,[4] T. Pilař,[45] D. Pinci,[22] S. Playfer,[47] M. Plo Casasus,[34] F. Polci,[8] G. Polok,[23] A. Poluektov,[45,31] E. Polycarpo,[2] D. Popov,[10] B. Popovici,[26] C. Potterat,[33] A. Powell,[52] J. Prisciandaro,[36] V. Pugatch,[41] A. Puig Navarro,[36] W. Qian,[4] J. H. Rademacker,[43] B. Rakotomiaramanana,[36] M. S. Rangel,[2] I. Raniuk,[40] N. Rauschmayr,[35] G. Raven,[39] S. Redford,[52] M. M. Reid,[45] A. C. dos Reis,[1] S. Ricciardi,[46] A. Richards,[50] K. Rinnert,[49] V. Rives Molina,[33] D. A. Roa Romero,[5] P. Robbe,[7] E. Rodrigues,[51] P. Rodriguez Perez,[34] G. J. Rogers,[44] S. Roiser,[35] V. Romanovsky,[32] A. Romero Vidal,[34] J. Rouvinet,[36] T. Ruf,[35] H. Ruiz,[33] G. Sabatino,[22,k] J. J. Saborido Silva,[34] N. Sagidova,[27] P. Sail,[48] B. Saitta,[15,d] C. Salzmann,[37] B. Sanmartin Sedes,[34] M. Sannino,[19,i] R. Santacesaria,[22] C. Santamarina Rios,[34] E. Santovetti,[21,k] M. Sapunov,[6] A. Sarti,[18,l] C. Satriano,[22,m] A. Satta,[21] M. Savrie,[16,e] D. Savrina,[28,29] P. Schaack,[50] M. Schiller,[39] H. Schindler,[35] S. Schleich,[9] M. Schlupp,[9] M. Schmelling,[10] B. Schmidt,[35] O. Schneider,[36] A. Schopper,[35] M.-H. Schune,[7] R. Schwemmer,[35] B. Sciascia,[18] A. Sciubba,[18,l] M. Seco,[34] A. Semennikov,[28] K. Senderowska,[24] I. Sepp,[50] N. Serra,[37] J. Serrano,[6] P. Seyfert,[11] M. Shapkin,[32] I. Shapoval,[40,35] P. Shatalov,[28] Y. Shcheglov,[27] T. Shears,[49,35] L. Shekhtman,[31] O. Shevchenko,[40]

V. Shevchenko,[28] A. Shires,[50] R. Silva Coutinho,[45] T. Skwarnicki,[53] N. A. Smith,[49] E. Smith,[52,46] M. Smith,[51] K. Sobczak,[5] M. D. Sokoloff,[57] F. J. P. Soler,[48] F. Soomro,[18,35] D. Souza,[43] B. Souza De Paula,[2] B. Spaan,[9] A. Sparkes,[47] P. Spradlin,[48] F. Stagni,[35] S. Stahl,[11] O. Steinkamp,[37] S. Stoica,[26] S. Stone,[53] B. Storaci,[37] M. Straticiuc,[26] U. Straumann,[37] V. K. Subbiah,[35] S. Swientek,[9] V. Syropoulos,[39] M. Szczekowski,[25] P. Szczypka,[36,35] T. Szumlak,[24] S. T'Jampens,[4] M. Teklishyn,[7] E. Teodorescu,[26] F. Teubert,[35] C. Thomas,[52] E. Thomas,[35] J. van Tilburg,[11] V. Tisserand,[4] M. Tobin,[37] S. Tolk,[39] D. Tonelli,[35] S. Topp-Joergensen,[52] N. Torr,[52] E. Tournefier,[4,50] S. Tourneur,[36] M. T. Tran,[36] M. Tresch,[37] A. Tsaregorodtsev,[6] P. Tsopelas,[38] N. Tuning,[38] M. Ubeda Garcia,[35] A. Ukleja,[25] D. Urner,[51] U. Uwer,[11] V. Vagnoni,[14] G. Valenti,[14] R. Vazquez Gomez,[33] P. Vazquez Regueiro,[34] S. Vecchi,[16] J. J. Velthuis,[43] M. Veltri,[17,g] G. Veneziano,[36] M. Vesterinen,[35] B. Viaud,[7] D. Vieira,[2] X. Vilasis-Cardona,[33,n] A. Vollhardt,[37] D. Volyanskyy,[10] D. Voong,[43] A. Vorobyev,[27] V. Vorobyev,[31] C. Voß,[55] H. Voss,[10] R. Waldi,[55] R. Wallace,[12] S. Wandernoth,[11] J. Wang,[53] D. R. Ward,[44] N. K. Watson,[42] A. D. Webber,[51] D. Websdale,[50] M. Whitehead,[45] J. Wicht,[35] J. Wiechczynski,[23] D. Wiedner,[11] L. Wiggers,[38] G. Wilkinson,[52] M. P. Williams,[45,46] M. Williams,[50,p] F. F. Wilson,[46] J. Wishahi,[9] M. Witek,[23] S. A. Wotton,[44] S. Wright,[44] S. Wu,[3] K. Wyllie,[35] Y. Xie,[47,35] F. Xing,[52] Z. Xing,[53] Z. Yang,[3] R. Young,[47] X. Yuan,[3] O. Yushchenko,[32] M. Zangoli,[14] M. Zavertyaev,[10,a] F. Zhang,[3] L. Zhang,[53] W. C. Zhang,[12] Y. Zhang,[3] A. Zhelezov,[11] L. Zhong,[3] and A. Zvyagin[35]

(LHCb Collaboration)

[1]*Centro Brasileiro de Pesquisas Físicas (CBPF), Rio de Janeiro, Brazil*
[2]*Universidade Federal do Rio de Janeiro (UFRJ), Rio de Janeiro, Brazil*
[3]*Center for High Energy Physics, Tsinghua University, Beijing, China*
[4]*Laboratoire d'Annecy-le-Vieux de Physique des Particules, Université de Savoie, CNRS/IN2P3, Annecy-Le-Vieux, France*
[5]*Clermont Université, Université Blaise Pascal, CNRS/IN2P3, LPC, Clermont-Ferrand, France*
[6]*Centre de Physique des Particules de Marseille, Aix-Marseille Université, CNRS/IN2P3, Marseille, France*
[7]*Laboratoire de l'accelérateur linéaire, Université Paris-Sud, CNRS/IN2P3, Orsay, France*
[8]*Laboratory of Nuclear Physics and High Energy Physics, Université Pierre et Marie Curie, Université Paris Diderot, CNRS/IN2P3, Paris, France*
[9]*Fakultät Physik, Technische Universität Dortmund, Dortmund, Germany*
[10]*Max-Planck-Institut für Kernphysik (MPIK), Heidelberg, Germany*
[11]*Physikalisches Institut, Ruprecht-Karls-Universität Heidelberg, Heidelberg, Germany*
[12]*School of Physics, University College Dublin, Dublin, Ireland*
[13]*Sezione INFN di Bari, Bari, Italy*
[14]*Sezione INFN di Bologna, Bologna, Italy*
[15]*Sezione INFN di Cagliari, Cagliari, Italy*
[16]*Sezione INFN di Ferrara, Ferrara, Italy*
[17]*Sezione INFN di Firenze, Firenze, Italy*
[18]*Laboratori Nazionali dell'INFN di Frascati, Frascati, Italy*
[19]*Sezione INFN di Genova, Genova, Italy*
[20]*Sezione INFN di Milano Bicocca, Milano, Italy*
[21]*Sezione INFN di Roma Tor Vergata, Roma, Italy*
[22]*Sezione INFN di Roma La Sapienza, Roma, Italy*
[23]*Henryk Niewodniczanski Institute of Nuclear Physics Polish Academy of Sciences, Kraków, Poland*
[24]*AGH University of Science and Technology, Kraków, Poland*
[25]*National Center for Nuclear Research (NCBJ), Warsaw, Poland*
[26]*Horia Hulubei National Institute of Physics and Nuclear Engineering, Bucharest-Magurele, Romania*
[27]*Petersburg Nuclear Physics Institute (PNPI), Gatchina, Russia*
[28]*Institute of Theoretical and Experimental Physics (ITEP), Moscow, Russia*
[29]*Institute of Nuclear Physics, Moscow State University (SINP MSU), Moscow, Russia*
[30]*Institute for Nuclear Research of the Russian Academy of Sciences (INR RAN), Moscow, Russia*
[31]*Budker Institute of Nuclear Physics (SB RAS) and Novosibirsk State University, Novosibirsk, Russia*
[32]*Institute for High Energy Physics (IHEP), Protvino, Russia*
[33]*Universitat de Barcelona, Barcelona, Spain*
[34]*Universidad de Santiago de Compostela, Santiago de Compostela, Spain*
[35]*European Organization for Nuclear Research (CERN), Geneva, Switzerland*
[36]*Ecole Polytechnique Fédérale de Lausanne (EPFL), Lausanne, Switzerland*
[37]*Physik-Institut, Universität Zürich, Zürich, Switzerland*

[38]*Nikhef National Institute for Subatomic Physics, Amsterdam, The Netherlands*
[39]*Nikhef National Institute for Subatomic Physics and VU University Amsterdam, Amsterdam, The Netherlands*
[40]*NSC Kharkiv Institute of Physics and Technology (NSC KIPT), Kharkiv, Ukraine*
[41]*Institute for Nuclear Research of the National Academy of Sciences (KINR), Kyiv, Ukraine*
[42]*University of Birmingham, Birmingham, United Kingdom*
[43]*H. H. Wills Physics Laboratory, University of Bristol, Bristol, United Kingdom*
[44]*Cavendish Laboratory, University of Cambridge, Cambridge, United Kingdom*
[45]*Department of Physics, University of Warwick, Coventry, United Kingdom*
[46]*STFC Rutherford Appleton Laboratory, Didcot, United Kingdom*
[47]*School of Physics and Astronomy, University of Edinburgh, Edinburgh, United Kingdom*
[48]*School of Physics and Astronomy, University of Glasgow, Glasgow, United Kingdom*
[49]*Oliver Lodge Laboratory, University of Liverpool, Liverpool, United Kingdom*
[50]*Imperial College London, London, United Kingdom*
[51]*School of Physics and Astronomy, University of Manchester, Manchester, United Kingdom*
[52]*Department of Physics, University of Oxford, Oxford, United Kingdom*
[53]*Syracuse University, Syracuse, New York, USA*
[54]*Pontifícia Universidade Católica do Rio de Janeiro (PUC-Rio), Rio de Janeiro, Brazil (associated to Universidade Federal do Rio de Janeiro (UFRJ), Rio de Janeiro, Brazil)*
[55]*Institut für Physik, Universität Rostock, Rostock, Germany (associated to Physikalisches Institut, Ruprecht-Karls-Universität Heidelberg, Heidelberg, Germany)*
[56]*Institute of Information Technology, COMSATS, Lahore, Pakistan (associated to Syracuse University, Syracuse, New York, USA)*
[57]*University of Cincinnati, Cincinnati, Ohio, USA (associated to Syracuse University, Syracuse, New York, USA)*

[a]P. N. Lebedev Physical Institute, Russian Academy of Science (LPI RAS), Moscow, Russia.
[b]Università di Bari, Bari, Italy.
[c]Università di Bologna, Bologna, Italy.
[d]Università di Cagliari, Cagliari, Italy.
[e]Università di Ferrara, Ferrara, Italy.
[f]Università di Firenze, Firenze, Italy.
[g]Università di Urbino, Urbino, Italy.
[h]Università di Modena e Reggio Emilia, Modena, Italy.
[i]Università di Genova, Genova, Italy.
[j]Università di Milano Bicocca, Milano, Italy.
[k]Università di Roma Tor Vergata, Roma, Italy.
[l]Università di Roma La Sapienza, Roma, Italy.
[m]Università della Basilicata, Potenza, Italy.
[n]LIFAELS, La Salle, Universitat Ramon Llull, Barcelona, Spain.
[o]Hanoi University of Science, Hanoi, Vietnam.
[p]Massachusetts Institute of Technology, Cambridge, Massachusetts, USA.

Bibliography

[1] Lyndon Evans and Philip Bryant. LHC Machine. *Journal of Instrumentation*, 3(08):S08001, 2008.

[2] G. Aad et al. The ATLAS Experiment at the CERN Large Hadron Collider. *JINST*, 3:S08003, 2008.

[3] K. Aamodt et al. The ALICE experiment at the CERN LHC. *JINST*, 3:S08002, 2008.

[4] S. Chatrchyan et al. The CMS experiment at the CERN LHC. *JINST*, 3:S08004, 2008.

[5] A. A. Alves Jr. et al. The LHCb detector at the LHC. *JINST*, 3:S08005, 2008.

[6] Oliver Sim Bruning, Paul Collier, P Lebrun, Stephen Myers, Ranko Ostojic, John Poole, and Paul Proudlock. *LHC Design Report*. CERN, Geneva, 2004.

[7] R Aaij et al. Measurement of $\sigma(pp \to b\bar{b}X)$ at $\sqrt{s} = 7$ TeV in the forward region. *Physics Letters B*, 694(3):209 – 216, 2010.

[8] B. Aubert et al. The BABAR detector. *Nuclear Instruments and Methods in Physics Research Section A: Accelerators, Spectrometers, Detectors and Associated Equipment*, 479(1):1 – 116, 2002. Detectors for Asymmetric B-factories.

[9] A. Abashian et al. The Belle detector. *Nuclear Instruments and Methods in Physics Research Section A: Accelerators, Spectrometers, Detectors and Associated Equipment*, 479(1):117 – 232, 2002. Detectors for Asymmetric B-factories.

[10] E. Norrbin and T. Sjostrand. Production and hadronization of heavy quarks. *Eur.Phys.J.*, C17:137–161, 2000.

[11] T Bird, S Easo, U Kerzel, R W Lambert, and K Vervink. Time dependent semileptonic studies: correcting for missing momentum and the effect of multiple interactions.

Technical Report LHCb-INT-2011-004. CERN-LHCb-INT-2011-004, CERN, Geneva, Feb 2011.

[12] K.A. Olive et al. Review of particle physics. *Chin.Phys.*, C38:090001, 2014.

[13] Roel Aaij et al. Measurement of *CP* asymmetries in the decays $B^0 \to K^{*0}\mu^+\mu^-$ and $B^+ \to K^+\mu^+\mu^-$. *JHEP*, 1409:177, 2014.

[14] Roel Aaij et al. Measurement of the $\bar{B}^0 - B^0$ and $\bar{B}^0_s - B^0_s$ production asymmetries in pp collisions at $\sqrt{s} = 7$ TeV. *Phys.Lett.*, B739:218–228, 2014.

[15] K. Lai, W. A. Leibovich, and A. Petrov. $D^\pm$ production asymmetry at the LHC from heavy quark recombination. *Phys. Rev. D*, 90:054022, Sep 2014.

[16] R. Aaij et al. Precision Measurement of CP Violation in $B^0_s \to J/\psi K^+K^-$ Decays. *Phys. Rev. Lett.*, 114:041801, Jan 2015.

[17] Roel Aaij et al. Measurement of B^+_c production in proton-proton collisions at $\sqrt{s} = 8$ TeV. Technical Report arXiv:1411.2943. LHCB-PAPER-2014-050. CERN-PH-EP-2014-269, CERN, Geneva, Nov 2014.

[18] R. Aaij et al. Measurement of the lifetime of the B^+_c meson using the $B_c \to J/\psi\pi^+$ decay mode. *Physics Letters B*, 742(0):29 – 37, 2015.

[19] R. Aaij et al. First observation of a baryonic B^+_c decay. *Phys. Rev. Lett.*, 113:152003, Oct 2014.

[20] E. Noether, D. Nachr, and D. Gesellsch. Invariante Variationsprobleme. *Nachr. D. Knig. Gesellsch. D. Wiss. Zu Gttingen, Math-phys (1918) 235.*

[21] C. S. Wu, E. Ambler, R. W. Hayward, D. D. Hoppes, and R. P. Hudson. Experimental Test of Parity Conservation in Beta Decay. *Phys. Rev.*, 105:1413–1415, Feb 1957.

[22] D.J. Griffiths. *Introduction to elementary particles.* Wiley, 1987.

[23] Hilary Greaves and Teruji Thomas. On the CPT theorem. *Studies in History and Philosophy of Science Part B: Studies in History and Philosophy of Modern Physics*, 45(0):46 – 65, 2014.

[24] J. H. Christenson, J. W. Cronin, V. L. Fitch, and R. Turlay. Evidence for the 2π Decay of the K^0_2 Meson. *Phys. Rev. Lett.*, 13:138–140, Jul 1964.

[25] R. Blair et al. The CDF-II detector: Technical design report. 1996.

[26] S. Abachi. The D0 upgrade: The Detector and its physics. 1996.

[27] Makoto Kobayashi and Toshihide Maskawa. CP Violation in the Renormalizable Theory of Weak Interaction. *Prog.Theor.Phys.*, 49:652–657, 1973.

[28] Nicola Cabibbo. Unitary Symmetry and Leptonic Decays. *Phys.Rev.Lett.*, 10:531–533, 1963.

[29] S.W. Herb, D.C. Hom, L.M. Lederman, J.C. Sens, H.D. Snyder, et al. Observation of a Dimuon Resonance at 9.5-GeV in 400-GeV Proton-Nucleus Collisions. *Phys.Rev.Lett.*, 39:252–255, 1977.

[30] J. J. Aubert et al. Experimental observation of a heavy particle J. *Phys. Rev. Lett.*, 33:1404–1406, 1974.

[31] Ling-Lie Chau and Wai-Yee Keung. Comments on the Parametrization of the Kobayashi-Maskawa Matrix. *Phys. Rev. Lett.*, 53:1802–1805, Nov 1984.

[32] Lincoln Wolfenstein. Parametrization of the Kobayashi-Maskawa Matrix. *Phys. Rev. Lett.*, 51:1945–1947, Nov 1983.

[33] Measurement of CP violation in $B^0 \to J/\psi K^0_S$ decays. Technical Report CERN-PH-EP-2015-076. LHCB-PAPER-2015-004, CERN, Geneva, Mar 2015.

[34] C. Jarlskog. Commutator of the Quark Mass Matrices in the Standard Electroweak Model and a Measure of Maximal CP Nonconservation. *Phys. Rev. Lett.*, 55:1039–1042, Sep 1985.

[35] CKMFitter Collaboration. Predictions of selected flavor observables within the standard model. *Phys. Rev. D*, 84:033005, Aug 2011.

[36] UTfit Collaboration. The unitarity triangle fit in the standard model and hadronic parameters from lattice QCD: a reappraisal after the measurements of Δm_s and $BR(B \to \tau\nu)$. *Journal of High Energy Physics*, 2006(10):081, 2006.

[37] Christian Elsasser. "$b\bar{b}$ cross section plots". Accessed September 25, 2015.

[38] Sjöstrand, Torbjörn and Mrenna, Stephen and Skands, Peter. A brief introduction to PYTHIA 8.1. *Comput.Phys.Commun.*, 178:852–867, 2008.

[39] LHCb detector performance. *International Journal of Modern Physics A*, 30(07):1530022, 2015.

[40] R. Aaij et al. Performance of the LHCb Vertex Locator. *Journal of Instrumentation*, 9(09):P09007, 2014.

[41] P R Barbosa-Marinho et al. *LHCb VELO (VErtex LOcator): Technical Design Report*. Technical Design Report LHCb. CERN, Geneva, 2001.

[42] P R Barbosa-Marinho et al. *LHCb inner tracker: Technical Design Report*. Technical Design Report LHCb. CERN, Geneva, 2002. revised version number 1 submitted on 2002-11-13 14:14:34.

[43] Performance of the LHCb Outer Tracker. *Journal of Instrumentation*, 9(01):P01002, 2014.

[44] P R Barbosa-Marinho et al. *LHCb outer tracker: Technical Design Report*. Technical Design Report LHCb. CERN, Geneva, 2001.

[45] M. Adinolfi et al. Performance of the LHCb RICH detector at the LHC. *The European Physical Journal C*, 73(5), 2013.

[46] S Amato et al. *LHCb RICH: Technical Design Report*. Technical Design Report LHCb. CERN, Geneva, 2000.

[47] S Amato et al. *LHCb calorimeters: Technical Design Report*. Technical Design Report LHCb. CERN, Geneva, 2000.

[48] P Perret and X Vilasis-Cardona. Performance of the LHCb calorimeters during the period 2010-2012. Technical Report LHCb-PROC-2014-019. CERN-LHCb-PROC-2014-019, CERN, Geneva, Aug 2014. see LHCb-TALK-2014-236.

[49] A. A. Jr. Alves et al. Performance of the LHCb muon system. *Journal of Instrumentation*, 8(02):P02022, 2013.

[50] P R Barbosa-Marinho et al. *LHCb muon system: Technical Design Report*. Technical Design Report LHCb. CERN, Geneva, 2001.

[51] R. Aaij et al. The LHCb trigger and its performance in 2011. *Journal of Instrumentation*, 8(04):P04022, 2013.

[52] L. Breiman, J. H. Friedman, R. A. Olshen, and C. J. Stone. *Classification and regression trees*. Wadsworth international group, Belmont, California, USA, 1984.

[53] Robert E. Schapire and Yoav Freund. A decision-theoretic generalization of on-line learning and an application to boosting. *Jour. Comp. and Syst. Sc.*, 55:119, 1997.

[54] The LHCb collaboration. Measurement of the track reconstruction efficiency at LHCb. *Journal of Instrumentation*, 10(02):P02007, 2015.

[55] A. Powell et al. Particle identification at LHCb. *PoS*, ICHEP2010:020, 2010.

[56] A study of CP violation in $B^{\mp} \to Dh^{\mp}$ $(h = K, \pi)$ with the modes $D \to K^{\mp}\pi^{\pm}\pi^0$, $D \to \pi^+\pi^-\pi^0$ and $D \to K^+K^-\pi^0$. Mar 2015. To be submitted to PRD.

[57] Michael Gronau and David London. How to determine all the angles of the unitarity triangle from $B^0_d \to DK_s$ and $B^0_s \to D\phi$. *Physics Letters B*, 253(34):483 – 488, 1991.

[58] Michael Gronau and Daniel Wyler. On determining a weak phase from charged B decay asymmetries. *Physics Letters B*, 265(12):172 – 176, 1991.

[59] G. Wilkinson, C. Thomas, and S. Malde. Analysis in progress using CLEOc data.

[60] David Atwood, Isard Dunietz, and Amarjit Soni. Enhanced CP violation with $B \to KD^0(\bar{D}^0)$ modes and extraction of the CKM angle γ. *Phys.Rev.Lett.*, 78:3257, 1997.

[61] David Atwood, Isard Dunietz, and Amarjit Soni. Improved methods for observing CP violation in $B^{\pm} \to KD$ and measuring the CKM phase γ. *Phys. Rev. D*, 63:036005, Jan 2001.

[62] R. Aaij et al. Observation of CP violation in $B^{\pm} \to DK^{\pm}$ decays. *Phys. Lett. B*, 712(arXiv:1203.3662. LHCB-PAPER-2012-001. CERN-PH-EP-2012-071):203–212. 14 p, Mar 2012.

[63] R. Aaij et al. Observation of the suppressed ADS modes $B^{\pm} \to [\pi^{\pm}K^{\mp}\pi^+\pi^-]_D K^{\pm}$ and $B^{\pm} \to [\pi^{\pm}K^{\mp}\pi^+\pi^-]_D \pi^{\pm}$. *Phys. Lett. B*, 723(arXiv:1303.4646. CERN-PH-EP-2013-038. LHCB-PAPER-2012-055):44–53. 20 p, Mar 2013. Comments: 14 pages, 3 figures.

[64] Vladimir V Gligorov. A single track HLT1 trigger. (LHCb-PUB-2011-003, CERN-LHCb-PUB-2011-003, LHCb-INT-2010-053), 2011.

[65] V. V. Gligorov and M. Williams. Efficient, reliable and fast high-level triggering using a bonsai boosted decision tree. *JINST*, 8:P02013, 2013.

[66] Andreas Hoecker, Peter Speckmayer, Joerg Stelzer, Jan Therhaag, Eckhard von Toerne, and Helge Voss. TMVA: Toolkit for Multivariate Data Analysis. *PoS*, ACAT:040, 2007.

[67] D Hill, M John, N Hussain, and G Wilkinson. Analysis of $B^{\pm} \to Dh^{\pm}$ with $D \to K\pi, KK, \pi\pi, K\pi\pi\pi, \pi\pi\pi\pi$ final states.

[68] M Clemencic et al. The LHCb simulation application, Gauss: Design, evolution and experience. *J. Phys. Conf. Ser.*, 331:032023, 2011.

[69] I. Belyaev et al. Handling of the generation of primary events in Gauss, the LHCb simulation framework. *Nuclear Science Symposium Conference Record (NSS/MIC)*, IEEE:1155, 2010.

[70] D. J. Lange. The EvtGen particle decay simulation package. *Nucl. Instrum. Meth.*, A462:152–155, 2001.

[71] S. Agostinelli et al. Geant4: a simulation toolkit. *Nucl. Instrum. Meth.*, A506:250, 2003.

[72] Piotr Golonka and Zbigniew Was. PHOTOS Monte Carlo: A precision tool for QED corrections in Z and W decays. *Eur.Phys.J.*, C45:97–107, 2006.

[73] Kyle Cranmer. Kernel estimation in high-energy physics. *Computer Physics Communications*, 136(3):198 – 207, 2001.

[74] Tomasz Skwarnicki. *A study of the radiative cascade transitions between the Upsilon-prime and Upsilon resonances*. PhD thesis, Institute of Nuclear Physics, Krakow, 1986.

[75] Muriel Pivk and Francois R. Le Diberder. sPlot: A statistical tool to unfold data distributions. *Nucl.Instrum.Meth.*, A555:356–369, 2005.

[76] R. Aaij et al. Studies of beauty baryon decays to D^0ph^- and $\Lambda_c^+h^-$ final states. *Phys. Rev. D*, 89:032001, Feb 2014.

[77] H Gordon, R W Lambert, J van Tilburg, and M Vesterinen. A Measurement of the $K\pi$ Detection Asymmetry. Technical Report LHCb-INT-2012-027. CERN-LHCb-INT-2012-027, CERN, Geneva, Feb 2013.

[78] D Hill, M John, M Vesterinen, and M Stahl. The $B^{\mp}$ production asymmetry in Run I and the CP asymmetry of $B^{\mp} \to J/\psi K^{\mp}$.

[79] Victor Mukhamedovich Abazov et al. Measurement of direct CP violation parameters in $B^{\pm} \to J/\psi K^{\pm}$ and $B^{\pm} \to J/\psi \pi^{\pm}$ decays with 10.4 fb^{-1} of Tevatron data. *Phys.Rev.Lett.*, 110(24):241801, 2013.

[80] V.V. Kiselev. Decays of the B_c meson. hep-ph/0308214, 2003.

[81] Hui-feng Fu, Yue Jiang, C.S. Kim, and Guo-Li Wang. Probing non-leptonic two-body decays of B_c meson. *Journal of High Energy Physics*, 2011(6), 2011.

[82] Dong-Sheng Du and Zheng-Tao Wei. Space-like Penguin effects in B_c decays. *Eur. Phys. J. C*, 5(4):705–709, 1998.

[83] G. Punzi. Sensitivity of searches for new signals and its optimization. In L. Lyons, R. Mount, and R. Reitmeyer, editors, *Statistical Problems in Particle Physics, Astrophysics, and Cosmology*, page 79, 2003.

[84] Y. Amhis et al. Averages of b-hadron, c-hadron, and τ-lepton properties as of early 2012. 2012.

[85] Lorenzo Moneta, Kevin Belasco, Kyle Cranmer, Sven Kreiss, Alfio Lazzaro, Danilo Piparo, Gregory Schott, Wouter Verkerke, and Matthias Wolf. The RooStats Project, February 2011.